CR 168202
PWA-5907-19

NASA

AEROTHERMAL MODELING
PHASE I

FINAL REPORT

Contract NAS3-23524

May 27, 1983

Prepared for
NASA-Lewis Research Center
Cleveland, Ohio 44135

by

Geoffrey J. Sturgess, Program Manager
Commercial Engineering
Pratt & Whitney Aircraft
UNITED TECHNOLOGIES CORPORATION

1.REPORT NO.	2. GOVERNMENT AGENCY	3.RECIPIENT'S CATALOG NO.
NASA CR 168202		

4.TITLE AND SUBTITLE	5. REPORT DATE
Aerothermal Modeling Program - Phase I Final Report	July 1983
	6. PERFORMING ORG. CODE
7.AUTHOR(S) Geoffrey J. Sturgess, Program Manager	8. PERFORMING ORG. REPT. NO. PWA-5907-19
9.PERFORMING ORG. NAME AND ADDRESS UNITED TECHNOLOGIES CORPORATION Pratt & Whitney - Commercial Engineering East Hartford, Connecticut 06108	10. WORK UNIT NO. 11. CONTRACT OR GRANT NO. NAS3-23524
12. SPONSORING AGENCY NAME AND ADDRESS National Aeronautics and Space Administration Lewis Research Center 21000 Brookpark Road, Cleveland, Ohio 44135	13. TYPE REPT./PERIOD COVERED Final Rept. 7/82 - 5/83 14. SPONSORING AGENCY CODE

15. SUPPLEMENTARY NOTES
NASA Project Manager, Edward J. Mularz
US Army Research & Technology Laboratories (AVSCOM), Propulsion Laboratory,
NASA-Lewis Research Center, 21000 Brookpark Road, Cleveland, Ohio 44135

16. ABSTRACT

The National Aeronautics and Space Administration is sponsoring a two-phase program to evaluate the capability of current computational fluid dynamics codes for use as a design and analysis tool in gas turbine engine combustor development, and to improve the quantitative accuracy of such codes as necessary.

This report describes the Phase I study to evaluate the physical modeling embodied in the codes. The objectives were to identify shortcomings in the models and to provide a program plan to improve the quantitative accuracy. The physical models studied were for: turbulent mass and momentum transport, heat release, liquid fuel spray, and gaseous radiation. The approach adopted was to test the models against appropriate benchmark-quality test cases from experiments in the literature for the constituent flows that together make up the combustor real flow.

The results of the Phase I effort indicate that considerable work remains to be done before the computational fluid dynamics codes can be recognized as viable design and analysis tools. This work covers both physical models and numerical methods.

17. KEY WORDS (SUGGESTED BY AUTHOR(S))	18. DISTRIBUTION STATEMENT
Aerothermal modeling Fluid dynamics codes Turbine Engine Hot Section Technology (HOST)	

19. SECURITY CLASS THIS (REPT)	20. SECURITY CLASS THIS (PAGE)	21. NO. PGS	22. PRICE *
UNCLASSIFIED	UNCLASSIFIED		

* For sale by the National Technical Information Service, Springfield, VA 22161

FOREWORD

This document was prepared by the Commercial Engineering Division of the Pratt & Whitney Aircraft Group of United Technologies Corporation, East Hartford, Connecticut, to describe an evaluation of the suitability of contemporary computational fluid dynamics codes to serve as design and analysis tools in the development of combustors for gas turbine engines. The evaluation was accomplished under the National Aeronautics and Space Administration-sponsored Aerothermal Modeling Program, Phase I, Contract NAS3-23524. The work was performed under the direction of National Aeronautics and Space Administration Project Monitor, Dr. Edward J. Mularz.

Key Commercial Engineering Division contributors to this program were: Dr. Geoffrey J. Sturgess, Technical Program Manager and Principal Investigator, and Dr. Saadat A. Syed and Mr. Keith R. McManus, both of Powerplant Analysis.

Subcontract support in assembling the experimental data base was furnished by United Technologies Research Center, a Division of United Technologies Corporation; key United Technologies Research Center contact was Dr. John B. McVey. Numerous colleagues of Dr. McVey contributed their services as gatekeepers in the areas of their technical expertise. Mr. Louis M. Chiappetta also computerized the data base.

This report has been assigned the Contractor's report number PWA-5907-19.

TABLE OF CONTENTS

TABLE OF CONTENTS (continued)

LIST OF ILLUSTRATIONS

LIST OF ILLUSTRATIONS (continued)

LIST OF ILLUSTRATIONS (continued)

LIST OF ILLUSTRATIONS (continued)

LIST OF ILLUSTRATIONS (continued)

LIST OF TABLES

1.0 SUMMARY

The National Aeronautics and Space Administration is sponsoring a two-phase program to evaluate the capability of current computational fluid dynamics codes for use as a design and analysis tool in gas turbine engine combustor development, and to improve the quantitative accuracy of such codes as necessary.

This report describes the Phase I study to evaluate the physical modeling embodied in the codes. The objectives were to identify shortcomings in the models and to provide a program plan to improve the quantitative accuracy.

The Pratt & Whitney Aircraft 2D-TEACH and 3D-TEACH computer codes have been used as the basis of the study, representing as they do, state-of-the-art modeling.

In Phase I the physical models studied were for: turbulent mass and momentum transport, heat release, liquid fuel spray, and gaseous radiation. The approach adopted was to test the models against appropriate benchmark-quality test cases from experiments in the literature for the constituent flows that together make up the combustor real flow.

The results of the Phase I effort indicate that considerable work remains to be done before the computational fluid dynamics codes can be recognized as viable design and analysis tools. This work covers both physical models and numerical methods.

2.0 INTRODUCTION

Computational fluid dynamics codes have shown potential for application to the internal flows represented by the gas turbine engine combustion chamber (References 1 and 2). The motivations for such an application are powerful (Reference 3). One man's reasonably balanced view of the place of such numerical modeling in the engineering of a combustor has been presented by Odgers (Reference 4), and an approach to modeling combustors has been described (Reference 5). However, although calculations of specific combustion chamber flows using particular models have been made, e.g., References 6 and 7, and many comparisons with measurements exist for flows relevant to combustors, e.g., References 8 and 9, no complete, systematic study has been carried out concerning the performance of these models.

In response to the recommendations of References 1 and 2, the Aerothermal Modeling Program is being undertaken. The overall objective of the program is to provide as a design tool a quantitative capability in aerothermal modeling for gas turbine engine combustion chambers.

The objectives of this Phase I study are to provide a complete assessment of the available numerical modeling capability, and to recommend a comprehensive program for model improvement. The model studied and the assessment of it are reported here. The recommended program for model improvement is reported separately.

3.0 PROGRAM DESCRIPTION

As part of a large research project entitled Turbine Engine Hot Section Technology (HOST), the Aerothermal Modeling Program was initiated by the National Aeronautics and Space Administration at the Lewis Research Center to provide a quantitatively accurate numerical modeling capability for the design and development of gas turbine engine combustion chambers. This effort is planned in two phases, consisting of an assessment of modeling capability and improvement of the accuracy of modeling. The Phase I study, which is described in this report, consisted of two major tasks:

Task 1 - Model and Benchmark Definition, involved describing the models to be evaluated, establishing a data base of relevant experiments, and selecting benchmark quality test cases from the data base.

Task 2 - Model Assessment, where the models were run for the test cases and the calculations compared with the measurements, assessment of the resulting performance including identification of deficiencies, and, a program plan was prepared for model improvement.

3.1 Program Goals

Phase I specific program goals are as follows:

1. To define a detailed computational fluid dynamics code and describe its constituent modules and their interaction to show the usefulness of the output.

2. To define an assessment procedure and assemble a structured experimental or analytical data base that is compatible with this procedure, identifying shortcomings in the data base.

3. To select from the data base experiments of benchmark quality against which the model can be compared.

4. To assess the model calculations against the experimental measurements to identify weaknesses.

5. To formulate a comprehensive program plan that seeks to improve the model to quantitative accuracy.

3.2 Program Schedule

The Phase I program covered a period of 9 months. Of this effort, 4 months elapsed time was devoted to assembling the data base, and 5 1/2 months to assessing the model performance. There was some overlap of these tasks. The period of performance and scope of the study were such that an extremely detailed analysis of the specifics of any particular model failure could not be carried out.

3.3 Program Approach

The program was directed towards state-of-the-art numerical modeling and was to critique all relevant physical modeling, numerical methods and grid systems. The experimental data base was to be formed from either experiments in the literature or, experiments performed on a real gas turbine combustor.

4.0 MODEL DESCRIPTION

A brief description of the models is given. This description covers the modeling of the equations, the physical models that provide closure to the equations, the discretization of the equations in finite difference form, and the solution algorithms. Most of the developments are presented in two-dimensions in the interest of brevity; extension to three-dimensions follows logically.

The model selected for this study is derived from the TEACH codes developed initially as a teaching aid at Imperial College, London, England, (Reference 10). The acronym TEACH (Teaching Elliptic Axisymmetric Characteristics Heuristically) represents a generic solution technique. This model was used in the study as two computer programs developed by Pratt & Whitney Aircraft: 2D-TEACH and 3D-TEACH. The 2D-TEACH code can solve axisymmetric or planar geometries, while 3D-TEACH can solve fully three-dimensional problems. These codes represent current production state-of-the-art calculations. Relation to the design system is given.

4.1 Outline of Calculation

Figure 1 presents a flow diagram of the calculation process. It is divided into four major sections: assembly and modeling of equations, physical modeling, computer solution, and output.

The currently most practical approach to solving a complex turbulent flow is to stay within the framework of continuum mechanics and to use a statistical description of the turbulence, coupled with the accepted Eulerian flow description provided by the Navier-Stokes equations of motion. Hence, an instantaneous quantity in the Navier-Stokes equations is described as the sum of a time-averaged value and a randomly fluctuating value.

When the statistical description of an instantaneous quantity is substituted into the Navier-Stokes equations and time-averaged, the resulting equation set is known as the Reynolds equations (Reference 11). These equations are similar to the Navier-Stokes equations except that time-averaged quantities are used, and for the appearance of time-averaged correlations of fluctuating quantities.

Turbulent motions increase the apparent viscosity of a fluid by some orders of magnitude. If laminar diffusion terms are therefore very much smaller than turbulent diffusion terms, then neglect of fluctuations in laminar viscosity is acceptable. It is a frequently used practice (Reference 12) to also neglect terms involving fluctuating density, although this implies that temperature differences in the flow are not large. For variable density flows, an alternative, density-weighted decomposition of the conservation equations (Favre averaging) is sometimes used. The choice of weighted or unweighted equations is presently somewhat arbitrary (Reference 13). Favre-averaging requires modeling terms like $\overline{\rho' u'}$ which then appear in the equations. Since this presents some difficulties, unweighted equations were used.

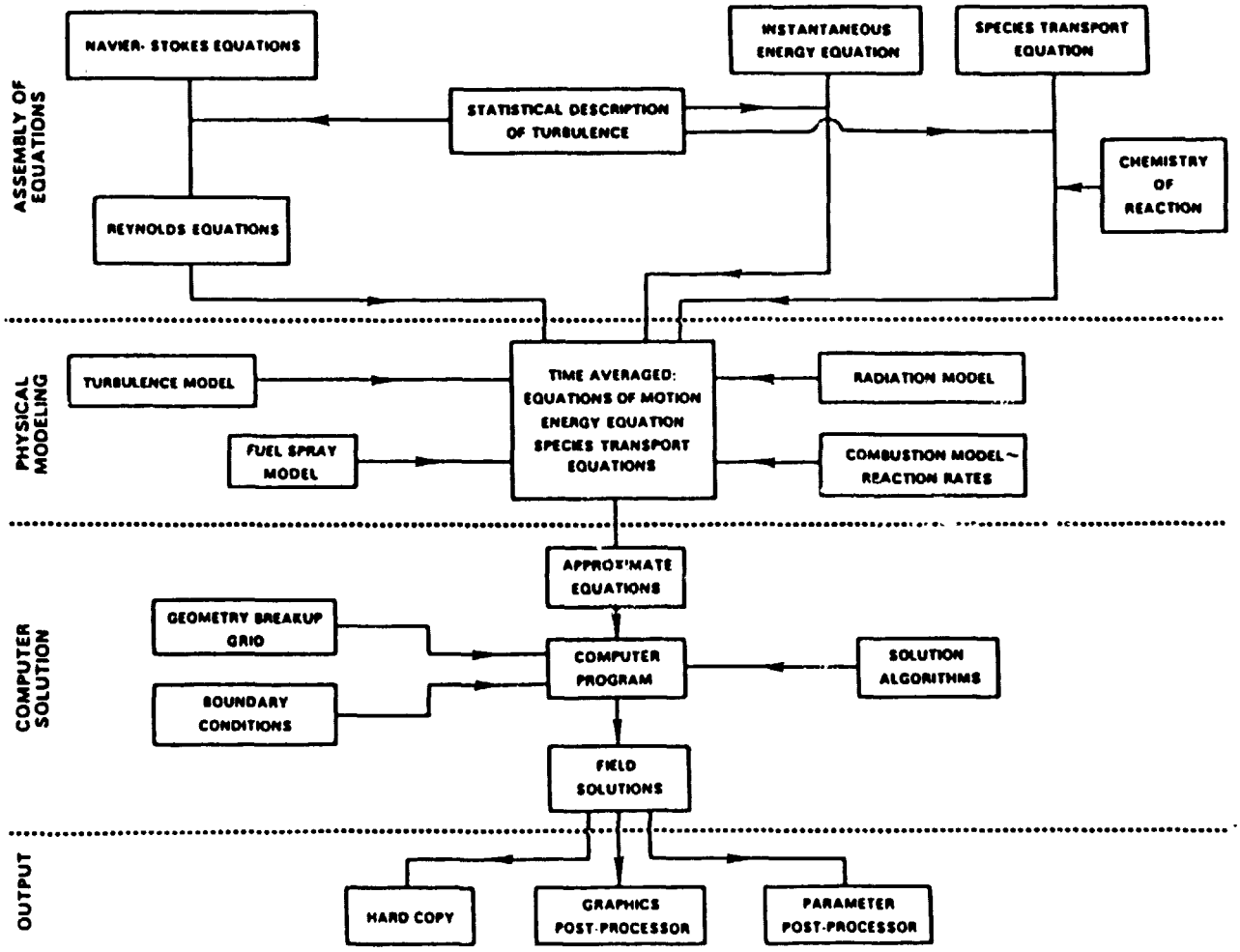

Figure 1 Flow Diagram of Calculation Process

The simplifications of neglecting fluctuating laminar viscosity and fluctuating density terms give Reynolds equations that are expressed in terms of time-mean quantities and cross-correlations of fluctuating velocities such as $\bar{\rho}\,\overline{u'_i u'_j}$. These are the Reynolds stresses, and they result in a closure problem. Turbulence modeling provides the necessary descriptions of the Reynolds stresses in known or determinable quantities.

When the flow consists of more than one chemical species, modeling is also required for the turbulent mass fluxes $\bar{\rho}\,\overline{u'_j m'_\ell}$. These terms arise from applying the statistical treatment of turbulence to an instantaneous species transport equation. The instantaneous energy equation is given the same treatment.

If the flow is two-phase, the presence of the liquid or solid phase can be accounted for by introducing a void fraction term, Ω. This allows coupling of the phases since when Ω is unity the equations revert to their original form and when $0<\Omega<1$ the gaseous phase responds to the presence of the other phase.

The modeled equations can be algebraically manipulated into a general form that simplifies solution. As an example, for steady state flow in two-dimensional cylindrical coordinates:

$$\frac{\partial}{\partial x}\left(\bar{\rho}_g \Omega \bar{u}_g \bar{\phi}\right) + \frac{\partial}{r\partial r}\left(r\bar{\rho}_g \Omega \bar{v}_g \bar{\phi}\right) = \frac{\partial}{\partial x}\left(\Omega \Gamma_{eff,\phi} \frac{\partial \bar{\phi}}{\partial x}\right) \tag{1}$$

$$+ \frac{\partial}{r\partial r}\left(r\,\Omega \Gamma_{eff,\phi} \frac{\partial \bar{\phi}}{\partial r}\right) + S_{\Omega,\phi} + S_{d,\phi}$$

where,

ϕ = any of the independent variables

$\Gamma_{eff,\phi}$ = an appropriate turbulent exchange coefficient, depending on what ϕ represents

$S_{\Omega,\phi}$ = a so-called "source term" for the gaseous phase which lumps together all other terms in a given equation not included in the first four terms in Equation 1.

$S_{d,\phi}$ = a droplet source term for a liquid phase, and,

subscript 'g' denotes gas phase

Figure 2 gives the appropriate set of source terms for each ϕ. To obtain these terms the chemical species transport equation was applied to a simple, irreversible, one-step chemical reaction. Closure was provided by a two-equation turbulence model, requiring transport equations for the kinetic energy of turbulence K, and its dissipation ε, and the assumption that turbulent heat and mass diffusivities can be related to momentum diffusivity by turbulent Prandtl and Schmidt numbers, σ_t. In Figure 2, $\bar{S}_{fu}$ denotes the time-averaged reaction rate of the fuel, and Q_R is the net volumetric heat exchange due to radiation.

To complete the equation set an equation of state is provided:

$$\bar{\rho} = \frac{\bar{P}}{R\,\bar{T}\left(\frac{\bar{m}_{ox}}{Mw_{ox}} + \frac{\bar{m}_{fu}}{Mw_{fu}} + \frac{\bar{m}_{PR}}{Mw_{PR}}\right)} \qquad (2)$$

where Mw is the molecular weight.

The temperature term is calculated in an iterative manner from the composition and enthalpy values using temperature versus enthalpy tables for the individual species.

4.2 Physical Models

Modeling is used to describe the relevant physical processes in order to provide closure to the equations. A turbulence model is required to provide the turbulent momentum and mass fluxes, the chemical reaction rate is found from a combustion model, a spray model yields droplet source terms, and the heat transfer due to radiation is given by a radiation model.

The models used in the present versions of the TEACH series of codes are defined and described briefly below. The particular models presented do not represent the only choices. They were selected on a pragmatic basis with the demands of the intended application to the fore, and with deference to the state of the modeling.

4.2.1 Turbulence

In order to solve the Reynolds equations for the mean quantities the Reynolds stresses have to be described. The so-called two equation, or K-ε, turbulence model is currently used.

Reynolds stresses can consist of two parts - a shear stress and a normal stress - on the faces of an elemental volume in the flow.

EQUATION	ϕ	Γ_{ϕ}	$S_{\Omega,\phi}$
CONTINUITY	1	0	0
x MOMENTUM	$\bar{u}$	μ_{eff}	$\Omega\left(\bar{\rho}g_x - \frac{\partial \bar{P}}{\partial x}\right) + \frac{\partial}{\partial x}\Omega\left(\mu_{eff}\frac{\partial \bar{u}}{\partial x}\right) - \frac{2}{3}\frac{\partial}{\partial x}\Omega(\bar{\rho}K + \mu_{eff}\nabla\cdot\bar{v}) + \frac{\partial}{r\partial r}\Omega\left(r\,\mu_{eff}\frac{\partial \bar{v}}{\partial x}\right)$
r MOMENTUM	$\bar{v}$	μ_{eff}	$\Omega\left(-\frac{\partial P}{\partial r} + \frac{\bar{\rho}\bar{w}^2}{r} - \frac{2\mu_{eff}\bar{v}}{r^2}\right) + \frac{\partial}{\partial x}\Omega\left(\mu_{eff}\frac{\partial \bar{u}}{\partial r}\right)$ $+\frac{\partial}{r\partial r}\Omega\left(r\,\mu_{eff}\frac{\partial \bar{v}}{\partial r}\right) - \frac{\partial}{\partial r}\Omega\left[\frac{2}{3}(\bar{\rho}K + \mu_{eff}\nabla\cdot\bar{v})\right]$
θ MOMENTUM	$\bar{w}$	μ_{eff}	$\Omega\left(-\frac{\bar{\rho}\bar{v}\bar{w}}{r} - \frac{\mu_{eff}\bar{w}}{r^2} - \frac{\bar{w}}{r}\frac{\partial \mu_{eff}}{\partial r}\right)$
FUEL MASS FRACTION	$\bar{m}_{fu}$	μ_{eff}/σ_{fu}	$-\bar{S}_{fu}\,\Omega$
OXIDANT MASS FRACTION	$\bar{m}_{ox}$	μ_{eff}/σ_{ox}	$-R\bar{S}_{fu}\,\Omega$
PRODUCTS MASS FRACTION	$\bar{m}_{PR}$	μ_{eff}/σ_{PR}	$(1+R)\,\bar{S}_{fu}\,\Omega$
TURBULENCE ENERGY	K	μ_{eff}/σ_K	$\left(P_K^* - \bar{\rho}\varepsilon\right)\Omega$
ENERGY DISSIPATION	ε	$\mu_{eff}/\sigma_\varepsilon$	$\left(\nabla\cdot\bar{v}\right)\varepsilon + C_{\varepsilon_1}P_K\,\varepsilon/K - C_{\varepsilon_2}\bar{\rho}\,\varepsilon^2/K\Big)\Omega$
ENERGY	$\bar{H}$	μ_{eff}/σ_H	$\frac{1}{2}\frac{\partial}{\partial x}\Omega\left(\mu_{eff} - \frac{\mu_{eff}}{\sigma_H}\right)\frac{\partial}{\partial x}\left(\bar{u}^2 + \bar{v}^2 + \bar{w}^2\right)$ $+\frac{1}{2}\frac{\partial}{r\partial r}\Omega\left[r\left(\mu_{eff} - \frac{\mu_{eff}}{\sigma_H}\right)\right]\frac{\partial}{\partial r}\left(\bar{u}^2 + \bar{v}^2 + \bar{w}^2\right) + \Omega Q_R$

where

$$P_K^* = 2\mu_t\left[\left(\frac{\partial \bar{v}}{\partial r}\right)^2 + \left(\frac{\partial \bar{u}}{\partial x}\right)^2\right] + \mu_t\left(\frac{\partial \bar{w}}{\partial r} - \frac{\bar{w}}{r}\right)^2 + \mu_t\left(\frac{\partial \bar{v}}{\partial x} + \frac{\partial \bar{u}}{\partial r}\right)^2 + 2\mu_t\left(\frac{\bar{v}}{r}\right)^2 + \mu_t\left(\frac{\partial \bar{w}}{\partial x}\right)^2$$
$$-\frac{2}{3}\nabla\cdot\bar{v}\,(\bar{\rho}K + \mu_t\nabla\cdot\bar{v})$$

Figure 2 Source Term $S_{\Omega,\phi}$ for Gas Transport Equations

To address the shear stress portion of the Reynolds stress Boussinesq's analogy is used. In laminar flow, Stoke's law relates the shear stress in a flowing fluid to the viscosity of the fluid through the velocity gradient. Turbulence increases the apparent viscosity of the fluid by some orders of magnitude due to transfer of energy from the mean flow through the eddy cascade to the smallest eddies, where it is dissipated eventually on the molecular level as heat. Boussinesq drew an analogy with laminar flow to relate shear stress in a turbulent fluid to an "eddy viscosity", μ_t. With eddy viscosity modeling, an expression is then needed for μ_t.

The Prandtl-Kolmogorov definition of eddy viscosity (References 14 and 15) is used currently. Since specific μ_t (eddy viscosity per unit mass) has to have dimensions of L^2/T, it can be written,

$$\mu_t = V_T^m \, l^n \tag{3}$$

where, V_T = velocity scale related to the turbulence

l = length scale appropriate to V_T, and,

m, n = unknown indices.

If the specific kinetic energy of turbulence is defined as

$$K = \frac{1}{2}(\overline{u'^2} + \overline{v'^2} + \overline{w'^2}) \tag{4}$$

then, V_T equal $\sqrt{K}$ is appropriate, and l then characterizes the size of the eddies containing the turbulence energy, where,

$$l = l_T \; ; \; l_T = C_\mu \, K^{3/2}/\varepsilon$$

and, C_μ = constant

ε = dissipation rate of turbulence

Hence, with the regular definition of μ_t,

$$\mu_t = \bar{\rho} \, \frac{C_\mu \, K^2}{\varepsilon} \tag{5}$$

The normal strains on an elemental volume due to turbulence pressure can be represented by summing the net fluctuating specific dynamic pressures in each direction, i.e.,

$$\bar{P}_t = \frac{1}{3} \left(\overline{u'^2} + \overline{v'^2} + \overline{w'^2} \right)$$

Using Equation 4, this reduces to,

$$\bar{P}_t = 2/3\ K \tag{6}$$

Hence, the Reynolds stresses can be written in two-dimensions, using tensor notation,

$$-\bar{\rho}\,\overline{u'_i u'_j} = \mu_t \left(\frac{\partial \bar{u}_i}{\partial x_j} + \frac{\partial \bar{u}_j}{\partial x_i} \right) - 2/3\ \bar{\rho}\ K\ \delta_{ij} \tag{7}$$

where δ_{ij} is the Kronecker delta such that i equals j denotes a normal stress and δ equals unity, while i not equal to j denotes tangential stress only and δ equals zero.

For variable density flows an additional term of $-2/3\mu_t\delta_{ij}[\bar{u}_i(\partial\bar{\rho}/\partial x_i)]/\bar{\rho}$ appears on the right hand side of Equation 7.

Equation 5 supplies μ_t.

In Equation 5 the eddy viscosity has been expressed in terms of K and ε. Transport equations for these can be derived as follows: For K, multiply each of the instantaneous momentum equations by its respective fluctuating velocity component, sum the three resulting equations, and then time-average. For ε, differentiate the instantaneous momentum equations, multiply throughout by $\nu\,\partial u_j/\partial x_j$, sum, and time-average, (Reference 16). Some additional modeling of fluctuating terms is then required.

The modeled form of the K-equation is:

$$\frac{\partial \bar{\rho}\bar{u}_j K}{\partial x_j} = \frac{\partial}{\partial x_j}\frac{\mu_t}{\sigma_k}\frac{\partial K}{\partial x_j} + \bar{\rho}\left[\mu_t \left(\frac{\partial \bar{u}_i}{\partial x_j} + \frac{\partial \bar{u}_j}{\partial x_i} \right) - \frac{2}{3}\left(\bar{\rho} K + \mu_t \frac{\partial \bar{u}_k}{\partial x_k} \right)\delta_{ij} \right] \frac{\partial \bar{u}_i}{\partial x_j} - \rho\,\varepsilon \tag{8}$$

Similarly the form of the ϵ-equation is:

Convection Diffusion Production

$$\frac{\partial \bar{\rho}\bar{u}_j \varepsilon}{\partial x_j} = \frac{\partial}{\partial x_j}\frac{\mu_t}{\sigma_\varepsilon}\frac{\partial \varepsilon}{\partial x_j} + \left(\varepsilon \frac{\partial \bar{u}_i}{\partial x_i} - C_{\varepsilon 1}\,\bar{\rho}\frac{\varepsilon}{K}\,\overline{u'_i u'_j}\,\frac{\partial \bar{u}_i}{\partial x_j} \right) \tag{9}$$

Dissipation

$$-\bar{\rho}\,C_{\varepsilon 2}\,\frac{\varepsilon^2}{K}$$

The model contains five empirical constants, C_μ, σ_K, σ_ϵ, $C_{\epsilon 1}$, and $C_{\epsilon 2}$. "Standard" values for these constants are given in Table 1. C_μ comes from near-wall shear stress and turbulence energy measurements, where production and dissipation of turbulence are nearly equal; it is consistent with a law of the wall (log-law). $C_{\epsilon 2}$ comes from the decay of grid turbulence, $C_{\epsilon 1}$ comes from near-wall turbulence considerations, and σ_K and σ_ϵ come from "computer optimization" to give good answers over a range of flows.

Table 1

Standard Values for Turbulence Model Constants

Constant	Value
C_μ	0.09
$C_{\epsilon 1}$	1.44
$C_{\epsilon 2}$	1.92
σ_K	1.0
σ_ϵ	1.3

For variable density flows the turbulent heat and mass fluxes must be calculated. The flowfield is found from an effective turbulent eddy viscosity. It is consistent to also base the turbulent heat and mass transfer on an effective thermal or mass eddy diffusivity.

The eddy diffusivity approach gives for the flux of a scalar,

$$- \overline{u'_i \theta'} = \Gamma_t \frac{\partial \tilde{\theta}}{\partial x_i} \tag{10}$$

where θ is a scalar such as temperature or specie concentration. This is the so-called gradient hypothesis where the turbulent transport of θ is proportional to the mean gradient of θ.

The turbulent eddy diffusivity (or the exchange coefficient Γ) is physically always the same order of magnitude as the turbulent kinematic eddy viscosity ν_t, and their ratio is called the turbulent Prandtl or Schmidt number σ_t, where,

$$\sigma_t = \frac{\nu_t}{\Gamma_t} \tag{11}$$

In mean field closures the isotropic turbulent Prandtl/Schmidt number has to be specified. Knowledge of σ_t is used as a means of finding Γ_t from an already calculated value of μ_t obtained using Equation 5. Thus, transport of momentum is taken as the basic gradient hypothesis transport process, rather than transport of a scalar quantity.

A recommended value for σ_t has been 0.9. This is now considered appropriate for boundary layer flows only, and a value of 0.7 has been recommended for general flows (Reference 13). A value of 0.5 has been recommended for recirculation zones, (Reference 17).

4.2.2 Fuel Spray

The fuel spray model has to provide information on the droplet source terms in Equation 1. This information is required for each cell formed by the finite difference mesh upon which the equation is solved.

The approach used is to calculate droplet trajectories through the flow field. This method involves embedding the droplet equations of motion in Lagrangian form into the Eulerian framework of the gas-phase equations.

The spray is represented by individual droplets, termed the "computational droplet." Each computational droplet represents a "parcel" of like droplets all having the same initial size, velocity vector and temperature. All the droplets in the actual spray are represented by a size distribution. A Rosin-Rammler distribution is computationally convenient to use. The actual spray size distribution is sampled statistically to produce the computational droplets; real fuel flow rate is maintained at its correct value. The computational droplets are fired into the gas field.

The droplet equation of motion is due to Soo (Reference 18) with his subsequent simplifying reductions, together with the assumption that the fuel vapor produced by the droplet has an initial velocity equal to that of the droplet. This yields,

$$m_d \cdot \frac{du_{d,i}}{dt} = m_d F_i (u_{g,i} - u_{d,i}) + m_g g_i \qquad (12)$$

where,

$$Fi = \frac{3}{8} C_D \frac{\rho_g}{\rho_d r_d} \left| (u_{g,i} - u_{d,i}) \right| \qquad (13)$$

$u_{d,i}$ = droplet velocity in x, r and θ directions, respectively, i.e., u_d, v_d, w_d

r_d = droplet radius (droplets assumed spherical)

C_D = drag coefficient (relationship of Williams, Reference 19)

Then, the droplet position at any instant of time is given by,

$$\frac{dx}{dt} = u_d \; ; \quad \frac{dr}{dt} = v_d \; ; \quad r\,\frac{d\theta}{dt} = w_d \tag{14}$$

The turbulent diffusion of droplets is accounted for by a stochastic approach (Reference 20). In the droplet equation of motion, Equation 12, $u_{g,i}$ is interpreted as the instantaneous value of gas velocity, i.e.

$$u_{g,i} = \bar{u}_{g,i} + u'_{g,i} \tag{15}$$

The time-mean value $\bar{u}_{g,i}$ is obtained from the flow field solution. The instantaneous value $u'_{g,i}$ can be obtained using random sampling of an assumed Gaussian probability distribution function for turbulence energy, and the turbulence is taken as being isotropic. The standard deviation of $u_{g,i}$ is then,

$$\sigma = \left(\frac{2}{3}K\right)^{\frac{1}{2}} \tag{16}$$

K being the specific kinetic energy of turbulence, which is available throughout the field from the gas-phase solutions. The fluctuating velocity $u'_{g,i}$ can then be obtained from Equation 5. Hence, with isotropy,

$$u_g = \bar{u} + u' \; ; \quad v_g = \bar{v} + u' \; ; \quad w_g = \bar{w} + u'$$

The time interval over which the droplet equations are integrated is the time which a particular instantaneous velocity interacts with the droplet. To determine this time interval it is assumed that an instantaneous velocity is associated with a particular turbulent eddy. The droplet interacts with the eddy until either the droplet traverses the eddy or, the eddy is broken up, whichever occurs first. The length scale of the eddy is obtained from the turbulence model as,

$$l_T = C_\mu K^{\frac{3}{2}} / \varepsilon$$

and the transit time is determined analytically from a simplified and linearized form of the droplet equation of motion.

The droplet source terms that arise from this Particle Source in Cell (PSIC) technique (Reference 21), involve for each computational cell,

(i) mass transfer between droplets and gas (continuity equation), $S_{d,m}$

(ii) momentum transfer (momentum equations), $S_{d,u}$; $S_{d,v}$; $S_{a,w}$

(iii) enthalpy exchange (energy equation), $S_{d,h}$

(iv) specie exchange (specie equations), S_{d,m_1}

(v) radiation exchange (energy equation), $S_{d,R}$

Expressions for these source terms may be written as follows:

$$S_{d,m} = \sum_{L=1}^{N} \left[\frac{1}{M} \sum_{K=1}^{M} \left(\dot{m}_{d1} - \dot{m}_{d2} \right)_K \right]_L \tag{17}$$

where, $\dot{m}_{d1}$, $\dot{m}_{d2}$ = mass flux of liquid droplets at inlet and outlet of cell

M = number of droplets representing size range L

N = total number of size ranges representing the spray

and,

$$\dot{m}_{d1} = \frac{\Pi}{6} \rho_d D_{d1}^3 \dot{n}_L$$

$$\dot{m}_{d2} = \frac{\Pi}{6} \rho_d D_{d2}^3 \dot{n}_L \tag{18}$$

where, $\dot{n}_L$ = number of real droplets per second in size range L crossing cell

D_d = diameter of droplet

Similarly,

$$S_{d,u} = \sum_{L=1}^{N} \left\{ \frac{1}{M} \sum_{K=1}^{M} \left[(\dot{m}u)_{d,2} - (\dot{m}u)_{d,1} \right]_K \right\}_L \tag{19}$$

$$S_{d,v} = \sum_{L=1}^{N} \left\{ \frac{1}{M} \sum_{K=1}^{M} \left[(\dot{m}v)_{d,2} - (\dot{m}v)_{d,1} \right]_K \right\}_L \tag{20}$$

$$S_{d,w} = \sum_{K=1}^{N} \left\{ \frac{1}{M} \sum_{K=1}^{M} \left[(\dot{m}w)_{d,2} - (\dot{m}w)_{d,1} \right] K \right\} L \qquad (21)$$

$$S_{d,h} = \sum_{L=1}^{N} \left[\frac{1}{M} \sum_{K=1}^{M} (\dot{m}_{d,1} - \dot{m}_{d,2}) (H_{fu} - L_{evap}) K \right] L \qquad (22)$$

$$S_{d,ml} = \sum_{L=1}^{N} \left[\frac{1}{M} \sum_{K=1}^{M} (F_l \dot{m}_{d1} - F_l \dot{m}_{d2}) K \right] L \qquad (23)$$

where,

F_l = fraction of specie in droplet, (F_l = 1.0 for pure fuel and zero for oxidant and products, normally; see combustion model).

Finally,

$$S_{d,R} = \frac{4\sigma}{V} \sum_{L=1}^{N} \left[\frac{1}{M} \sum_{K=1}^{M} (\dot{n}_L \, t_L \, \pi \, r_d^{\,2}) K \right] L \; E_d \, (T_d^{\,4} - T_g^{\,4}) \qquad (24)$$

where, t_L = time required for the droplets to cross cell

E_d = emissivity of the droplets

T_d = temperature of droplets

T_g = gas temperature

σ = Stefan - Boltzman constant

V = cell volume

Phenomenological modeling is used to provide closure to Equations 17 and 19-24. Provision is made for fractional distillation of a multi-component fuel.

At a wall the droplet can be either reflected, or remain on the wall. If it remains on the wall it is taken out of the calculation. If it is reflected, new initial velocity conditions are specified. This means that the sign of the velocity component normal to the wall is altered, and tracking is resumed. A droplet is only reflected when it crosses an axis of symmetry. Note that the analysis takes no account of either droplet collision or secondary breakup after the spray is formed.

4.2.3 Combustion

The time-averaged chemical reaction rate $\bar{S}_{fu}$ in Figure 2 is provided by the combustion model.

The current model is very simple. It neglects molecular transport and chemical kinetics completely, and has been classified as a hydrodynamics only procedure. The argument is that in turbulent flames the time scale of chemical reaction is much smaller than the time scale of turbulence and, therefore, reaction rate is determined by mixing of fuel and air since for all practical purposes, the chemical reaction rate is infinitely fast. Hence, rate of reaction is influenced only by the time scale of turbulence. This is the familiar "mixed is burned" hypothesis, and is appropriate for the gas turbine combustor when operating at high power conditions.

The time-average reaction rate appearing in the source terms is obtained from the model of Magnussen and Hjertger (Reference 22). This approach deals with the inhomogeneities which appear in the mixture as a consequence of the interactions between turbulence and chemical reaction, through a modification of Mason and Spalding's eddy breakup model (Reference 23).

The modified eddy breakup model as applied presently can be described as follows. In lean diffusion flames fuel and oxidant occur in separate eddies, and the rate of reaction is determined by the rate of eddy dissipation. Consequently, there will be a relationship between turbulent fluctuations in the flow and the mean concentration of active species. Accordingly, the volumetric reaction rate of fuel can be expressed,

$$\bar{S}_{fu} = \bar{\rho} A_1 \bar{m}_{fu} (\varepsilon/K) \qquad (25)$$

where, $\bar{m}_{fu}$ = local time-mean mass fraction of fuel

ε/K = reciprocal of eddy life time

A_1 = constant

In regions of the flame where the time-mean mixture is rich, the oxidant will be the reacting species that shows the greatest intermittency. Hence, in this case it is the dissipation of the oxidant-bearing eddies that limit reaction rate. Hence,

$$\bar{S}_{fu} = \bar{\rho} A_1 \frac{\bar{m}_{ox}}{R} \left(\frac{\varepsilon}{K}\right) \tag{26}$$

where, $\bar{m}_{ox}$ = local time-mean mass fraction of oxidant.

In premixed flames eddies will contain both fuel and oxidant simultaneously, and such eddies will be separated by eddies containing hot products. Reaction rate is determined in this case by flame spread, and by dissipation of hot-eddies when the concentration of hot products is low. These two processes were combined into a single equation of the same form as Equations 25 and 26,

$$\bar{S}_{fu} = \bar{\rho} A_1 A_2 \frac{\bar{m}_{pr}}{(1+R)} \cdot \left(\frac{\varepsilon}{K}\right) \tag{27}$$

where, $\bar{m}_{pr}$ = local time-mean mass fraction of products

A_2 = constant

In general, even diffusion flames will contain some level of premixing, so Equations 25-27 will apply simultaneously. Thus, the reaction will proceed at a rate determined by the lowest of the three rates.

The values used for the constants are those recommended by Magnussen and Hjertager, i.e.,

$$A_1 = 4.0 \; ; \; A_1 A_2 = 2.0 = A_3 \tag{28}$$

4.2.4 Radiation

The radiation model provides the heat transfer due to radiation, Q_R. The approach adopted is a relatively simple one, consistent with the simple combustion model.

It is assumed that the radiating medium is grey. The radiation transport equation for this medium then becomes independent of the frequency of radiation (Reference 24). This equation when integrated over the 4π solid angle yields the following "energy equation" for the radiation field,

$$\nabla \cdot \underline{F_R} = CK (E_M - E_R) \tag{29}$$

where

E_R = Radiation energy density = $\frac{1}{C} \int_{4\pi} I \, d\omega$

F_R = Radiation flux = $\int_{4\pi} I \underline{\Omega}\, d\omega$

$E_M = \frac{4\sigma T^4}{C}$

C = speed of light
σ = Stefan-Boltzman constant
T = temperature
I = radiation intensity which a function of direction and position
ω = solid angle
K = Absorption coefficient
$\underline{\Omega}$ = direction vector

If the radiation transport equation is multiplied by the direction vector and integrated over 4π solid angle, the following "momentum equation" for the radiation field is obtained.

$$C\nabla \cdot \underline{\underline{P_R}} = - K \underline{F_R} \tag{30}$$

where $\underline{\underline{P_R}}$ = Radiation Pressure = $\int_{4\pi} I \underline{\Omega}\, \underline{\Omega} \cdot d\omega$

To close the above set of equations (Equations 29, 30) $\underline{\underline{P_R}}$ is expressed in terms of E_R by expanding the radiation intensity in a Taylor series in $\underline{\Omega}$ and truncating it after the first two terms. This yields a relation between radiation energy density and radiation pressure which when substituted in Equation 30 yields

$$\underline{F_R} = \frac{-C}{3K} \nabla E_R \tag{31}$$

Putting Equation 31 in Equation 29 gives

$$\nabla \cdot \left(\frac{1}{3K} \nabla E_R \right) = K \left(E_R - E_M \right)$$

This equation, in the presence of absorbing/emitting particles, can be written in cylindrical coordinates as:

$$\frac{\partial}{\partial x} \frac{1}{3K_e} \frac{\partial T_R^4}{\partial x} + \frac{1}{r} \frac{\partial}{\partial r} \frac{r}{3K_e} \frac{\partial T_R^4}{\partial r} + K \left(T_g^4 - T_R^4 \right) + E_p K_p \left(T_p^4 - T_R^4 \right) = 0 \tag{32}$$

$T_R^4 = 1.0/4\sigma \int Idw = \frac{C}{4\sigma}$ x radiation energy density.

I = Radiation intensity

w = Wave length

σ = Stefan-Boltzman Constant

T_g = Gas temperature

T_p = Particle temperature

K = Absorption Coefficient

K_e = Effective absorption Coefficient, $K_e = K + K_p + 4/3D_H$

D_H = Hydraulic diameter of the enclosure

E_p = Particle emissivity

The wall boundary condition can be written as:

$$-\frac{1}{3K_e}\frac{\partial T_R^4}{\partial n} = \frac{1}{2}\left[\left(1 - r_w\right) T_R^4 - E_w T_w^4\right] \Big/ \left(1 + r_w\right) \qquad (33)$$

where

E_w = Emissivity of the wall

r_w = Reflectivity of the wall

n = Direction normal to the wall surface

T_w = Wall temperature

The solution of the modeled radiation transport equation, Equation 32, requires the specification of the gas absorption coefficient K. The evaluation of K for combustion gases over the range of temperatures and pressures encountered in the combustor can be very complex. The gas absorption coefficient is therefore calculated as a frequency averaged absorption coefficient. It can be shown, that

$$K = \left.\frac{dE_m}{dx}\right|_{x = 0} \qquad (34)$$

where E_m = Emissivity of the gas mixture.

The problem now reduces to calculating the emissivity of the combustion gases.

Barteld's (Reference 25) model is incorporated. This model is simple but general enough so that constants used to curve-fit data for one set of operating conditions can be used under a different set.

This model assumes that the combustion gases are made up of a mixture of four gray gases whose emissivity can be calculated as:

$$E_m = \sum_{n=1}^{4} a_{g,n}\left(T_g\right)\left(1 - e^{-K_n p x}\right) \tag{35}$$

where

x = path length, length of the control volume

$a_{g,n} = b_{1n} + b_{2n} T_g + b_{3n} T_g^2 + b_{4n} T_g^3$

K_n = constant

p = partial pressure of products of combustion

The constants K_1 and b_{11}, etc., are given in Table 2. These constants were determined by making a curve-fit for the combustion products of methane. The fit was made over the temperature range 1800°R (1000°K) to 3600°R (2000°K) and a partial pressure - path length range of 0.01 - 4.0 ft. atmospheres (0.003 - 1.2 bar meter) - at an average pressure of one atmosphere. This model should be adequate for predicting radiation from gaseous fuel fired combustors at low pressures.

This model was modified to take into account collision broadening due to high ambient pressures. The following modification was made:

$$E_m = \sum_{n=1}^{4} a_{g,n}\left(T_g\right)\left(1 - e^{-K_n P^{1/4} p x}\right) \tag{36}$$

where P is the ambient pressure. The constants remain unchanged.

From Equations 34 and 36 the absorption coefficient needed for the radiation transport equation can be obtained as:

$$K = \left.\frac{dE_m}{dx}\right|_{x=0} = P^{1/4} p \left(\sum_{n=1}^{4} a_{g,n}\left(T_g\right) K_n\right) \tag{37}$$

Table 2

Constants of Four Gray Gas Model for the Products of Methane Combustion

n	b_{1n}	$b_{2n} \cdot 10^3$	$b_{3n} \cdot 10^6$	$b_{4n} \cdot 10^9$	k_n
1	+.218	+.283	+.065	-.026	0.106
2	+.535	-.240	+.009	+.002	1.653
3	+.131	+.089	-.127	+.032	21.212
4	+.116	-.132	+.053	-.008	146.308

4.3 Solution Procedure

An outline of the solution procedure for the set of equations (Figure 2) represented by the general transport equation of Equation 1 is provided in sufficient detail that appreciation can be gained of how the elements of this procedure might influence solution accuracy.

Rearrangement of the equations into the general form represented by Equation 1 enables one solution algorithm to be used for all equations. The equation set is solved using a steady state, implicit, finite difference numerical procedure. An initial guess is made of the field variables, and these guesses are iteratively updated until the solutions have converged. Convergence is deemed to have been obtained when the absolute sum of the residuals over the whole grid of each variable goes below a specified value.

The solution procedure is the standard TEACH approach: A hybrid (upwind/central) finite differencing scheme (Reference 26) is used to discretize the equations. Velocities and pressures are obtained through the SIMPLE algorithm (Reference 27) and the finite difference equations are solved by the ADI method (Reference 28) using the TDMA.

4.3.1 Discretization of the Equations

The finite difference analog of the differential equations is obtained by overlaying a computational mesh on the flow domain to be calculated, and obtaining the basic finite difference form of the partial derivatives for every node of the mesh from a control volume approach, (Reference 29). The finite difference expressions, when substituted back into the differential equations, yield a set of linearized, algebraic equations for every node of the mesh.

There are a number of ways to derive the finite difference analogs of partial differential equations. The control volume or finite volume approach, because it is based on the satisfaction of macroscopic physical laws such as conservation of mass, momentum and energy, usually leads to more accurate results. Figure 3 illustrates the mesh and the control volume established about a considered mode, P. The conservation property is essential when combustion is taking place.

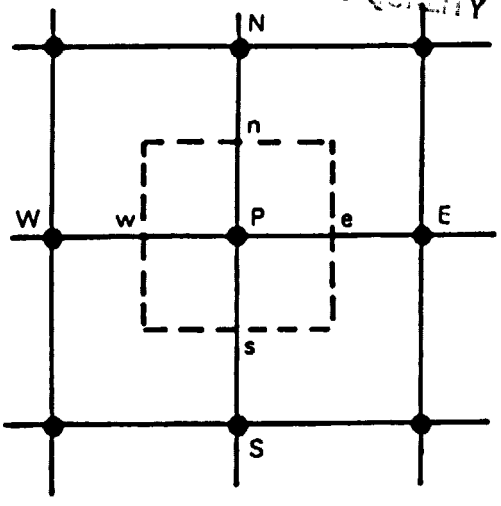

Figure 3 2D- Control Volume for the Finite Difference Scheme

The generalized transport equation for variable ϕ has a source term S_ϕ, (see Equation 1 and Figure 2, for example). This term is linearized thus,

$$S_\phi = A\,\phi_p + B$$

and integrated over the control volume as,

$$\int (A\,\phi_p + B)\,dV = A\,\phi_p \cdot vol + B \cdot vol = S_p\,\phi_p + S_u \qquad (38)$$

where,

$$vol = \int_V dV = \int_{xw}^{xe} \int_{rs}^{rn} r\,dr\,dx \quad \text{for two-dimensions in cylindrical coordinates.}$$

The remainder of Equation 1 is also integrated over the control volume and added to Equation 38 to give,

$$C_E\,\phi_e - C_W\,\phi_w + C_N\,\phi_n - C_S\,\phi_s = D_E(\phi_E - \phi_p) - D_W\,(\phi_p - \phi_W) + D_N\,(\phi_N - \phi_p) \qquad (39)$$

$$- D_S\,(\phi_p - \phi_s) + (S_p\phi_p + S_u)$$

where, C_E, C_N, etc., are convection coefficients,

$$C_E = (\bar{\rho}\bar{u})_e a_e \; ; \; C_N = (\bar{\rho}\bar{v})_n a_n \text{ etc.}$$

a_e, a_n being cell face areas, and

D_E, D_N, etc., are diffusion coefficients,

$$D_E = \left(\frac{\Gamma_{\phi,eff}}{\Delta x}\right)_e a_e \quad \text{etc.}$$

When certain weighting factors are introduced, Equation 39 can be manipulated with the aid of continuity, and normalized, to give the form,

$$A_P \phi_P = A_N \phi_N + A_S \phi_S + A_E \phi_E + A_W \phi_W + S_u \tag{40}$$

where,

$$A_P = A_N + A_S + A_W + A_E - S_P \tag{41}$$

and, A_N, A_S, etc., are functions of the convection and diffusion coefficients and the weighting factors.

Equation 40 is the finite difference form of Equation 1 for ϕ. To solve it evaluation of the weighting factors is required. The difference scheme used to evaluate the weighting factors is based on the hybrid differencing scheme of Spalding (Reference 26).

The hybrid differencing scheme is unconditionally stable and the solution is bounded. It uses second order central differencing for convection and diffusion fluxes when the absolute value of cell Péclét number is less than or equal to two. When Péclét number is greater than two, first order upwind differencing is used for convection fluxes, and diffusion fluxes are neglected altogether. The switch of differencing is done both locally and directionally in the computational grid. Péclét number defines the relative importance of convective and diffusive transport, and,

$$Pe_e = C_E/D_E \; ; \; Pe_w = C_W/D_W, \text{ etc.}$$

Applying the scheme it can be shown that for example, for

$$\begin{aligned} P_e < 2 \; &; \; A_N = C_N \\ -2 \le P_e \le 2 \; &; \; A_N = D_N - C_N/2 \\ P_e > 2 \; &; \; A_N = 0 \end{aligned} \tag{42}$$

Similarly, for the other A's.

$$\begin{aligned} P_e < 2 \;;\; A_S &= 0 \\ -2 \le P_e \le 2 \;;\; A_S &= D_S + C_S/2 \\ P_e > 2 \;;\; A_S &= C_S \end{aligned} \tag{43}$$

$$\begin{aligned} P_e < 2 \;;\; A_E &= C_E \\ -2 \le P_e \le 2 \;;\; A_E &= D_E - C_E/2 \\ P_e > 2 \;;\; A_E &= 0 \end{aligned} \tag{44}$$

$$\begin{aligned} P_e < 2 \;;\; A_W &= 0 \\ -2 \le P_e \le 2 \;;\; A_W &= D_W + C_W/2 \\ P_e > 2 \;;\; A_W &= C_W \end{aligned} \tag{45}$$

The spatial differencing of the convective terms of the conservation equations in an Eularian coordinate system can result in numerical diffusion occurring. Use of a higher order differencing scheme eliminates or significantly reduces this diffusion. However, use of central differencing introduces an oscillatory behavior into the solution. This "wiggling" can lead to nonphysical behavior (Reference 30). The use of an upwind or donor-cell technique eliminates wiggling; however, this is accomplished by the introduction of a diffusive-like term into the difference equations. Thus, while "numerical damping" suppresses oscillation, it leads to significant additional diffusion of the convected parameter. For flows with combustion, these parameters might be species concentration, temperature, etc. Unfortunately, diffusion of these quantities is responsible in a physical sense for flame propagation. Therefore, a severe restriction can be placed on the quality of quantitative prediction (Reference 31).

To successfully use the hybrid differencing scheme for complicated flows, care must be taken in establishing the computational grid upon which the calculations are performed. The approximations of the algebraic expressions used to represent the partial differential equations become asymptotically exact as the distance between the nodes set up by the grid, and used to link the algebraic expressions, is reduced. In the limit, the number of nodes can be increased until an asymptote to the solution to the differential equations is achieved. In practice, this increase is limited by computer storage and the cost of the calculation. However, it is not just the number of nodes that are used which is important in determining the accuracy of a solution, but also the distribution of those nodes within the flow field to be determined (References 13, 32). This nodal distribution is important because whenever

curvature of the flow in the streamwise coordinate direction exists, a truncation error arises in the solution (Reference 33). In addition, there is also a problem in multidimensional flows of streamline-to-grid skewness (Reference 34). With upwind differencing, these effects start to have a damaging effect on solution accuracy when the Péclét number exceeds two.

4.3.2 Pressure Algorithm SIMPLE

The acronym SIMPLE stands for Semi-Implicit Method for Pressure Linked Equations. This algorithm is formulated to obtain a pressure field and correct the velocity field in such a manner that continuity and momentum equations are simultaneously satisfied. The need for a pressure algorithm arises because pressure does not appear as an independent variable in any of the transport equations.

The procedure adopted is the following: The pressure field, P*, is guessed and the momentum equations are solved using this field. The resulting velocity field u* contains the right vorticity but may or may not satisfy continuity. Hence, an equation for the potential function, P', is derived whose solution yields velocity and pressure corrections, u_i' and P', respectively, which preserve vorticity and satisfy continuity. The derivation of this equation requires a relationship between u_i' and P' to be found. The following relationship is assumed,

$$\bar{\rho} u_i' = - \Gamma_i \frac{\partial P'}{\partial x_i} \tag{46}$$

where Γ_i is deduced from the linearized momentum equations.

The continuity equation can then be written as

$$\frac{\partial(\bar{\rho} u_i)}{\partial x_i} = \frac{\partial \bar{\rho}(u_i^* + u_i')}{\partial x_i} = \frac{\partial \bar{\rho} u_i^*}{\partial x_i} - \frac{\partial}{\partial x_i}\left(\Gamma_i \frac{\partial P'}{\partial x_i}\right) = 0 \tag{47}$$

Hence

$$0 = \frac{\partial}{\partial x_i} \Gamma_i \frac{\partial P'}{\partial x_i} - D^* \tag{48}$$

$$\text{where } D^* = \frac{\partial \bar{\rho} u^*_i}{\partial x_i} \tag{49}$$

Equation 47, which is known as the pressure correction equation, is cast in the form of a generalized transport equation (the convection term is set to zero), and is solved using the algorithm which is used to solve all the other transport equations. Knowing P', u_i' is obtained from Equation 46.

4.3.3 ADI Method

The set of finite difference equations, Equation 40, are solved by means of the following line by line iteration method. This method known as the Alternating Direction Implicit Method (Reference 28) was initially formulated for unsteady equations; its adaptation to steady state equations is sometimes also known as the Alternating Direction Iterative Method.

If the ϕ values on two of the four neighboring nodes of a considered node P are assumed as known, then Equation 39 can be recast as

$$A_P \phi_P = A_N \phi_N + A_S \phi_S + C' \tag{50}$$

where

$$C' = A_E \phi_E + A_W \phi_W + Su \tag{51}$$

In Equation 50, neighboring values ϕ_E and ϕ_W are assumed as known. This assumption reduces the finite difference equation to a three point equation which can now be solved using any fast matrix inversion technique. Once the equation set is solved the direction is reversed and now ϕ_N and ϕ_S are assumed as known, which produces the following equation:

$$A_P \phi_P = A_E \phi_E + A_S \phi_S + C'' \tag{52}$$

where

$$C'' = A_N \phi_N + A_S \phi_S + Su \tag{53}$$

Equation 52 can also be solved by matrix inversion. In the above equations the most recent values of ϕ are used.

4.3.4 TDMA

The ADI method reduces the finite difference equation, Equation 40, which is a five point equation to two, three point equations, Equations 50 and 52, which are solved successively using the Tri Diagonal Matrix Algorithm (TDMA). This algorithm is explained below.

Equation 50 can be rearranged for the j^{th} point as

$$\phi_j = B_j \phi_{j+1} + C_J \phi_{j-1} + D_j$$

where

$$B_j = A_N/Ap \ , \ C_j = A_S/Ap$$

$$D_j = (A_W \phi_W + A_E \phi_E + S_u)/Ap$$

The points on the computation grid range from 1 to Nj in the N-S direction with points 1 and Nj on the boundaries. Since the boundary values ϕ_1 and ϕ_{NJ} are known, equations for ϕ_2 to ϕNJ-1 are solved. The set of equations then becomes:

$$\begin{aligned}
\phi_2 &= B_2\ \phi_3 + C_2\ \phi_1 + D_2 \\
\phi_3 &= B_3\ \phi_4 + C_3\ \phi_2 + D_3 \\
&\ \ \vdots \\
\phi_{Nj-1} &= B_{Nj-1}\ \phi_{Nj} + C_{Nj-1}\ \phi_{Nj-2} + D_{Nj-1}
\end{aligned} \tag{54}$$

Now since ϕ_1 is known ϕ_2 can be eliminated from Equation 54 and so on, yielding a general recurrence relation

$$\phi_j = A_j\ \phi_{j+1} + D_j' \tag{55}$$

To get the relation for A_j and D_j' Equation 55 is written as

$$\phi_{j-1} = A_{j-1}\ \phi_j + D_{j-1}'$$

Now putting in the value of ϕ_j from Equation 50

$$\phi_j = \left(\frac{A_N}{A_P - A_S \cdot A_{j-1}}\right)_j \phi_{j+1} + \left[\frac{C_j' + A_S D_{j-1}'}{A_P - A_S A_{j-1}}\right]_j \tag{56}$$

Comparing Equation 54 and 56 yields coefficients for the recurrence formula

where $$A_j = A_N / (A_P - A_S A_{j-1})_j \tag{57}$$

$$D_j' = (A_S D_{j-1}' + C_j') / (A_P - A_S A_{j-1})_j \tag{58}$$

Using Equations 57 and 58, ϕ_j can be calculated from Equation 55. Having solved for ϕ_j on one N-S line, ϕ_j's on the next N-S line are solved and so on until the entire solution domain is swept. The same treatment is then applied in the W-E direction (Equation 52). It is usually necessary to sweep between 1 and 3 times per iteration for optimum solution time.

4.3.5 Under-Relaxation

Since the finite difference equations are nonlinear in nature the convergence is facilitated and sometimes divergence is avoided by under-relaxing the value of ϕ being calculated as:

$$\phi_P^R = F \quad \phi_P^{New} - (1-F) \quad \phi_P^{Old} \tag{59}$$

where F is an under-relaxation factor which is less than one.

The way in which the above relation is introduced into the numerical procedure is as follows:

$$A_P^R = Ap/F \tag{60}$$

$$S_u^R = S_u + (1 - F) A_P^R \phi^{Old}$$

It can easily be shown that the effect of introducing the above modifications is to under-relax Φ_P according to Equation 59.

Some skill is required to select the under-relaxation factors that are best suited to a particular problem.

4.3.6 Solution Procedure

The following procedure is used to obtain the solution:

1. Guess fields for all variables.
2. Assemble coefficients of momentum equations and solve for U* and V* using prevailing pressures.
3. Solve the pressure correction equation and update velocities and pressures.
4. Solve equations for other variables.
5. Update fluid properties such as viscosity and density.
6. Test for convergence. If not attained use prevailing fields as new guesses and repeat from step 2 until convergence is attained.

4.4 Computer Codes

The equations to be solved, the physical models and the numerical schemes described above are embodied in computer programs. There are two codes relevant for this study. They are known as 2D-TEACH and 3D-TEACH.

The acronym TEACH is used to denote the generic solution procedure. The prefix 2D or 3D defines the dimensional capability of the code; 2D implying planar or axisymmetric flows can be calculated, and 3D implying full three-dimensional capability. The internal organization of the two codes is similar, and the interactive menus, commands and cautions used are also similar so that a user can operate either code with equal facility. The 3D-TEACH code can regress for

a two-dimensional problem to produce the same solution as 2D-TEACH. Either interactive or batch running is available. These codes exist as production codes. This means that they are documented and maintained, and are user-friendly.

Both codes are generalized such that complex geometric boundaries and inflows can be represented without reprogramming. The coordinate system used is orthogonal with choice of either cylindrical or cartesian coordinates. The basic finite difference method causes the calculation mesh to be constrained by the coordinate system. With a chosen coordinate system therefore, the geometry has to be "discretized" to fit this system. Hence, complex geometries have to be represented by a series of "stair-steps". The consequences of this are that wall shear stresses and heat transfer cannot be correctly calculated for curved walls or walls inclined to the major axes. Inflow and outflow through the elements of the stair-steps is permitted. In addition, solid bodies can be placed inside the flowfield and may contain mass sources or sinks within them. Therefore, within the constraints of the coordinate system, the codes have great geometric flexibility. There is a choice of either English or S.I. units in both codes. The 3D-TEACH code is provided with cyclic boundary conditions for handling repeating segments (as in an annular combustor).

The planned use of the codes is for calculation of the bulk flows in the combustor. Adjacent to solid boundaries the local Reynolds number of the flow based on local velocity and distance from the wall becomes very small, and the turbulence model, which was developed for high Reynolds numbers, becomes inappropriate. For this reason and reasons of economy, the calculation does not proceed right through the boundary layer to the solid wall; boundary layer wall functions are used instead, and are patched on to the bulk solution.

The codes are provided with appropriate pre- and post-processors for the convenience of the user. The pre-processor allows the user to interactively create or edit a flow geometry and automatically builds an input file. For 2D-TEACH a graphics post-processor generates profile, contour, streamline and streakline plots; a quasi-three-dimensional representation of profile plots to show flow development is also available. This post-processor is extended for 3D-TEACH to include a production version of Brigham Young University's geometric modeling system MOVIE.BYU. The streakline routine and the spray model are available to generate dynamic representations of the flow and droplet trajectories during an interactive terminal session with the codes.

The 2D-TEACH and 3D-TEACH codes represent state-of-the-art numerical modeling capability, and are available as production computer programs in regular engineering use.

4.5 Relation to Design System

A TEACH session on the computer is the computational equivalent to performing a physical experiment or test. All the data, and more, of an actual experiment or test is available for whatever subsequent manipulation is required. In fact, the computational experiment is infinitely more flexible than physical experimentation.

In a single terminal session, the dynamics of the isothermal flow field may be studed using streaklines, and, using a color terminal, the experience is exactly like observing a water-analogy rig flow visualization. Combustion can then be turned on and the hot flow field observed in similar fashion; the trajectories of fuel droplets injected into and contributing to this field can be observed to study penetration and evaporation if desired. Profiles of axial, radial and tangential mean velocities, temperatures, pressures, densities, mass fractions of fuel, oxidant and combustion products can be displayed at positions throughout the field. They can also be assembled into a quasi-three-dimensional plot so the field development can be readily displayed. If desired, contour plots may be selected. Post-processors can generate from the field information global parameters such as outlet temperature pattern and profile factors, mixedness, recirculation zone size, strength and mass recirculated, pressure recovery, loss coefficients, etc., as desired. For more detailed studies turbulence quantities, and surface shear stress and heat transfer coefficients can be produced.

The information generated is available immediately off the terminal screen as semi-permanent hardcopy, within 2-3 hours as permanent hardcopy through a Calcomp plotter, or as microfiche for storage. The entire output can be saved in a restart file for subsequent operations.

Parametric studies of the effect of operating conditions or geometric variations are easily accomplished using the pre-processor to modify the input. There are of course, no experimental facility or instrumentation limitations to restrict the range of operating conditions that may be run, and there are no extensive delays for hardware rework.

The literally staggering potential of computational fluid dynamics, as indicated above, suggests how it might be used in a design system.

Figure 4 shows a possible revision to the design system where a module for a comprehensive Computational Fluid Dynamics Model is added. The process begins with the specification of design criteria and ends with certification of the engine. Within this design system the module labeled Computational Fluid Dynamics is apparent as exerting a monitoring and controlling function extending from preliminary layout through engine test-development and encompassing all stages between. Note that rig testing is now limited to proof-testing, and that engine development testing is much more effective due to the insight fed back from the added module. Note also that the system is now predictive: performance information becomes available at or before the preliminary layout stage, and diffuser and shroud flow calculations provide

boundary conditions to the combustor calculations. The Liner Cooling Analysis module is now provided with realistic flow conditions on either side of the combustor liner as boundary conditions allowing improved calculation of temperature distributions over the liner surface.

In Figure 4 the Computational Fluid Dynamics Model module does not replace the Preliminary Design System module. It is presently believed that the combination of phenomenological modeling and mathematical modeling embodied in the two modules working together represents the cost effective approach to design.

Figure 5 provides an illustration of the potential use of the codes with an axisymmetric study of the dump region in the dump-diffuser of a combustion chamber. Flow is represented in this two-dimensional axisymmetric calculation by streamlines. The use of stair-steps is shown clearly.

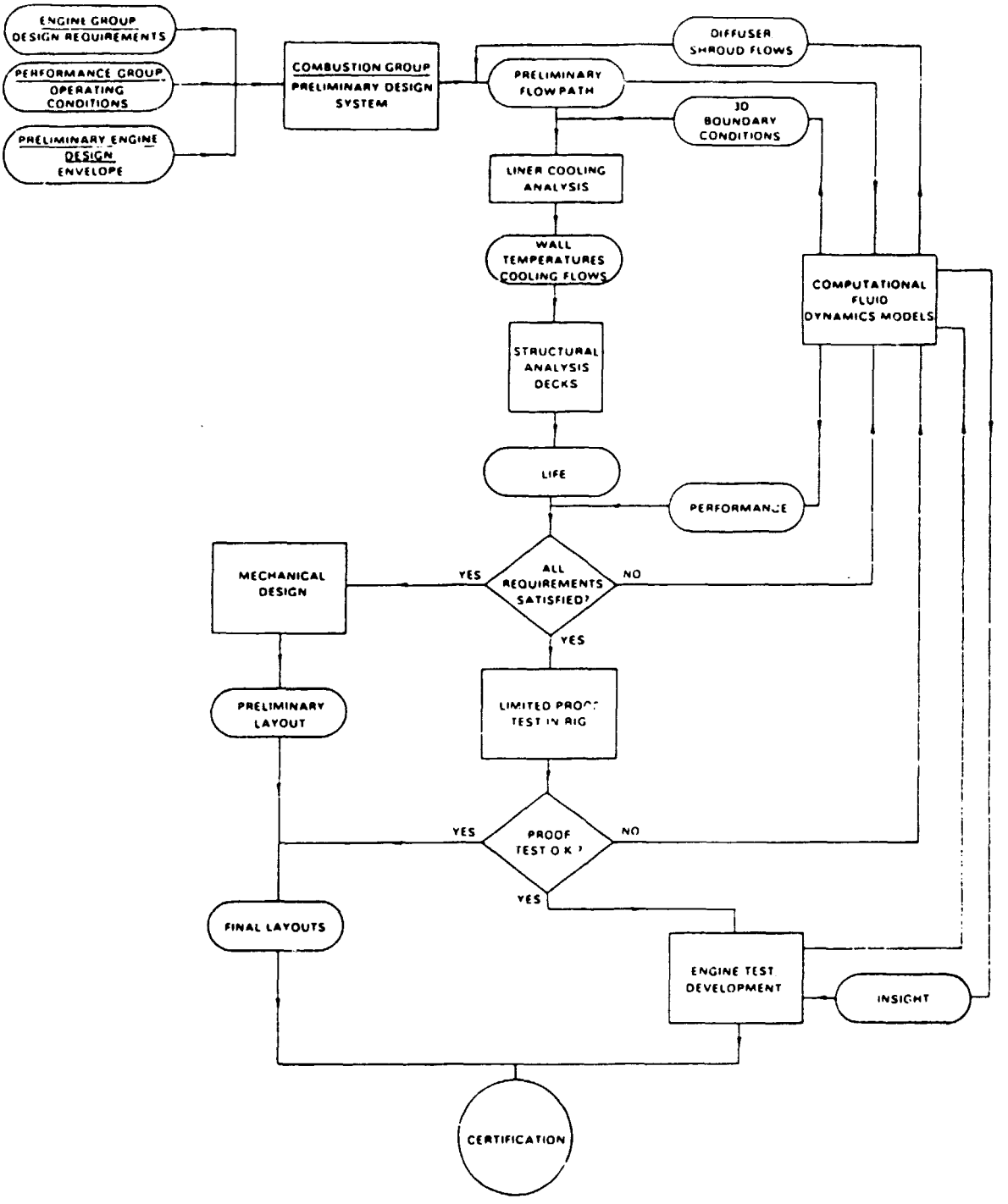

Figure 4 Possible Revision to Design System with Computational Fluid Dynamic Modeling

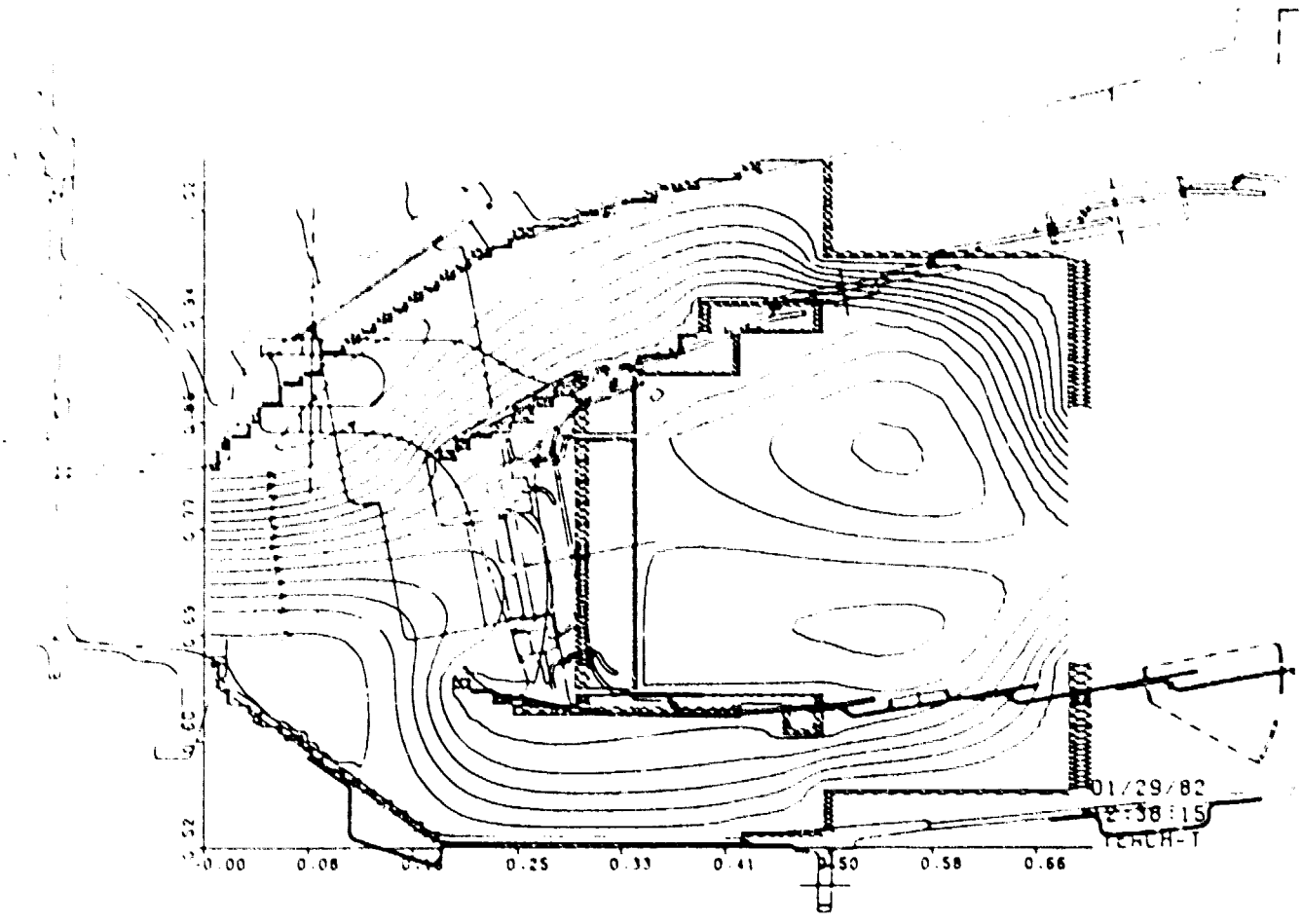

Figure 5 Illustration of Use of 2D-TEACH, To Calculate a Dump Flow

5.0 ASSESSMENT PHILOSOPHY

The sub-models and the computer code embodying them have been briefly described above in order to define what is to be evaluated. To carry out a realistic performance evaluation of these models an unambiguous approach is required.

Real combustor flows are three-dimensional, multiphase, turbulent and chemically reacting flows. Detailed measurements of real combustor flows are costly and present many severe difficulties. Analyses of such flows require that all of the effects present in the flow be treated simultaneously. All of the physical models - together with the numerics - are exercised. Therefore, it is nearly impossible to separate effects in order to assess the performance of the individual elements in this situation. If the performance of individual models cannot be assessed, then it is impossible to identify specific shortcomings and to make recommendations for improvements.

It was concluded that individual models should be examined one at a time in progression. Experiments of increasing complexity that require invoking multiple models should be approached in sequence so that the progressive performance is evaluated. Cognizance of the effects of the numerics on solution accuracy would be maintained.

It was decided that the type of experiment which is most suitable for use in evaluating model elements is one conducted with high quality hardware under laboratory conditions where operating variables can be controlled, and where extensive and careful measurements are made and the experiment is documented fully and carefully. Complex flows should only be examined to determine the extent to which individual model elements interact and to establish that the solution procedures are workable in complex flows.

6.0 DATA BASE DESCRIPTION

To evaluate the modeling a set of suitable experiments is required. Such experiments have been organized into a data base.

6.1 Class of Data

The class of experimental data to be sought and used to establish the data base against which the performance of the modeling can be assessed was determined by the decisions to eschew real combustor flows and to rely on laboratory quality experiments.

The general philosophy adopted to test the models required that the flows in the gas turbine combustor be considered in terms of their main constituent processes. These processes are:

1. Thermal radiation
2. Fuel spray development and flow field interaction
3. Combustion reactions and kinetics
4. Fluid mechanics
5. Soot formation

Each main process was subdivided as appropriate. For example, fluid mechanics was broken down into the constituent flows as follows:

a) co-axial jets,
b) swirling jets,
c) jets in sudden expansions,
d) jets in crossflow,
e) wall jets,
f) bluff-body recirculations

This procedure required that experiments be located in the literature for each of the constituent subdivisions. In addition, redundant experiments were required to ensure generality of any conclusions drawn about a particular flow/model performance.

6.2 Assessment Procedure

Experiments of a particular constituent flow were assessed for their suitability for inclusion in the data base against a number of criteria established to define an ideal experiment. These criteria encompassed minimum dimensionality, well-behaved flow, continuous variation of test parameters, known boundary conditions, progression in flow complexity and extensive instrumentation. Use of flow visualization as a diagnostic aid was also considered desirable. A suitable experiment might also be an analytic solution or an alternative but established calculation procedure.

1) Minimum necessary flow dimensionality. Experiments in which the flows can be represented as one- or two-dimensional are desirable. Three-dimensional flow situations should be used only when specifically testing three-dimensional flow modeling capability.

2) Well-behaved flows. Flows in which instabilities, periodicity, or changes in gross behavior occur as flow conditions change are to be avoided. For example, flows in which the location of reattachment points of separated flow regions could undergo significant shifts as Reynolds number is changed over the range of interest should be avoided (unless, of course, this is the flow feature being tested).

3) Continuous variation of test parameters. Experiments that are conducted over a wide range of values of test parameters rather than at isolated sets of conditions.

4) Known boundary conditions. Entrance and exit flow profiles must be specified as completely as possible. Velocity, temperature and pressure profiles are required. Concentration profiles are important for reacting flow experiments; initial droplet size, velocity and spatial distributions are required for two-phase flows. For assessing turbulence models, initial profiles of turbulence intensity and integral length scale are vital.

5) Progression in flow complexity. The ideal experiment for assessing flow models would consist of a series of experiments of increasing flow complexity such that the creditability of the analysis can be checked in stages. For example, the initial tests for a given flow geometry should be single-component, isothermal flow visualization tests which could be used to check the fluid mechanic aspects of the analysis. Two-component gaseous flows could be used to check the ability to predict mass diffusion; thermal diffusion could be checked using gases introduced with different initial conditions, reacting gaseous mixtures the next stage. A similar progression of experiments with two-phase flows can be constructed.

6) Extensive instrumentation. Flow mapping experiments in which nonintrusive techniques are used to characterize flows throughout the chamber volume are highly desirable. Estimates of instrument precision should be made and possible sources of bias identified. Redundant measurements performed with different instruments are valuable.

Another class of data is available for use in validating the computational accuracy of the model. These data are in reality results of computations carried out using well-developed and proven codes which have been in use over the years to treat simple flows wherein one particular physical phenomenon is of interest. Results of calculations performed using the combustor flow analysis given the proper boundary conditions must agree with the well-developed codes if the computational aspects of the model are to be considered valid.

A subjective numerical rating was applied to each experiment considered suitable. The scale ran from 0 (poor) to 10 (good), and the score depended on how the experiment measured up against the criteria above.

The survey was a limited effort. Undoubtedly there exist other works which might qualify as benchmark quality test cases. Experiments receiving a score were included in the data base, and those receiving no numerical rating were not included. For those experiments that received rankings, the assessments of how well the experiment fulfilled the various criteria are given in Table 3. Experiments reviewed and not included in the data base are given in Table 4.

It should be pointed out that the individual experiments may not have been conducted for the purpose of generating data to be used to validate combustor aerothermal flow models, and therefore the degree to which the experimental results meet the criteria, as reflected by the numerical ranking, should not be construed as a general score on the quality of the experiment.

A number of soot formation experiments were reviewed; however, it was concluded that these were not suitable for the present purposes and they were not pursued further. A new and continuing experiment by Santoro et al appears to hold the promise for the future (Reference 69).

Table 3

Tabulation of Data Base Entries

Experiment	Ref	Minimum Flow Dimensionality	Well-Behaved Flow	Known and Usable Boundary Conditions	Continuous Variation of Conditions	Progression in Flow Complexity	Extensive Instrumentation	Extended Operation	Rating
Johnson & Bennett	35	Yes	Yes	Some uncertainty due to diffuser-like entrance geometry	No	Some--with Johnson & Roback	Adequate	Moderate	7
Johnson & Roback	36	Yes	Yes	Initial radial velocity component desired	No	Some, see above	Adequate	Moderate	6
Habib & Whitelaw	37	Yes	Yes	Initial radial velocity component desired	Little	Some	No scalar transport data	Moderate	6
Vu & Gouldin	38	Yes	Yes, with some uncertainty	Measurements immediately upstream of entrance plane required	Little	Yes, with later hot flow tests in similar rig	Marginal (intrusive)	Moderate	4
Yoon & Lilley	39	Yes	Non-recirculating flow at entrance plane found only at limited conditions		Little	No	Limited	Limited	4
Kamatoni & Greber	40	Yes	Yes	Jet initial conditions not completely specified	Some	Some	Marginal (intrusive)	Little	5
Crabb & Whitelaw	41	Yes	Yes	Adequate	Little	Some, with Khan	Adequate	Moderate	6
Khan & Whitelaw	42	Yes	Yes	Adequate	Little	Some	Marginal	Moderate	5
Khan & Whitelaw	42	Yes	Yes	Adequate	Little	Some	Marginal	Moderate	4
Roquemore et al	43	Yes	No	Yes, at certain conditions	Some	Some	Good	Adequate	4
Hutchinson & Whitelaw	44	Yes	Not indicated otherwise	Entrance conditions uncertain	No	Yes	Adequate	Good	4
Mellor, Chigier & Beer	45	Yes	Yes	Adequate	No	No	Limited	Little	7
Holdeman & Walker	46	Yes	Yes	No	Yes	Yes	Limited	Good	2
Wu	47	Yes	Yes	No	Some	No	Adequate	No	3
Goodridge et al	48	Yes	Yes	No	Yes	No	Adequate	No	3
Grossmandler	49	Analytical, not in data base							8
Semerjian & Segalman	50	Analytical, not in data base							9

Table 4

Tabulation of Experiments Not in Data Base

Source	Ref	Category	Subcategory	Description
Crabb	41	Isothermal	Jets in crossflow	Multiple jets at 90° to crossflow-effects of nonuniform jet spacing
Ramsey & Goldstein	51	Isothermal	Jets in crossflow	Single heated jet at variable angle to crossflow
Roquemore et al	52	Exothermic		Propane in air diffusion flame at base of bluff body
Roquemore et al	53	Exothermic		Explores nonstationary behavior of above
Starner & Bilger	54	Exothermic		Horizontal hydrogen jet flame in rectangular airflow with moveable upper and lower walls
Kent & Bilger	55	Exothermic		Continuation of above
Starner & Bilger	56	Exothermic		Extension of original work
Bilger & Beck	57	Exothermic		Supplements Kent & Bilger
Depsky	58	Exothermic		Methane/air flame in coaxial swirling jets
Oven, Gouldin & McLean	59	Exothermic		Continuation of earlier work by Depsky
Hutchinson et al	44	Exothermic		Natural gas/air furnace
Baker et al	60	Exothermic		Continuation of Hutchinson et al
Hutchinson et al	61	Exothermic		Continuation of above
Founti et al	62	Exothermic	Liquid fuel	Continuation of Hutchinson et al
El Banhawy & Whitelaw	63	Exothermic	Liquid fuel	Rotating cup injector in nonswirling airstream with sudden expansion
Brum & Samuelson	64	Exothermic/ Isothermal		Propane/CO_2 into air-three coaxial streams with middle stream swirling
Noyce et al	65	Exothermic		Propane/air in stylized GT combustor
Yule et al	66	Spray		Twin fluid atomizer with kerosene into coaxial air jets
Modaress et al	67	Spray		Glass beads into coaxial stream of air
Soloman et al	68	Spray		Air atomizing oil spray into quiescent environment

6.3 Organization

The collected data were organized into the following categories:

1) Isothermal flow - Flow field structure

   Data on confined flows with and without swirl, with and without an initial sudden expansion.

2) Isothermal flow - Jet Penetration

   Data on confined flows into which penetrate single jets or rows of jets.

3) Exothermic flow

   Data on confined flows with heat release.

4) Sprays

   Data on the spatial and size distributions of sprays.

5) Radiation

   Data on measured radiation heat fluxes in furnaces.

An example of the collated data for a particular experiment is given in Table 5. All of the information contained on a descriptive input sheet is contained in the data base, together with tables of the measured quantities.

6.4 Management

The collected and collated data sets of interest are contained in a data base stored in structured format on a magnetic tape. The data base is readily accessible through a user-generated retrieval system. By this means the data base is made readily transportable, and it can be installed on any moderately-sized computing system. The retrieval system is not transportable since it will be machine-dependent because of the different file manipulation procedures employed by different computing sytems. Addition to the data base is an easy procedure.

By way of example, a description is given as Appendix A1 of the retrieval system used with the data base at Pratt & Whitney Aircraft. A tape-copy of the data base itself has been supplied to the National Aeronautics and Space Administration (NASA).

Table 5

Example of Data Bank Input

CATEGORY: Isothermal Flow SUBCATEGORY: Flow Field Structure

SOURCE: Habib, M. A. and J. H. Whitelaw: Velocity Characteristics of Confined Jets With and Without Swirl, ASME 79-WA/FE-21, ASME Winter Annual Meeting, December 1979. (Imperial College)

EXPERIMENT DESCRIPTORS:

Type:	Experiment
Dimensionality:	2-D
Medium:	Air
Injectant:	None
Description:	Coaxial jets (with and without annulus jet swirl) undergo sudden expansion into cylindrical duct

MEASURED PARAMETERS:

Mean axial velocity
RMS axial velocity fluctuation

VARIED PARAMETERS:

Annulus to central jet axial velocity ratio
Annulus flow swirl number

INITIAL CONDITION MEASURED:

Axial velocity, tangential velocity, turbulence kinetic energy and turbulence momentum transport (LV)

INSTRUMENTATION:

Laser anemometer
Three-hole pitot probe

BENCH MARK EXPERIMENT RATING: 6

COMMENTS:

Experiments were conducted for three cases: (1) annulus to center jet velocity ratio of 3 and zero swirl; (2) velocity ratio of 3 with annulus flow swirl number = 0.23 and no center jet swirl; (3) velocity ratio of 1.0 and zero swirl. Reynolds numbers of annulus flow were 77,500, 76,000 and 50,500 for the three cases; Reynolds number of center jet was 18,800, 18,540 and 35,500 for the three cases. Seeding technique employed was silicone spray separately injected into plenums supplying the individual flows. Reasonable agreement between these LDA measurements and pitot tube and hot wire measurements is shown.

A configuration similar to that employed in these experiments was later employed in experiments conducted by Johnson and Bennett. The Johnson and Bennett passage radii differed to some degree and the tube separating the inner and outer jet had a tapered trailing edge as opposed to a blunt trailing edge employed in these experiments. The Johnson and Bennett work includes measurements of (scalar) concentrations and concentration fluctuations. Data on the initial conditions found in the data bank have been furnished by the authors via private communication.

This work has been published in ASME Journal of Fluids Engineering, Vol. 102, (1980), pp. 45-53. Additional information may be found in:

Habib, M. A and J. H. Whitelaw: Velocity Characteristics of a Confined Coaxial Jet, ASME Journal of Fluids Engineering, Vol. 101 (1979), pp. 521-529.

7.0 TEST CASES

7.1 Selection

Benchmark quality test cases were selected from the data base. A total of 13 test cases were submitted for approval. From this list of cases, eleven were selected by the National Aeronautics and Space Administration for calculation; (Table 6) several of the selected cases involved multiple operating conditions or geometry variations.

From Table 6 it may be appreciated that Test Cases 1-5 inclusive and Test Cases 10 and 11 are flows that are representative of the majority of the features contained in the primary zone of gas turbine engine combustion chambers; Test Cases 6-8 address features of the dilution zone. Test Case 9 is primarily appropriate for afterburners and ramjets.

Table 6

Selected Test Cases

Case No.	
1. Johnson & Bennett	-- Coaxial non-swirling suddenly-expanded but confined jets
2. Johnson & Roback	-- Coaxial swirling suddenly-expanded but confined jets
3. Habib & Whitelaw	-- As case nos. 1 & 2
4. Vu & Gouldin	-- Confined coaxial swirling streams
5. Yoon & Lilley	-- Confined suddenly-expanded swirling jet with outlet restriction
6. Crabb & Whitelaw	-- Single jet in crossflow
7. Khan & Whitelaw	-- Row of jets in crossflow
8. Khan & Whitelaw	-- Opposed rows of jets in crossflow
9. Roquemore et al	-- Confined coaxial jets behind bluff body (reacting and non-reacting)
10. Mellor, Chigier & Beer	-- Hollow cone liquid spray in air
11. Semerjian & Segalman	-- Radiation (spectral) calculation

The concentration on nonreacting flows should be noted. In addition, Cases 1-3 appear to involve excessive redundancy for suddenly expanded jets, as do Cases 2-5 for swirling flows. This emphasis arises for three reasons: (1) the practical importance of these flows, (2) the deficiencies and limitations of the individual experiments, and (3) the importance of thoroughly assessing the significance of the turbulence model, the correctness of which is fundamental to achieving accuracy in any turbulent flow calculation.

The reasons for the selection of each case will be discussed briefly.

7.1.1 Test Cases 1 and 2 - Johnson & Bennett and Johnson & Roback

These two test cases are really an extension of the same experiment. The experiment is shown in Figure 6. Measurements without swirl and with swirl in the outer jet are covered. It satisfies most benchmark criteria, but fails to provide known boundary conditions, a tragic omission. This experiment is particularly important as a benchmark because it uses a configuration that is close to a gas turbine engine (can) combustor, and because of the potential to extend the configuration progressively all the way to reacting flows. It is also important because of its unique turbulent mass transport measurements.

7.1.2 Test Case 3 - Habib & Whitelaw

The configuration of the experiment, Figure 7, is very close to the configuration of Test Cases 1 and 2, and again, both swirling and non-swirling cases are covered. It therefore provides an interesting backup to these cases. As a benchmark the experiment satisfies some criteria to a degree; it fails to provide adequate boundary conditions. Comparison measurements using a pitot tube, hot wire probe and LDV (laser doppler velocimeter) are included.

7.1.3 Test Case 4 - Vu & Gouldin

This case covers similar ground to Cases 1-3, and represents a further co-axial jet system; however, both jets are swirling and there is no sudden expansion. Of particular interest is the fact that the swirl direction of the outer jet was reversed to provide data for both counter swirling and co-swirling jets. Although this experiment has been viewed as one with progression in flow complexity to reacting flows, this is not really the case since a different swirl system was used for the combusting cases. Measurements were made using hot wires. Figure 8 gives the configuration.

7.1.4 Test Case 5 - Yoon & Lilley

This is a further swirling flow experiment using a single swirling jet and a sudden expansion. It simulates a gas turbine engine can combustor as indicated in Figure 9. A contraction is provided at the outlet to minimize reverse flow of external fluid along the centerline. There may also be some difficulty with flow separation off the flat swirler vanes used. Measurements were made with a 5-hole pitot tube. As a benchmark experiment it satisfies some of the criteria; however, only one sub-case is to be considered.

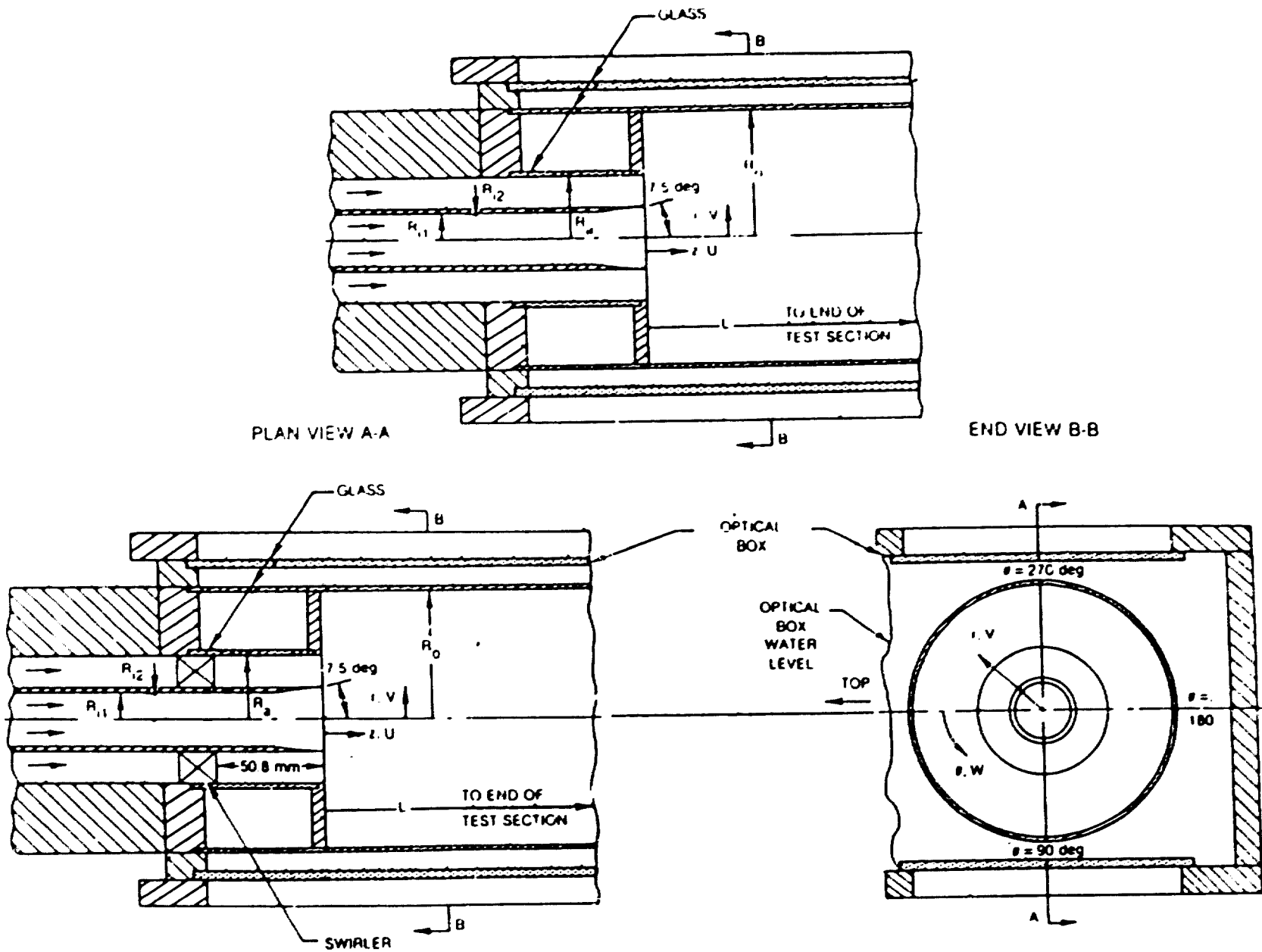

Figure 6 Johnson et al, Cases 1 and 2 (References 35-36)

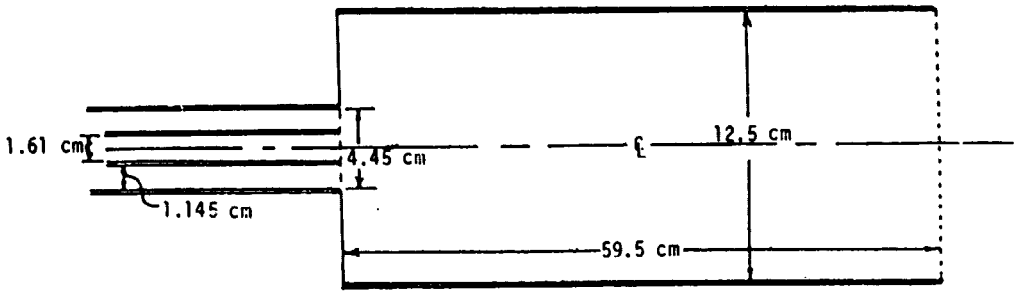

Figure 7 Habib & Whitelaw, Case 3 (Reference 37)

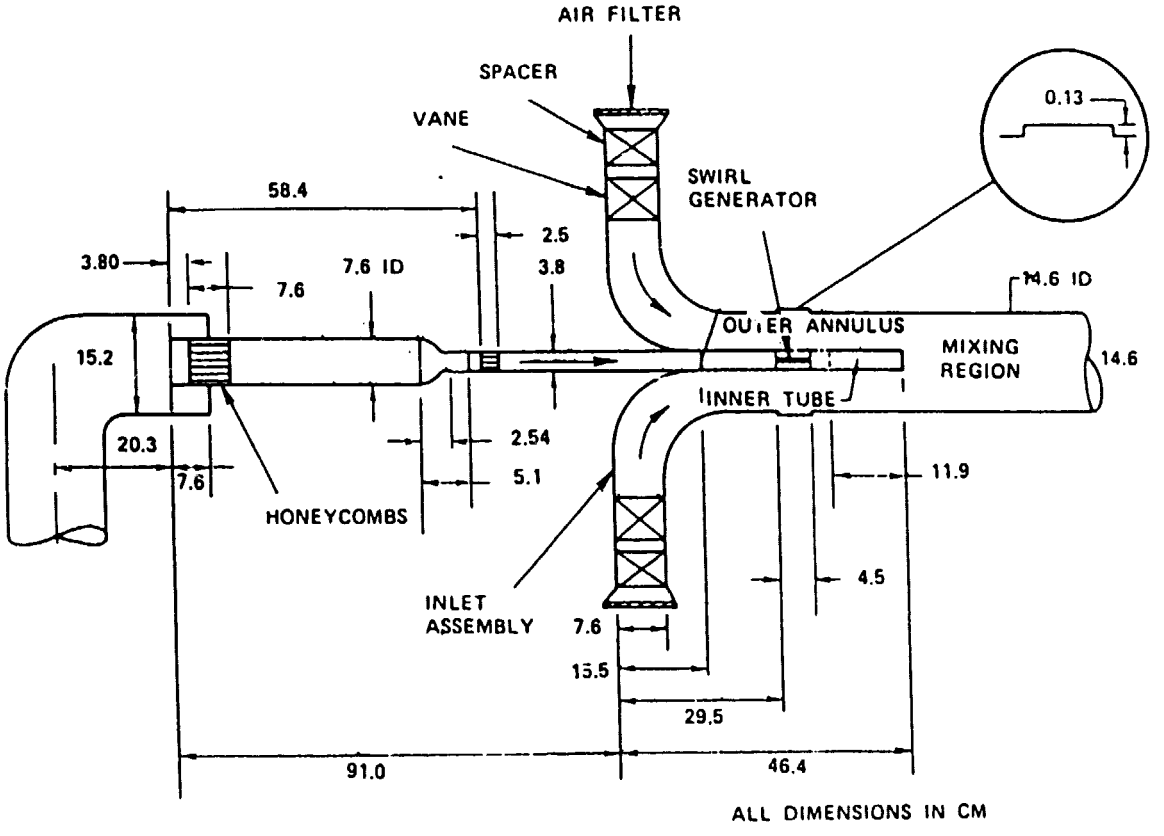

Figure 8 Vu & Gouldin, Case 4 (Reference 38)

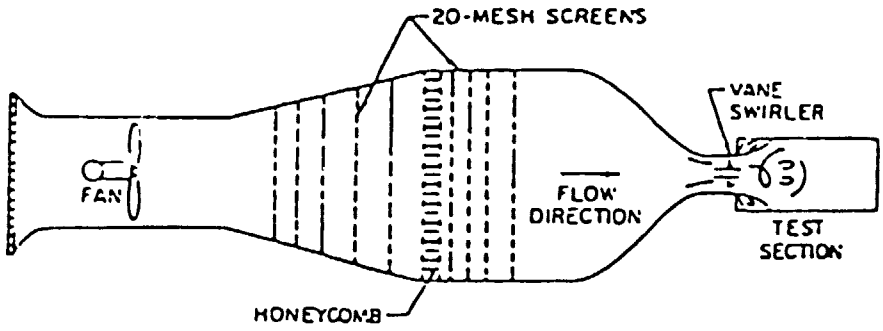

Test Section

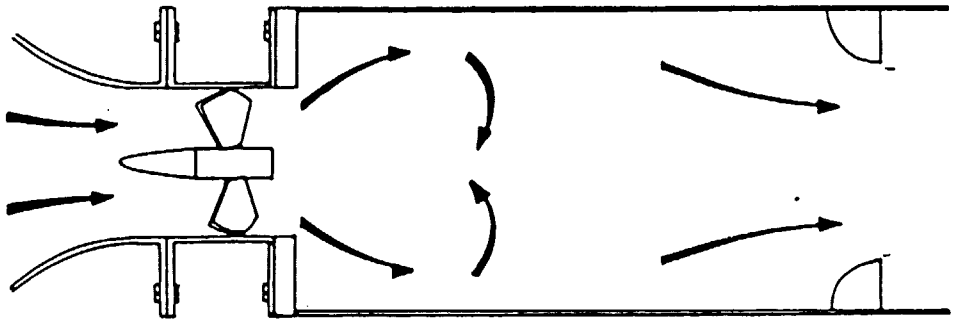

Figure 9 Yoon & Lilley, Case 5 (Reference 39)

7.1.5 Test Case 6 - Crabb & Whitelaw

This is a single jet in crossflow. It satisfies a few benchmark criteria, although there are some difficulties with the boundary conditions. It provides an introduction to the multiple jet experiments to follow.

7.1.6 Test Cases 7 and 8 - Khan & Whitelaw

These test cases are an extension of Test Case 6, and of each other. They involve multiple jets. Figure 10 illustrates the experiment. The data are primarily based on pitot tube measurements.

a) MULTIPLE JETS IN CROSS FLOW
b) OPPOSED MULTIPLE JETS IN CROSS FLOW

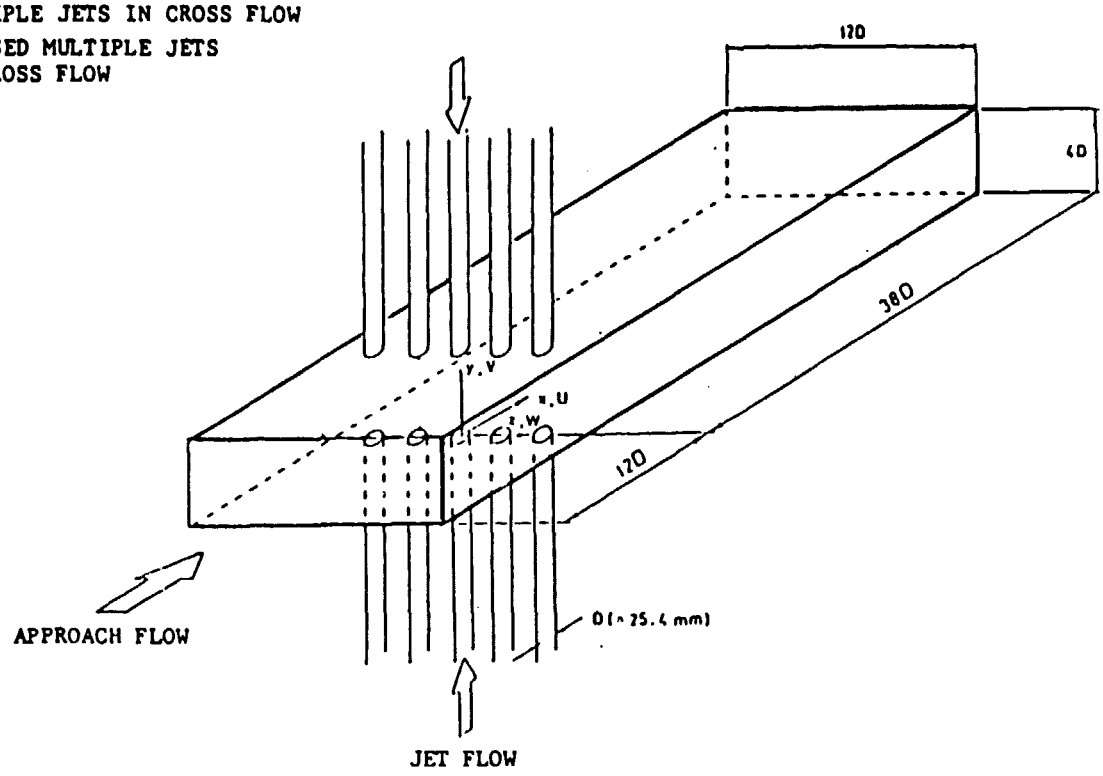

Figure 10 Khan & Whitelaw, Cases 7 and 8 (Reference 42)

7.1.7 Test Case 9 - Roquemore et al

This experiment is illustrated in Figure .. and involves a reacting flow. The flow is not like that in a regular gas turbine combustor. However, it is an experiment that is backed by extensive isothermal measurements and flow visualization. Unfortunately, it is a flow that is nonstationary. It also has very low heat release levels. With respect to the benchmark criteria it is otherwise generally a good experiment.

7.1.8 Test Case 10 - Mellor, Chigier & Beér

The experiment is far from ideal and is very limited in scope. However, in view of the limited availability of such experiments, there was little choice but to include it. The liquid spray is of water, and measurements were obtained photographically. Figure 12 shows the experimental arrangement.

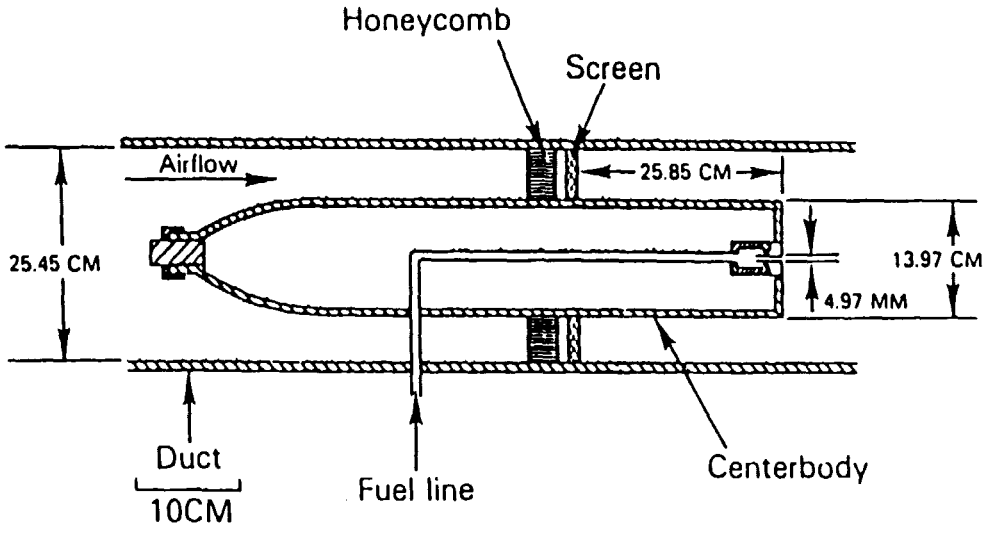

Figure 11 Roquemore et al, Case 9 (Reference 43)

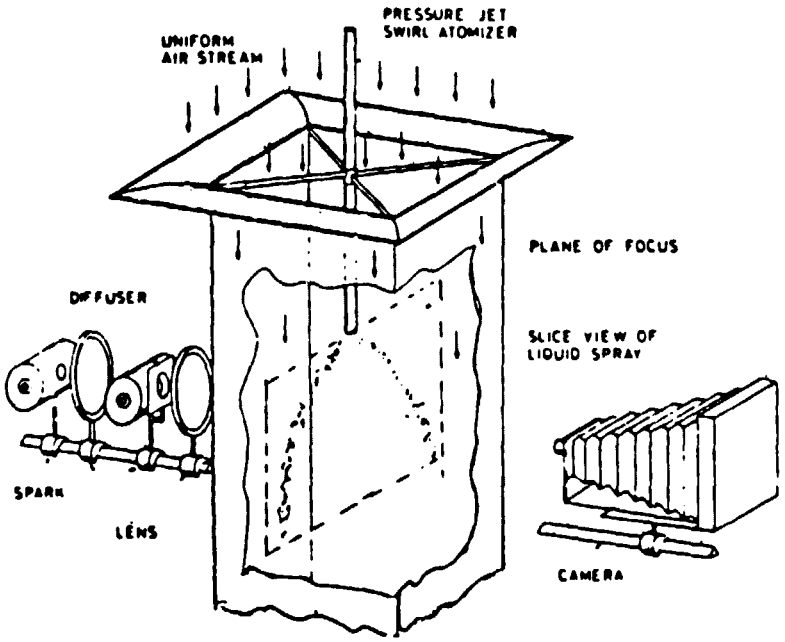

Figure 12 Mellor et al, Case 10 (Reference 45)

7.1.9 Test Case 11 - Semerjian & Segalman

This case is a numerical test case for direct comparison of the radiation model with a calculation using a substantiated and more exact method.

7.2 Review of Test Cases

A test case may imply a series of experiments conducted by a particular group of researchers at a specific laboratory.

The most common shortcoming encountered almost universally in the test cases was found to be the lack of well-defined inlet boundary conditions. The importance of these quantities has not been fully appreciated.

The computer codes require as inlet boundary conditions the following information concerning the entering flow, in addition to obvious property values: profiles of mean velocity components, profiles of turbulence intensity, and a characteristic dimension ℓ_T, related to turbulent eddy size.

The turbulence intensities are used to calculate the specific kinetic energy of turbulence K,

$$K = 1/2\ (\bar{u}'^2 + \bar{v}'^2 + \bar{w}'^2) \tag{61}$$

where u', v' and w' represent the fluctuating velocities along the x, r, θ axes respectively. The characteristic dimension is used to calculate the dissipation rate of turbulence energy ε,

$$\varepsilon = \frac{C_\mu (K)^{3/2}}{\ell_T} \tag{62}$$

where C_μ is a constant commonly taken as 0.09.

The turbulence model yields the eddy viscosity μ_t, as

$$\mu_t = \bar{\rho}\ \frac{C_\mu (K)^2}{\varepsilon} \tag{63}$$

The Reynolds stresses are needed for closure to the Reynolds-averaged equations of motion, and they are then formed from the stress-tensor,

$$-\bar{\rho}\,\overline{u'_i u'_j} = \mu_t \left(\frac{\partial \bar{u}_i}{\partial x_j} + \frac{\partial \bar{u}_j}{\partial x_i}\right) - 2/3\,\bar{\rho}\ K\delta_{ij} - 2/3\,\frac{\mu_t}{\bar{\rho}}\ \delta_{ij}\left[\bar{u}_i \frac{\partial \bar{\rho}}{\partial x_i}\right] \tag{64}$$

for variable density flows.

(Away from the inlet, transport equations are solved for K and ε.)

If the initial mean velocity components are not adequately specified, the equations of motion will result in the calculation of unrepresentative flow trajectories immediately downstream of the inlet plane. If the inlet turbulence quantities are also incorrectly specified there is an additional small but apparent effect on the flow trajectories through terms obtained from Equation 64 and containing μ_t and K (see Figure 2).

Incorrect specification of inlet turbulence quantities can have a further adverse effect if the flow is a reacting one. This is because the eddy break-up combustion model relates the reaction rate of fuel to the eddy lifetime, K/ϵ. An incorrect specification hence results in an incorrect density field. Since density is strongly coupled to the flow field, an incorrect density changes the flow field completely. The incorrect density, especially if it is lower than the actual density, cannot be corrected in the downstream region as the length scale is modified by the internal flow field.

The importance of inlet conditions to solution accuracy is highlighted in Reference 70.

A number of pertinent swirling flow cases were selected. Most of these were bedeviled by inadequate specification of inlet boundary conditions, and several important features of swirling flows were also not satisfactorily covered by these experiments. These features were:

1) Delineation of conditions whereupon a swirling flow is inertia dominated as opposed to being turbulence dominated.

2) Exploration of the critical swirl number range for confined flows, including the influence of the confining geometry shape and the actual distributions of velocity in exiting the swirl generator.

3) Effects of backpressure on confined swirling jets.

The work of Lilley and coworkers (References 39, 71-74) does look at some aspects of items 2 and 3. However, the instrumentation used is intrusive and yields time-mean information only. Intrusive instrumentation can change the nature of the flow being measured, and time-mean information alone is insufficient to completely test turbulence models. Furthermore, the number of traverse stations used in these experiments is severely limited. This does not permit a comprehensive flow picture to be built up. In addition, under certain circumstances the flow suffers from formation of a central vortex core extending upstream from the exit. The flow is therefore not specified by the measured inlet conditions. The swirl generator used has flat vanes, and at high angles of attack these vanes are stalled. The hub of the swirler is large and has a bluff trailing edge. The generator itself is situated close to the dump plane. The swirling flow therefore has a fairly high degree of circumferential nonuniformity associated with it, and perhaps some radial instability. These conditions are not likely to be reflected in the measured inlet conditions.

Although the Lilley study is yielding useful qualitative information on swirling flows confined in sudden expansions and is highlighting areas for further investigation, in current form it is not really suited for the present purposes of model validation.

Yoon and Lilley (Reference 74) have observed that backpressure on a confined swirling jet can dramatically influence the nature of the recirculation established, Figure 13. It should be noted that the relative dimensions in Lilley's experiment with exit blockage are close to those of a real combustor. This flow and effect are therefore clearly of great practical significance. Similar effects have been reported in furnaces by Mathur & Maccallum (Reference 75) and by Baker et al (Reference 60). This effect needs to be explored in detail, particularly in relation with combustor dome shape.

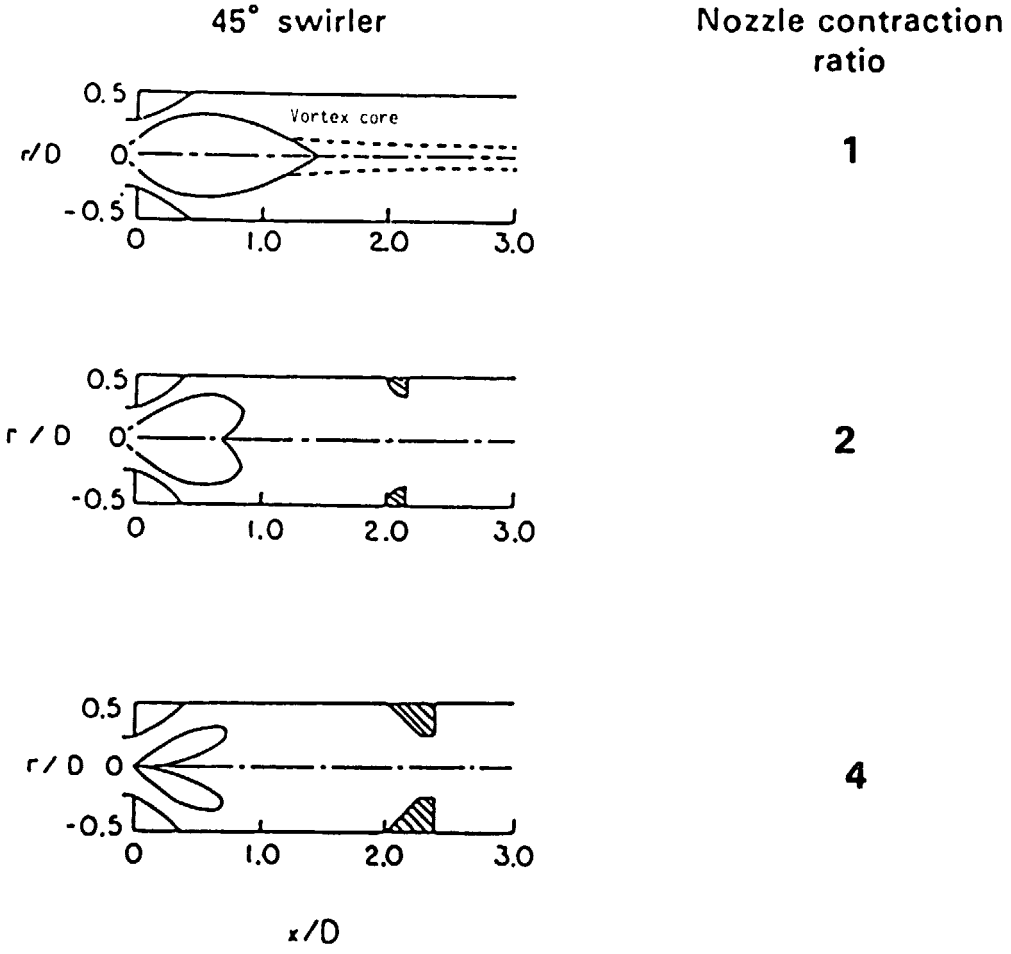

Figure 13 Influence of Back-Pressure on Swirling Flow (Yoon & Lilley)

It would be extremely useful if isothermal and reacting flow experiments could be carried out in the same apparatus so that a natural progression in understanding could be followed. Reacting flows alone invoke simultaneous use of several of the models and separation of effects can be difficult.

Generally, such progression has not been done. Gouldin for example, made extensive isothermal flow measurements in one apparatus (Reference 38) that was chosen as Test Case 4. However, the experiment was extended to reacting flows in a different apparatus (References 76 and 77) using a different central swirl generator. Although some cold flow measurements are given in the new apparatus (Reference 77), they are not extensive enough to be useful. The "same" flow field is also being studied by Sommer (Reference 78), but using a central swirl generator that is different yet again. Preliminary experimental results at comparable swirl numbers are compared against numerical calculations made by Ramos for Vu & Gouldins' apparatus and against Vu & Gouldins' measurements. The measured results and calculations are compared as if the two sets of apparatus were identical, even though the measurements show the flows are clearly very different, especially for the case of co-rotation.

When an experiment does progress from isothermal flow to reacting flow the progression is usually done in a single step. The intermediate steps of isothermal constant density multiple specie, variable density multiple specie, or variable density single specie, nonreacting flows are neglected. A reacting flow simultaneously exercises the turbulence and combustion models at the least. It should be remembered that the turbulence model covers transport of both momentum and mass. Since the mass transported could be fuel, it is important that this aspect of the turbulence model be explored separately before seeking to evaluate the combustion model.

Few experiments in the literature provide sufficient measurements to permit a separate evaluation of the turbulent mass transport in the flowfield prior to considering the reacting flow condition. Exceptions to this generality are the experiments of Johnson & Bennett (Reference 35), Johnson & Roback (Reference 36), and Roquemore et al (References 43 and 79).

Combusting-flow experiments (as opposed to industrial tests) commonly tend to be limited in heat release rate for three reasons:

1. facility limitations,
2. operating costs, and
3. mensuration difficulties

As a result, such laboratory experiments are frequently carried out at atmospheric pressure, modest to low inlet air temperatures, and low overall equivalence ratios. The consequence of such operating conditions is that combustion is almost always reaction-rate limited.

The combustion and radiation sub-models chosen for the calculation procedure are as simple as possible. As the models were to be simple, the choice was made appropriate to the major application, i.e., the modern, efficient, high-power gas turbine engine combustor, operating at greater-than-idle speed conditions.

It becomes extremely difficult to find suitable laboratory experiments against which to test such models. The actual test cases used were reaction rate controlled and had such low radiation fluxes that they were actually "noise" compared to the fluxes in the application.

The test case selected for combustion and radiation model comparisons was Case No. 9 in Reference 78. This choice was made because of the isothermal, variable density companion measurements available that permitted some amelioration to be made of the difficulties of getting the turbulent mass transport correct. Unfortunately, the reacting flow measurements were made at atmospheric pressure, ambient inlet air temperature, and equivalence ratios less than 0.1 (due to a rich blow-off problem, Reference 52). As was expected under such circumstances, comparison of temperature profiles revealed the effects of a finite reaction rate that is just not present in the model. Similarly, the maximum radiation flux comparisons for this experiment were made at a level less than one-twentieth those of a gas turbine combustor.

The liquid fuel spray model has a number of facets which have to be examined: droplet tracking, turbulent diffusion of droplets, droplet heat-up, fractional distillation of a multi-component fuel, and coupling of the gas and liquid phases. The experiment selected to evaluate the spray model (Test Case No. 10, Table 6, and Reference 45) enabled study of only one of these - droplet tracking in a uniform airstream. This of course, was a desirable feature for a first step in a liquid system in that several simultaneous processes did not have to be separated. Water was injected and atomized in a low turbulence, ambient temperature airstream at a mass ratio of 4×10^{-3}, water to air, and at this loading the water droplets did not significantly influence the flow structure and did not undergo evaporation of any significance.

The final constituent flow to be considered was a three-dimensional one, the jet-in-crossflow, as both a single jet and as a line of jets. The experimental data for this class of flows is generally in fair shape. Difficulties arise concerned with representing initially circular jets with the constraints of a rectilinear grid, attempting to control numerical diffusion, (a hopeless task with present computer storage), and the cost of the calculations. There is confusion concerning the operating conditions for the lines of opposed jets, (Reference 42), that prevents meaningful comparisons of measurements and calculations from being made. Comparisons of concentrations for the line of jets cannot be made as the experiment is non-symmetrical.

8.0 MODEL PERFORMANCE

8.1 Considerations for Evaluating Model Performance

The models studied were for:

1. Turbulence (momentum and mass transport)
2. Combustion (for heat release)
3. Liquid fuel spray
4. Gaseous radiation

These physical models are not independent of each other. The interactions between models are strong, and this coupling is illustrated in Figure 14. The interrelationships between models dictate that a hierarchy of models be established, as Figure 15 shows. Note the appearance in Figures 14 and 15 of numerics, and its premier position in the hierarchy. Although the subject of numerics is not a physical modeling topic, it dominates all the subsequent physical modeling through the false diffusion it introduces via the generic TEACH solution procedure. Although numerics is not part of the study undertaken, its effects must be constantly remembered when considering the performance of the physical models.

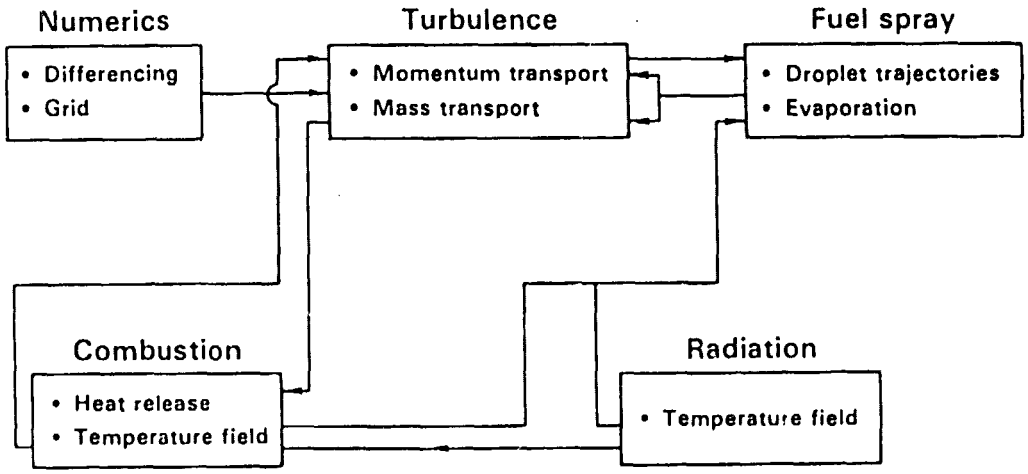

Figure 14 Interrelationship of Physical Models

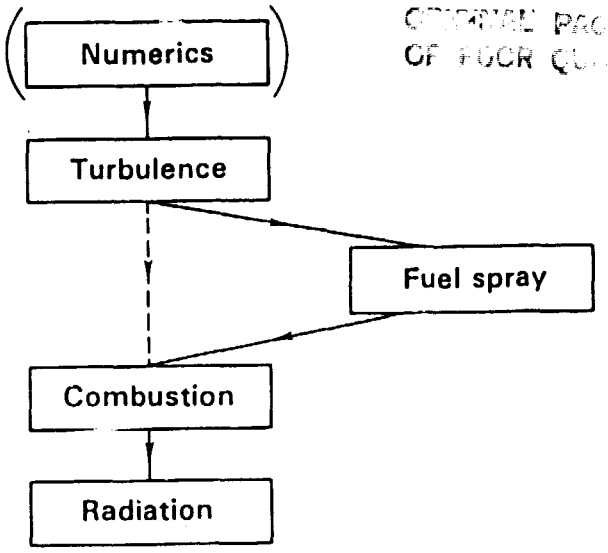

Figure 15 Hierarchy of Physical Models

Figure 1 gives a diagram of the calculation process. The position of the physical modeling section is clear and the influence of the following section has been described. One further section is relevant - the assembly of the equations.

When the modeled conservation equations were assembled, they were written in unweighted form, and terms involving fluctuating density were neglected. The implication of this step is that density differences in the flow are not large - obviously not too good an assumption for combusting flow cases where temperatures in the field can vary widely from point-to-point and with time.

For variable density flows a density-weighted decomposition of the conservation equations is sometimes used. This is known as Favre averaging. For example, the instantaneous velocity in unweighted form is written,

$$u = \bar{u} + u' \tag{65}$$

where $\bar{u}$ and u' are the time-average and fluctuating velocities respectively, and in density-weighted form,

$$\rho u = \overline{\rho u} + \rho u'' = \bar{\rho}\tilde{u} + \rho u'' \tag{66}$$

where the tilda denotes a Favre-averaged velocity, so

$$\tilde{u} = \frac{\overline{\rho u}}{\bar{\rho}} \quad \text{and,} \quad \bar{u} = \tilde{u} - \frac{\overline{\rho' u'}}{\bar{\rho}} \tag{67}$$

The choice of weighted or unweighted equations is somewhat arbitrary (Reference 13). The Favre-averaging approach requires modeling of terms like $\overline{\rho' u'}$, which then appear in the equations. For these reasons (Reference 12), Favre-averaging was not used. However, use of Favre-averaging yields density-weighted property values. Some instruments measure weighted values while others may measure unweighted values. This should be borne in mind when considering comparisons of calculations and measurements.

As will be realized from the cautions presented above, unambiguous assessment of the performance of the physical models proved to be very difficult. There is strong evidence to believe that many of the shortcomings which in the past have been blamed on the turbulence model typically, were in fact, to large measure due to poorly specified inlet boundary conditions (Reference 70), and to numerical diffusion.

8.2 Calculation of Test Cases

The results of the calculations of the test cases will be presented by flow, i.e.:

1. coaxial jets,
2. swirling jets,
3. variable density jets,
4. liquid spray,
5. reacting flow,
6. jets-in-crossflow, and
7. radiation.

Only a small portion of the total of the calculations and comparisons of calculation and data can be made. Results will be chosen to illustrate specific points. Additional information was provided to NASA through specific task reports.

8.2.1 Coaxial Jets

The study of coaxial jets is actually a study of coaxial jets in confined sudden expansions, using Test Cases 1 and 3 in the configurations shown in Figures 6 and 7. The physical model exercised is the turbulence model. Case 1 uses water-flow and Case 3 uses air-flow. Table 7 gives the relative velocities and dimensions, information on the type of inlet boundary condition used, and the grid sizes upon which the calculations were made. Note that the relative dimensions of the two experiments were about the same, and that there is a progression in jet velocity ratio from 1 to 3.

Test Case 1 had been predicted blind previously using a combination of measured and standard guessed inlet boundary conditions, (Reference 80). The predictions had generally been good with one notable exception - the centerline mean axial velocity variation in the initial region was incorrect.

Table 7

Coaxial Jets in a Confined Sudden Expansion
(Turbulence Model)

Experiment	u_{ann}/u_{pipe}	d_{ann}/d_{pipe}	d_{duct}/d_{ann}	Boundary/Conditions	Grid
Habib & Whitelaw	1.0, 3.0	2.76	2.81	Measured	30x39
Johnson & Bennett	3.11	1.93	2.07	Measured + 2 sets est.	52x38

It was felt that the difficulties with centerline axial velocities were due to the guessed inlet boundary conditions for the inner jet. An attempt was made to "improve" the assumptions for the inner jet region:

(i) the dividing lip of the central pipe was modeled as being infinitely thin rather than the 0.4 mm used in Reference 80.

(ii) the turbulence intensity for the outer jet was improved by introducing an increase through the lip-wall boundary layer, as shown in Schlichting (Reference 81).

(iii) the grid was refined to try to capture the potential core of the central jet (52 x 38 grid).

(iv) the diffusing flow at the exit of the central jet was calculated using a validated, parabolic matching computer code (Reference 82).

These conditions were felt to represent improved realism for the input boundary conditions over the original assumption, even though any possible elliptic effects of the downstream flow on the central jet are neglected.

Figure 16 compares the measurements of centerline axial velocities with the original predictions from Reference 80 and the calculations made using the revised boundary conditions for the central jet. Although the present calculations do not agree perfectly with the measurements, they apparently represent a significant improvement over the original results. Note that the effect extends to at least 10 duct radii downstream from the plane of the sudden expansion.

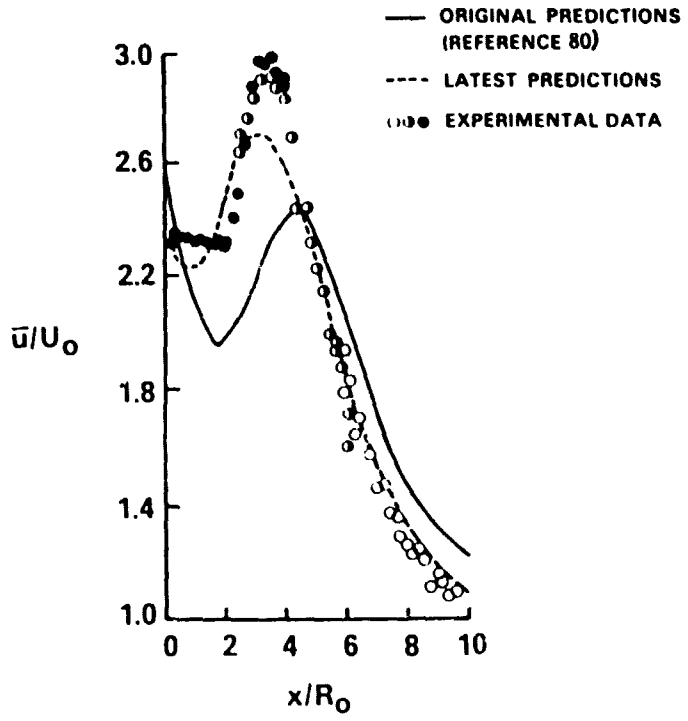

Centerline Mean Axial Velocities

Johnson & Bennett's Coaxial Jets in Confined Sudden Expansion

Figure 16 Revised Boundary Conditions Improve Centerline Velocities

Unfortunately, the change in boundary conditions destroyed the relatively good agreements obtained in Reference 80 for all other quantities at all axial stations. An example of this is shown in Figure 17 where a comparison is presented of radial profiles of fluctuating axial velocities at 0.836 duct radii downstream. The corrected calculations have the jets spreading too rapidly compared to the measurements. Too much turbulence is being calculated as a result of the new boundary conditions, this is reflected in the turbulent transport, and hence in the spreading rates.

It is interesting to note that when the experiment was originally set up, the flow downstream of the sudden expansion plane was not quite symmetric. To improve symmetry, a perforated-plate restrictor was introduced upstream in the supply pipe for the central jet. Prior to introduction of this restrictor, measured centerline axial velocities did fall on the originally predicted curve with the original (Reference 80) boundary conditions.

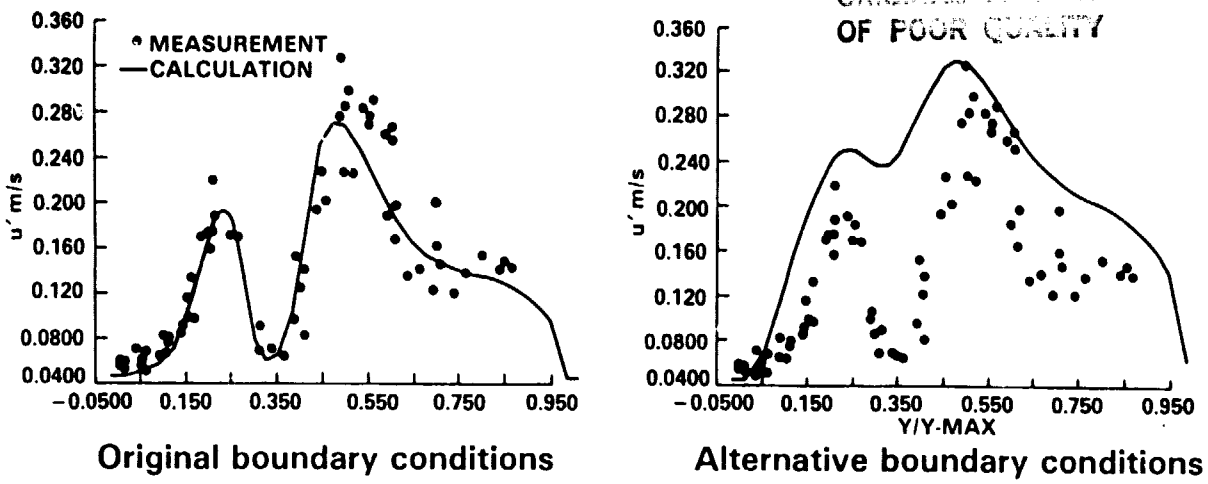

Example: Fluctuating axial velocity at x/R_0 of 0.836

Figure 17 Revised Boundary Conditions Worsen Radial Profiles of All Other Variables

The results of the comparison indicate that this experiment is closely controlled by subtle inlet boundary conditions. The latest boundary assumptions appear less "exact" than the original assumptions. The real boundary conditions may fall somewhere between the two sets of assumptions, but it is impossible to tell.

The ability of the code to correctly calculate the effects of jet velocity ratio on centerline axial velocities for nonswirling axial jets is illustrated for Case 3 in Figure 18. Measured inlet conditions were available for this experiment. The quality of radial profiles is illustrated in Figure 19 for mean axial velocity at 7.7 cm from the expansion plane for Case 3 at a jet velocity ratio of unity.

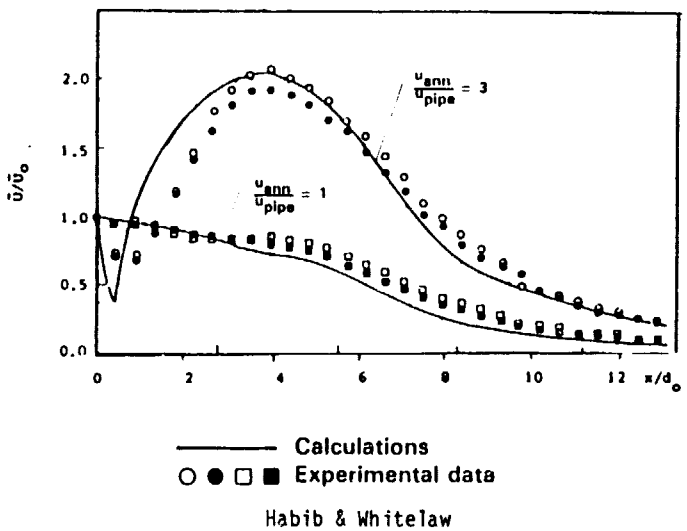

Figure 18 Effect of Jet Velocity Ratio on Centerline Axial Velocity Distribution is Correctly Calculated

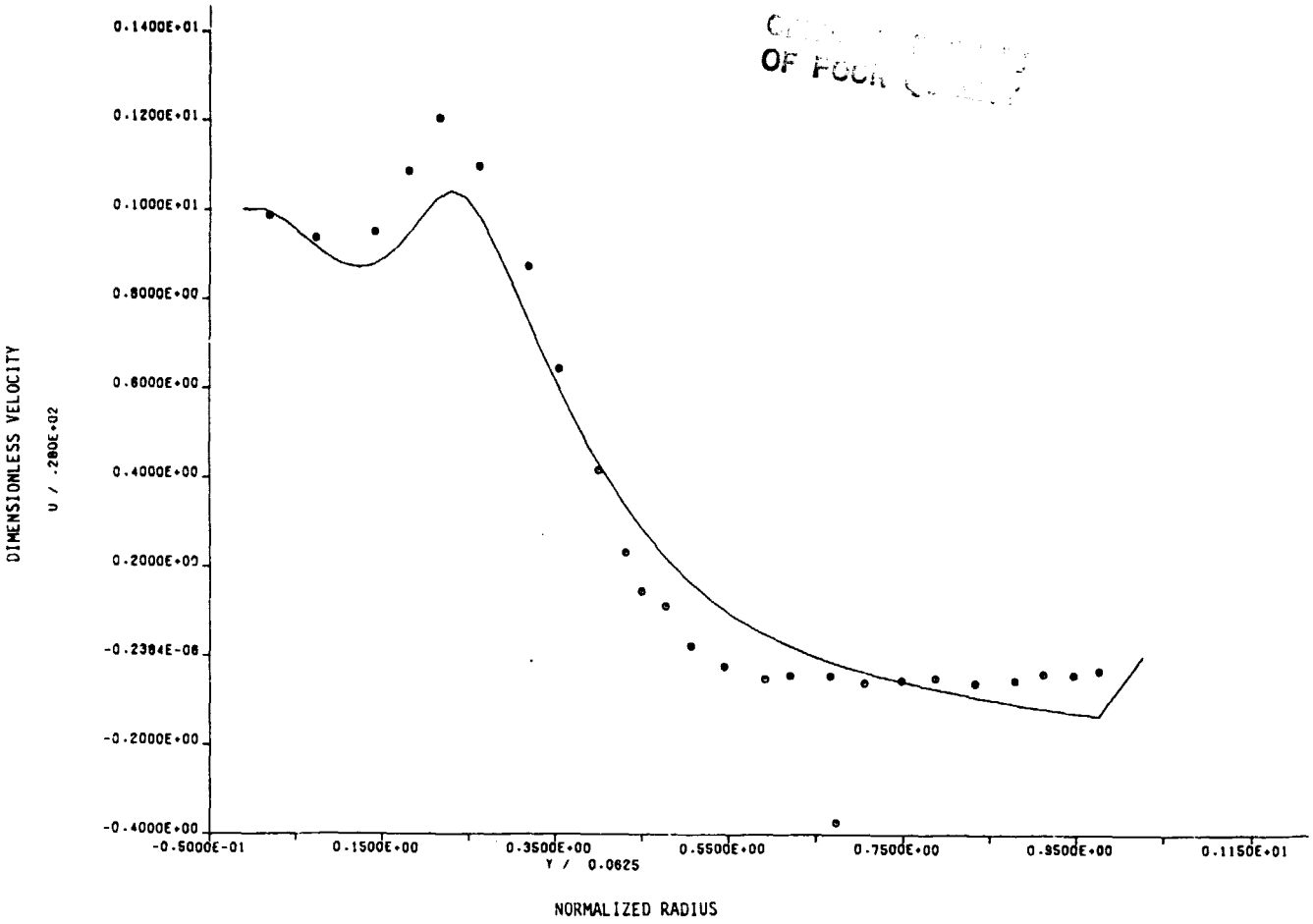

Figure 19 Example of Profile Agreement for Test Case 3, (Habib & Whitelaw), Nonswirling Jets

The type, size and strength of the recirculation zones generated are important features of the flow. Table 8 compares measured values with those from the calculations as a function of velocity ratio. For the velocity ratio of 3.11, results for the original (Reference 80) boundary conditions are presented. The agreements are generally encouraging.

For Case 1 fluorescein dye was introduced as a tracer into the water flow of the central jet to give constant density variable specie mixing of the two concentric jets. This permitted the turbulent mass transport side of the turbulence model to be investigated.

Table 8

Recirculation Zone Comparison for Cases 1 and 3

$\frac{U_{ann}}{U_{pipe}}$	Measured			Calculated		
	Length cm.	Strength m/s	Type	Length cm.	Strength m/s	Type
1.0	36.25	-5.54	step	34	-4.78	step
3.0	40.0	-7.56	step	34	-8.04	step
3.11	28	-0.27	step	26	-0.33	step*

*Original boundary conditions

The original calculations (Reference 80) supported the reduced value for turbulent Schmidt number of 0.5 chosen as a result of an earlier recirculation zone study, (Reference 17). This is demonstrated in Figure 20 which compares calculated radial profiles of mean concentration of dye for a range of turbulent Schmidt numbers with the measurements. However, consideration of Figure 21 in which the calculations are based on the revised inlet boundary conditions, indicates the turbulent Schmidt number should be higher than 0.5.

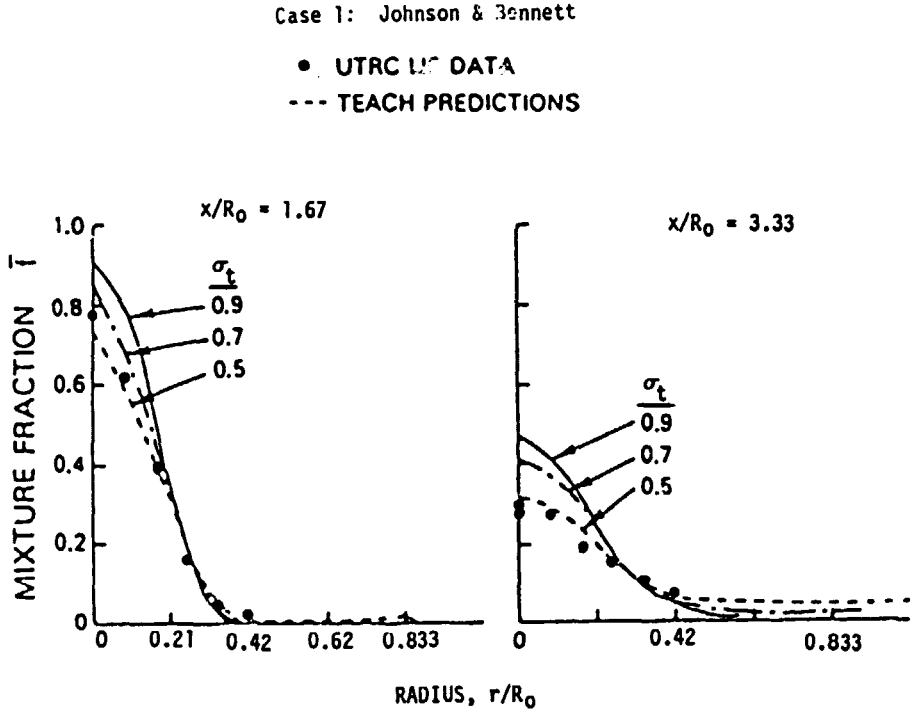

Figure 20 Influence of Turbulent Schmidt Number on Mean Mixture Fraction Profiles for Original Boundary Conditions

Case 1: Johnson & Bennett

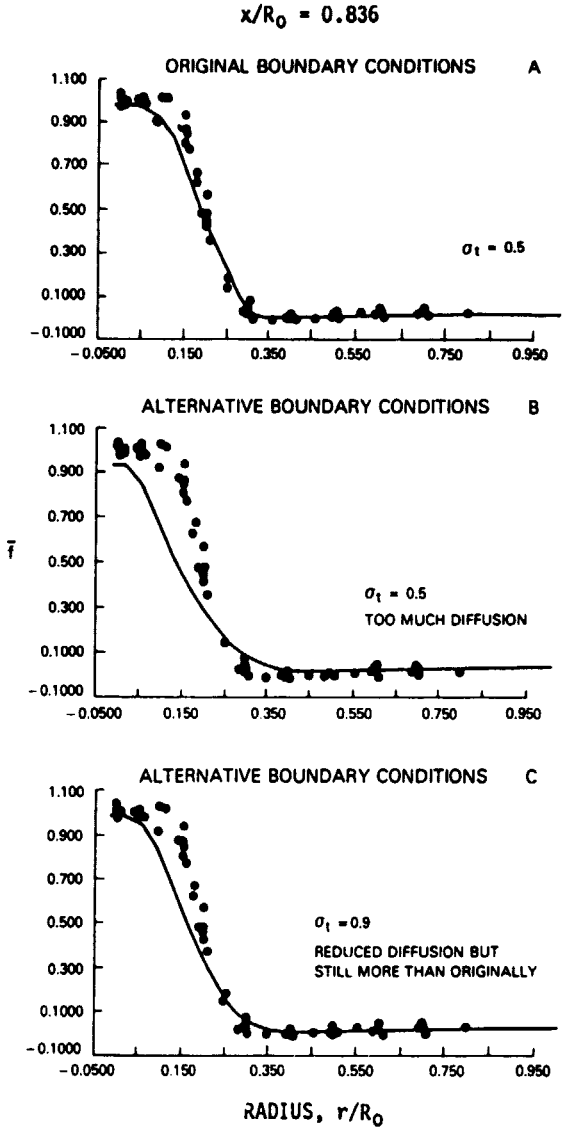

Figure 21 Influence of Boundary Conditions on Apparent Turbulent Schmidt Number

Figures 20 and 21 show that opposite conclusions concerning the physical modeling can be reached depending on which set of inlet boundary conditions is used.

8.2.2 Swirling Jets

The study of swirling jets involved suddenly-expanded and confined coaxial jets with swirl in the outer jet (Test Cases 2 and 3), confined coaxial swirling streams with both co-rotation and counter-rotation (Test Case 4) and, a confined suddenly-expanded swirling jet with outlet restriction (Test Case 5). Table 9 gives the jet velocity ratios, relative dimensions and swirl numbers for these cases; information on the types of boundary conditions used and the calculation grids is included. Test Cases 2 and 3 were extensions of the nonswirling jet cases discussed above.

Table 9

Confined Swirling Jets and Coaxial Swirling Jets in Confined Sudden Expansions (Turbulence Model)

Experiment	u_{ann}/u_{pipe}	d_{ann}/d_{pipe}	d_{duct}/d_{ann}	S.N.	Boundary Conditions	Grid
Habib & Whitelaw	3.0	2.76	2.81	0.23	Estimated	Various
Johnson & Roback	2.31	1.93	2.07	0.47	Measured + estimated	38 x 33
Vu & Gouldin	0.68 0.67	3.9 3.9	1.0 1.0	i = 0.58, o = 0.54 i = 0.49, o = -0.51	Both measured + estimated	67 x 41 67 x 41
Yoon & Lilley*	0	1.0	2.0	0.53	Measured	50 x 32

*Outlet constricted, contraction ratio = 4:1

For Case 2, Johnson & Roback, the calculations were started at the first measurement plane, which was just downstream of the expansion plane. This was done because of the uncertainty associated with the inlet boundary conditions in the jets themselves. It is unsatisfactory for two reasons:

1. it gives up on calculating the expansion, and
2. the input length scales of turbulence (to calculate dissipation) are unknown.

For the present, the central part of the flow was assumed to have originated from the center jet and to have a length scale of 3 percent of the pipe diameter. The outer part of the flow was assumed to come from the annular jet and to have a length scale equal to 3 percent of the annular height of the passage. These assumptions neglect both the large dissipation associated with the flow expansion, and the fact that the outermost portion of the flow is a recirculation zone. The computational representation of the measured velocity profiles forming the inlet conditions is given in Figure 22.

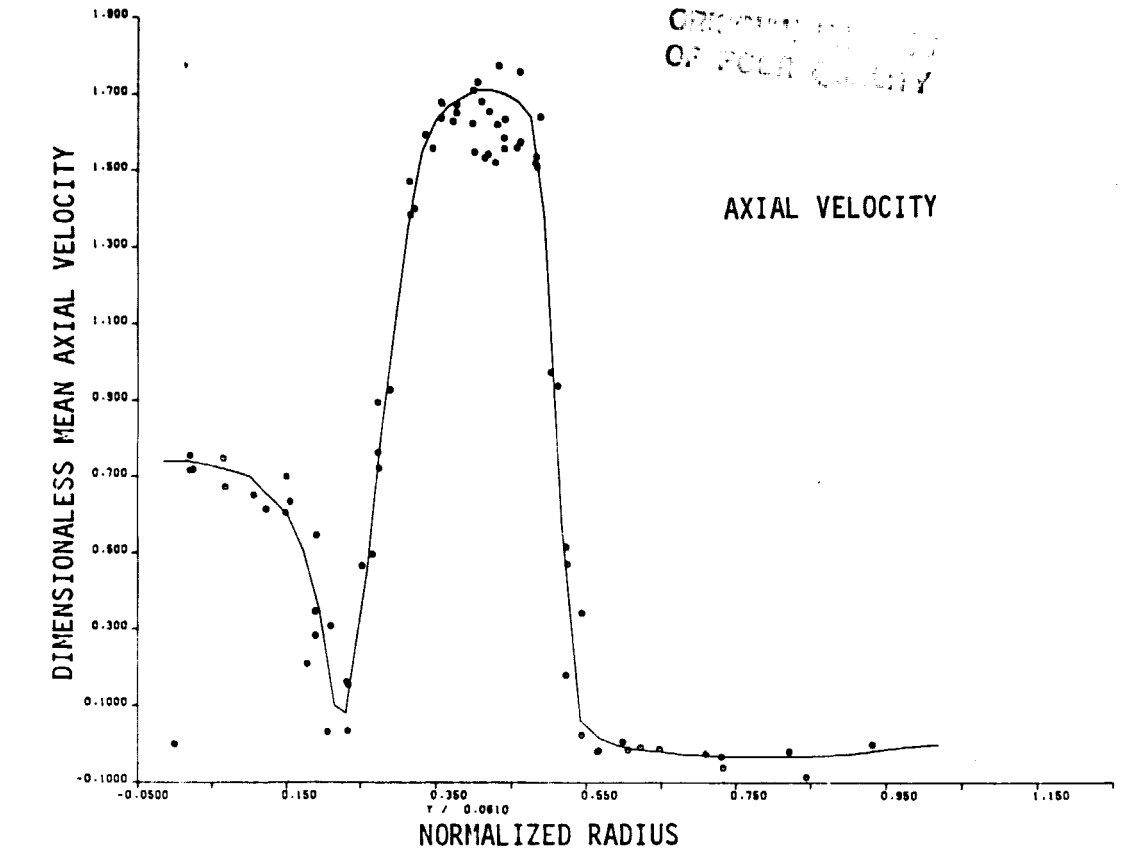

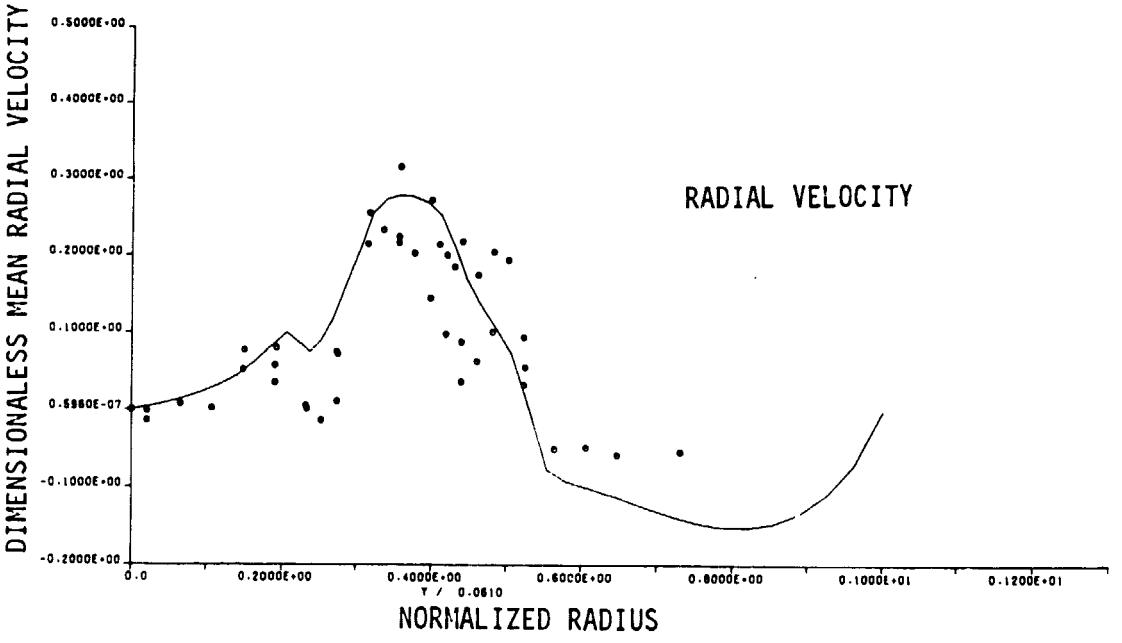

Figure 22 Starting Profiles for Test Case 2 (Johnson & Roback) at 0.51 cm from Expansion

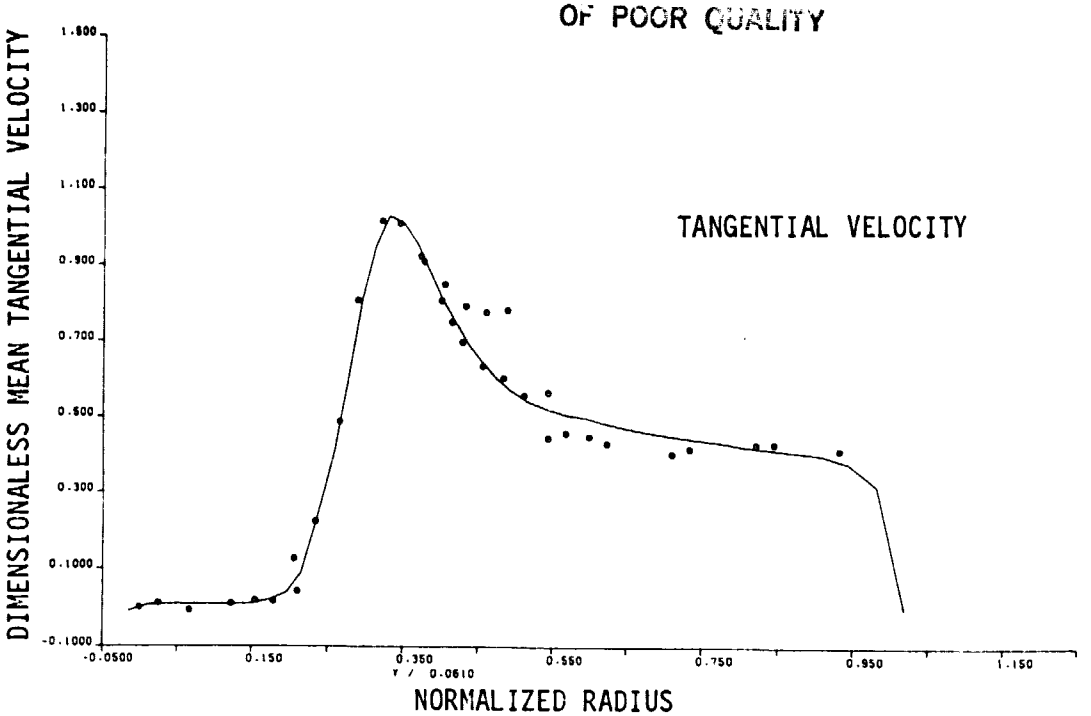

Figure 22 (continued)

Shown in Figure 23 is a comparison of measured and calculated mean axial velocities along the centerline. It can be seen that the calculations predict the presence of the measured central recirculation zone. Its strength appears to be about correct but its length is underestimated by about 15 percent, while the position of the forward stagnation point is underestimated by about the same amount.

The general flow development can be described as follows: The development of axial velocity is calculated fairly well to 5.08 cm (x/R_0 = 0.833). This is just about the end of the measured outer recirculation zone. At a station of 10.2 cm (x/R_0 = 1.67) from the expansion, the calculated and measured profiles diverge because of discrepancies in the calculated central recirculation zone compared to the actual recirculation zone: The calculated width of the recirculation is considerably less than the measured width. This difference causes the calculated velocity around the recirculation to be much lower than the measured velocity because of the reduced blockage. Further downstream at 20.3 cm (x/R_0 = 3.33), outside the central recirculation, the agreement in velocities is improved as the blockage effects are removed. At stations further downstream than 30.5 cm (x/R_0 = 5.0), a discrepancy in velocities appears in the center of the flow, while the calculated and measured velocities for the outer region are in good agreement.

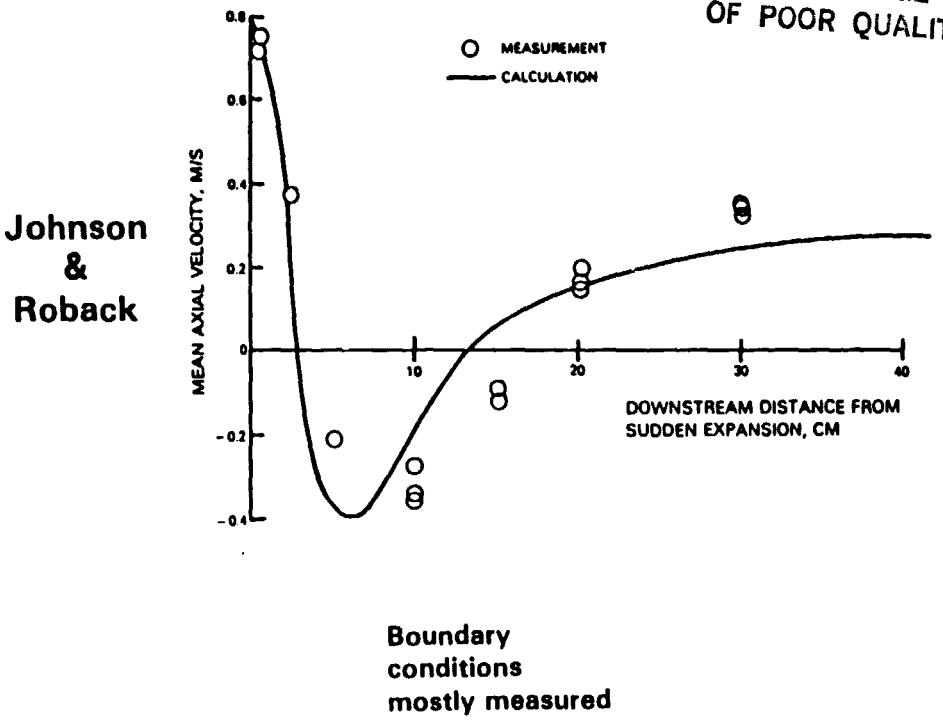

Figure 23 Comparison of Centerline Axial Velocities for Test Case 2 (Johnson & Roback)

The distribution of swirl velocity is in excellent agreement with the measurements to a station of 15.2 cm (x/R_0 = 2.49) from the expansion. At subsequent downstream stations, there is a progressive deterioration in agreement of calculated and measured radial profiles. Over most of the radius, the measured tangential velocity is approximately constant and only drops off to zero on the centerline from a radius of about 2 cm (r/R_0 = 0.33). Further downstream than 30.5 cm (x/R_0 = 5.0) the calculated flow approximates a forced vortex while the measured flow approximates a free vortex in the outer region, with a forced vortex core, Figure 24.

There is a large experimental uncertainty in the measurement of radial velocity and a large scatter in the data as a result. The calculations of radial velocity are qualitatively correct with fair quantitative agreement downstream to 2.5 cm (x/R_0 = 0.41) from the expansion. The calculations are qualitatively correct at 5.8 cm (x/R_0 = 0.95), but severe underestimation of the maximum values occurs in the outer regions of the flow. At 10.2 cm (x/R_0 = 1.67) there is very little radial activity and the calculated and measured profiles are in good agreement.

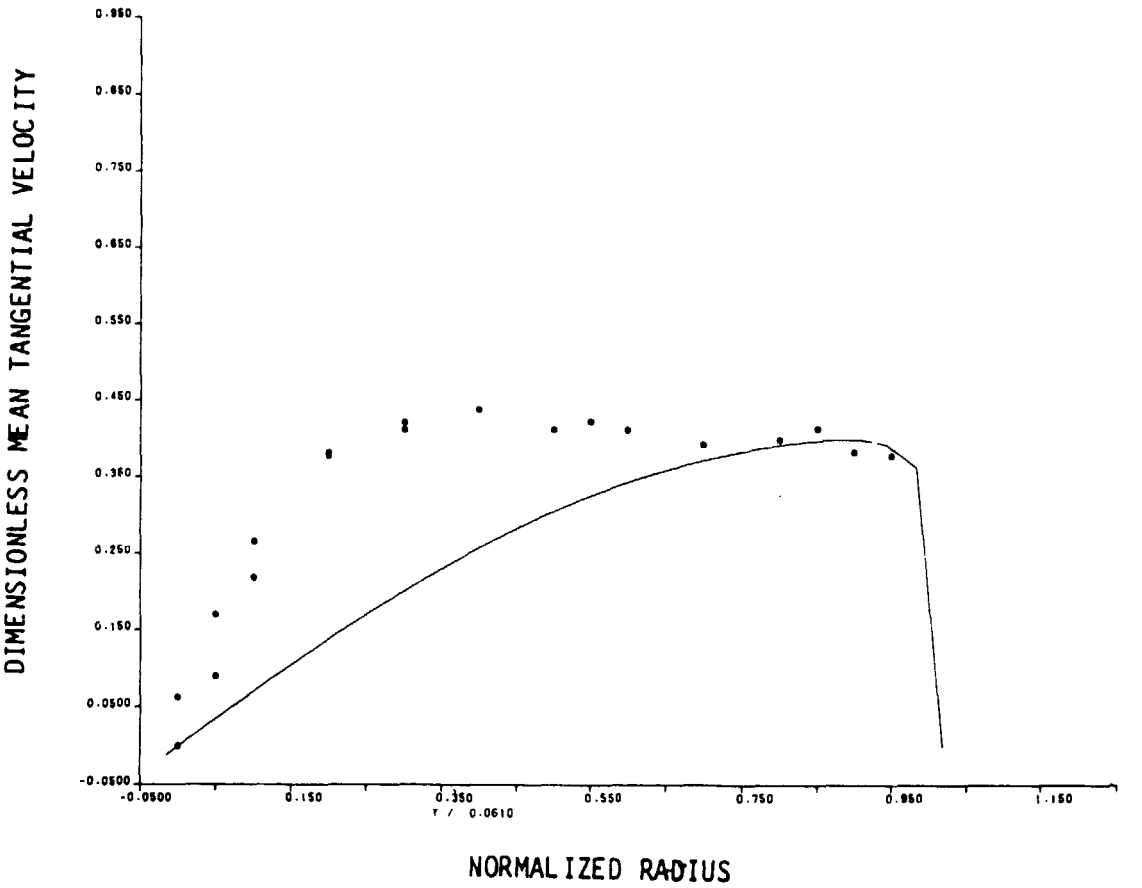

Figure 24 Test Case 2 (Johnson & Roback) at 30.5 cm from Expansion Showing Discrepancy Between Calculated and Measured Profiles of Tangential Velocity

The calculations of radial velocity profiles go astray upstream of the axial position where the character of the tangential velocity profiles departs from that of the measured profiles (between 2.5 to 5.8 cm, and 15.2 cm respectively). The discrepancy in tangential velocity profiles is probably generated in part by incorrect calculation of the upstream radial equilibrium. The measurements of mean axial and radial velocities at downstream stations indicate that the tangential velocity profile at 40.5 cm (x/R_0 = 6.64) is in equilibrium. A free vortex is not a stable profile, and viscosity effects at the core modify the profile to the stable forced vortex form locally, as indicated at 40.5 cm. Therefore the discrepancy in tangential profiles could also be due in part to an inadequate calculation of eddy viscosity across the radius.

The inlet boundary conditions available for Test Case 3, Habib & Whitelaw, were less than complete. No details of the swirl generator are provided to permit jet interaction effects to be investigated, as was the case for Vu and Gouldin's swirling flow experiment, Test Case 4. Inlet boundary conditions of distributions of $\bar{u}$ and $\bar{w}$ velocities were obtained from Reference 83, as was the distribution of kinetic energy of turbulence for the inner passage. No information was provided on K for the outer passage, so some assumptions were necessary. In all cases $\bar{v}$ was taken as zero.

The first calculation was made on the 30 x 39 grid used for the nonswirling case. The turbulence intensity for the outer passage was taken as a uniform 8.2 percent; length scales for both passages were assumed to be 3 percent of the passage height.

A further calculation was made with the same boundary conditions but the grid was coarsened to 20 x 39 to be closer to the grid used by Habib & Whitelaw.

The results of these two calculations are compared in Figure 25 with the calculation of Habib & Whitelaw, and the measured data for centerline axial velocities.

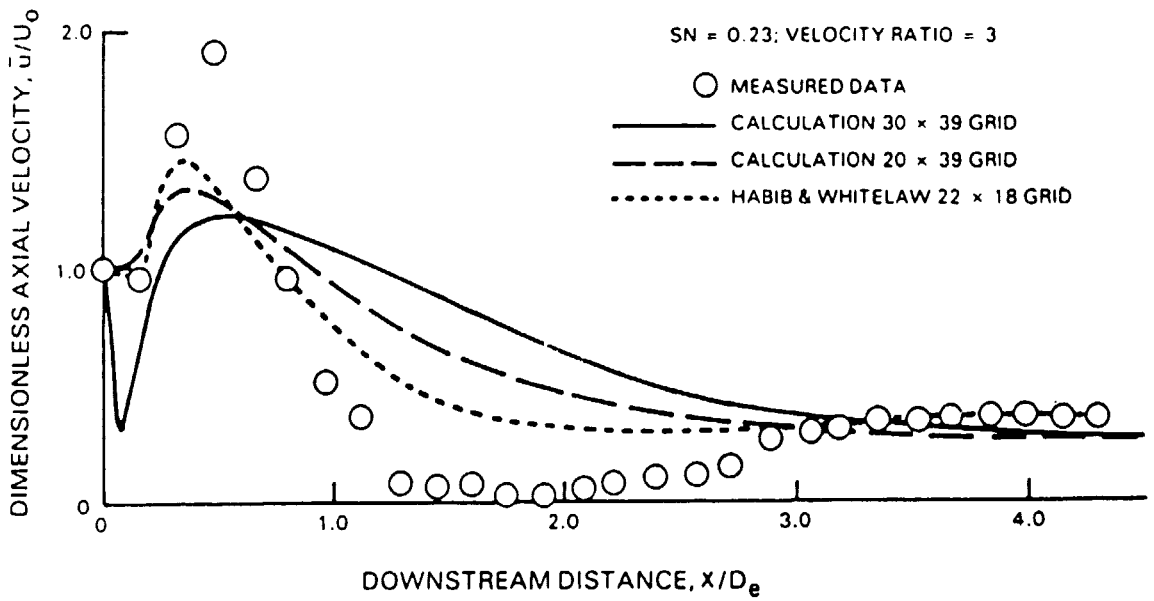

Figure 25 Centerline Axial Velocities in Test Case 3 (Habib & Whitelaw) Compared With Various Calculations

Habib & Whitelaw's calculations, made on a 22 x 18 grid, are qualitatively correct in that they predict the initial dip in velocity followed by a recovery, then a decay followed by a slight recovery to a downstream value that is almost constant. However, the first recovery is underestimated, as is the magnitude of the velocity depression that follows it. The downstream plateau value is correctly predicted quantitatively.

The present calculations with the 30 x 39 grid show extremely poor agreement with the measured data. Coarsening the grid to 20 x 39 gave an improvement for x/D_e less than 0.5, but the calculations were not even phenomenologically correct for x/D_e greater than unity.

The discrepancies on centerline velocities are so severe that it is not worthwhile presenting radial profiles of velocity and other quantities.

To investigate the flow behavior calculated by Habib & Whitelaw with a relatively coarse grid of 18 x 22 gridlines, calculations were made with a grid of this density. It was suspected that careful placement of the gridlines could be used to selectively supplement with numerical diffusion, the diffusion calculated by the turbulence model, as hinted by Jones & Whitelaw (Reference 13).

Unfortunately, the distribution of nodes actually used by Habib & Whitelaw is not given in their paper. It was therefore necessary to proceed with their 18 x 22 mesh in arbitrary fashion. The radial distribution was fixed (and arranged to define the passages adequately); the axial distribution was initially given an expansion factor of 1.10, then made more uniform by reducing the expansion factor to 1.05. Finally, two axial fluid blocks were used; each block was given an expansion factor which would produce a dense grid at their common face, which was placed in the region of measured maximum centerline velocity decay rate. The object of these gridline distributions was to examine reduced numerical diffusion in the measured region of rapid velocity decay, and allow it to increase in the measured velocity recovery region.

Figure 26 shows the results of this study and the measured data. The results are presented in terms of centerline mean axial velocities. The grid with an expansion factor of 1.10 has sufficient gridline density close to the expansion plane to capture the measured initial depression of velocity. However, the increasing numerical diffusion with increasing distance reduces the gradient of axial velocity quite severely after about 7 cm downstream. The nearly uniform grid line distribution does not capture the initial velocity depression; however, the velocity gradient after 7 cm is increased slightly. The mesh based on two axial fluid blocks with expansion factors which result in a clustering of gridlines in the region from 10 to 40 cm, really increases the velocity gradient for distances greater than 10 cm downstream and depresses the velocities below those of the other calculations for 30 to 60 cm.

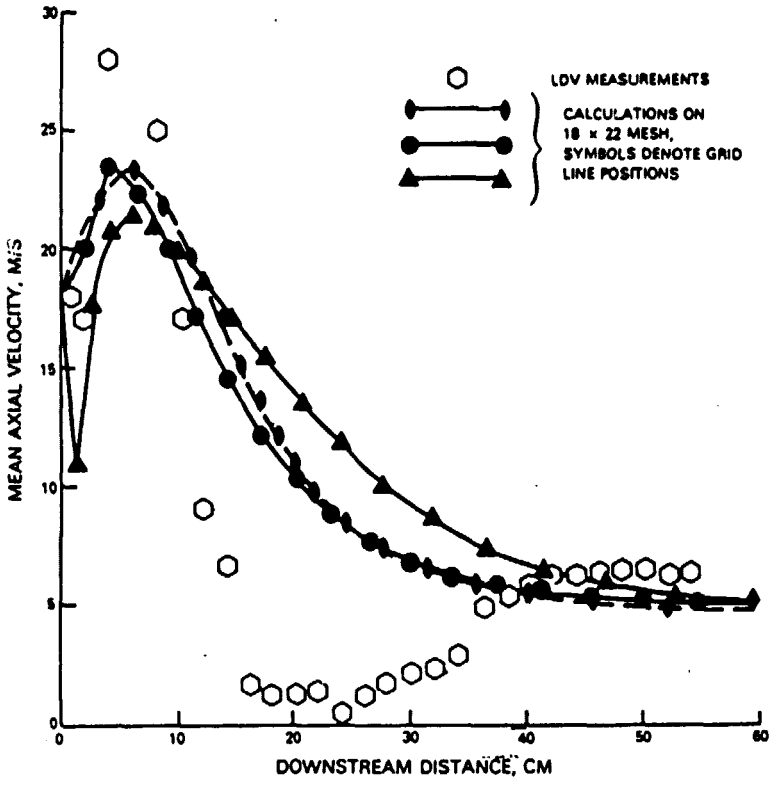

Figure 26 Test Case 3 (Habib & Whitelaw) With Coarse Grid Showing Result Manipulation Through the Calculation Grid

Although the study shown in Figure 26 does not reproduce either the measured data or Habib & Whitelaw's calculation, the following can be deduced: (1) Habib & Whitelaw's calculations cannot be grid-independent as claimed; (2) placing additional gridlines in the region from 8 to 15 cm with a consequent reduction in the region from 15 to 50 cm, might well reproduce the correct phenomenological behavior for this experiment; (3) by careful placement of gridlines solutions can be manipulated, accidentally or otherwise, to cover up shortcomings in the physical turbulence model.

The experiment of Vu & Gouldin, Test Case 4, provided measured profiles of necessary quantities, except turbulence length scale, in the plane of confluence for the two swirling streams. However, there was clearly evidence in the experiment of an elliptic effect of the downstream flow on the swirling central jet prior to it issuing from the central tube, (see Figure 8). The implication of this was that it might be better to start the calculation upstream of the confluence plane.

It was decided that the calculation domain should begin at the downstream face of the central swirler for the inner jet, and in the plane of the confluence for the concentric outer jet.

The profiles measured at the confluence plane were used for the outer jet, and the turbulence length scale was assumed as 3 percent of the jet annular height. Inlet boundary conditions for the central jet were calculated.

The procedure used for the central jet was as follows: The axial swirler is fed by means of a long approach pipe of about 19 pipe diameters in length, so the flow was assumed to be both turbulent and fully developed at the swirler face (stretching the work of Nikuradse, see Reference 81). For the mean Reynolds number of the tube the dimensionless velocity profile was calculated assuming a power law distribution with an index appropriate to the Reynolds number. Since the axial flow swirler has an unswirled flow through its open hub, the flow split between the vanes of the swirler and the open port in the hub was calculated through matching the one-dimensional flow pressure loss characteristics of each separate flow path. The air deviation angles achieved by the swirl vanes were estimated as a function of radius, accounting for blade pitch to chord ratio, and thickness to pitch ratio. The calculated angles varied from 2.9° close to the hub to 63.3° at the tip. From the above information the variation of axial and tangential velocities with radius was found; radial velocities at the swirler exit plane were taken to be zero, see Table 10.

Table 10

Central Tube Swirler Exit Conditions

R cm	u m/s	θ°	w m/s
0.117	36.82	0	0
0.351	36.00	0	0
0.539	35.26	0	0
0.731	33.17	2.90	1.68
0.879	32.43	44.00	31.32
1.039	31.52	59.00	52.46
1.201	30.39	63.20	60.16
1.219	30.25	63.70	61.21
1.321	29.37	65.11	63.30
1.439	28.12	66.06	63.34
1.561	26.34	66.87	61.66
1.653	24.31	67.17	57.75
1.749	19.75	63.30	47.40

The radial stations given in Table 10 represent the grid lines used to input the profiles. The calculated values in Table 10 were scaled as necessary to ensure that the step functions actually input to the computer calculation to represent the profiles did preserve continuity.

The assumed values for turbulence intensity and length scale of turbulence followed the recommendations of Reference 17 with an intensity of 8.2 percent and a scale proportional to the open hub diameter for the central region and proportional to the circumferential distance between swirl vanes for the outer region.

The inlet conditions for the central tube were maintained constant for both coflow and counterflow swirl cases.

Figure 27 shows the centerline axial velocity variations with downstream distance for counterswirl and coswirl cases respectively. The experimental data (References 38, 84) are compared to the present calculations. The zero distance position represents the confluence of the two streams.

Shown also in Figure 27 are calculations of the experiment made by Srinivasan and Mongia (Reference 85) and Rhode (Reference 86). Both sets of additional calculations were performed with codes that use solution procedures that may be described generically as TEACH procedures, differing only in programming details (References 87, 88, 89). They use the same type of turbulence modeling as was used in the present calculations. Therefore, all three sets of solutions are directly comparable. The calculations presented should only differ from each other through the grids upon which the computations were made and the inlet boundary conditions used.

For grid-independent solutions, which are claimed by all the authors, differences exist due only to the boundary conditions. In Reference 85 the grid is not quoted directly but is inferred to be 30 x 25; in Reference 86 the grid was 30 x 24, while the present grid was 67 x 41. The calculation domains were identical for Reference 85 and the present results; for Reference 86 the calculations were started at the confluence plane of the streams.

Consideration of Figure 27 for the counterswirl case shows that all the calculations have the same character as the measurements. All underestimate the strength of the recirculation zone formed and overestimate its length. The initial values of the centerline axial velocity differ considerably with the two predicted values overestimating the measured value. Surprisingly, the initial value for Reference 85 is about twice that of the present calculations while the strengths of the recirculation are comparable. Rhode (Reference 86), who used the measurements for the initial values, predicted the weakest recirculation of all the calculations.

Consideration of the centerline axial velocities for the coswirl condition reveals the completely unsatisfactory nature of all three calculations.

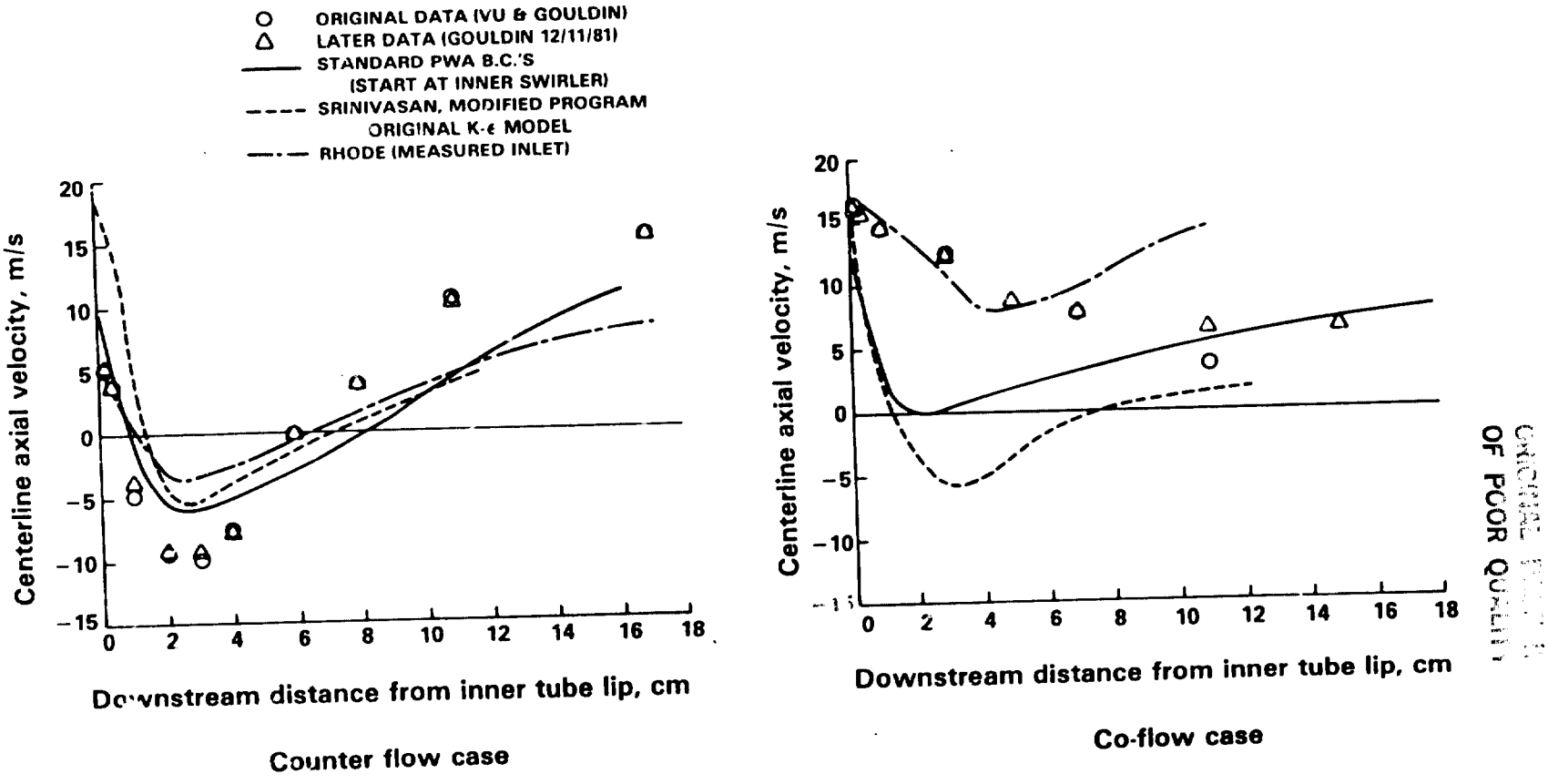

Figure 27 Comparison of Mean Axial Velocities Along Centerline for Test Case 4 (Vu & Gouldin)

The calculations of Reference 85 predict a recirculation that is not only not measured but is actually stronger than that calculated for the counterswirl case. For Reference 86, no recirculation is predicted but the calculation goes completely astray for downstream stations greater than 5 cm. The present prediction has the same general character as the other two calculations but does not yield a recirculation (just). The initial values of centerline axial velocity for References 85 and 86 agree with each other and the measurement; the present calculation underestimates this value.

Figure 27 for ccswirl is not displayed as a performance comparison between the three sets of calculations. It does illustrate the differences that can exist between three codes of nominally the same solution procedure which use the same physical modeling. There is greater difference between the respective calculations than there is between any one calculation and the experimental data. Such disparities between the calculations must be attributed to differences in either grid or assumed boundary conditions, or both.

A repeat of the present calculations for counterswirl with a coarsened grid of 31 x 27, which is close to that used by Srinivasan and Mongia (Reference 85) for the same calculation domain, increased the initial value of centerline axial velocity to about 13 m/s, reduced the maximum reverse velocity of the recirculation to about 1 m/s, and moved the forward stagnation point downstream and the rear one upstream to reduce the recirculation zone length to about 2 cm, see Figure 28. When compared to Table II this implies that the differences between the present calculations of Figure 27 and those of Reference 85 are more due to the inlet boundary conditions than grid differences.

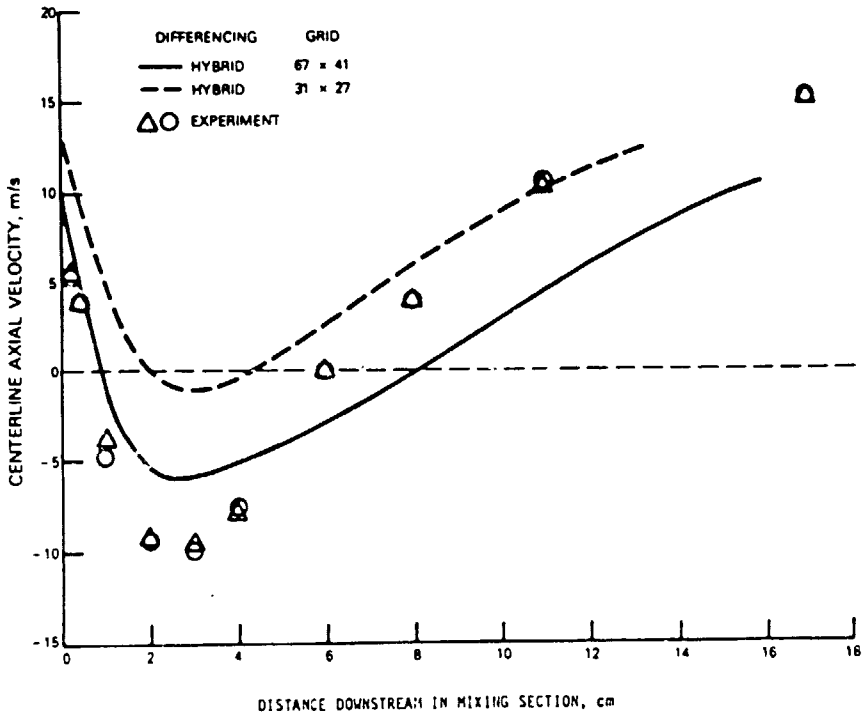

Figure 28 Centerline Axial Velocities for Test Case 4 Showing Effects of Grid

Table 11

Prediction of Counterswirl Recirculation Characteristics

Reference	85	86	Present	Measured
Forward stagnation, cm	1.4	1.1	0.9	0.55
Aft stagnation, cm	7.2	6.45	8.1	6.0
Length, cm	5.8	5.35	7.2	5.45
Strength, m/s	-5.5	-3.6	-6.0	-9.7
Position max. reverse vel. cm	2.7	2.5	2.7	3.0
Velocity grad. from recirculation (m/s)/cm	1.05	1.05	1.57	2.0

The actual inlet boundary condition assumptions for the three sets of calculations are given in Tables 12, 13 and 14. Table 12 gives the assumptions for the outer swirling stream, and compares those for the inner swirling stream for Reference 85 against those for the present calculations. In Table 13 a consistent set of inner swirling stream conditions for the present calculations are compared with those of Reference 86. The consistent conditions for the present work were obtained by averaging calculated radial values at the outlet from the central tube, which was where Rhode (Reference 86) started his calculations.

Table 12

Test Case 4: Assumed Turbulence Boundary Conditions

Inner Passage

Reference	u'_{rms}/u %	K m^2/s^2	l_T cm	ε $(m^2/s^2)/s$
85	4.47	2.75	0.0372	1.1×10^3
Present	8.2	4.2-11.9*	0.0363-0.088*	$88.5\text{-}4.9 \times 10^{3}$*

Outer Passage

Reference	u'_{rms}/u %	K m^2/s^2	l_T cm	ε $(m^2/s^2)/s$
85	4.47	1.27+	0.145	0.0891×10^{3}+
86	14.1	14.0+	0.0363	13×10^{3}+
Present	5.8	1.3-2.7*	0.162	126.4-252*

*Varies as function of radius

+Based on nominal conditions

Table 13

Test Case 4: Comparison of Turbulence Conditions at Confluence of Streams

Inner Passage

Reference	u'_{rms}/u %	K m^2/s^2	l_T cm	ε $(m^2/s^2)/s$
Rhode (86)	14.1	27.5	0.0363	35.9×10^3
Present (Averaged)	12.0	24.6	0.0313	35.0×10^3

Table 14

Assumed Mean Velocity Boundary Conditions

	Inner Passage			Outer Passage		
	u	v	w	u	v	w
Reference	m/s	m/s	m/s	m/s	m/s	m/s
85	30.8	0	0, 33.18	calculated[x]	0	Calculated[x]
86	Measured	0	Measured	Measured	0	Measured
Present	36.8-19.75*	0	0, 1.7-47.4*	Measured	0	Measured

*Varies as function of radius

x but close to measured, see Reference 85

Table 14 contains information on the mean velocities. Note the assumptions of zero radial velocity. It is strongly believed that the design of the axial swirler would generate significant negative (towards the centerline) radial velocity components.

Table 13 shows that the average turbulence conditions for the inner stream came out to be remarkably close for Reference 86 and the present calculations. However, the results for coswirling streams are very different, as Figure 27 shows. This difference is believed to be due to the radial distributions of the turbulence quantities actually present in our calculations as opposed to the radially uniform values applied in Reference 86. It suggests that a swirl number (Reference 90) alone is not sufficient to characterize a swirling flow.

Figure 29 shows the calculated axial and tangential velocities at 0.2 cm downstream from the confluence of the two swirling streams for the counterswirl case. Figure 30 displays similar information for the coswirl case. Both sets of plots also contain points representing Gouldin's experimental data.

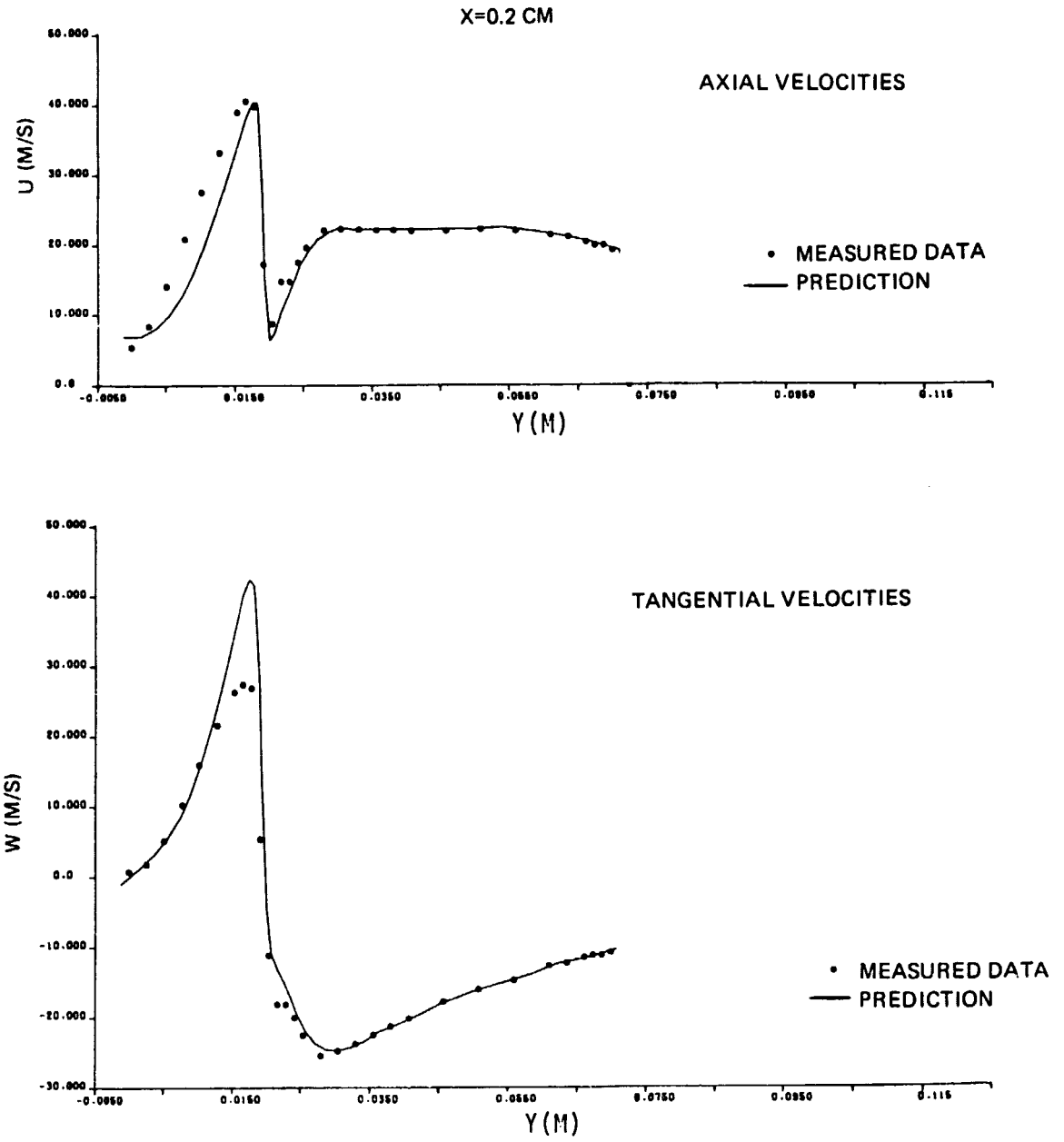

Figure 29 Mean Velocity Profiles Close to the Discharge of the Central Tube in Test Case 4 (Vu & Gouldin) for Counterswirling Flow

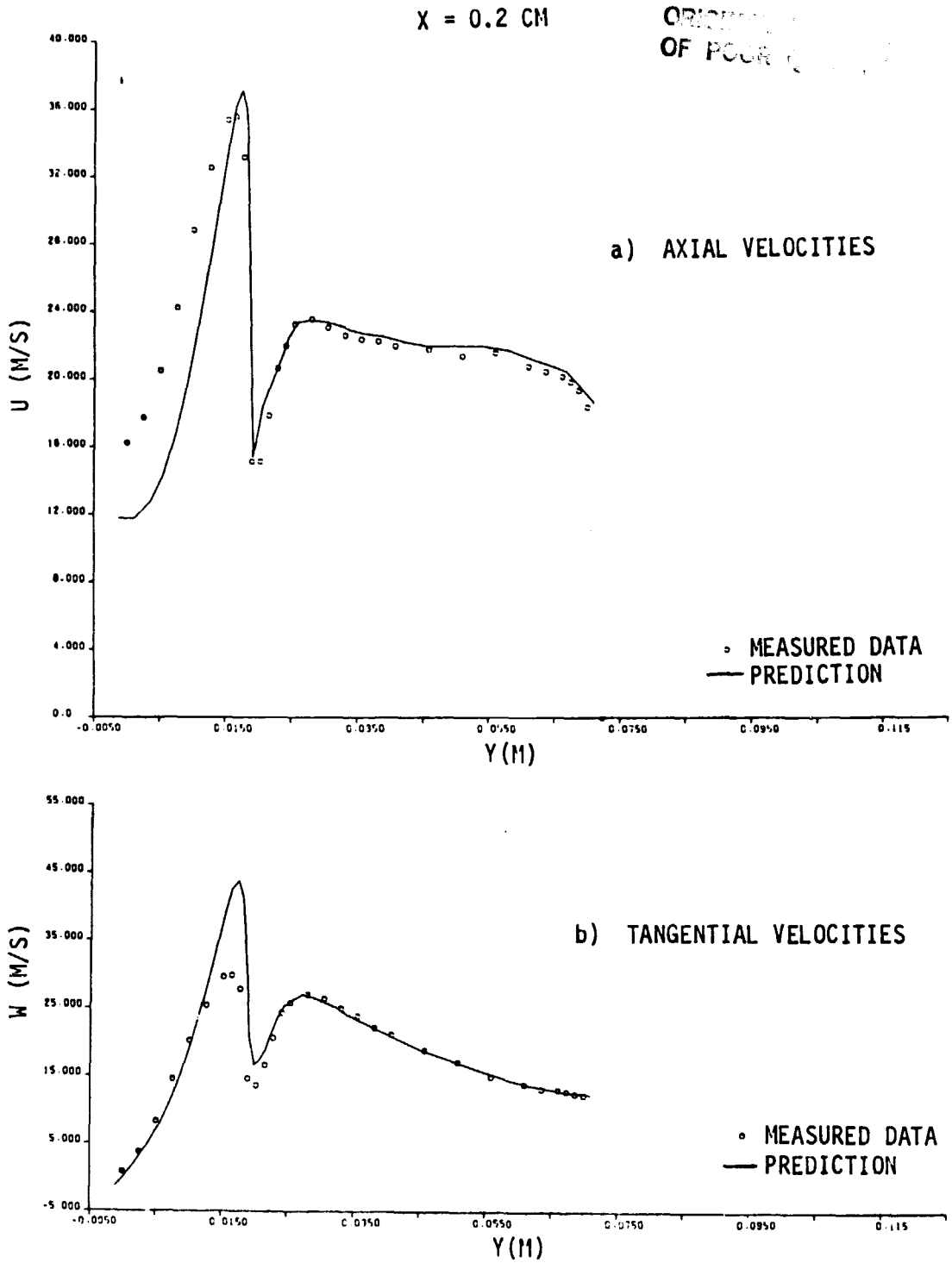

Figure 30 Mean Velocity Profiles Close to the Discharge of the Central Tube in Test Case 4 (Vu & Gouldin) for Coswirling Flow

Comparison of Figures 29 and 30 confirms the assertion that there is an influence of the outer stream on the inner stream prior to their actual physical confluence at the zero x-station. The central portions of the counterswirl and coswirl flows are different in both axial and tangential velocities, even though counterswirl was achieved by rotating the outer swirler vanes only.

In both swirl cases the agreement of the predicted tangential velocities with the measurements is excellent, except for the maximum values where the predictions overestimate the measurements by a considerable amount. The agreement of predictions and measurements is fairly good for axial velocities for the counterswirl case, although there is some underprediction in the inner flow. It is worse for coswirl where the centerline values are in extremely poor agreement with the measurements. It is apparent that the calculation is going wrong inside the central tube before the two swirling streams interact directly.

There are two possibilities that could account for failure inside the central passage: 1) boundary conditions and 2) anisotropic viscosity at the pipe wall.

It was assumed that the radial velocity component at the swirler exit was zero. This is unlikely to be the case. The swirler hub to tip radius ratio and the strong variation in air turning angle with radius are likely to induce a significant radial flow inward toward the swirler centerline. It would be expected that an inward radial velocity component at the swirler exit might reduce the excessive outward radial velocity component predicted for the central portion of the flow at the 0.2 cm station. This would drive up the axial velocities in Figures 29 and 30 and reduce the peak tangential velocities to improve the agreement of the initial profiles with the data.

It is known that a two-component viscosity is really necessary (Reference 91) to predict swirling pipe flow correctly. The K-ε turbulence model currently used does not have this capability.

Lack of anisotropic viscosity effects in the predictions could represent a genuine shortcoming in the model that is adversely influencing the relationship of the predictions to the data in the initial plane and the subsequent development downstream. However, the shortcomings in the initial profiles could equally well be due to incorrect and/or inadequate specification of boundary conditions at the exit from the center swirler.

Figure 31 represents in terms of axial velocities, the downstream development of the combined swirling flows for the coswirl case.

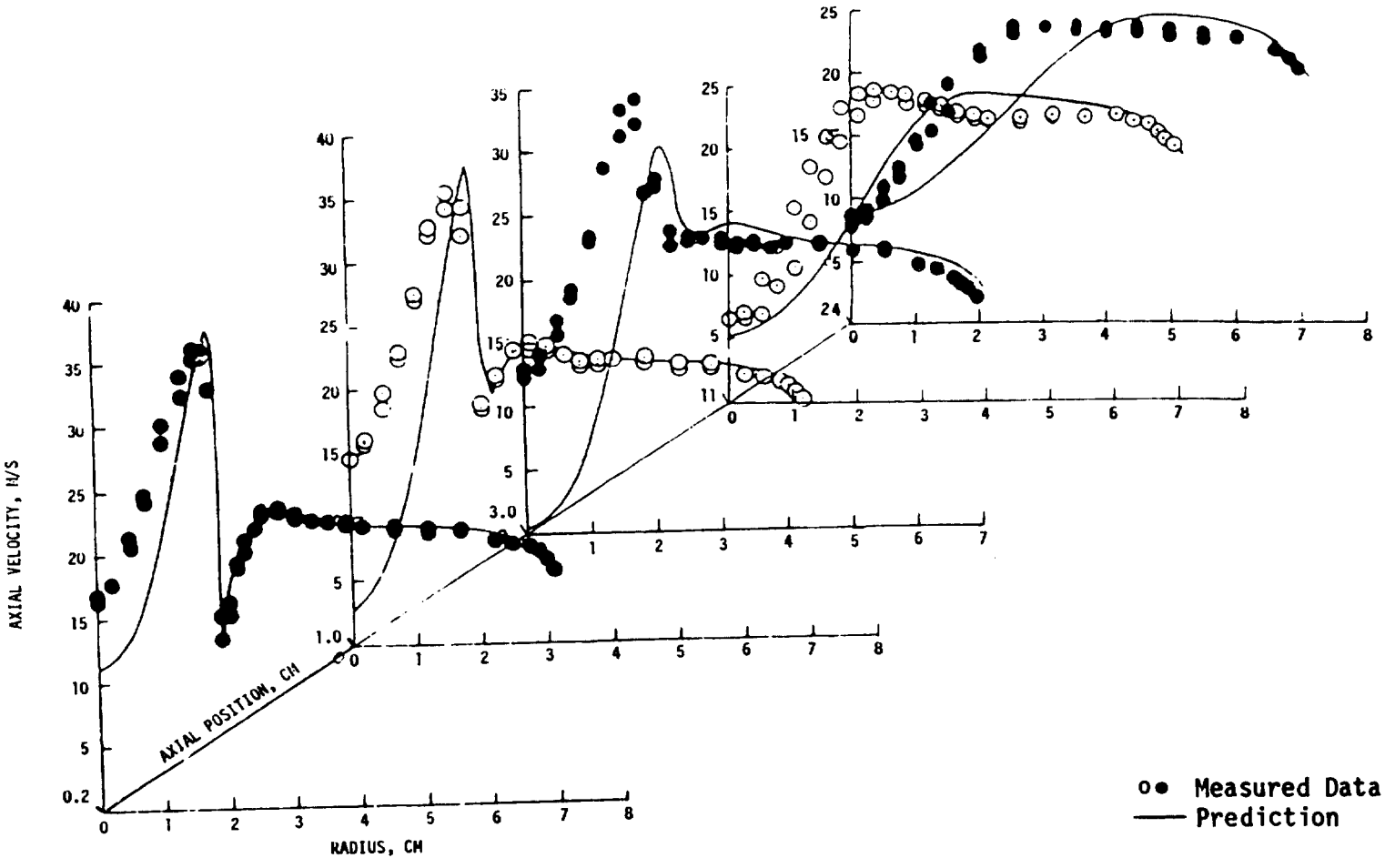

Figure 31 Downstream Development of Axial Velocity for Coswirling Case of Test Case 4 (Vu & Gouldin)

It can be seen from the experimental data shown in Figure 31 that by an x-station of 11 cm asymmetry in the flow has built up, although it seems to be reduced again by 24 cm. The predictions and the data agree extremely well at axial stations up to 3 cm, in the outer regions of the flow. Agreement along the centerline is very poor up to 11 cm from confluence, after which the agreement is good out to 24 cm. The outer shear layer is well-predicted out to 3 cm, while prediction of the inner shear layer although good initially, gets worse with increasing distance from injection.

The equivalent plot to Figure 31 for the counterswirl case shows much better agreement of predictions and measurements but has similar weaknesses.

Although the accuracy of the calculated mean velocity profiles barely justifies it, examples of the calculated turbulence quantities are given at one specific axial station in the counterswirl flowfield.

Figure 32 compares predicted and measured radial profiles of axial velocity u, tangential velocity w, radial velocity v, turbulence intensities u'_{rms}/u, v'_{rms}/u, w'_{rms}/u and just one of the Reynolds stresses $\overline{u'v'}/u^2$, for the counterswirl case at an axial station 3 cm from confluence of the two swirling streams. Figure 32 gives an idea of the amount of information to be assimilated since an equivalent of this figure exists for each axial station for each swirl case.

There was nothing special associated with the choice of the 3 cm station. The agreement of predictions with measurements varies with both axial station and with the quantity being compared. To present complete profiles of all quantities at each station for both swirl cases would result in an inordinate quantity of plots. With respect to Figure 32 it should be noted that Gouldin has expressed low confidence in the accuracy of the radial velocity measurements.

Also with respect to Figure 32 the following should be noted: the predicted fluctuating quantities are derived from the specific kinetic energy of turbulence, Equation 4, with the assumption of isotropic turbulence such that,

$$K = 3/2\ (\bar{u}'^2) \tag{68}$$

To calculate the Reynolds stress, the following was used,

$$\overline{u'v'} = \frac{\mu_t}{\bar{\rho}} \left(\frac{\partial \bar{u}}{\partial r} + \frac{\partial \bar{v}}{\partial x} \right) \tag{69}$$

with μ_t being obtained from Equation 5.

It can be seen from the figure that the features in the profile of each quantity are, in general, well predicted. Numerical accuracy is fair to fairly good, but far from being exact.

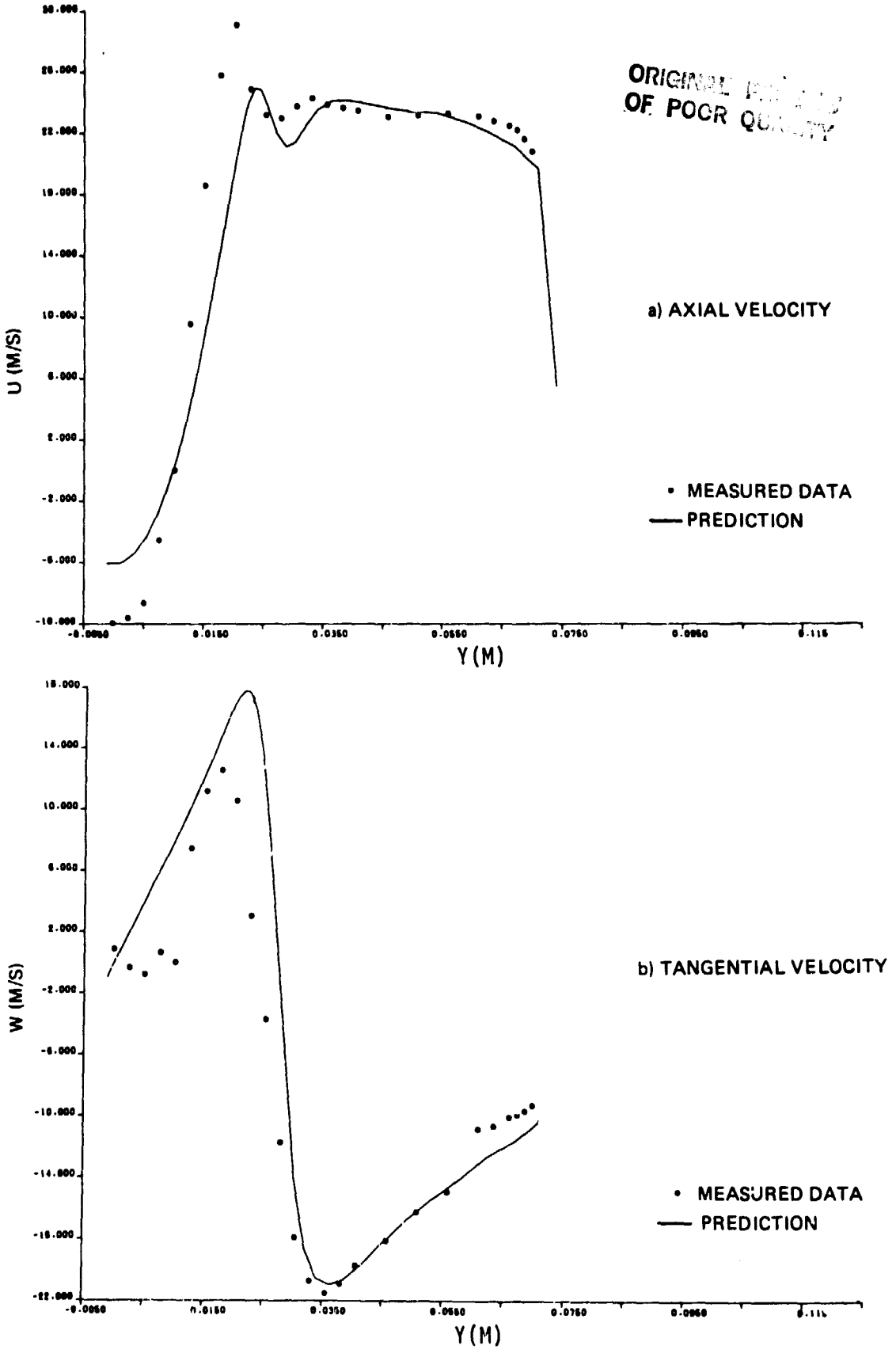

Figure 32 Radial Profiles of Flow Quantities 3 cm Downstream from Confluence of Counterswirling Streams in Test Case 4 (Vu & Gouldin)

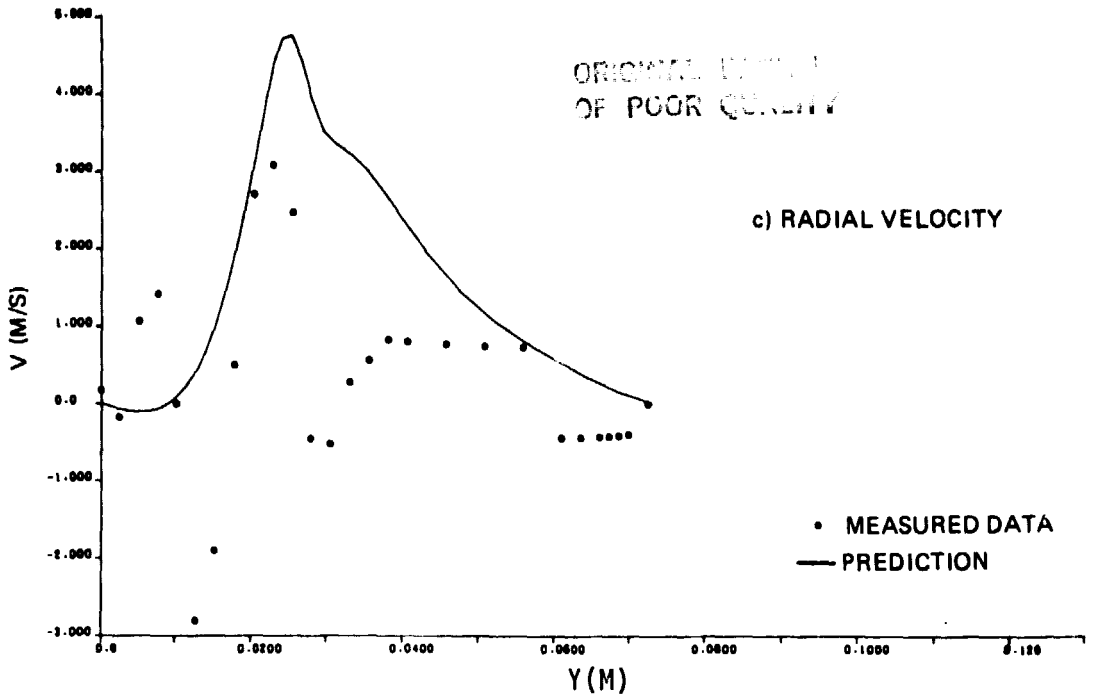

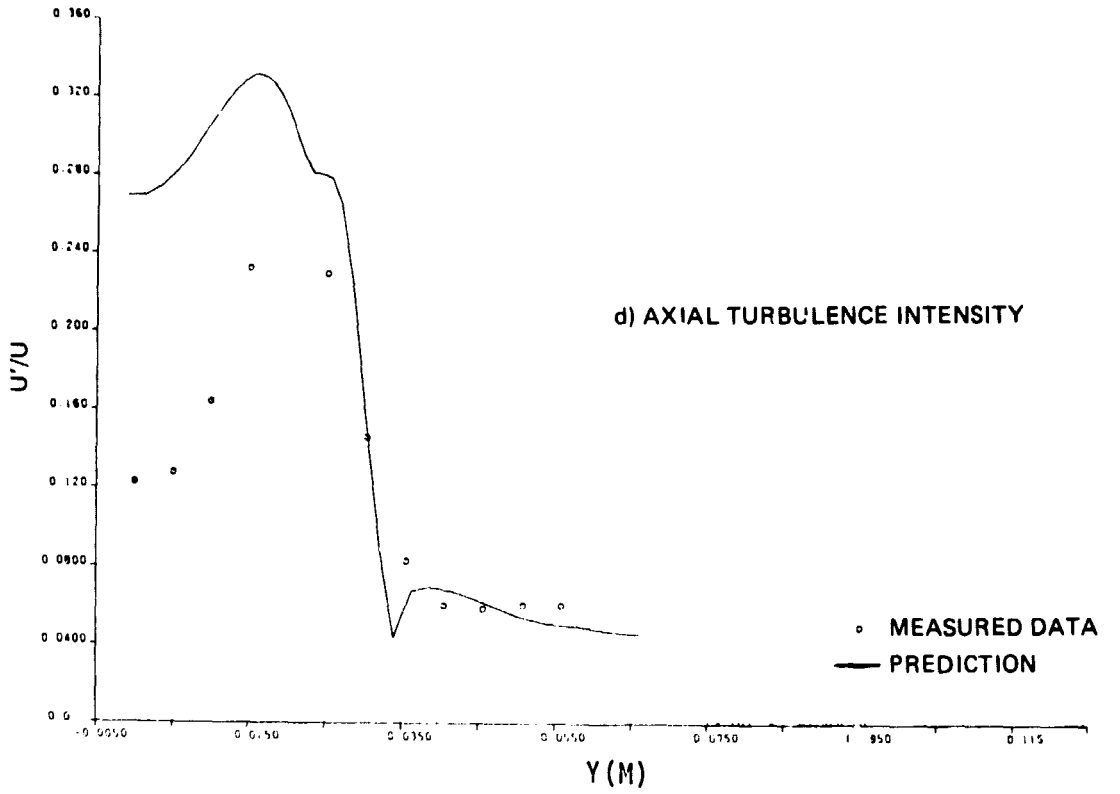

Figure 32 (continued)

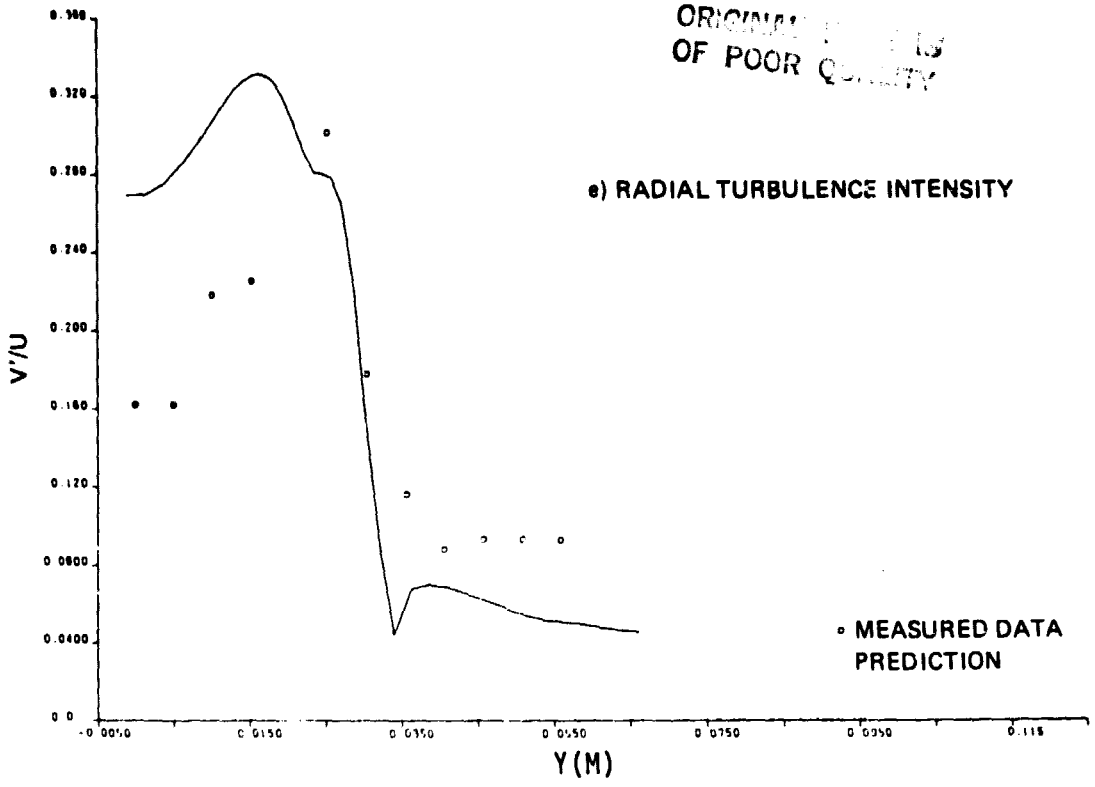

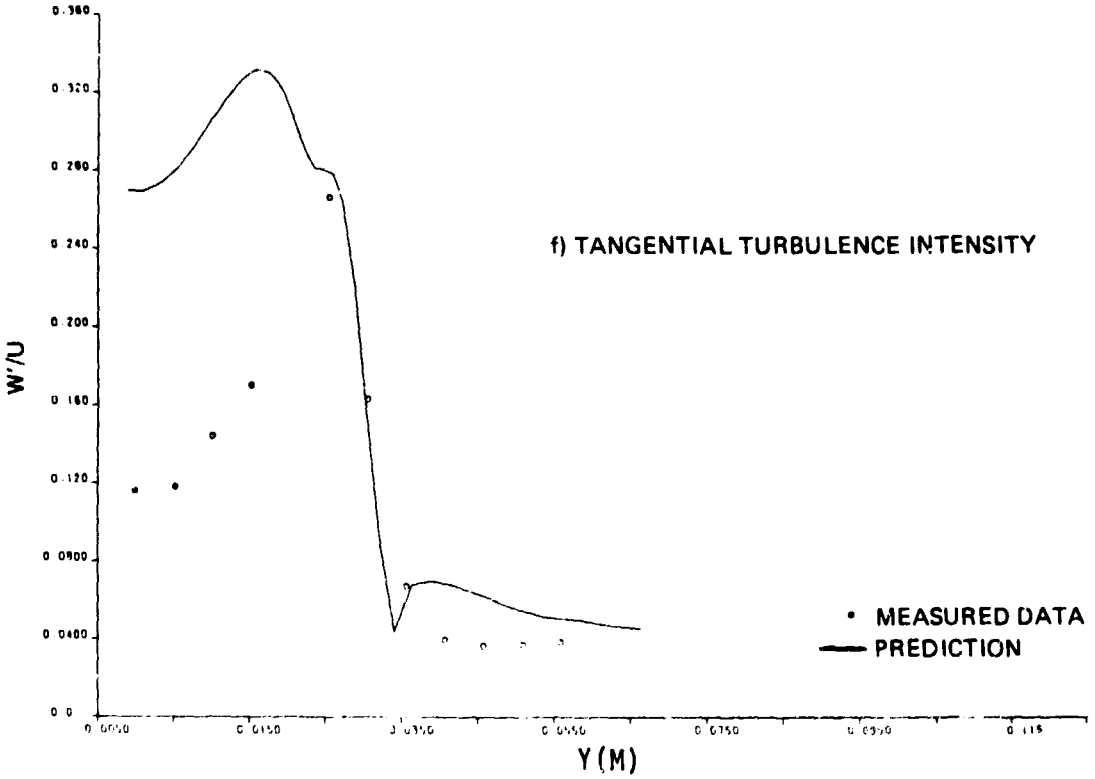

Figure 32 (continued)

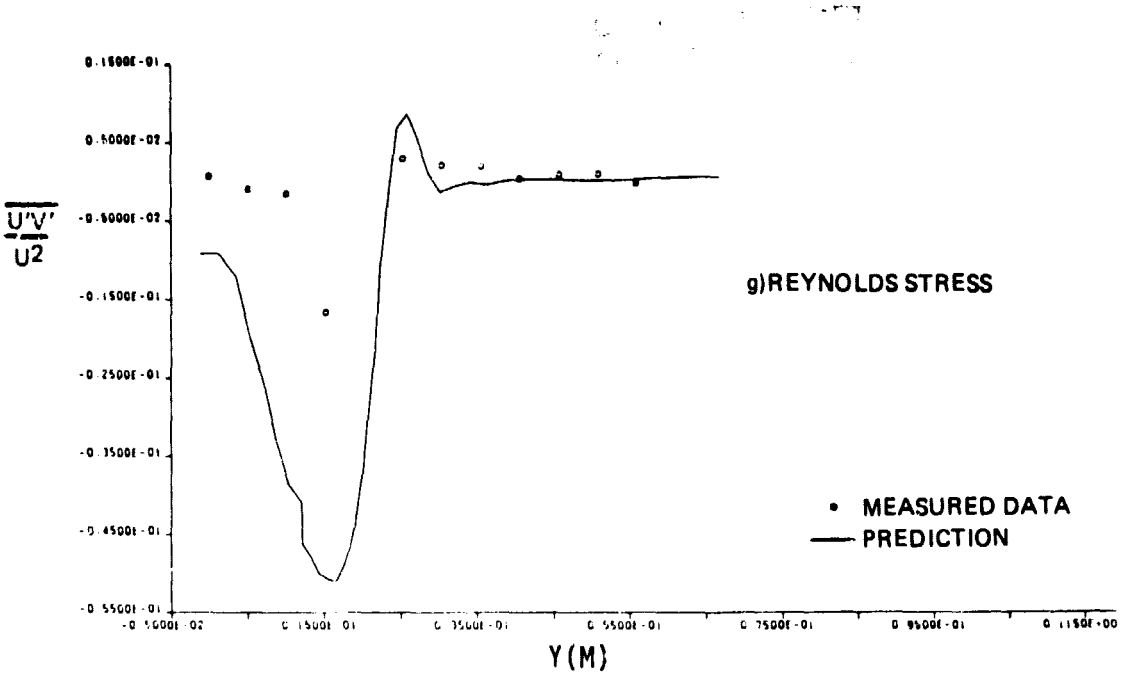

Figure 32 (continued)

To grasp the importance of the grid when hybrid differencing is used, the present calculations have been repeated on a coarser grid of 31 x 27. Although this grid has about the same number of nodes as, for example, Rhode's grid, the distribution is radically different since the present calculation is started inside the central passage.

The effects of numerical diffusion inside the central passage can be seen in Figure 33. Figure 33 compares radial profiles of tangential velocity for the two grids 0.2 cm downstream of the confluence of the streams. Smearing of peaks and troughs due to numerical diffusion can be identified clearly. It is arguable whether Figure 33a) or Figure 33b) represents the better prediction in an overall sense.

In Figure 34 downstream radial profiles of axial velocity for the two grids are compared. It can be seen that the coarse grid clearly gives superior predictions for both velocity components at the 17 cm station. In this case, the diffusion that the turbulence model is clearly failing to provide is being supplied by numerical diffusion.

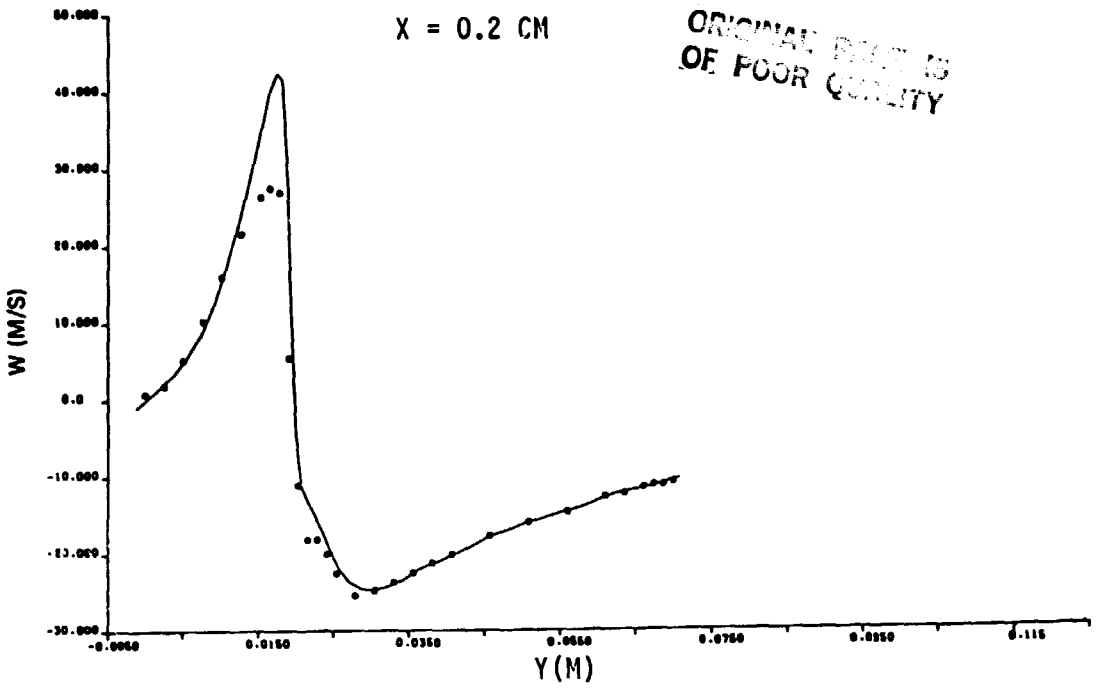

a) Hybrid Differencing, 67 x 41 Grid

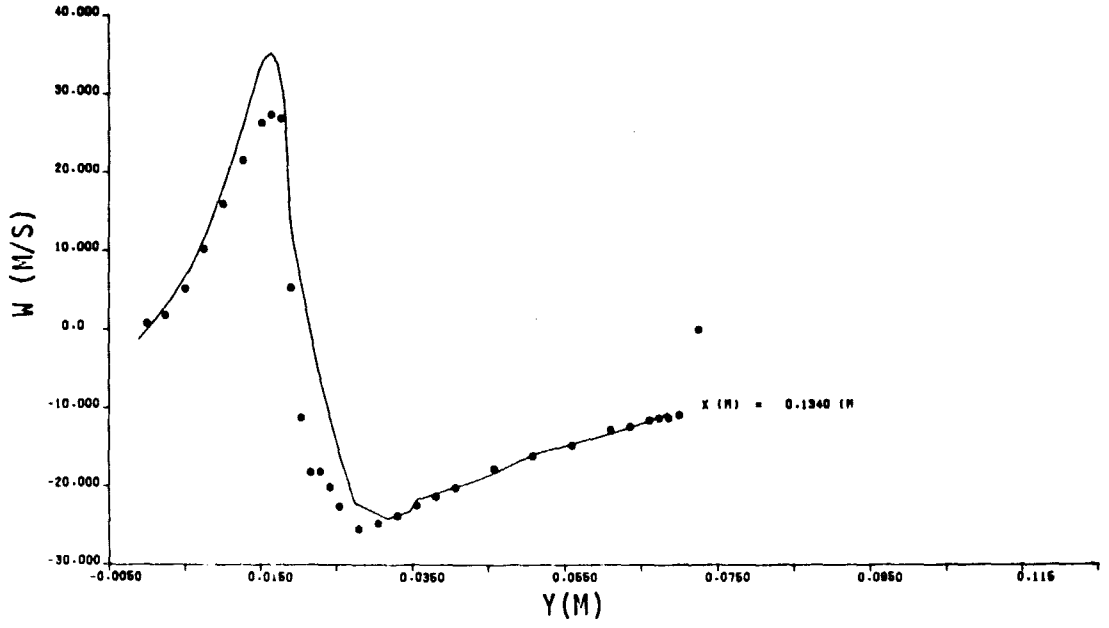

b) Hybrid Differencing, 31 x 27 Grid

Figure 33 Tangential Velocity Profiles Close to Mixing Plane for Counterswirl Showing Smearing Effect of Numerical Diffusion in Test Case 4 (Vu & Gouldin)

C-2

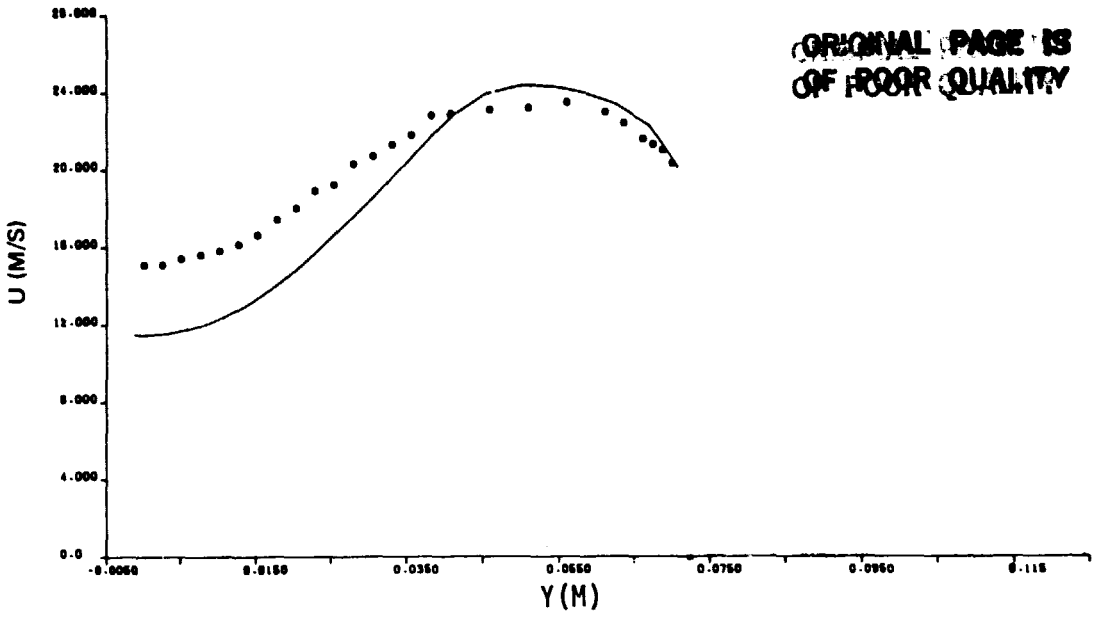

a) Hybrid Differencing, 67 x 41 Grid (Low False Diffusion)

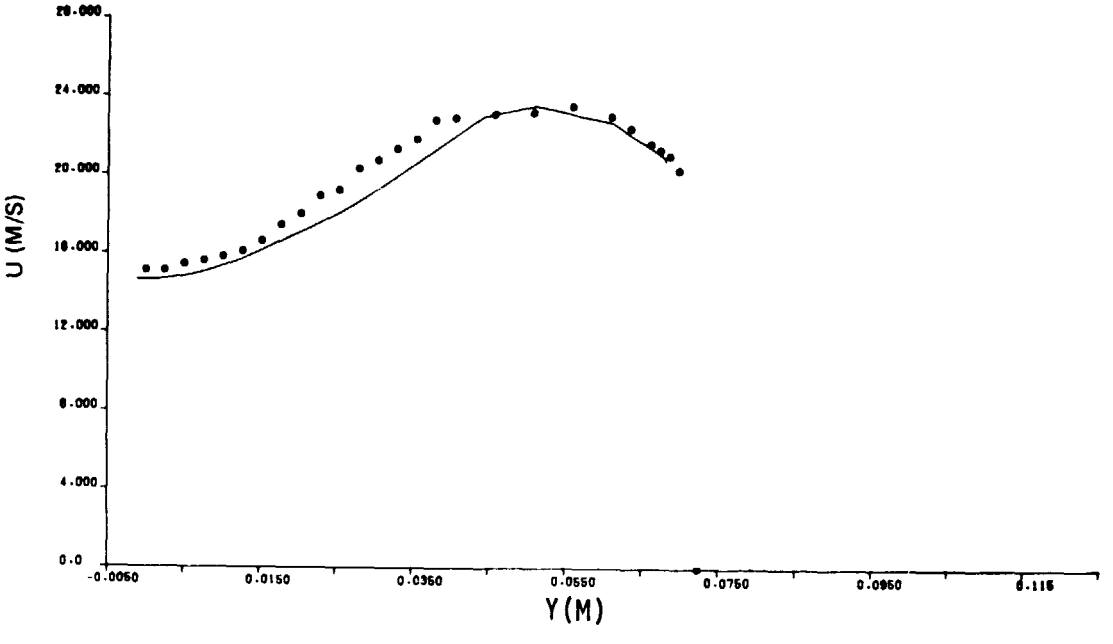

b) Hybrid Differencing, 31 x 27 Grid (False Diffusion)

Figure 34 Demonstration Through Axial Velocity Profiles That Turbulence Model Fails to Give Adequate Diffusion in Far Region of Field for Test Case 4 (Vu & Gouldin)

Test Case 5, one experiment of a continuing series by Lilley and coworkers, represented a swirling jet in a confined sudden expansion with an outlet nozzle, see Table 9. The swirler angle was selected as representing an intermediate swirl intensity. The nozzle contraction ratio was 4:1 and it was positioned such that the duct length to diameter ratio was 2:1. These dimensions were considered to be representative of a gas turbine combustor. The outlet nozzle also apparently eliminated the core-vortex problem (see Section 7.2) for the 45° swirler.

Measured mean velocity boundary conditions (References 39 and 92) at the plane of the sudden expansion were used to start the calculations. The turbulence intensity was taken as 12 percent, which Lilley verbally agreed was reasonable. The standard length scale assumption of 3 percent of the inlet diameter was used (swirler upstream of expansion plane and adequate geometric definition for alternative formulation not being available). The computational grid used was 57 x 32 and the calculation domain was extended past the nozzle plane in an attempt to ensure the correct back-pressuring effect was calculated. Measurements of profiles of mean velocity components were available for three axial stations in the simulated combustor.

In Figure 35 comparisons of measured and calculated mean velocity profiles are made for the 15 cm station. It can be seen that the code fails completely to calculate this flow, even in qualitative fashion. The failure is similar at the other two stations of 30 and 45 cm. Figure 36 shows the calculated streamlines.

Figure 13, which is constructed from Reference 74, demonstrates that the back-pressuring effect of the outlet nozzle results in the central recirculation zone developing a lobed character. The calculations yield a conventional recirculation zone shape. Whatever the merits or otherwise of the model for swirling flows, it is apparent that it fails to handle correctly the back-pressuring effect of the contraction.

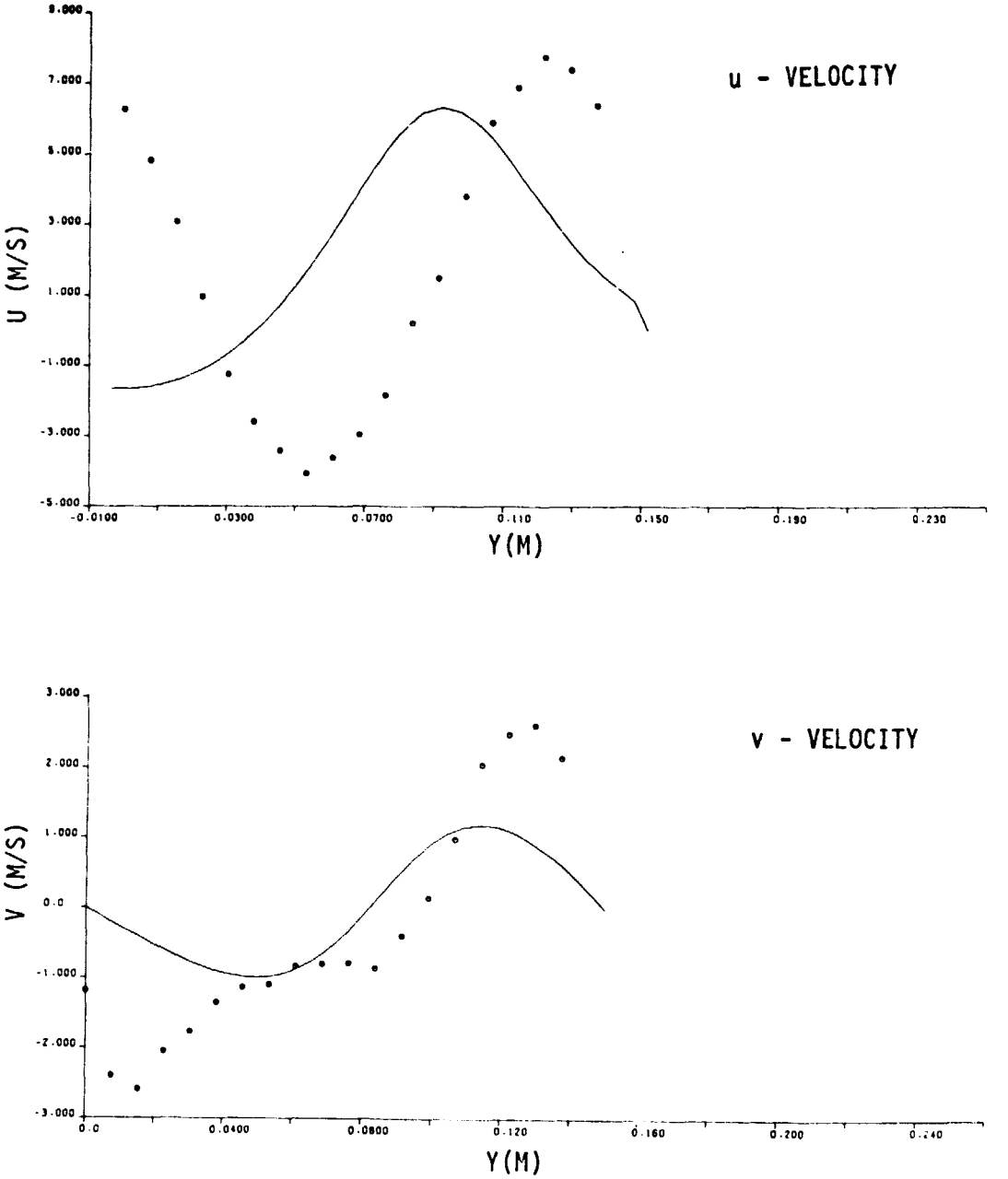

Figure 35 Profiles of Mean Velocities at 15 cm for Test Case 5 (Yoon & Lilley)

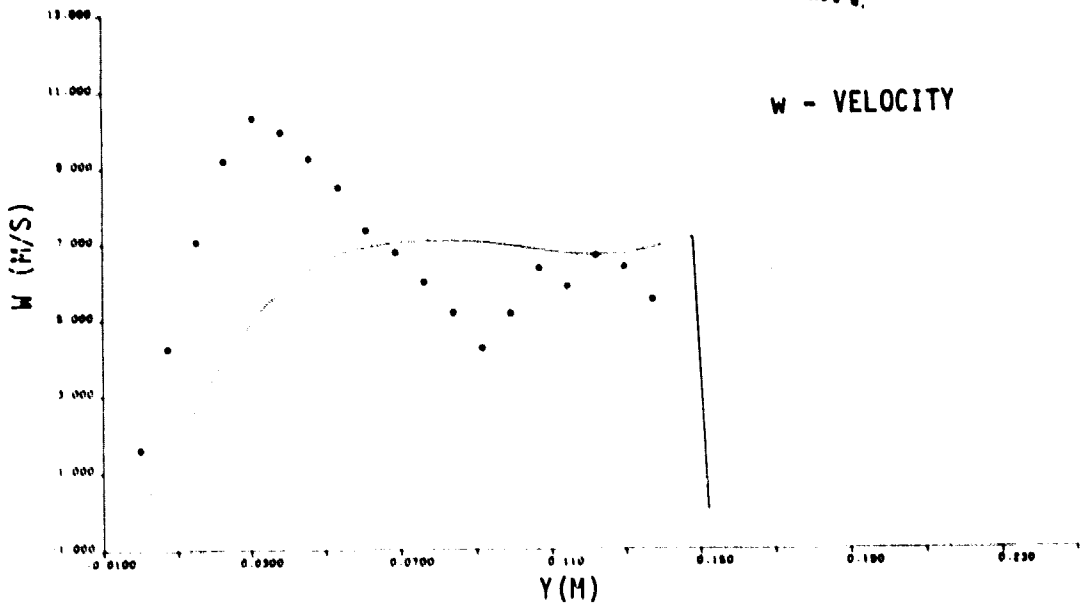

Figure 35 (continued)

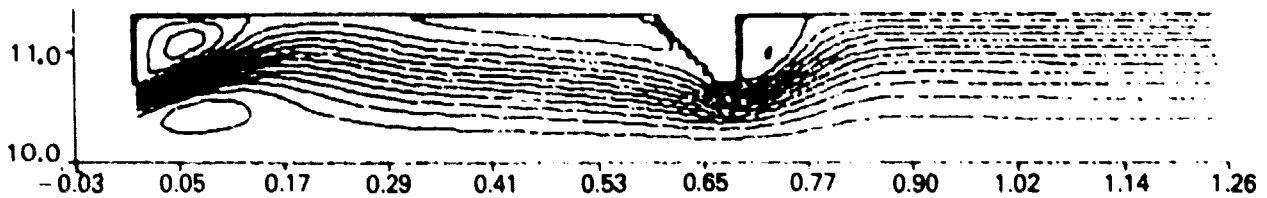

Figure 36 Test Case 5 (Yoon & Lilley), Calculated Streamlines Do Not Show the Effects of Back-Pressure on Swirling Flow as Demonstrated By the Measurements (compare with Figure 13)

8.2.3 Variable Density Jets

Test Case 9, Roquemore et al, was used to study variable density jets and to exercise the mass transport side of the turbulence model.

The experimental configuration, given in Figure 11, shows a small central jet of carbon dioxide (for present purposes, otherwise propane) with a coaxial air-jet that is removed by the presence of a bluff-body disk flameholder. The mixing jets are confined in a long, circular duct. Previous studies of parts of this experiment had established that:

1. the flowfield was dependent on the operating conditions (Reference 32),

2. when the central jet was dominant it behaved initially as if unconfined (Reference 93), and that a turbulent Schmidt number of 0.7 seemed appropriate for turbulent mass transfer.

The study reported in Reference 93 for dominant central jets was directed towards operating conditions where the outer air-jet in the experiment had almost negligible velocities relative to the CO_2 jet. It was necessary to establish if the 0.7 value found suitable for turbulent Schmidt number remained acceptable for the central jet dominant flow regime when the two jets had more comparable velocities.

The operating condition was selected as an airflow rate of 2 kg/s and a CO_2 flow rate of 16 kg/hr. Calculations were made using a range of turbulent Schmidt numbers and calculated profiles of mean mass fraction of CO_2 were compared with measured profiles to ascertain the best fit to the data.

Figure 37 gives the centerline decay of CO_2 for σ_t's of 0.3, 0.5 and 0.7, and Figure 38 gives radial profiles of CO_2 at 4 cm from the flameholder for this range of Schmidt numbers. The merit of the 0.7 value is obvious.

These calculations were made on a 49 x 46 grid, and the grid line placing was carefully refined to reduce numerical diffusion to a minimum by ensuring that central differencing from the hybrid scheme was used in all sensitive areas.

The boundary conditions used for this experiment have been described in References 32 and 93. The velocity profile of Reference 93 will be used for the unmeasured fuel jet. However, a further refinement has been made for the fuel tube turbulence characteristics. The turbulence distribution measured in a wind tunnel by Reichardt (Reference 81) formed the basis of these characteristics. It was assumed that w'_{rms} was equal to v'_{rms} for Reichardt's measurements such that,

$$K = 1/2\ (\bar{u}'^2 + 2\bar{v}'^2) \qquad (70)$$

and his peak axial turbulence intensity was scaled to match the centerline value measured by Roquemore at his 0.4 cm downstream station. This implies that the conditional potential core exists out to this station. These assumptions enable the distribution of turbulence specific kinetic energy to be determined for the exit plane of the fuel tube.

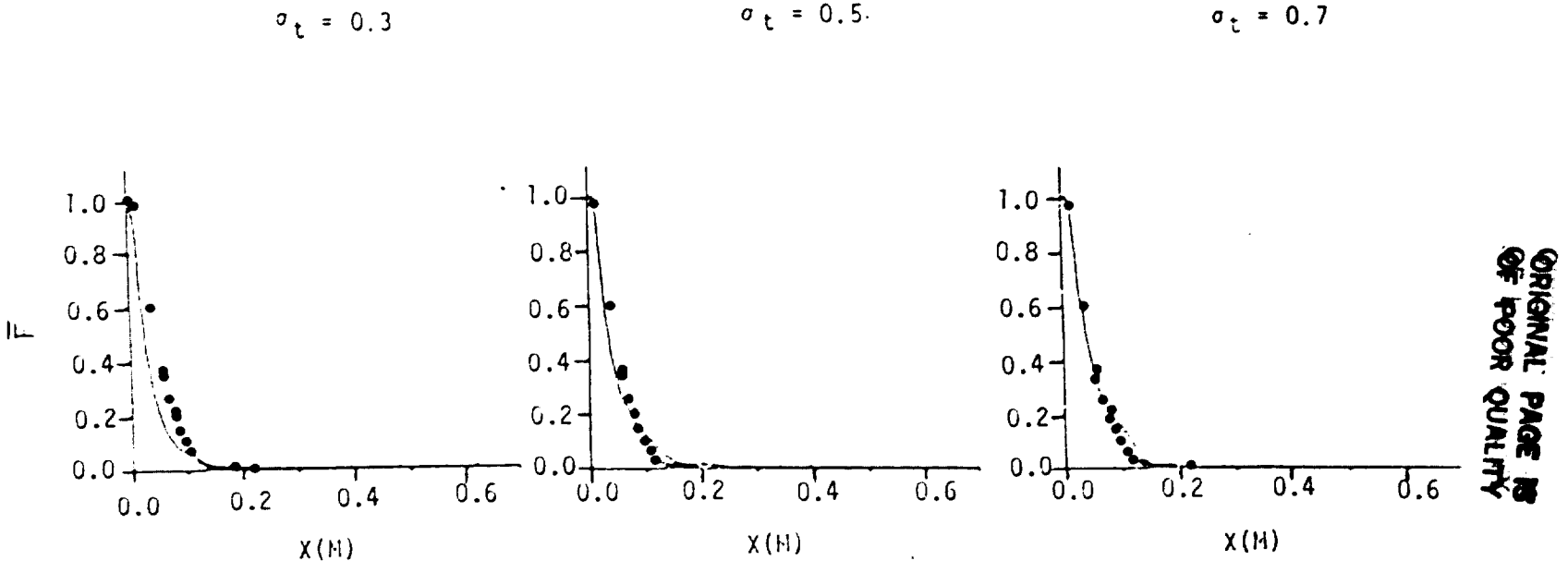

Figure 37 Effect of Turbulent Schmidt Number on Centerline Decay of CO_2 Concentration for Central Jet Dominant Flow Regime of Test Case 9 (Roquemore et al)

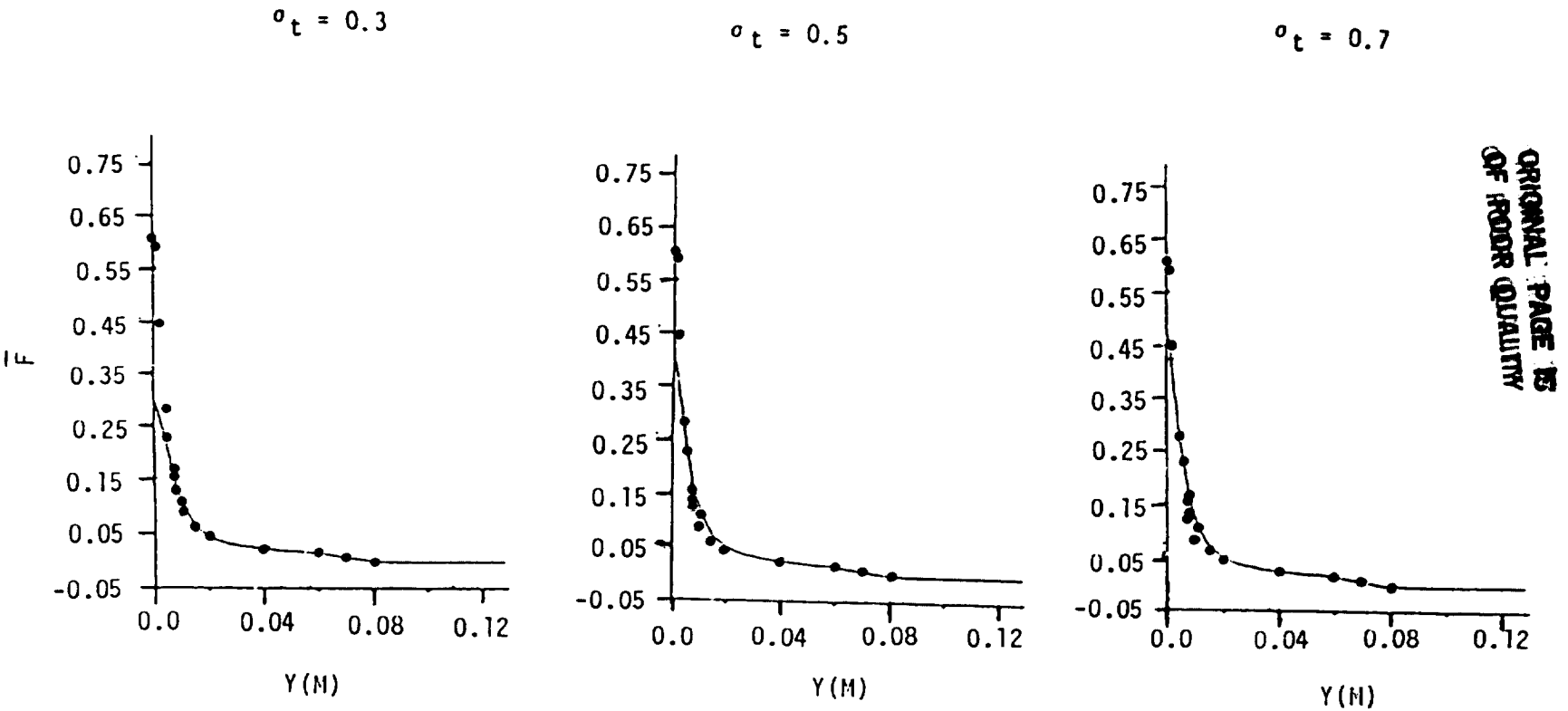

Figure 38 Effect of Turbulent Schmidt Number on Radial Decay of CO_2 Concentration at 4 cm Downstream for Central Jet Dominant Flow Regime of Test Case 9 (Roquemore et al)

The accuracy of these assumptions for the fuel tube was checked by calculating the flow for the conditions at which Roquemore made his downstream measurements (1 kg/s air and 4 kg/hr CO_2), and comparing predictions against measurements at the 0.4 cm station. The results of this comparison indicate that the boundary condition assumptions for the fuel tube are indeed good ones.

It had also been demonstrated in an earlier study of recirculation zones (Reference 17) that 0.5 was a more appropriate value for turbulent Schmidt number than the 0.9 originally recommended, (Reference 10). However, for the airjet-dominant flow regime of Roquemore's experiment use of 0.5 did not result in good agreement of the calculations and the measurements.

Experimental data were available for a case with 2 kg/s airflow and 6 kg/hr CO_2 flow, and these conditions represent an airjet dominant flow regime where the fuel jet is forced to undergo a stagnation by recirculating air, (see Reference 32). Calculations of this case were made with turbulent Schmidt numbers of 0.2, 0.3, 0.5 and 0.7.

Figure 39 shows the position of the predicted fuel stagnation point compared with the collected data in Reference 43. The prediction does not vary significantly with turbulent Schmidt number, and is in perfect agreement with the measured data. This agreement gives confidence in this calculation. In Figure 40 the effect of turbulent Schmidt number on centerline concentration of carbon dioxide is shown, and the results compared with measured data. It can be seen that reducing the turbulent Schmidt number improves the agreement of the prediction with data.

It would seem that a turbulent Schmidt number of 0.2 might be appropriate for this particular experiment.

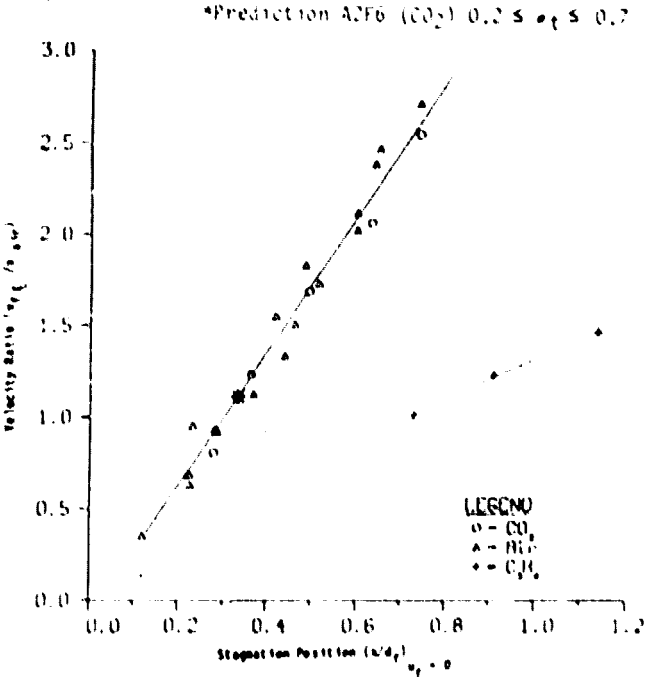

Figure 39 Fuel Stagnation Points for Test Case 9 (Roquemore et al)

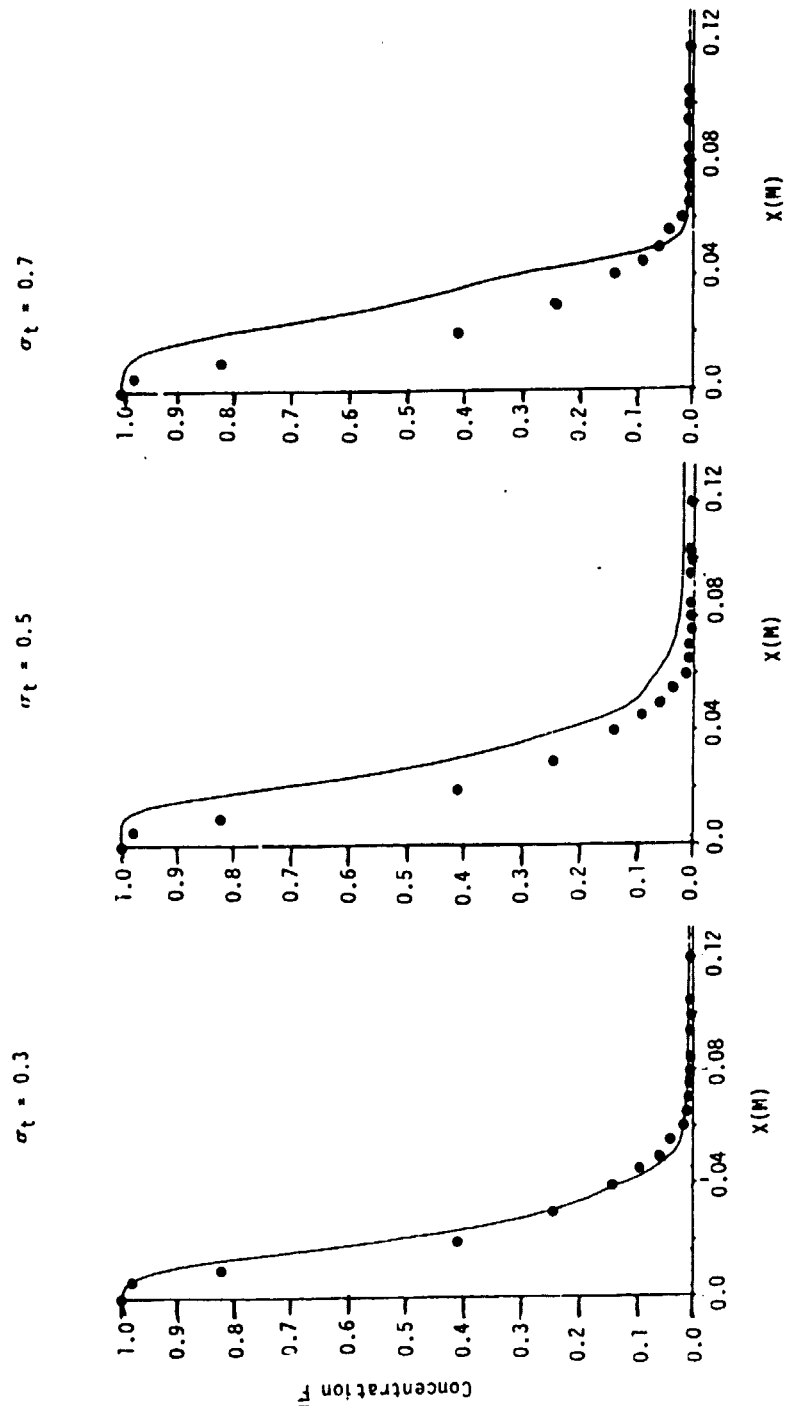

Figure 40 Effect of Turbulent Schmidt Number of Centerline Concentration CO_2 for 2 kg/s Air and 6 kg/hr CO_2 in Test Case 9 (Roquemore et al)

8.2.4 Liquid Spray

To evaluate the spray model Test Case 10, (Mellor et al, Reference 45), was selected. The experiment was such that only the droplet tracking aspects of the model would be exercised. However, that was considered to be a good starting point for a liquid spray which was produced by a real injector. The experiment was also valuable in that it provided considerable information on the formation of the spray.

The experiment consists of a 30.5 x 30.5 cm wind tunnel with a convergent intake. An air velocity of 14.7 m/s was established, and this was uniform across the tunnel. A swirl spray pressure atomizer was mounted on a slender sting aligned vertically with the tunnel axis to spray downwards. The atomizer had a flow number of 5.42 ($pph/\sqrt{psi}$) and sprayed 24.57 kg/hr of water with a cone angle of 84.4°. The Sauter Mean Diameter of the spray was measured as 91.8 μm. See Figure 12.

To model the experiment the square section wind tunnel was represented as being circular in cross-section, with a diameter of 30.5 cm. The atomizer dimension was small in comparison with the tunnel dimension so for the first part of the spray at least, this difference between the real tunnel and its model will be insignificant. The turbulence intensity of the airstream was assumed to be 1.5 percent, on the basis of experience with tunnels of similar design. The origin of the spray was taken to be the edge of the liquid sheet produced by the atomizer. This was given as 0.3 cm downstream from the face of the atomizer and at a radius of 0.28 cm.

The initial boundary conditions for the airstream are rather easily established; those for the spray are rather more difficult to obtain. Fortunately, sufficient information is provided in the report of the experiment to enable good estimates to be obtained for droplet initial conditions, if at some effort.

The optical technique used in the experiment for determining droplet velocities and trajectories enabled the necessary boundary condition information to be obtained for droplets at their origin in the fuel sheet breakup. This information was gathered for a large number of droplets, and was sorted by drop size. These data were organized statistically to produce characteristic velocities and angles as a function of drop size at origin.

Figure 41 displays a histogram for droplets of 60 microns diameter. The distribution of data is nearly normal for the droplet size range 60-90 microns; however, for both lower and higher drop sizes the distributions are skewed, and in some cases suggest two populations. The percentage cumulative relative frequencies were therefore plotted in Weibull probability form. Figure 42 is the Weibull probability plot for the 60 micron droplets. The characteristic velocity (the 63.2 percentile point) in this case is 28 m/s.

DROPLET VELOCITIES - 60 MICRON

TOTAL DATA = 59 LOWEST = 13 HIGHEST = 35.12
VERTICAL INTERVAL = .6 HORIZONTAL INTERVAL = 2.212

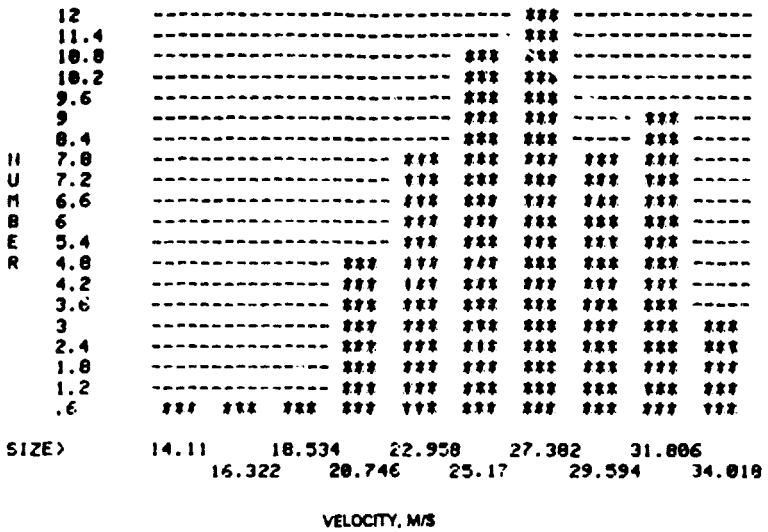

Figure 41 Histogram for Initial Velocities of 60 Micron Droplets in Test Case 10 (Mellor et al)

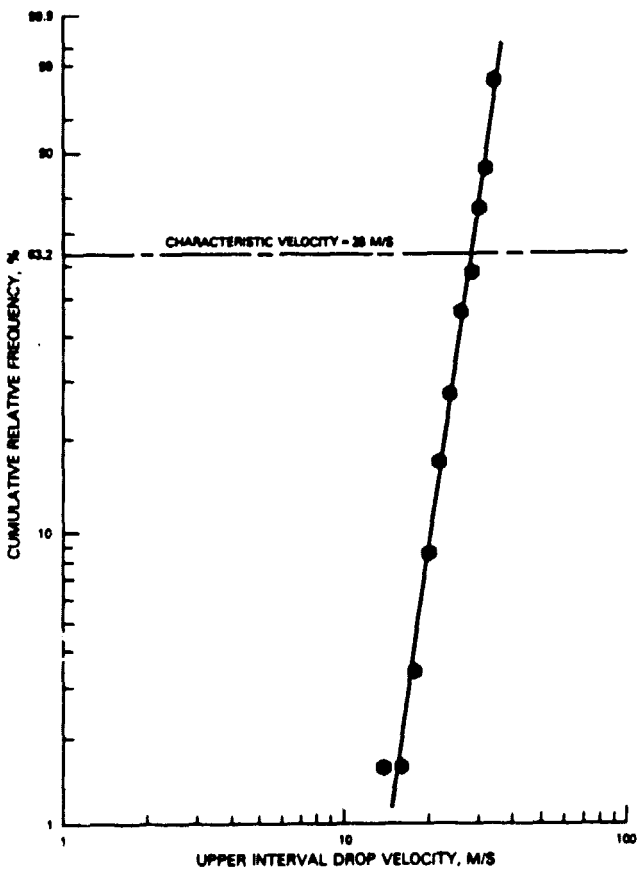

Figure 42 Weibull Probability Plot for the Initial Velocity of 60 Micron Droplets in Test Case 10 (Mellor et al)

The statistical procedure was repeated for each droplet size to produce the characteristic velocity plot given in Figure 43. Although there is some scatter a smooth curve can be drawn through the data, and this line passes through the undisturbed air velocity level for a zero diameter droplet.

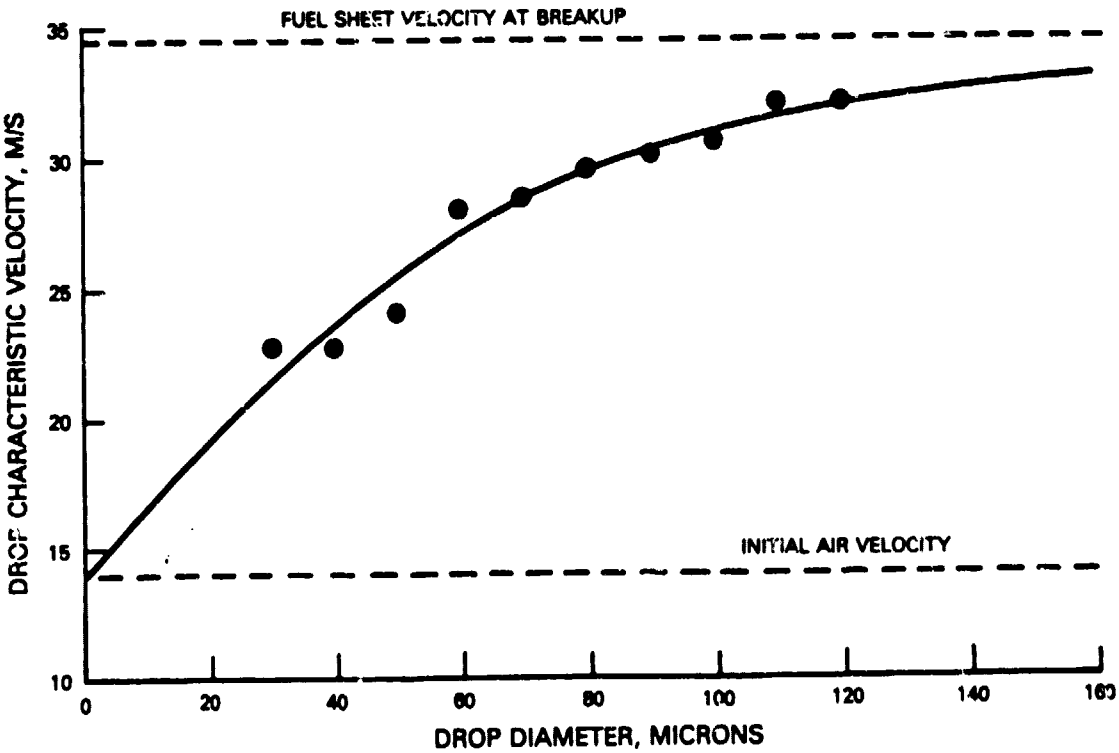

Figure 43 Weibull Characteristic Initial Velocities for Droplets at Breakup in Test Case 10 (Mellor et al)

A similar procedure was adopted for the droplet angle of trajectory at breakup. The evidence for there being two populations in the samples appeared to be stronger for the case of the angles. However, the accuracy of the measurement (taken from the projection of a "double blink" photographic slide and based on a line drawn between the centers of two circles only 1-2 circle diameters apart) cannot be high, and an increase in the data scatter is apparent. In many cases even the Weibull distribution was a poor representation of the sample.

The histogram for 80 micron droplets is given in Figure 44 to illustrate the tendency toward two populations in the data sample for angle of trajectory. The discontinuity in the Weibull probability plot of Figure 45 also indicates two populations in the sample. However, for the present purposes the data for all drop sizes have been treated as being a single population. Figure 46 gives the resulting characteristic angle of trajectory plot. This plot should be treated with some caution due to the uncertainty associated with the data.

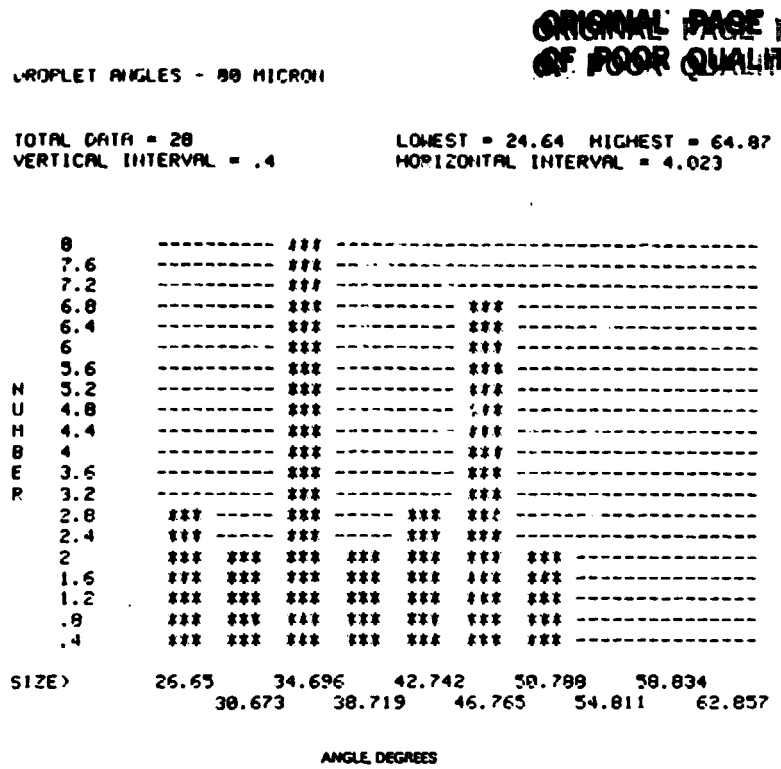

Figure 44 Histogram for Initial Trajectory Angle of 80 Micron Droplets in Test Case 10 (Mellor et al)

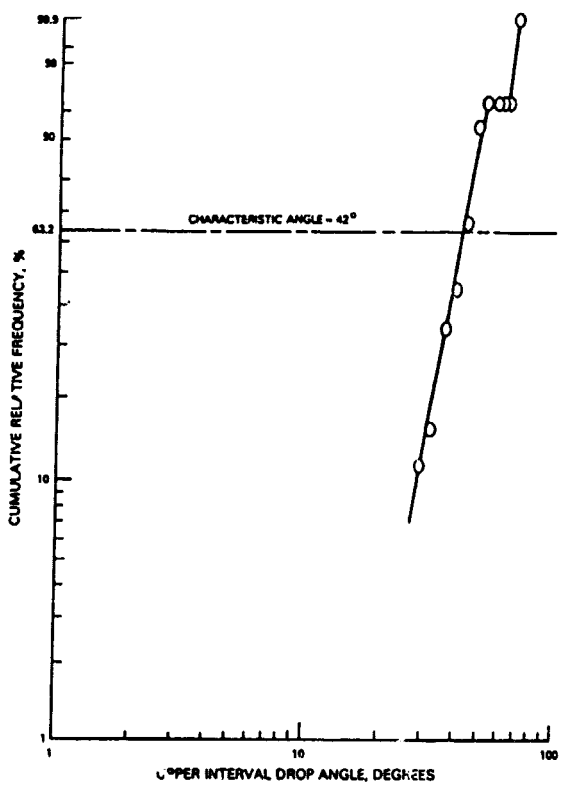

Figure 45 Weibull Probability Plot for the Initial Trajectory Angle of 80 Micron Droplets in Test Case 10 (Mellor et al)

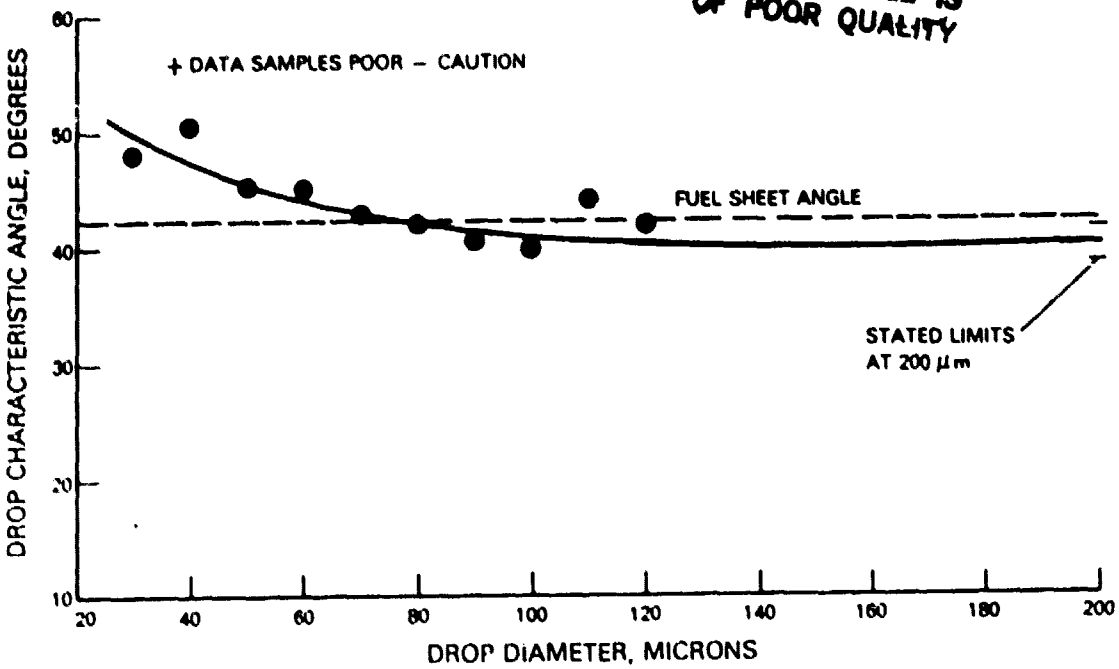

Figure 46 Weibull Characteristic Angles for Droplets at Breakup in Test Case 10 (Mellor et al)

The effect of turbulent dispersion on the spray is demonstrated in Figures 47 and 48 for the trajectories of 40, 80 and 200 micron droplets. The calculations in Figure 47 have no turbulent dispersion while those in Figure 48 do. The effect in this case is small, as might be expected for only 1.5 percent airstream turbulence intensity.

Comparisons of predictions with measured data for droplet velocities and trajectory angle are given in Figures 49 and 50 at three downstream positions in the spray and as a function of drop size.

The calculations for droplet velocity indicate that by 3 cm from the injector droplets with diameters equal to and less than about 35 μm have reached the velocity of the airstream. This indication does not change out to the 9 cm position. The measurements indicate that the size for terminal velocity at the closest station is about 20 μm. The agreement of measured and calculated velocities is good for droplets of 50 to 200 μm in diameter at the 3 and 6 cm downstream stations. At the 9 cm position the calculations tend to overestimate the measured velocities by a small amount. The effect of distance is shown for three droplet sizes in the crossplot of Figure 51. The calculations agree with the data in showing that droplet velocity increases rapidly at all distances with drop size up to about 100 μm diameter, and then increases less rapidly out to 200 μm diameter. For distances out to 9 cm from the injector a given droplet in the size range 70-170 μm does not lose much of its initial velocity.

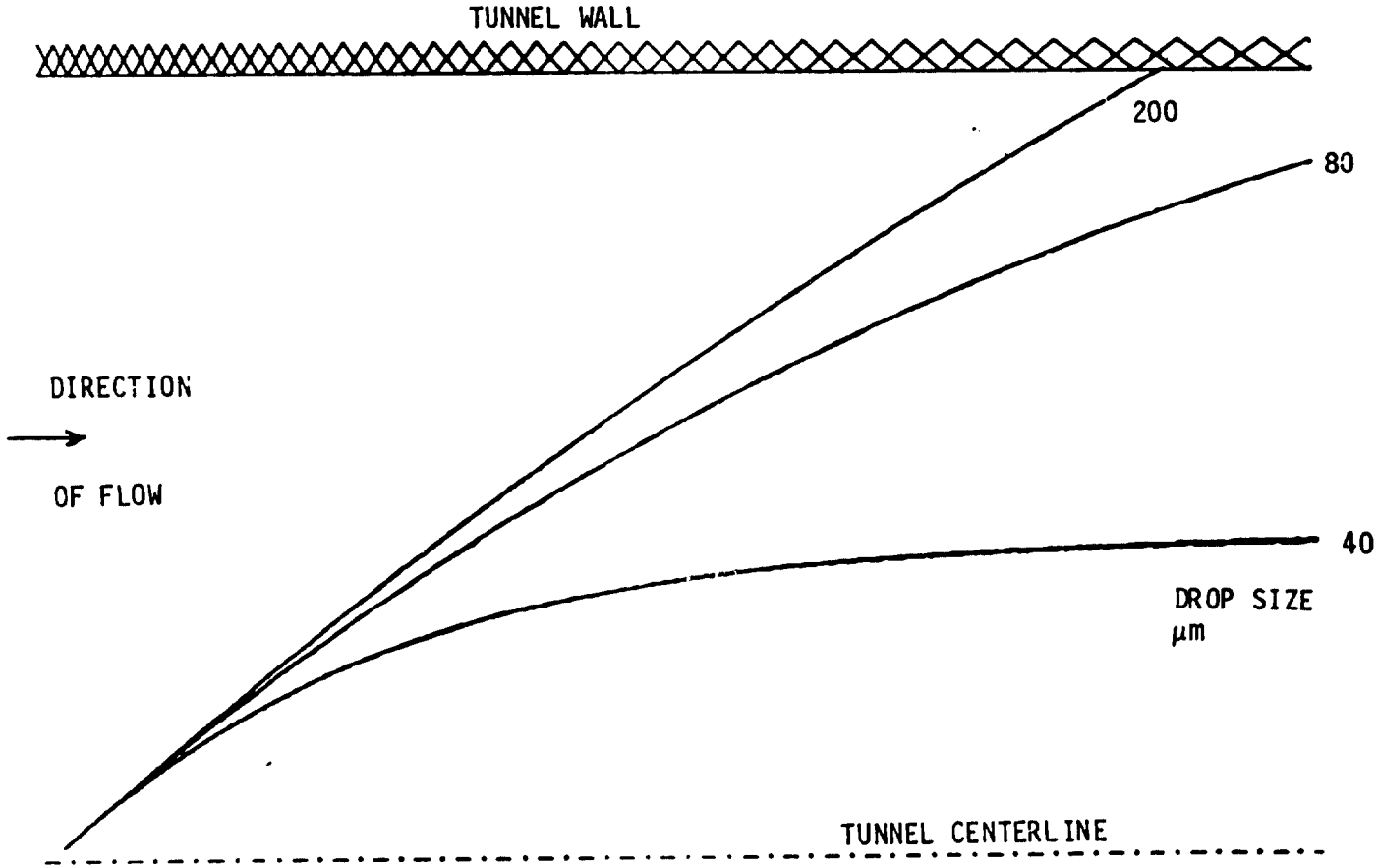

Figure 47 Sample Droplet Trajectories With No Turbulent Dispersion for Test Case 10 (Mellor et al)

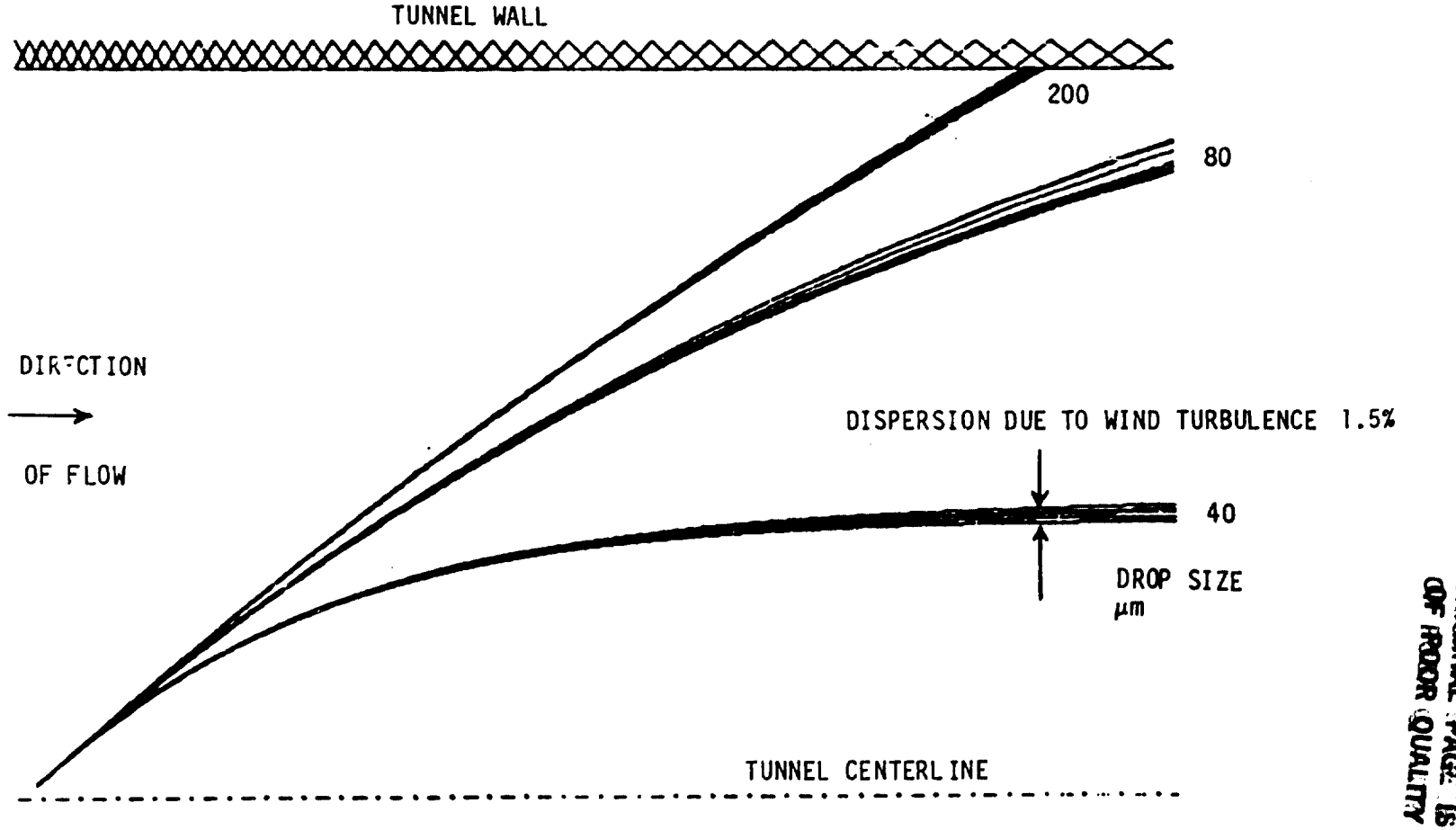

Figure 48 Effect of Wind Turbulence on Droplet Trajectories for Test Case 10 (Mellor et al)

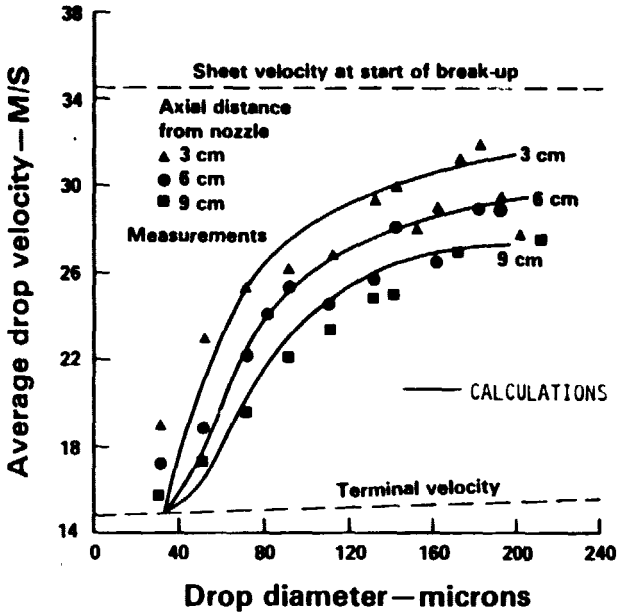

Figure 49 Variation of Average Drop Velocity with Drop Size at 3 Downstream Positions in the Spray for Test Case 10 (Mellor et al)

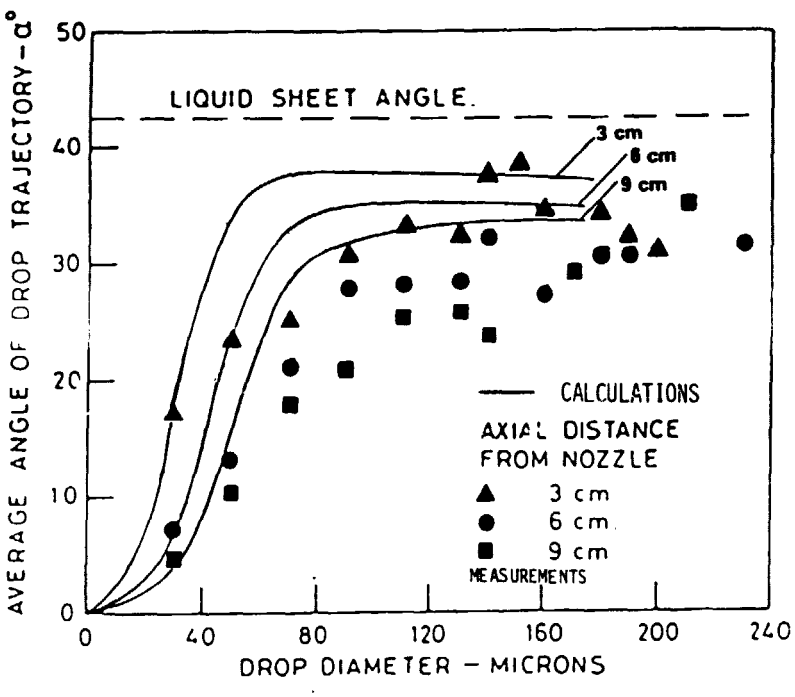

Figure 50 Variation of Average Angle of Trajectory With Drop Size at 3 Downstream Positions in the Spray for Test Case 10 (Mellor et al)

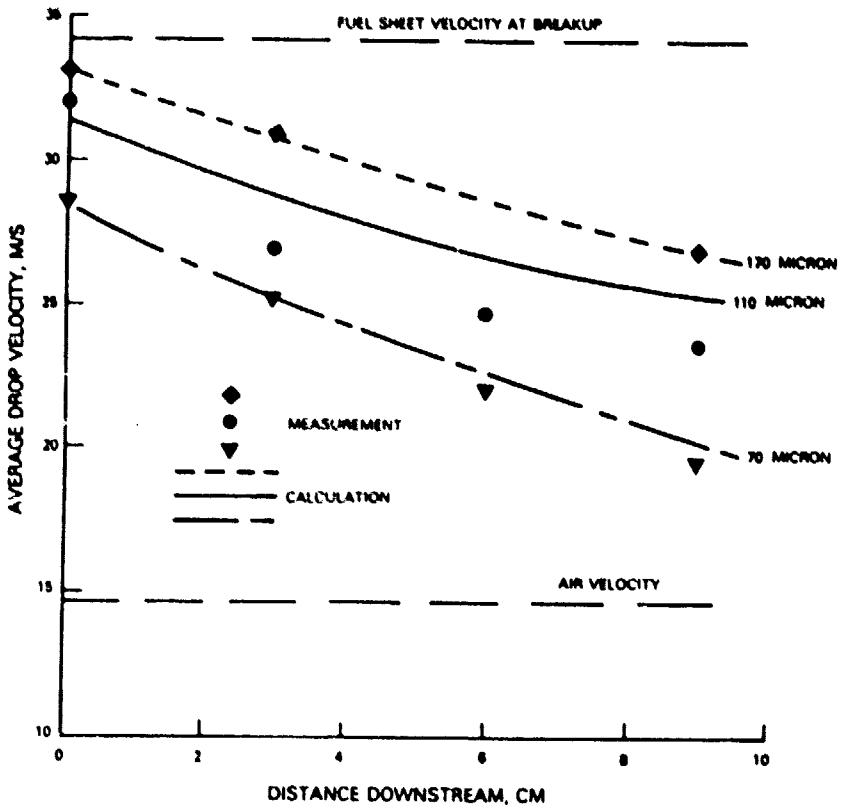

Figure 51 Variation of Average Droplet Velocity With Axial Distance From Injector in Test Case 10 (Mellor et al)

The agreements of calculation with measurement for droplet angles of trajectory shown in Figure 50 are not as satisfactory as for droplet velocity. In general, the calculations overestimate the angle, although agreement seems to be improving for droplet sizes above 160 μm. The measurements show that the smaller droplets are, in general, deflected more by the airstream than the calculations indicate. However, the 30 μm drops, which the calculations are moving at their terminal velocity by 3 cm, have measured angles in exact agreement with the calculated angles at all three axial positions. Despite the poor quantitative agreement, the calculations do reproduce the trends shown in the data that for droplets up to about 70 μm in diameter the average angle of trajectory increases rapidly; for droplets greater than 70 μm the average angle tends towards a constant value.

Figure 52 presents a cause and effect diagram that addresses the difficulties evident in Figure 50. The possible causes of the disagreement between the calculated angles and those measured are divided into four major categories: those concerned with the experiment, the atomization process itself, the physical laws incorporated into the model, and the way the data have been handled.

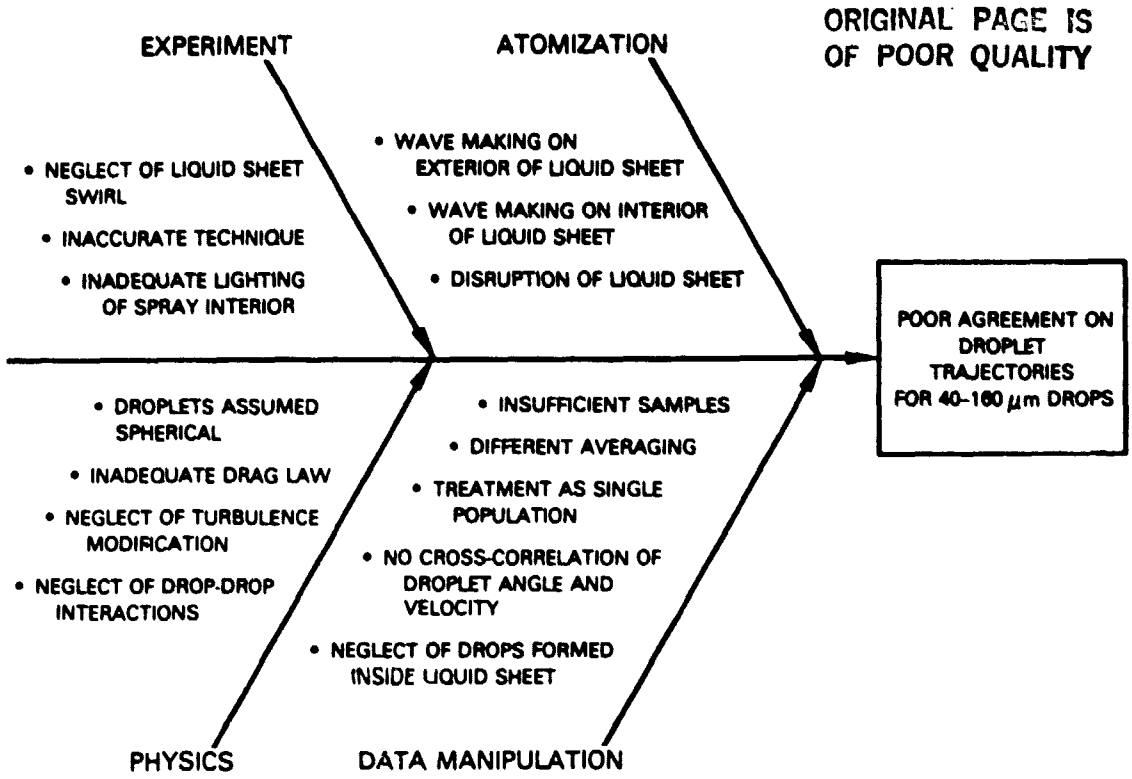

Figure 52 Cause and Effect Diagram for Figure 50

Of the causes associated with the experiment, the neglect of swirl and the basic techniques are discussed in the paper and the discussion on it. Inadequate lighting of the interior of the spray at the liquid sheet breakup is felt to be important in that it prevented a complete initial description of the spray origin to be obtained. This will be discussed in detail below.

The droplets in the spray originate from two possible mechanisms: breakup of the liquid sheet, and ligament formation from waves formed in the liquid sheet. The liquid sheet tends to break up through the development of holes in it, and subsequent disruption as sheet continuity is lost. This process tends to produce large drops. It would therefore be anticipated that at their origin the larger droplets would have velocities and angles close to those of the liquid sheet. Figures 7 and 8 of the original paper (Reference 45) and the present Figures 43 and 46 support this. The smaller droplets tend to be produced by secondary breakup of larger elements generated during the liquid sheet disruption, and through breakup of ligaments formed from the surface of the sheet by wave motion. The smaller drops hence tend at origin to have a wider range of initial velocities and angles than the larger drops. This is again supported by Figures 7 and 8 of Reference 45. The liquid sheet having two sides, an inside and an outside and often with somewhat different air-side boundary conditions, it could be expected that just downstream of breakup a drop sample of small droplets could contain three populations.

The nature of this atomization process, together with the inadequate lighting of the interior of the spray at breakup precluding measurement of droplets originating on the interior with angles less than that of the original sheet, would tend to bias the characteristic angles calculated and shown in Figure 46, to a value greater than the true average for all three populations of the smaller droplets. Mellor et al comment that the small droplets originating from the inner liquid sheet surface probably had angles below 20°. Inclusion of such a missing population would change the histogram of Figure 44 for example, significantly, and would result in a second discontinuity in the probability plot of Figure 45 so that three distinct characteristic angles could be obtained for droplets of this size.

Production of three distinct initial angles for a given drop size would require a cross-correlation to exist between droplet velocity and angle. Such information existed in part (for two of the populations) in the raw data of the experiment, but is lost in the data presentation given in the paper. No cross-correlation has been attempted in the present work.

Generation and use of a family of droplet velocity and angle relationships for each drop size range as initial conditions for the spray would require some changes in how droplet "average" velocity and angles at downstream positions in the spray are calculated. Such a procedure is closer to that used experimentally and should give better agreement with the measured "averages" presented in Figures 49, 50 and 51. Presently, the calculated averaging is done through the use of characteristic angles and velocities that do not represent all of the droplets originating at the breakup.

Droplets in the size range of 50-120 μm appear to have insufficient drag in the calculations of their trajectory. Figure 53 shows the drag law used and compares it with the data of Yuen and Chen (Reference 94), with which it is in general agreement up to a droplet Reynolds number of about 100. Under present conditions the critical Reynolds number of 100 applies to droplets of about 90 μm. Therefore the "dip" in the drag curve would apply for droplets of 50-120 μm. However, there is no justification to accept this as the explanation for the discrepancies of Figure 50.

Photographs of the spray show that the majority of the droplets are indeed spherical. The turbulence of the stream into which the spray is introduced is low initially so that turbulent dispersion of droplets does not have a significant effect on turbulence, as Figures 47 and 48 illustrate. Neglect of modification of the air turbulence by the spray is therefore not significant. The spray is a "thin" spray so that drop-drop interactions are believed not to be significant.

The most promising candidate from Figure 52 for the cause of the angle discrepancy therefore emerges as the treatment of droplet initial conditions.

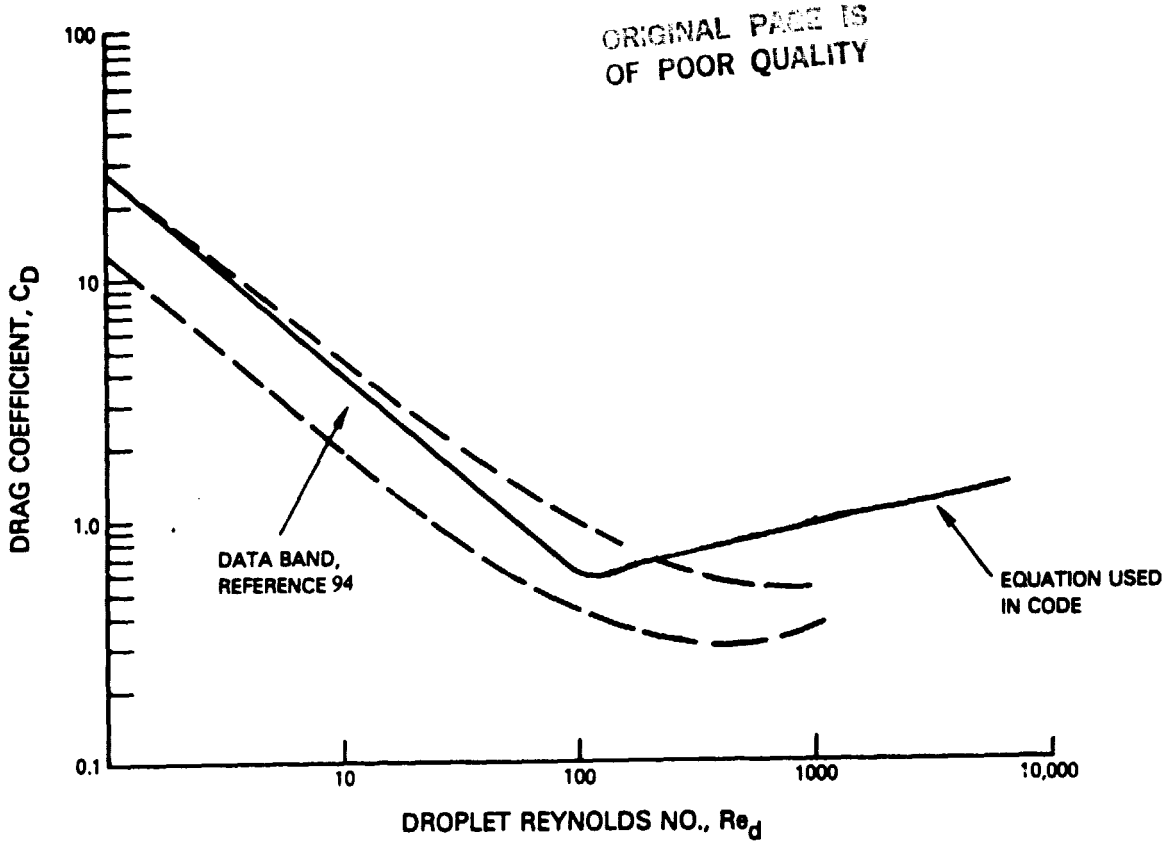

Figure 53 Drag Coefficient Information for Droplets

In Figure 54 the variations in mean drop size based on spatial distribution with axial and radial position are compared. In this comparison only the shapes of the distributions should be compared since different techniques were used to obtain these distributions. For the experiment the distributions are based on the arithmetic mean drop size obtained at a given distance from the real droplets. Because of the wide range of initial conditions with respect to angle of trajectory and velocity (see Figures 7 and 8 of Reference 45) the droplets are dispersed across the spray close to the injector. In the calculations the droplets are assigned a single initial angle and velocity according to their size from Figures 43 and 46. The level of mean droplet diameter in the calculations was affected by the range of droplet sizes considered. This range was 20-180 μm and it was divided into 7 intervals. The range was restricted by programming limitations in the computer code for the spray model. The actual size distribution ranged from 10-220 μm droplet diameter.

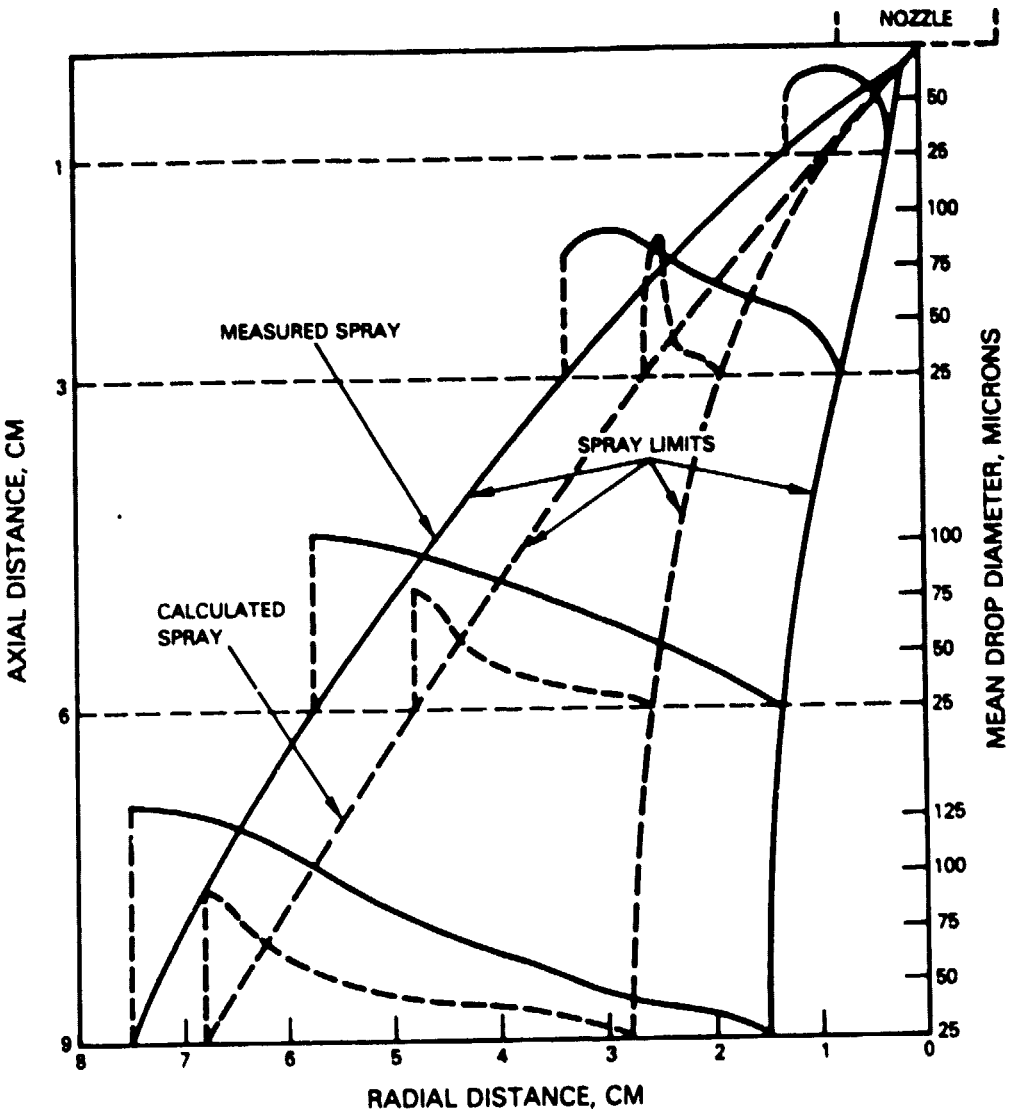

Figure 54 Variation of Mean Drop Size (Based on Spatial Distribution) With Axial and Radial Position for Test Case 10 (Mellor et al)

It can be seen that the shape of the mean size distribution in the spray at 9 cm is well represented by the calculations. This downstream distance represents an almost "fully developed" region of the spray where initial conditions are less influential and the concept and use of characteristic velocities and angles of trajectory for initial conditions in a calculation should be becoming appropriate. Thus, at distances downstream from the injector the well known migration of smaller droplets toward the center of the real spray results in the tendency toward the uniform distribution of mean drop sizes shown in the calculations.

8.2.5 Reacting Flow

Test Case 9 (Roquemore et al, Reference 43) was selected as the reacting flow experiment to evaluate the combustion model. This choice was made because the experiment had sufficient depth for the turbulent transport to be essentially eliminated as a source of uncertainty in the calculations, see Section 8.2.3.

The experiment consists of a long axisymmetric combustion tunnel employing a disk flameholder having a cylindrical forebody with a streamline nose. Gaseous propane is introduced as fuel from a small orifice in the center of the disk while air enters as an annular jet around the flameholder. Figure 11 gives the layout of the combustor.

Unfortunately, the experiment has a serious problem in that it is a nonstationary flow, (Reference 53). The nonstationary flow is associated with vortex shedding off the bluff body flameholder, (Reference 95), and in the range of flow rates of interest the eddy shedding could be acoustically coupled with the tunnel natural frequencies, (Reference 96). The nonstationary behavior has to be borne in mind when using this experiment.

The boundary conditions and the calculation grid used were defined in Section 8.2.3. Since the flow field for this experiment has two distinct (and steady) regimes depending on operating conditions (Reference 32), two sets of flow rates were used, 2 kg/s air and 4 kg/hr propane (A2P4) for the airjet-dominant regime and, 2 kg/s air and 16 kg/hr propane (A2P16) for the central fuel jet dominant regime; an attempt was made to find the breakthrough point where the fuel jet broke through the air recirculation, using fuel flow rates of 8-12 kg/hr propane. For the nonbroken-through regime the turbulent Schmidt number was taken as 0.2 and for the broken-through regime a value of 0.7 was used, these being based on the variable density isothermal study reported in Section 8.2.3. The calculations were started in the plane of the flameholder face.

The calculated flow fields for nonbroken-through and broken-through conditions are shown in Figures 55 and 56 respectively. The streamlines of Figure 55a) show the multiple stagnation points in the complex recirculation zone established in the wake of the flameholder. The main burning zone is attached to the flameholder, as Figure 55b) shows. When the fuel jet breaks through the air recirculation the main burning zone is downstream, with a pilot region on the flameholder, Figure 56b). The simpler recirculation zone shown in Figure 56a) seems to go with the reduced mixing implied by the higher value of turbulent Schmidt number.

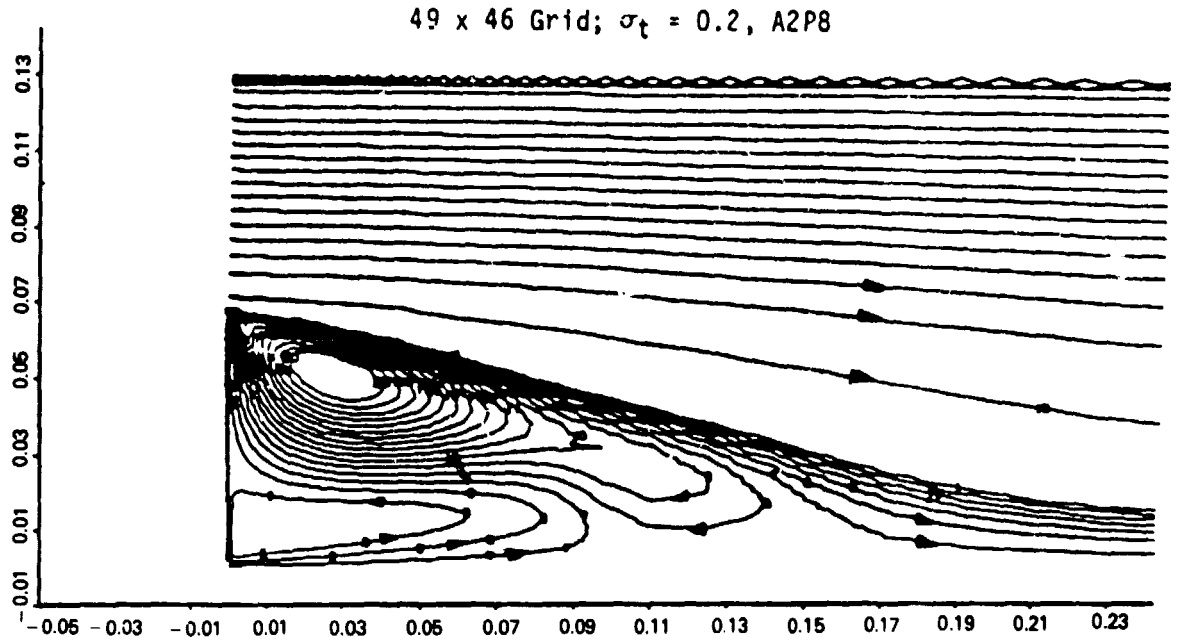

a) Streamlines

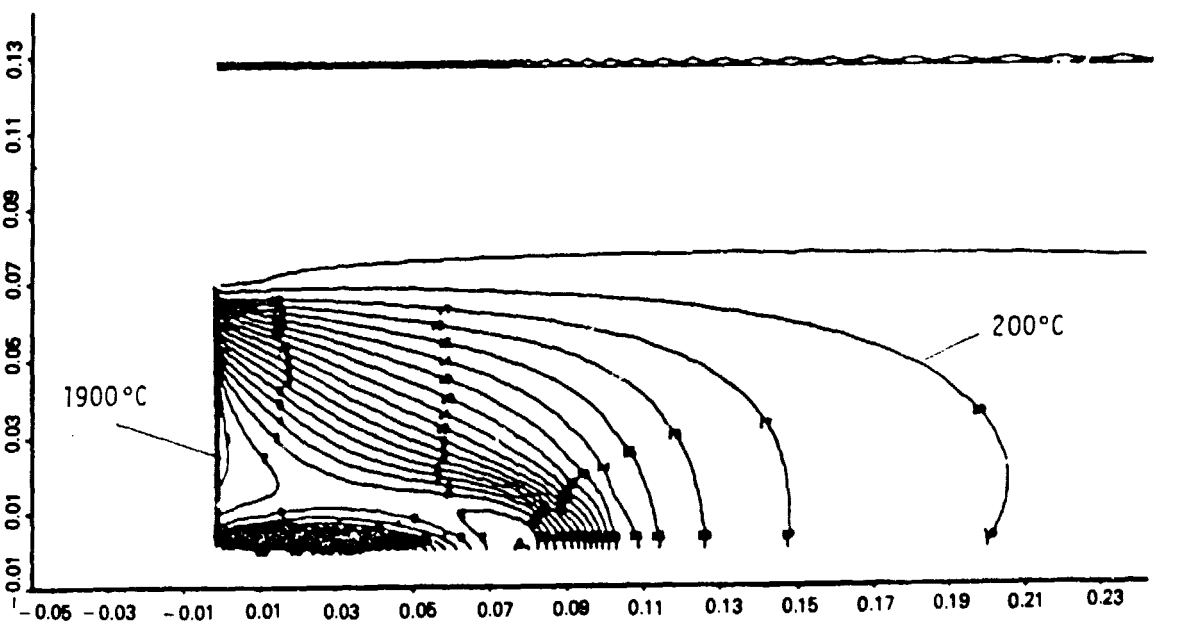

b) Isotherms

Figure 55 Reacting Flow Calculations for Nonbroken-Through Flow, Test Case 9 (Roquemore et al)

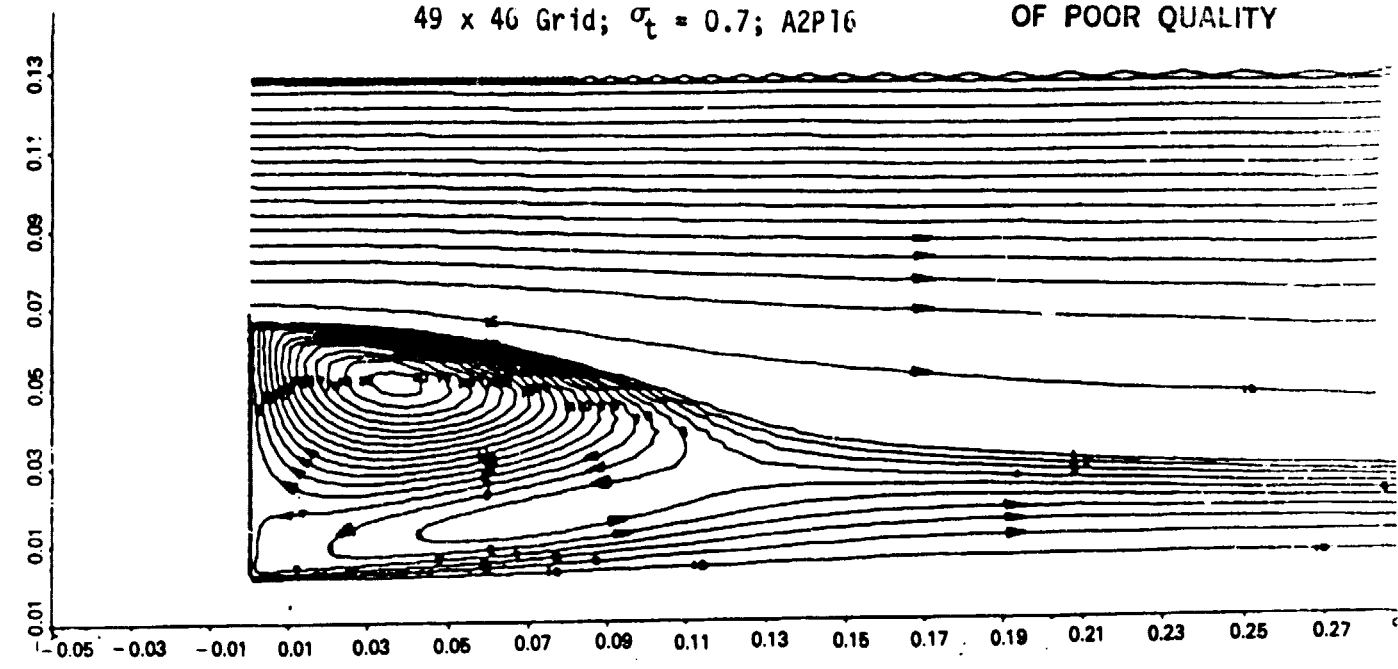

a) Streamlines

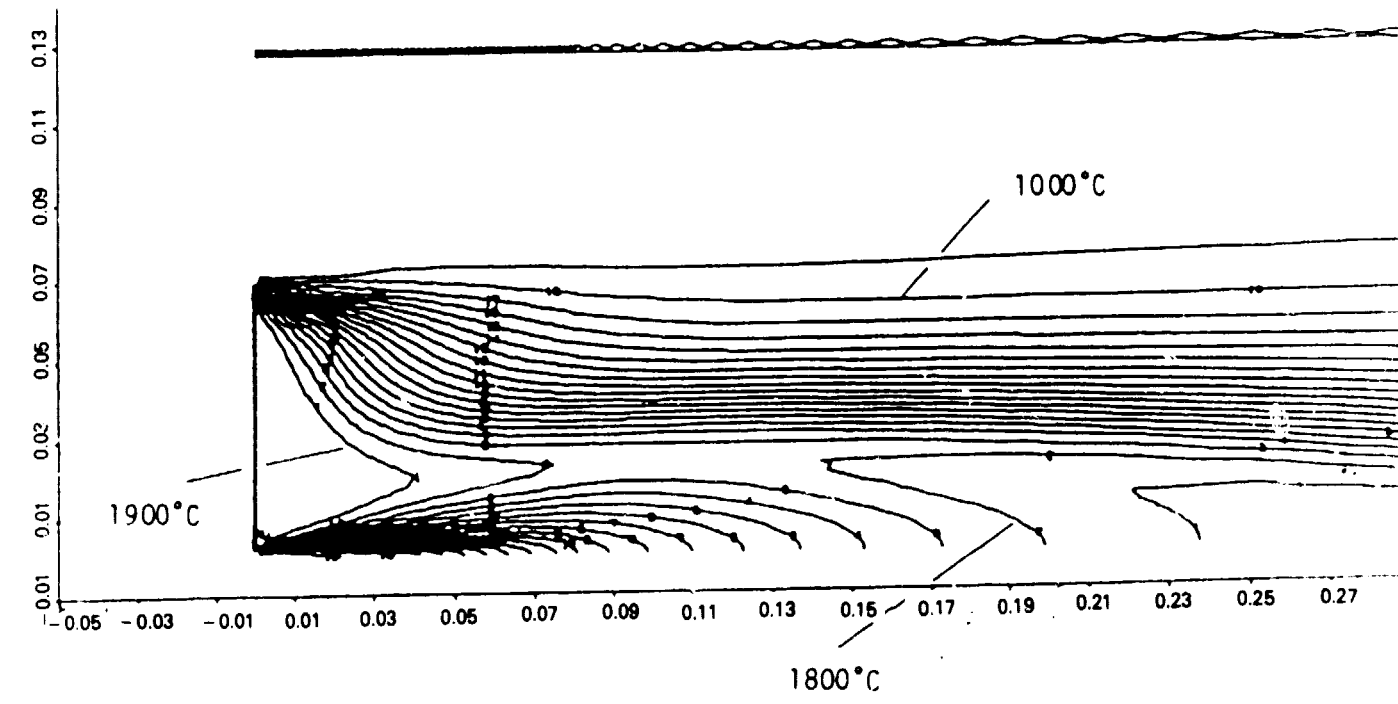

b) Isotherms

Figure 56 Reacting Flow Calculations for Broken-Through Flow, Test Case 9 (Roquemore et al)

To ascertain the importance of radiation, both gaseous and particulate, to the calculations the A2P8 reacting flow case was run on the fine grid with a turbulent Schmidt number of 0.5 for the following conditions: no radiation, gaseous radiation, a "small soot" case and, a "large soot" case. Sooting flames were considered because photographs of the flame (Reference 52) suggested some luminosity adjacent to the flameholder, and Roquemore (Reference 79) mentioned soot depositions on the face of the flameholder during the course of the run.

The "small soot"/"large soot" definitions were as given below. Small soot: particle diameter of 250Å and number density of 15×10^6 particles per cc; Large soot: particle diameter of 500Å and a number density of 20×10^6 particles per cc.

The large soot definition was based on a typical smoke number density/size relation derived from the measurements of Stockham and Betz (Reference 97) by scaling to a JT9D-7A size, reported hydrocarbon smoke sizes by Whelan (Reference 98), and carbon particle size measurements at the combustor exit in a JT9D experimental engine. This was felt to represent a likely upper limit. The small soot definition was derived from the large soot definition by tempering it according to the laboratory flames reported by Magnussen and Hjertager (Reference 22). The small soot case was felt to be closer to the flame under consideration. Soot, in both cases, was assumed to exist in a single zone in the flame to a downstream distance of 9 cm from the flameholder and out to a radius of 6.92 cm. The zone was sized based on the photographic evidence (Reference 52).

To make the radiation calculations, the measured temperature distribution on the flameholder face was averaged to a value of 750 degrees K; tunnel wall temperatures were assumed to be a uniform 340 degrees K. The emissivities of the flameholder and tunnel wall were 0.8 and 0.65 respectively. The former value was based on the soot depositions noted for the flameholder and the latter was an integrated mean for the tunnel walls and windows.

Plots of the centerline temperature distributions revealed a maximum difference between the no radiation and large soot cases of about 40 degrees K, occurring about 7.6 cm from the flameholder. Radial profiles of temperature at stations 6.3, 7.5 and 25.3 cm from the flameholders gave respective differences of 53, 56 and 3 degrees K. The peak difference occurred at a radius of 1.3 cm. These temperature differences are very small, and indicate that radiation is not an important source of heat loss in the test case. The maximum difference in temperature between the large soot and gas-only radiation was about 20 degrees K. This indicates that soot is not important either.

On the basis of the diagnostic testing described above, it was decided that gaseous radiation only need be considered.

Figure 57 presents information on the position of the fuel stagnation point in reacting flow for the A2P8 conditions. The original calculations referred to in the figure were made in 1980 using the 39 x 39 grid of Reference 32, σ_t of 0.5 and the original fuel jet inlet boundary conditions.

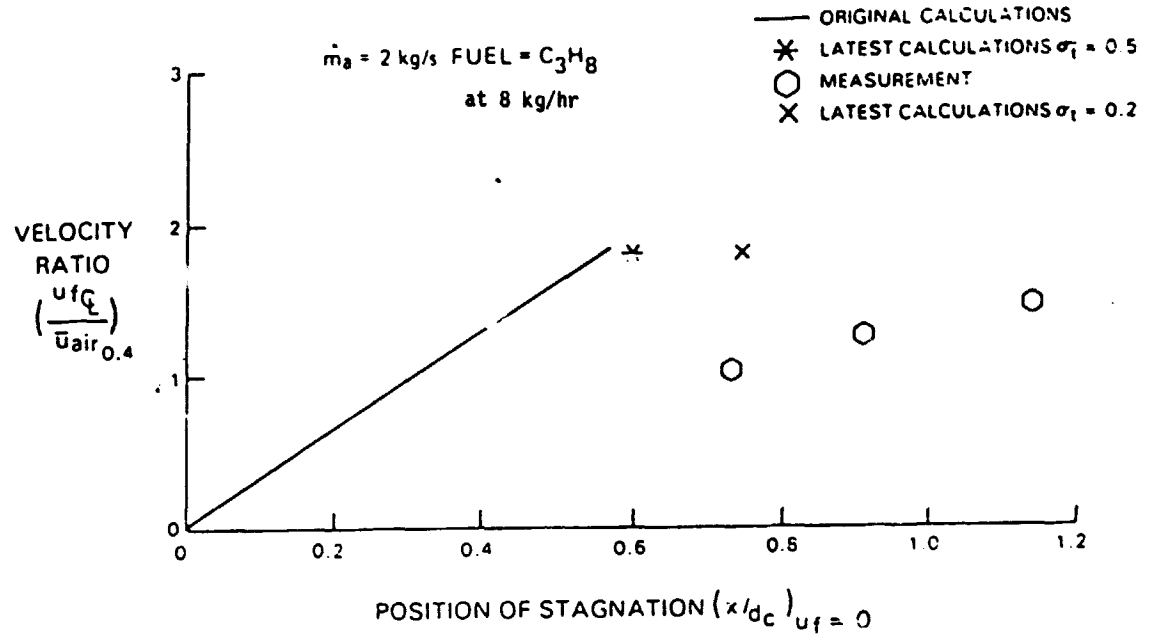

Figure 57 Fuel Stagnation Point in Reacting Flow for A2P8 in Test Case 9 (Roquemore et al)

The effects of the refined grid and revised fuel jet boundary conditions can be seen to be small. The reduction of turbulent Schmidt number to 0.2 moves the stagnation point significantly downstream, thereby improving the agreement with the measurements. However, breakthrough at these conditions is still not obtained from the calculation, whereas the measurements show the flow is actually broken-through.

The flow behavior is such that A2P8 is just about at the combusting case breakthrough point. It is a little optimistic to expect to be able to calculate such a singularity exactly. Even in isothermal flow the calculations required more fuel flow for breakthrough than the experiment indicated (Reference 32).

The earlier calculations had indicated that breakthrough took place off-axis due to distortion of the air recirculation zone by off-axis burning (Reference 96). Examination of the streamlines predicted by the current calculations suggested that sufficient off-axis burning was not taking place to give such a breakthrough, so that although the fuel stagnation point agreed with previous results, the character of the predictions had actually changed slightly from that of the original predictions. The change in character could be attributed to the reduction in diffusion due to the increased grid density.

To be sure that this was indeed so, a coarser grid of 39 x 39 was run with the same fuel jet boundary conditions. This was compared with the results of a 49 x 46 grid calculation; both calculations had no radiation so that the effects of grid alone could be studied. It was confirmed by comparing the two sets of calculated isotherms. The reduced false diffusion (of fuel) by the finer grid moves the peak temperatures of the flame radially inward and upstream compared to the coarse grid.

The unfortunate dynamic character of the experiment must be considered also with respect to the breakthrough point.

The nonstationary nature of the flame might have resulted in the necked down air recirculation zone (see Figure 55b) being fractured earlier than would have occurred otherwise (Reference 96). The fragile character of the hot gas connection between the pilot flame on the flameholder and the downstream flame can be appreciated. Early rupture of this connector could be induced by a superimposed oscillating pressure field as postulated in Reference 96. It might, therefore, be impossible for the present steady state codes to correctly predict the breakthrough point for this experiment.

Using the indicated turbulent Schmidt number for the broken-through flow regime, the A2P16 combusting case was calculated.

Figure 58 compares calculated and measured radial profiles of temperature at several axial stations. It is clear that the character of the flame is correctly predicted as burning off the centerline of the combustor. The radial positions of the maximum temperature are predicted fairly well, as are the widths of the flame. Maximum temperatures are considerably overpredicted however.

The discrepancies seen in Figure 58 between predicted and measured temperature levels are up to 700 degrees K. This level of discrepancy exceeds that normally anticipated for the physical modeling used.

There are two important sources of uncertainty; that associated with the combustion model, which is 200-300 degrees K (Reference 22), and that associated with neglect of fluctuating density, which is about 300 degrees K (Reference 99). These uncertainties are comparable. Since the study in Reference 22 was carried out neglecting fluctuating density effects, the uncertainty in the present case would not be expected to exceed 300 degrees K. It is apparent that some other effect must be accounted for.

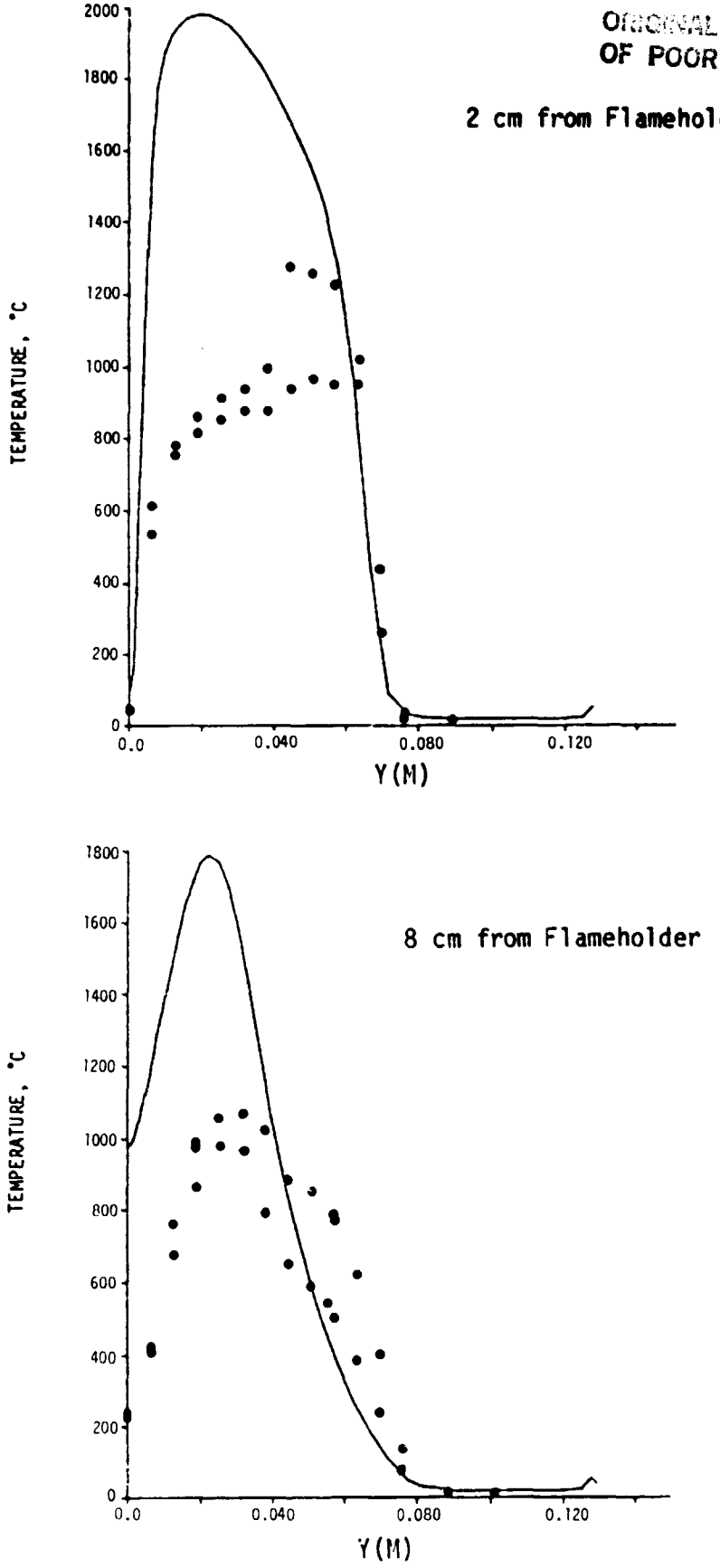

Figure 58 Radial Temperature Profiles for Test Case 9 (Roquemore et al) at A2P16 Conditions

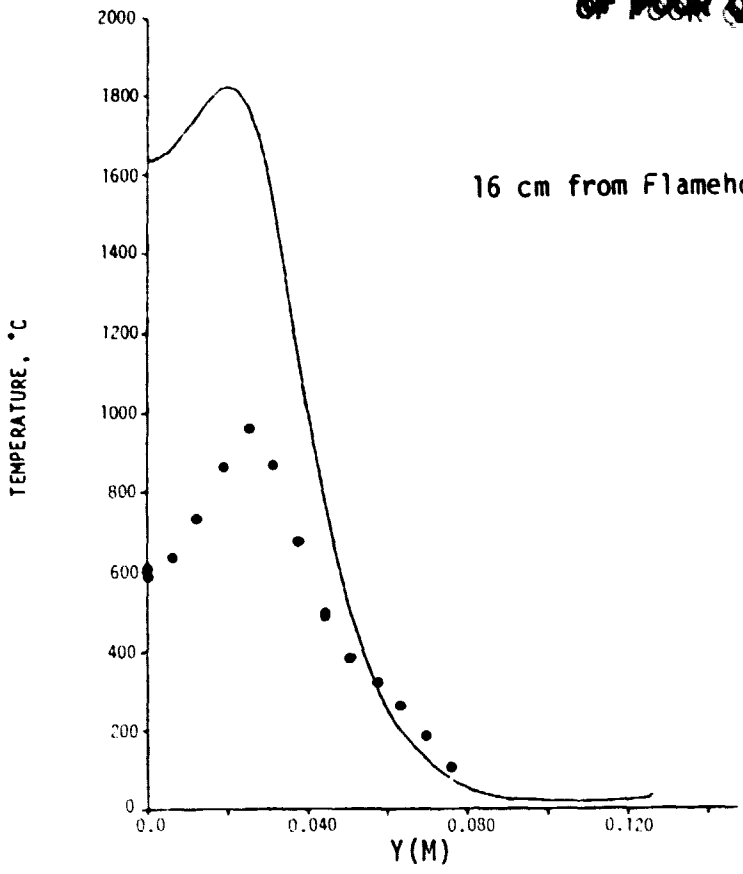

Figure 58 (continued)

In this particular experiment there is a source of uncertainty that can be associated with the temperature measurement itself. The overall equivalence ratio is extremely low, suggesting little carbon should be formed in the flame. At these flow conditions for distances from the flameholder greater than 8 cm ($x/d_f > 0.57$) the measured temperatures are less than 1200°K, see Figure 58. Very little luminosity is emitted from non-sooting flames by gases at temperatures of 1000°K and less. However, direct photographs of the flame have been taken, Reference 52. This implies the presence of temperatures higher than those actually measured and/or the presence of free carbon in the flame.

The flame has been shown to be nonstationary (Reference 53), with luminous ball-flames and alternating dark spaces in evidence to distances greater than x/d_f of 5. The presence of carbon particles, which give rise to the luminosity of the ball-flames when the overall equivalence ratio of the flow is so low, indicates that the fuel and air mixture in the balls, and hence the flame temperatures, are much higher than the average. The temperatures measured by the thermocouple with its relatively long response time (compared to the ball-flame frequency) are clearly average values for the ball-flames and the dark spaces between them.

The development of the ball-flames is described in References 95 and 96. A feel for what temperatures the ball-flames might represent can be obtained in crude fashion as given below for the furthest station from the flameholders for which data are available in the A2P16 case, i.e. x of 16 cm (x/d_f = 1.15). The 500 frame per second film clips given in References 52 and 95 suggest that the ball-flames are actually shed from the recirculation area at an x/df of about unity, and the calculations of wake development of Reference 96 are in reasonable agreement with this observation.

Using spectrophotometers, Roquemore et al (Reference 53) acquired time-resolved CH emission intensity records at a number of axial stations for operating conditions of 2 kg/s airflow and 18 kg/hr propane flow. At a downstream station of x/d_f equal to 2.86, where it was easy to distinguish distinct luminosity peaks on the traces presented in the reference, the flame was found to be present about 74 percent of the time. In Reference 100, for 2 kg/s airflow and 16 kg/hr propane flow, at this station a typical luminosity time history plot indicates the flame is present only about 40 percent of the time. While the percentage time that a flame exists at a location depends on both the axial location and the operating conditions, the values of 40 and 74 percent appear to represent reasonable possible lower and upper limits for the region of interest.

Through the use of conditional sampling (Reference 100), it was found that the most probable centerline mean axial velocity in nonluminous regions of the flow was 31.6 m/s at the stated operating conditions, while that in the luminous regions was 42 m/s. The value in the nonluminous regions was equal to that in the isothermal flow case at those operating conditions.

The information thus gleaned from References 53 and 100 can be used to obtain a crude estimate of the ball-flame temperature by weighting for the nonstationary nature of the flow. Thus,

$$\bar{T} = [\tau_f \bar{u}_f \bar{T}_f + (1-\tau_f)\ \bar{u}_{iso}\bar{T}_{iso}]/\bar{u} \pm \text{end error.} \qquad (71)$$

where,

$\bar{T}$ = averaged temperature read by long time constant thermocouples

τ_f = percent time a ball-flame is present

$\bar{u}_f$ = mean velocity of ball-flame

$\bar{T}_f$ = unknown ball-flame mean temperature

$\bar{u}_{iso}$ = mean velocity of nonluminous region

$\bar{T}_{iso}$ = mean temperature of nonluminous region

$\bar{u}$ = mean velocity of reacting flow obtained by unconditional sampling

In the present case $\bar{u}$ was 39 m/s, while $\bar{T}_{iso}$ was assumed equal to 293°K, the nonreacting flow condition.

The end error is used to match the radial profiles to the temperature outside the flame region. It arises because the weighting is not exact.

The expression for $\bar{T}$ was solved for $\bar{T}_f$ using the two values for τ_f, the measured velocities, and the assumed $\bar{T}_{iso}$. The corrected profiles were matched to a temperature of 293°K in the outer regions of the flow.

Figure 59 compares the measured data and the calculations for the axial station 16 cm from the flameholder with a possible band representing where the ball-flame temperatures might fall, depending on the actual intermittency of the flame. The figure indicates that if the flame were not intermittent, then reasonable agreement with predictions might be expected, subject to the uncertainties of the combustion model or the type of weighting used for the Reynolds equations.

Recent CARS measurements by Roquemore (Reference 101) indicate the ball-flames have temperatures of around 1900°K, while the dark spaces between have temperatures around 400°K. These measured temperatures agree well with the corrected data band shown in Figure 59.

The A2P4 case is far enough removed from the actual breakthrough point that a fair comparison of the calculations and measurements may be made. Figure 60 compares calculated and measured mean axial velocities along the combustor centerline. It shows that the right strength is calculated for the recirculation zone, but that the position of the fuel stagnation point is underestimated and that of the aft (air) stagnation point is overestimated. This is entirely consistent with the findings for isothermal conditions (Reference 32). (The measured velocities are for nonconditional sampling, but this appears appropriate within the recirculation zone.)

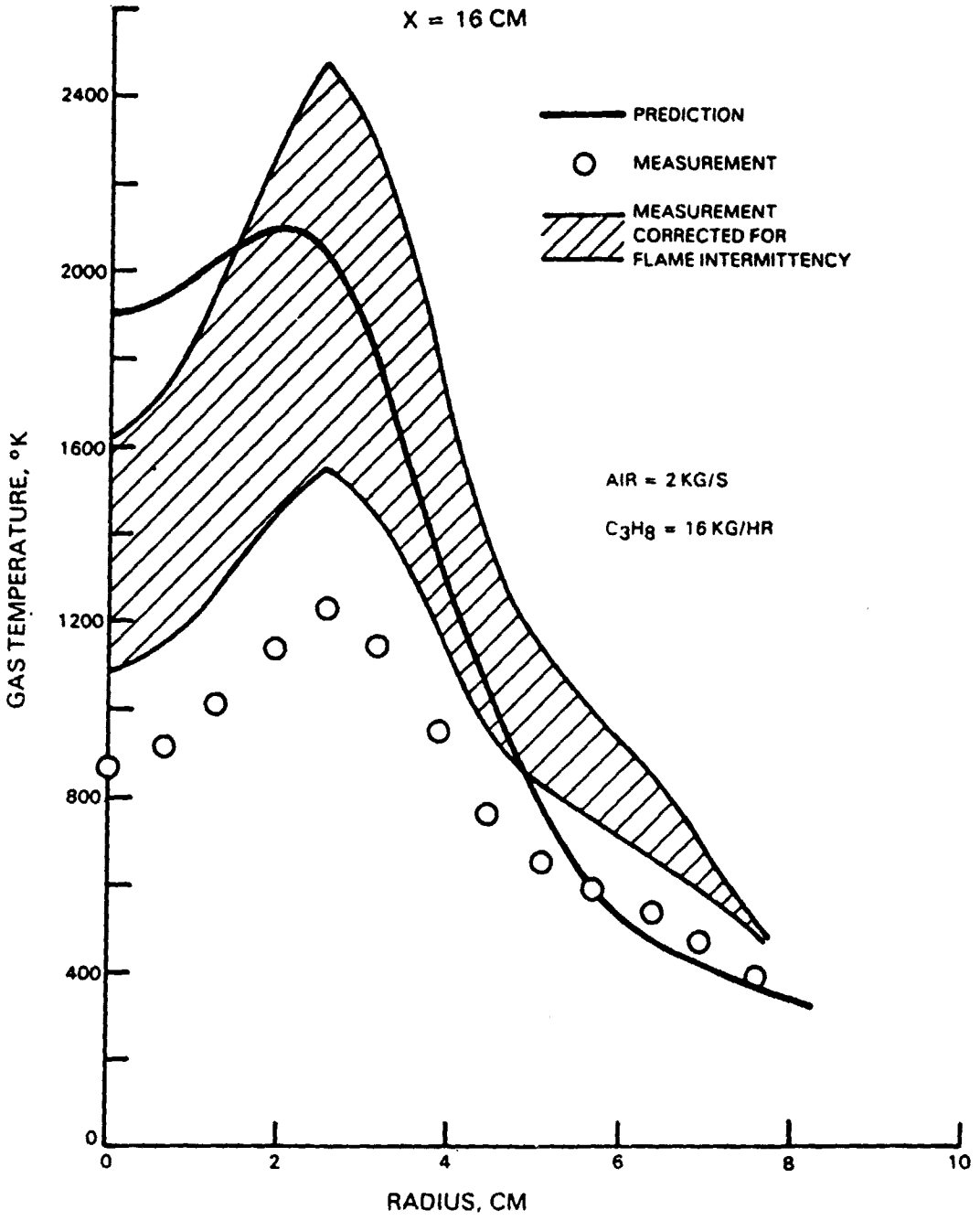

Figure 59 Correction of Measured Temperatures in Test Case 9 (Roquemore et al)

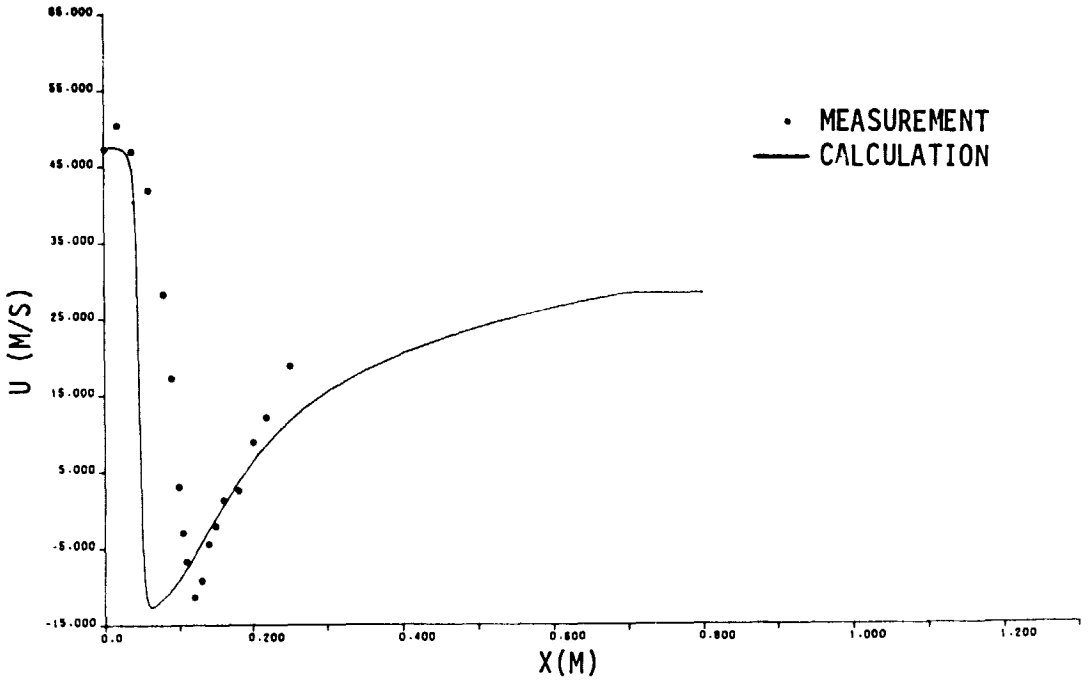

Figure 60 Centerline Axial Velocities for Test Case 9 (Roquemore et al) at A2P4 Conditions

The radial temperature profile comparisons at a number of axial stations for the A2P4 case are given in Figure 61. The respective levels of temperature should be viewed with reference to Figure 59, and only the characters of the calculated and measured flames considered at this point of understanding in the experiment.

It can be seen from Figure 61 that at all axial stations the overall width of the flame is correctly predicted, as is its character of off-axis burning initially. However, the calculated flame is burning much more rapidly than the measured flame. For example, at 6 cm downstream from the flameholder the peak temperature is calculated to be already on the centerline and maximum heat release is over, whereas the measurements show the flame still to be burning off-axis with higher temperatures than calculated. The radial width of the calculated major reaction zone is much narrower and the peak temperatures exist at smaller radii than the measurements show, at axial stations to 4 cm. At the 8 through 18 cm stations the measured temperatures are all greater than those calculated, showing that the actual reaction at these stations is less complete.

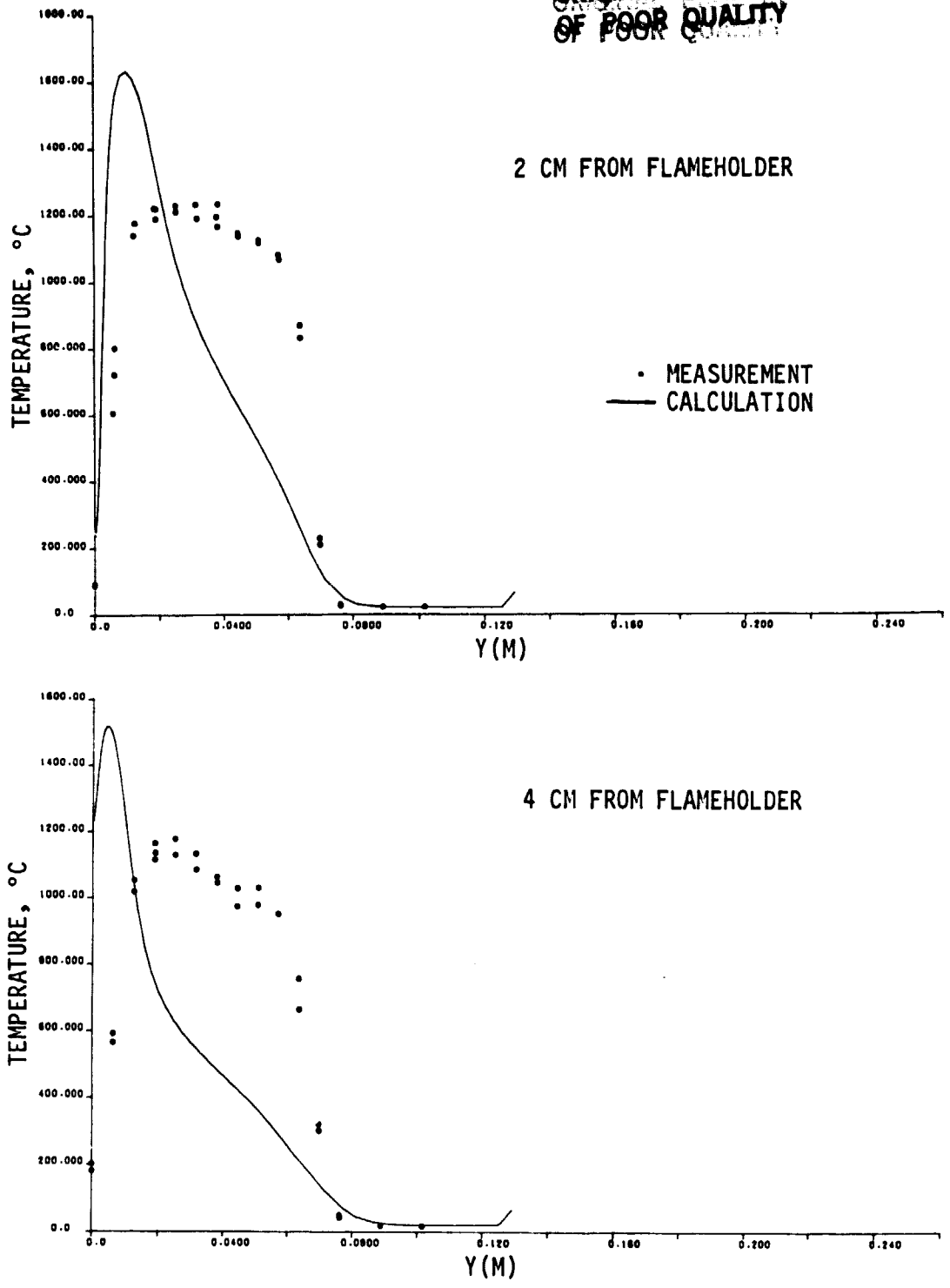

Figure 61 Radial Temperature Profiles for Test Case 9 (Roquemore et al) at A2P4 Conditions

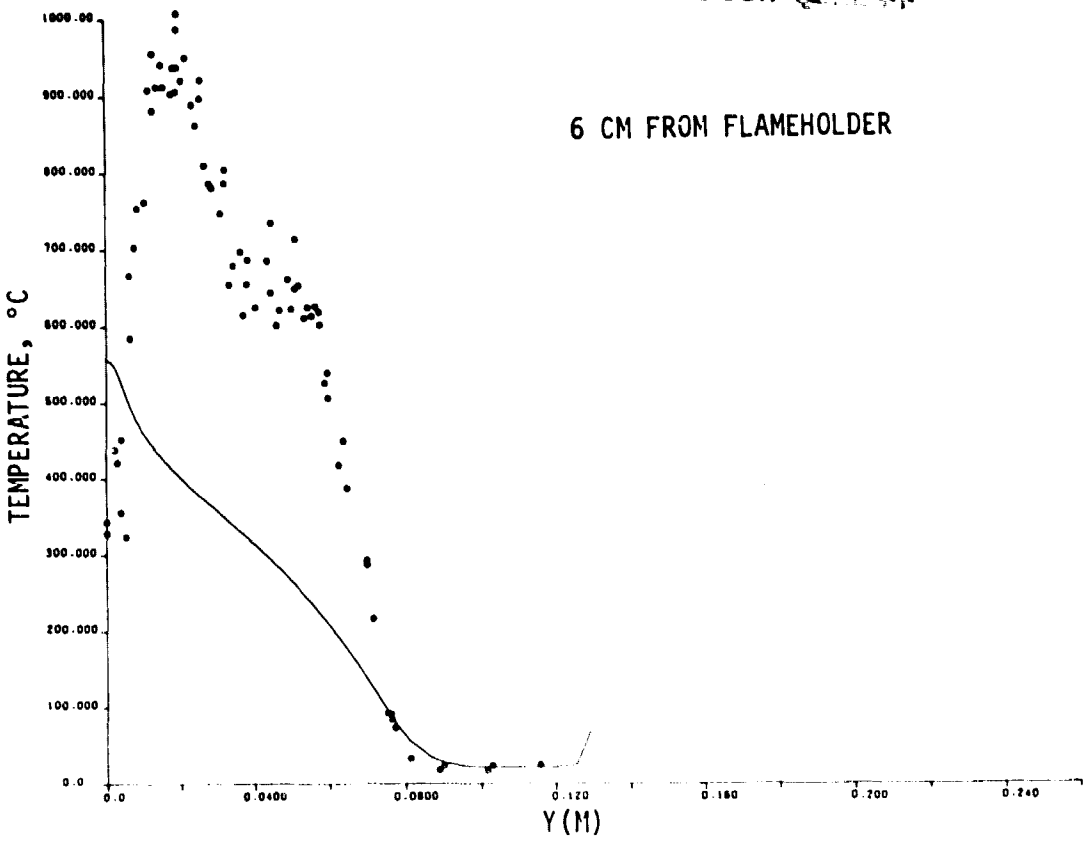

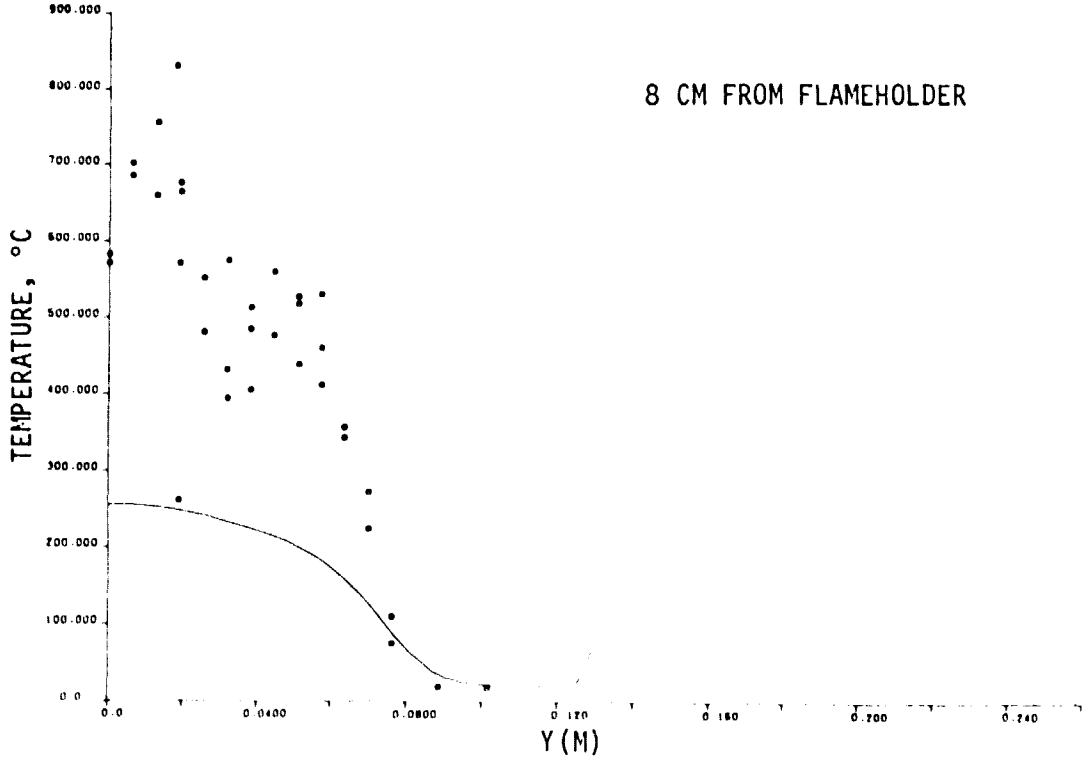

Figure 61 (continued)

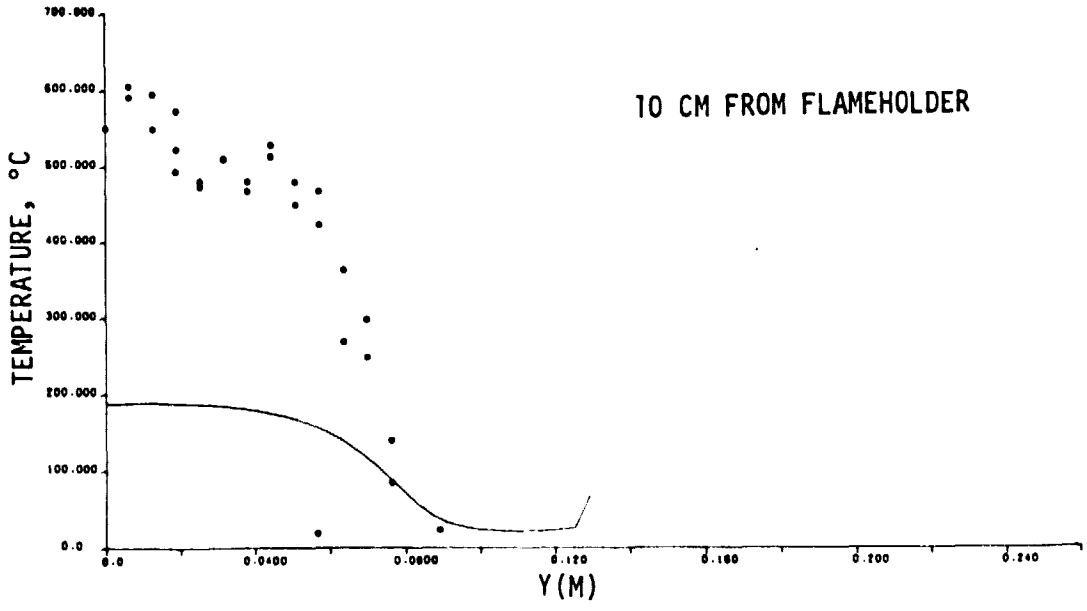

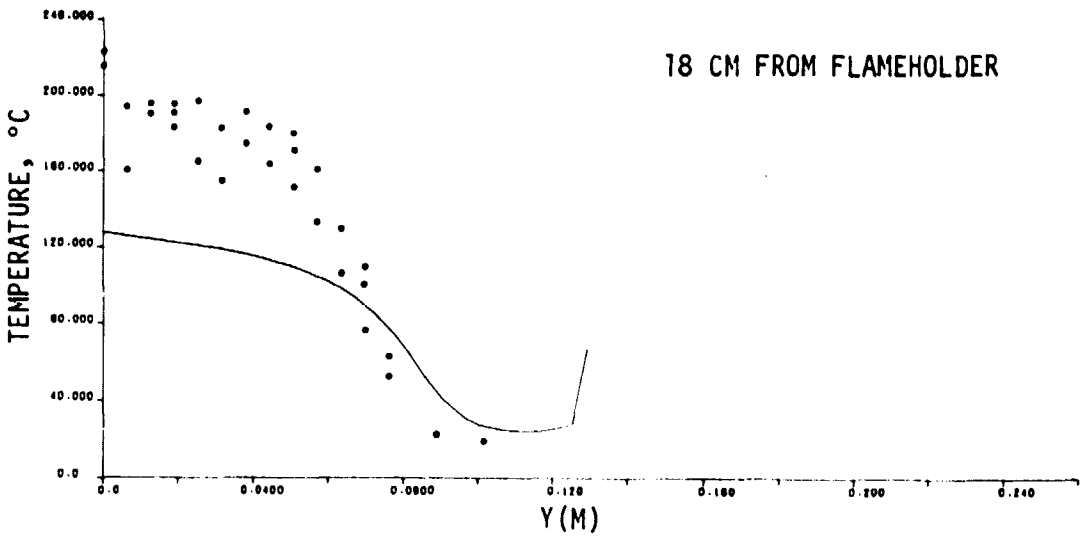

Figure 61 (continued)

8.2.6 Jets-In-Crossflow

This important class of flows was depicted by a series of experiments represented by Test Cases 6, 7 and 8, beginning with a single jet and progressively extending to multiple jet systems. Test Case 6 is a single jet in crossflow using the experiment of Crabb & Whitelaw; the experiments of Khan & Whitelaw are used for a row of jets in crossflow (Test Case 7) and for opposed rows of jets in crossflow (Test Case 8). The test configuration is essentially the same in all cases with just variation in the jet inlet ducting, and is illustrated for opposed jets in Figure 10.

The model exercised is the turbulence model, and the computer code is 3D-TEACH. In addition to the physical model performance in these flows, the effects of representation of circular jets in rectilinear form, and the behavior of the hybrid differencing in three-dimensions will be encountered. To save on grid lines, and hence on computer storage and calculation time, flow symmetry conditions were used wherever feasible.

For the single jet in crossflow, with a jet to cross-stream velocity ratio of 2.3, the calculations were performed for one-half of the jet and wind tunnel. The calculation domain extended 5 jet diameters upstream of the jet and 24 diameters downstream, for a total axial length of 30 diameters (76.2 cm); the half-width of the tunnel was 8.5 jet diameters (21.6 cm), while its height was 11.8 diameters (30 cm). The jet had a diameter of 2.54 cm.

A 35 x 18 x 16 grid was used. Care was taken to obtain a suitable match of the grid lines representing the orifice supplying the jet and the grid lines in the wind tunnel. The orifice was defined by 5 axial and 10 transverse grid lines. Originally, these were distributed uniformly. Although the grid lines themselves were uniformly distributed in the complete grid the relative displacement of vector and scalar fluid cells resulted in a nonuniform distribution of cells. This caused a convergence problem in the calculation. The number of grid lines within the jet initial plane was maintained, but their distribution was adjusted to give a uniform distribution of cells within the calculation domain. The calculation grid is shown in Figure 62.

The boundary conditions were a combination of measured inlet conditions and assumptions (Reference 102). The wind tunnel velocity was 12 m/s with a turbulence intensity of 0.55 percent, both assumed uniform. The length scale was taken as 3 percent of the tunnel hydraulic diameter. For the entering jet, the length scale was taken as 3 percent of the real jet hydraulic diameter. Turbulence intensity was taken to be the same as that assumed by Crabb, i.e.,

$$3/2 \left(\frac{u'_{rms}}{\bar{u}}\right)^2 \bar{u}^2 = 0.02$$

A measured $\bar{v}$-velocity profile was available for the jet, and this was applied to the modeled jet symmetrically.

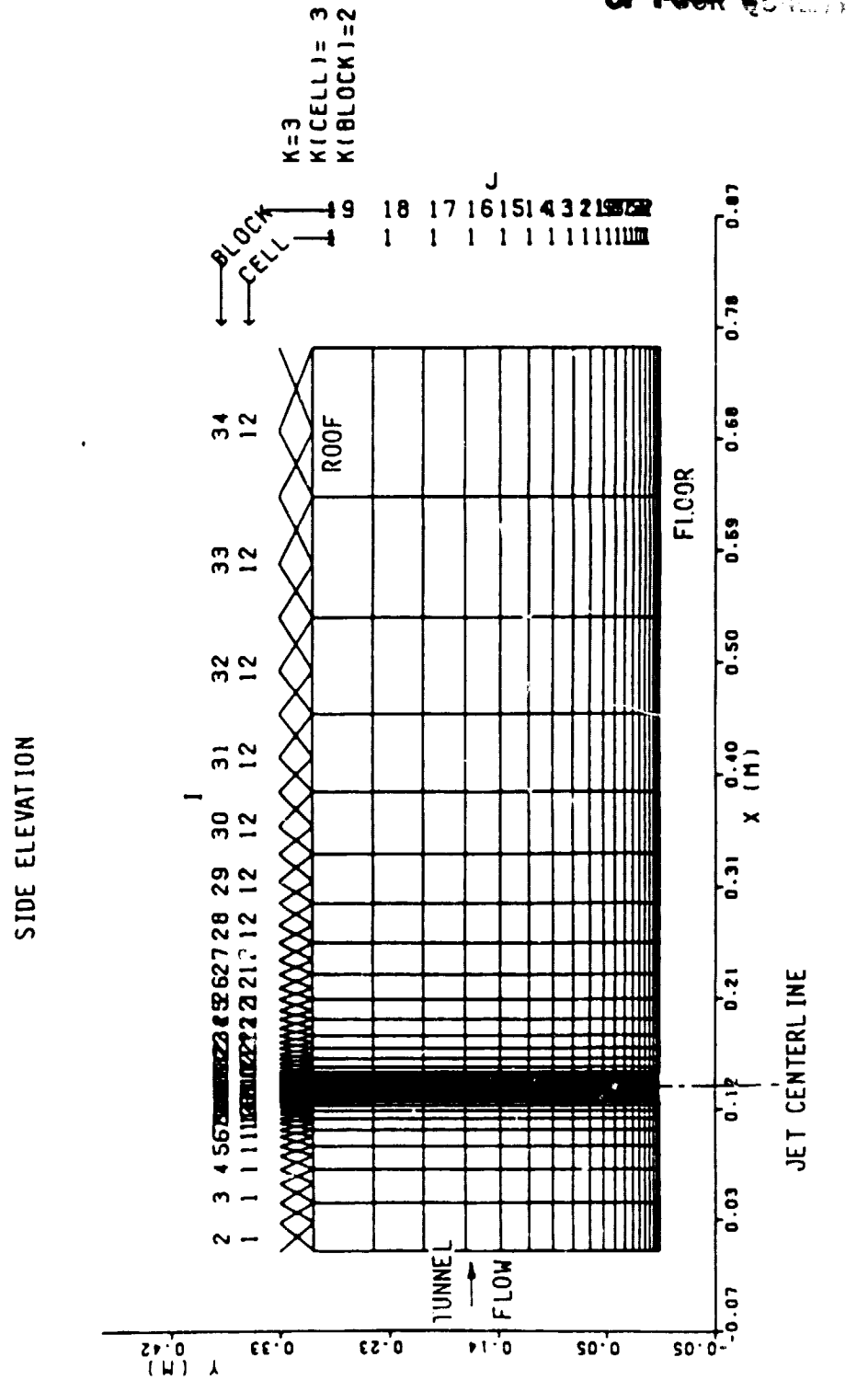

Figure 62 Grid for Single Jet in Crossflow, Test Case 6, (Crabb & Whitelaw)

ORIGINAL PAGE IS
OF POOR QUALITY

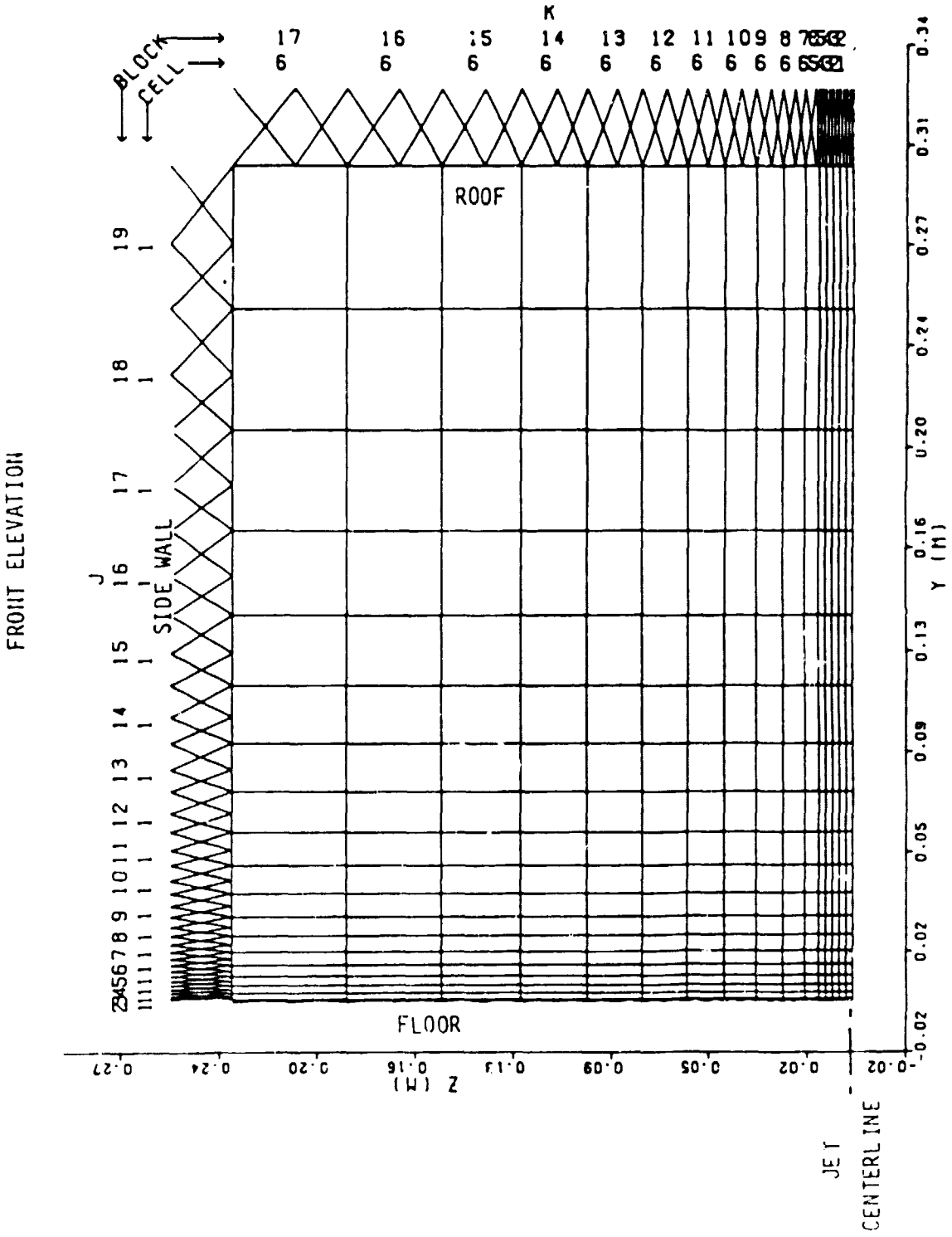

Figure 62 (continued)

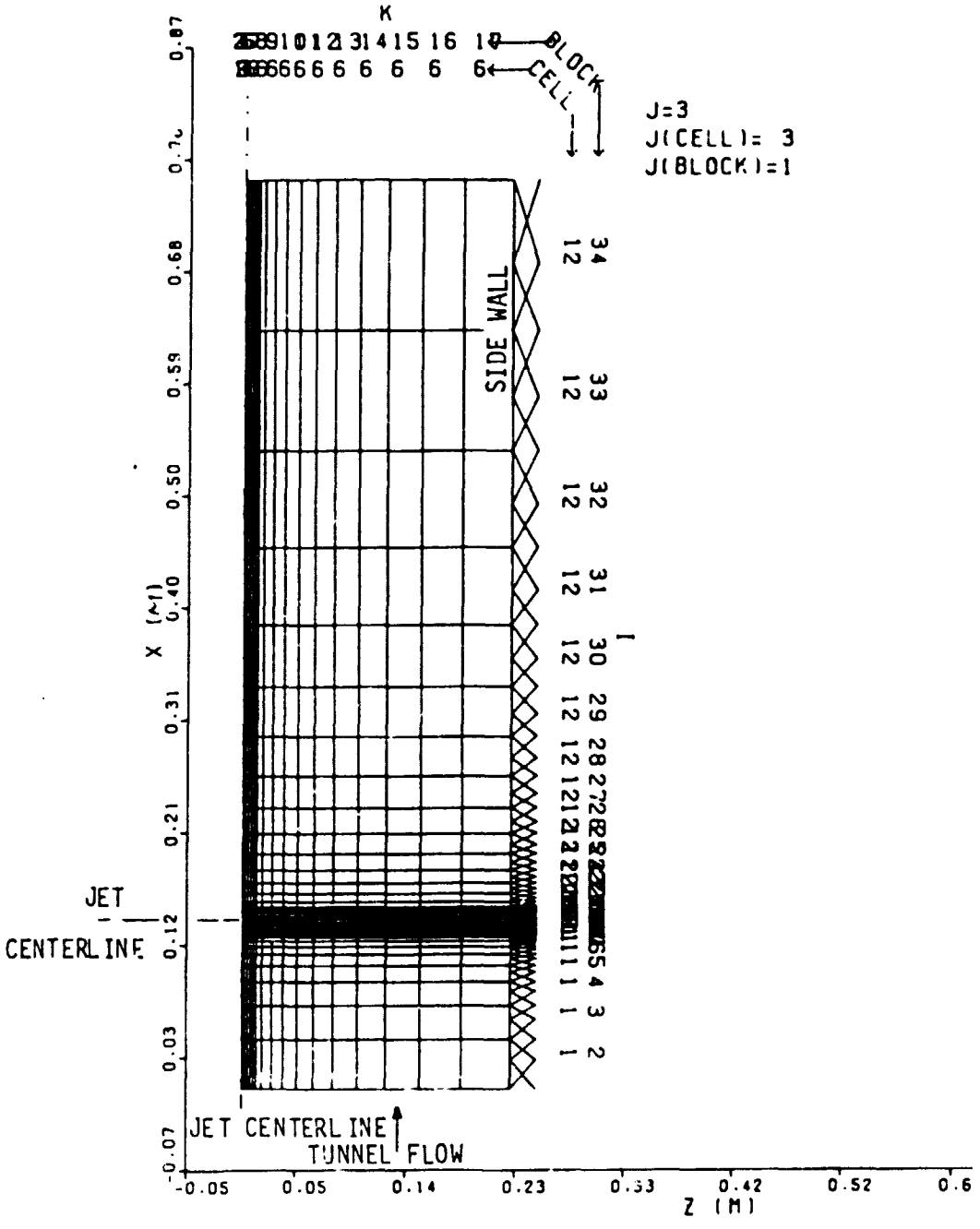

Figure 62 (continued)

The representation of the jet origin by a symmetrical stairstep pattern results in a jet cross sectional area that is 3.34 percent smaller than the actual area, and a modeled jet circumference that is 21.5 percent greater than the actual circumference. The hydraulic diameter of the modeled jet is therefore only 80 percent (2.02 cm) of the real jet (2.54 cm).

The calculations were made with the symmetrical inlet velocity profile for the jet measured by Crabb with zero crosswind. With the stairstep representation of the cross section and the fluid block representation of the inlet profiles, the modeled jet has a momentum ratio that is 3.6 percent less than the real jet; the modeled mass flow rate is 4.5 percent less. The initial blockage due to the modeled jet is that of the real jet (width equal to jet diameter).

The combination of the reduced momentum ratio for the modeled jet and reduced effective diameter, together with the increased initial surface area, would be expected to result in a reduced penetration compared to the real jet. The extent to which the jet mixes with the crosswind would be expected to increase as a result of the increased surface area. The numerical diffusion that results from the grid limitations is additive to these physical effects. Therefore, the calculations could be expected to be seriously in error when compared to measurements, irrespective of any deficiencies associated with the physical modeling embodied in the code.

The mass deficiency of the modeled jet compared to the real jet was corrected using the variable density capability of 3D-TEACH so that jet initial density was increased to achieve the true mass flow rate. The jet temperature was lowered accordingly. With this change the ratio of modeled to actual jet mass flow rates was 0.993, which was considered adequate. The effect of the artificial temperature change on jet penetration, development and mixing was considered to be negligible.

To better understand the development of the jet flow visualization is used. The visualization method used is streaklines: the simulation is based on the water-tunnel visualization technique, where the illuminated plane has finite thickness, although it is not large. It must be remembered, therefore, that the streakline plots in the figures are projections of a three-dimensional track onto a two-dimensional plane.

The x-station referred to is referenced to the beginning of the calculation domain: To compare with the calculations of Reference 102 for example, subtract 0.1397 m from the present x-values to line up with the jet origin centerline.

Figure 63 shows the axial development on the centerline of the jet. It can be seen that the flow is highly three-dimensional behind the jet at all axial stations downstream from the hole edge. Figure 64, at the (side) edge of the jet ($z = 0.01$ m) shows that the mainstream flows around the jet into the wake region. This crossflow is evident at a Z/D of 1, i.e., half a jet diameter beyond the edge of the hole ($z = 0.025$m) and at a height of half a jet diameter off the tunnel floor, Figure 65.

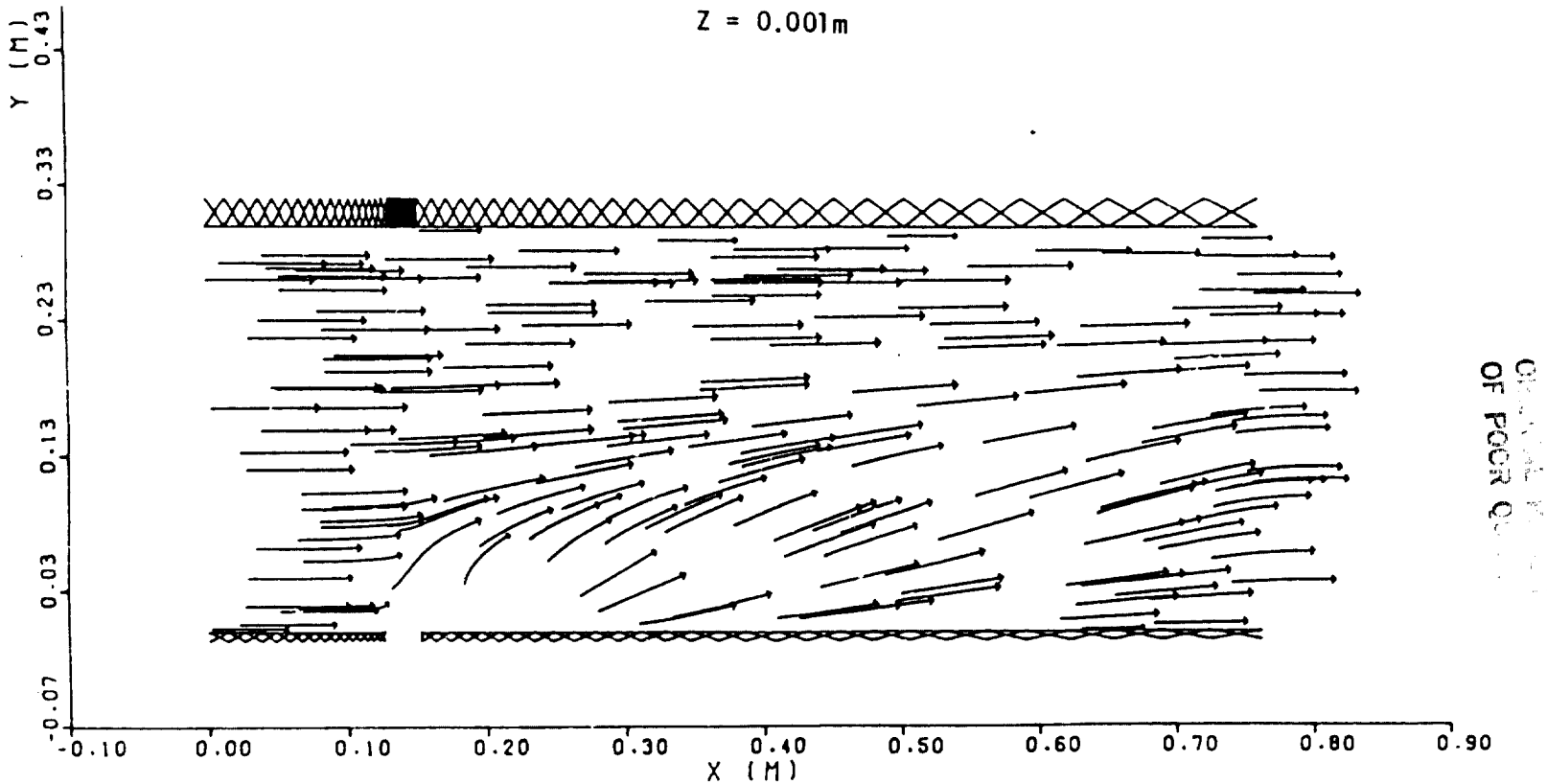

Figure 63 Flow Visualization of Single Jet in Crossflow, Test Case 6, (Crabb & Whitelaw) Using Streaklines - Axial Development on Jet Centerline

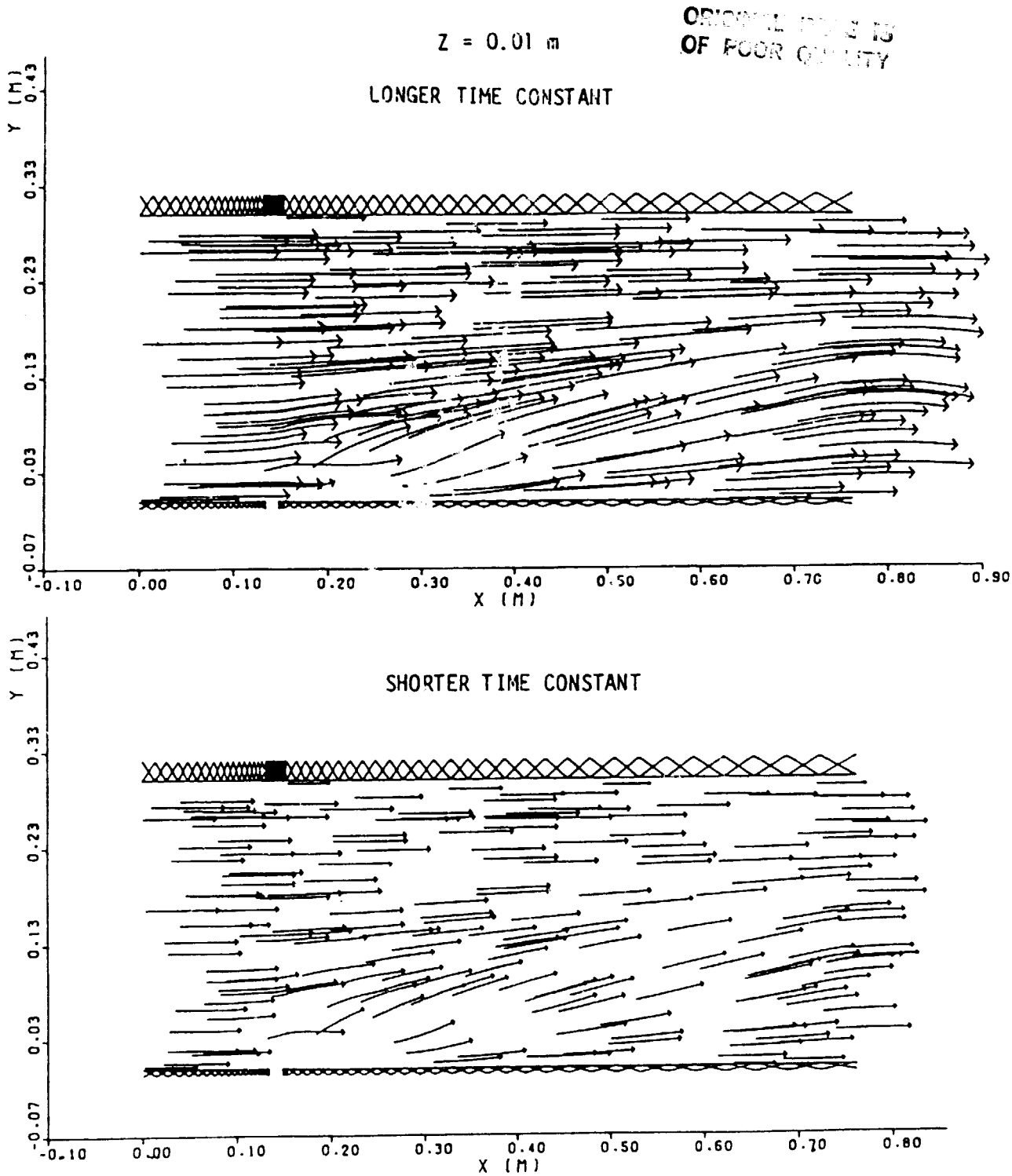

Figure 64 Single Jet in Crossflow - Flow Around Edge of Jet Into Wake Region

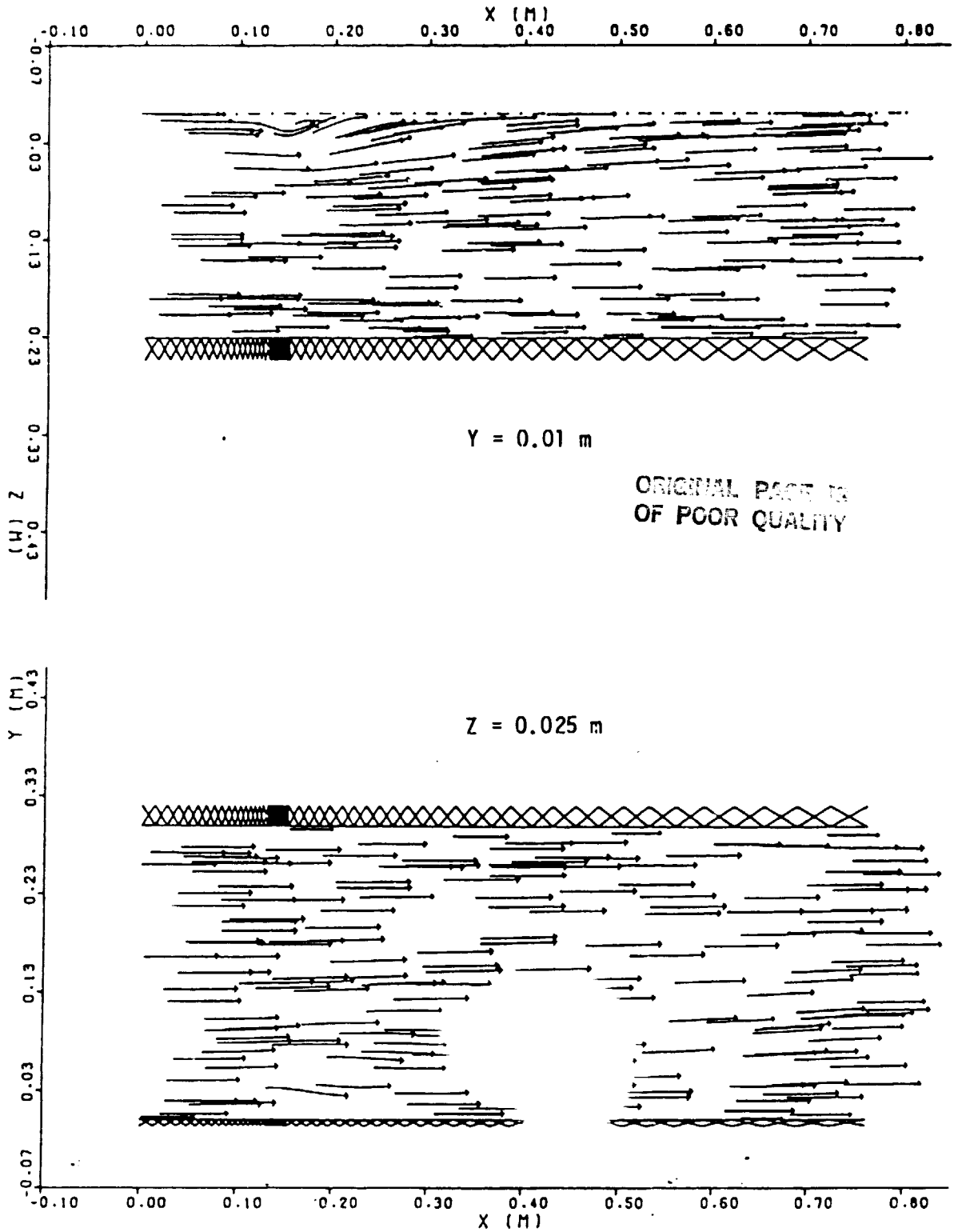

Figure 65 Single Jet in Crossflow - Flow Into Wake Region Away From Jet Origin

The cross-sectional development of the jet is illustrated in Figures 66, 67 and 68.

Figure 66 is for a station at x of 0.1m, or about 1.5 jet initial diameters upstream of the jet origin centerline; see Figure 63 for orientation. Two important features are apparent: circulation is developing upstream of the jet and, evidence of a bow wave can be seen developing.

Figure 67 illustrates the vortex development in the jet cross-section at a station of 0.2m. In this case, only a single vortex pair is visible (calculation is symmetrical about the jet centerline). It is not known whether the grid is inadequate to resolve the second pair of vortices or if they are physically absorbed into the main vortex pair in this case. The low initial jet penetration suggests that the latter explanation might be so, although a (rather unrealistic looking) additional vortex pair was calculated by Claus (Reference 102) for this experiment using a finer grid. If the calculations for this station are compared with those in Reference 102, the closest common station is that given for Figure 3c of the reference (x of 0.1746 m in the present coordinates). The comparison would be of streaklines in Figure 67 to velocity vectors in the reference.

Jet penetration and spreading can be seen by comparing Figure 67 to Figure 68 which is at a station of 0.5 m from the origin of the calculation. The centers of the vortex pair have moved upwards and transversely outwards.

Figure 69 presents profiles of mean axial velocity, normal to the wind tunnel flow and in the plane of the jet centerline. The profiles are at a number of streamwise positions. Velocity is nondimensionalized by the undisturbed cross-stream velocity, and distance by jet initial diameter.

At an x/D of negative unity, the point of inflection in the calculated profiles is noteworthy. It could represent the influence of the horseshoe vortex referred to above. The measured approach profile appears to be fairly well-represented by the calculations. On the jet vertical centerline (x/D equal to zero), there appears to be disagreement between the calculations and the measurements. If real, this could be due to the distortion of the jet velocity profile inside the supply pipe by the crosswind. This condition was not featured in these calculations due to lack of representative boundary conditions.

Immediately downstream of the jet origin things are changing rapidly. At an x/D of unity the calculations show a recirculation at the wall, while the measurements show a positive velocity adjacent to the wall. A positive velocity immediately behind the jet could be generated through crossflow from the horseshoe vortex. If so, the grid used in the calculations is not fine enough to resolve this feature. At subsequent downstream stations, x/D from 2.0 to 14, the wake region appears to be effectively captured by the calculations. However, the rapid mixing postulated for the calculations would result in rapid dissipation of the excess axial velocity of the jet over that of the crosswind. The calculations do yield this result, whereas the excess velocity persists in the measurements to at least x/D of 14.

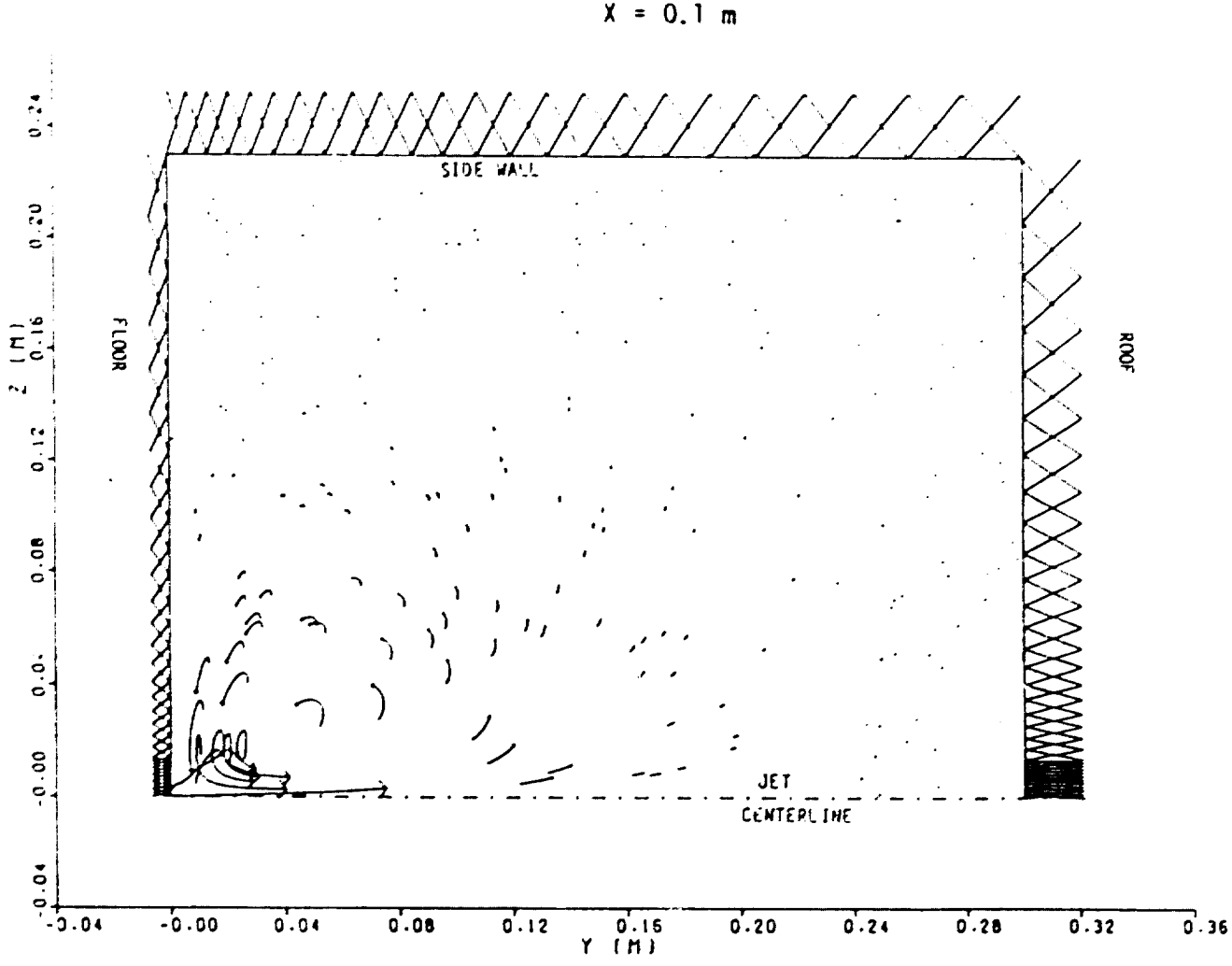

Figure 66 Single Jet in Crossflow - Development of Circulation Ahead of Jet and Formation of Bow Vortex

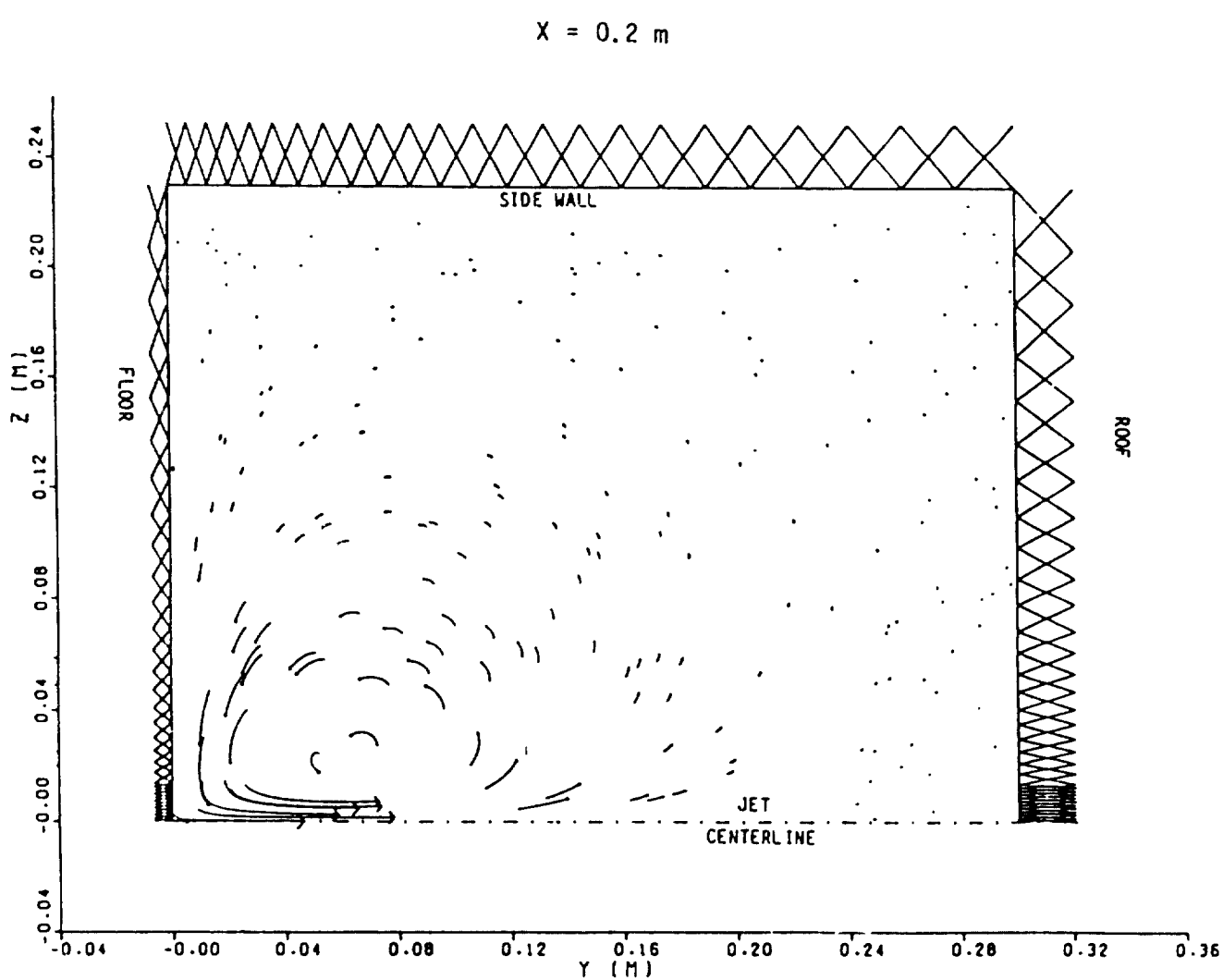

Figure 67 Single Jet in Crossflow - Development of Double Vortex Just Downstream of Jet Origin (Calculation Symmetrical About Centerline)

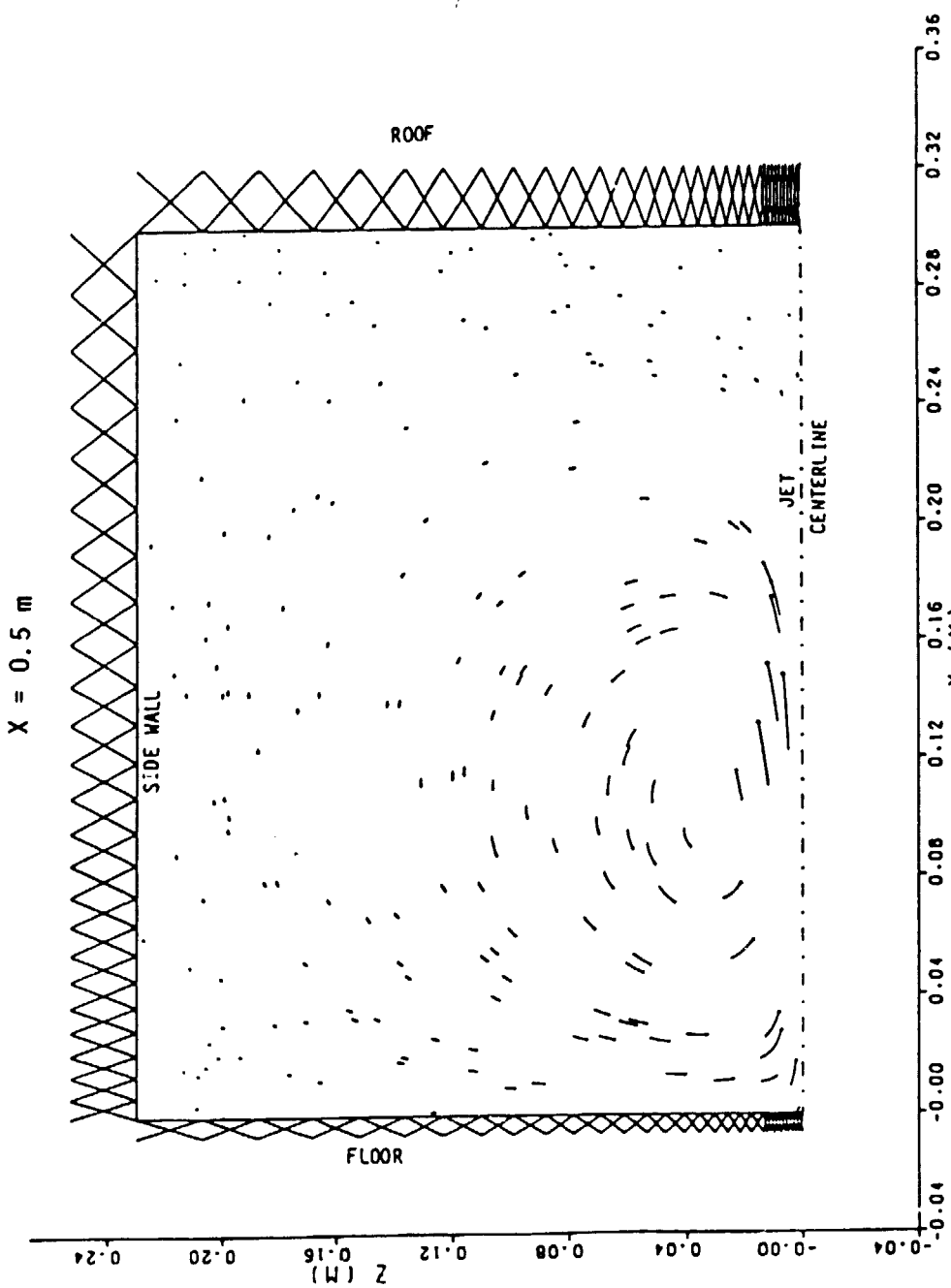

Figure 68 Single Jet in Crossflow - Jet Penetration and Transverse Spreading Through Movement of Vortex Centers

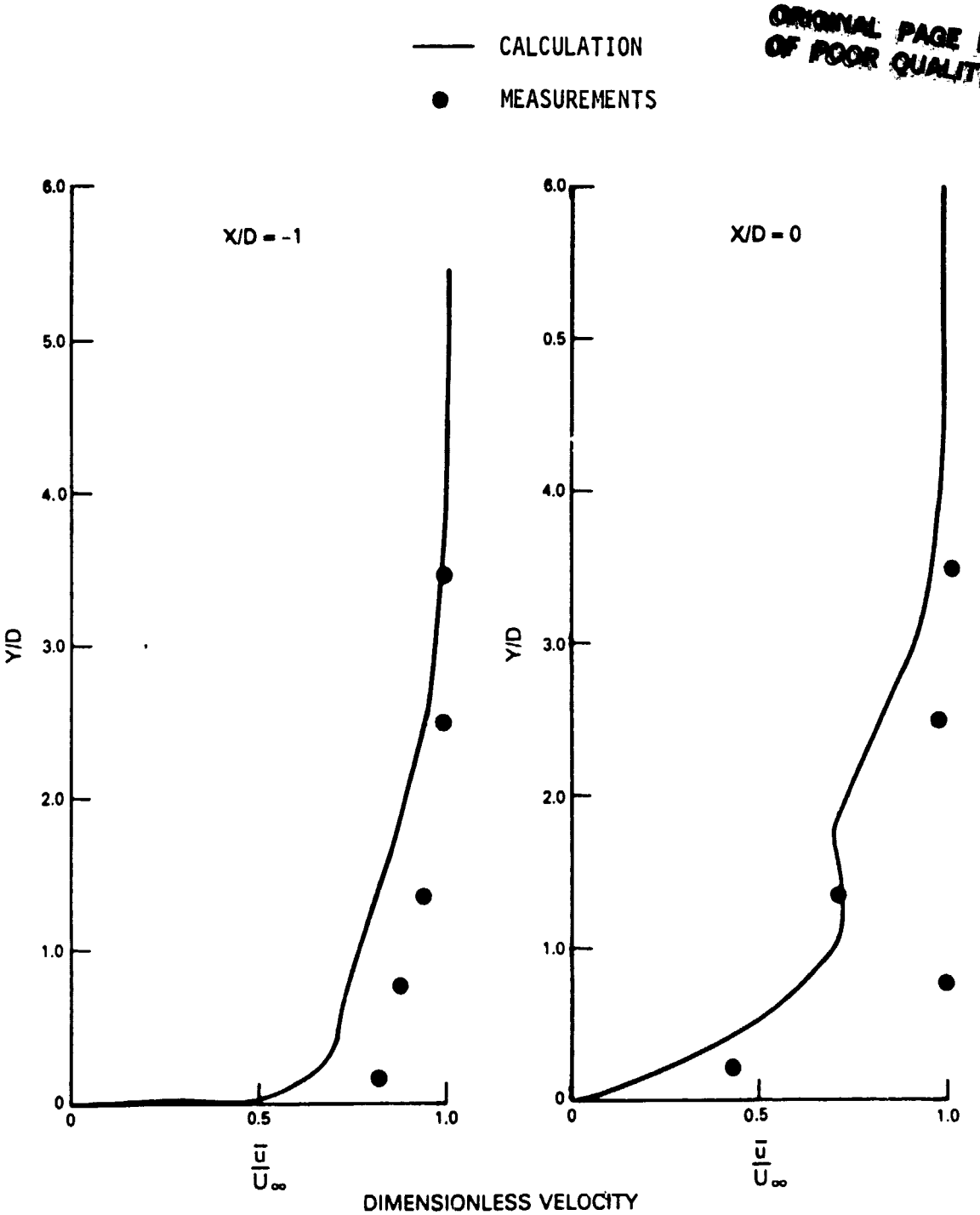

Figure 69 Single Jet in Crossflow Profiles of Mean Axial Velocity on Jet Centerline at a Number of Axial Positions

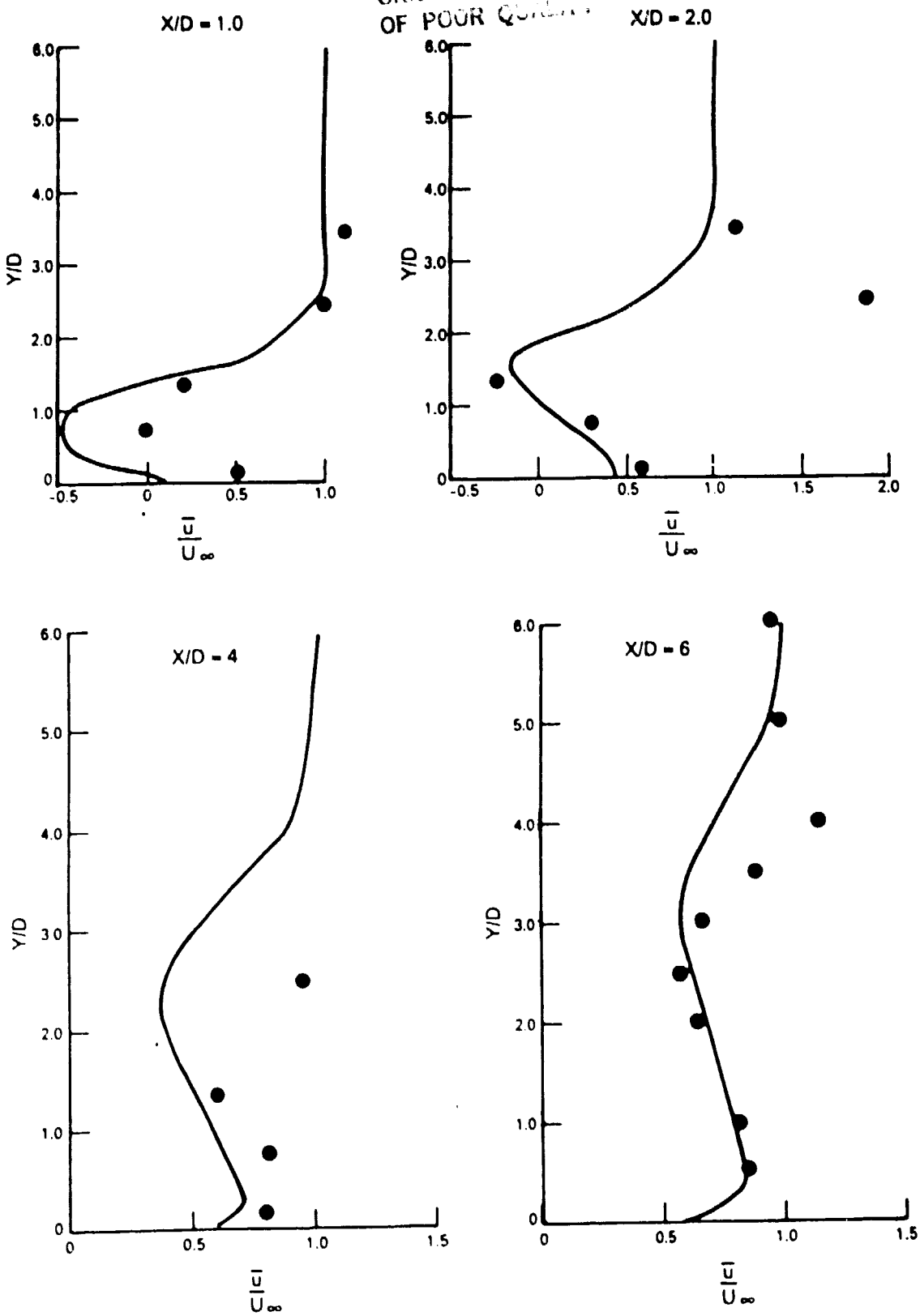

Figure 69 (continued)

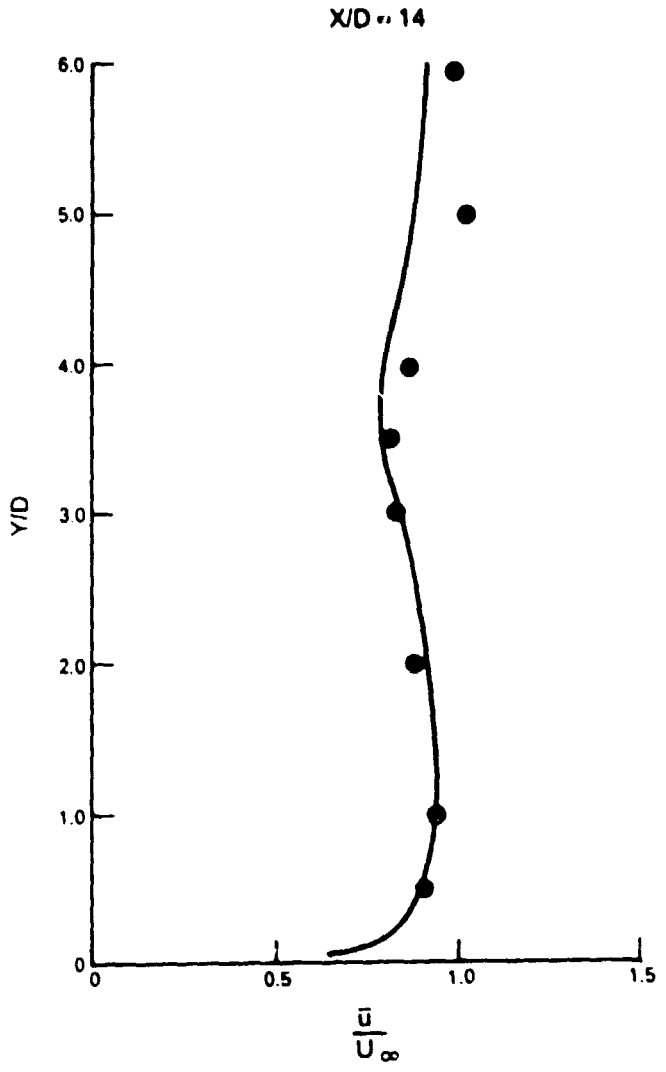

Figure 69 (continued)

Loss of the excess velocity makes it impossible to discern the jet trajectory from the calculations. Claus (Reference 102) required a 40 x 30 x 20 grid to capture the excess velocity.

Figure 70 shows isovels at a station x/D of 8 and compares the calculations against the measurements taken from Reference 41. The calculated isovels for y/D greater than 6 are speculative since the grid is too sparse in this area for good definition. In Figure 71 the present calculations are compared with those of Crabb.

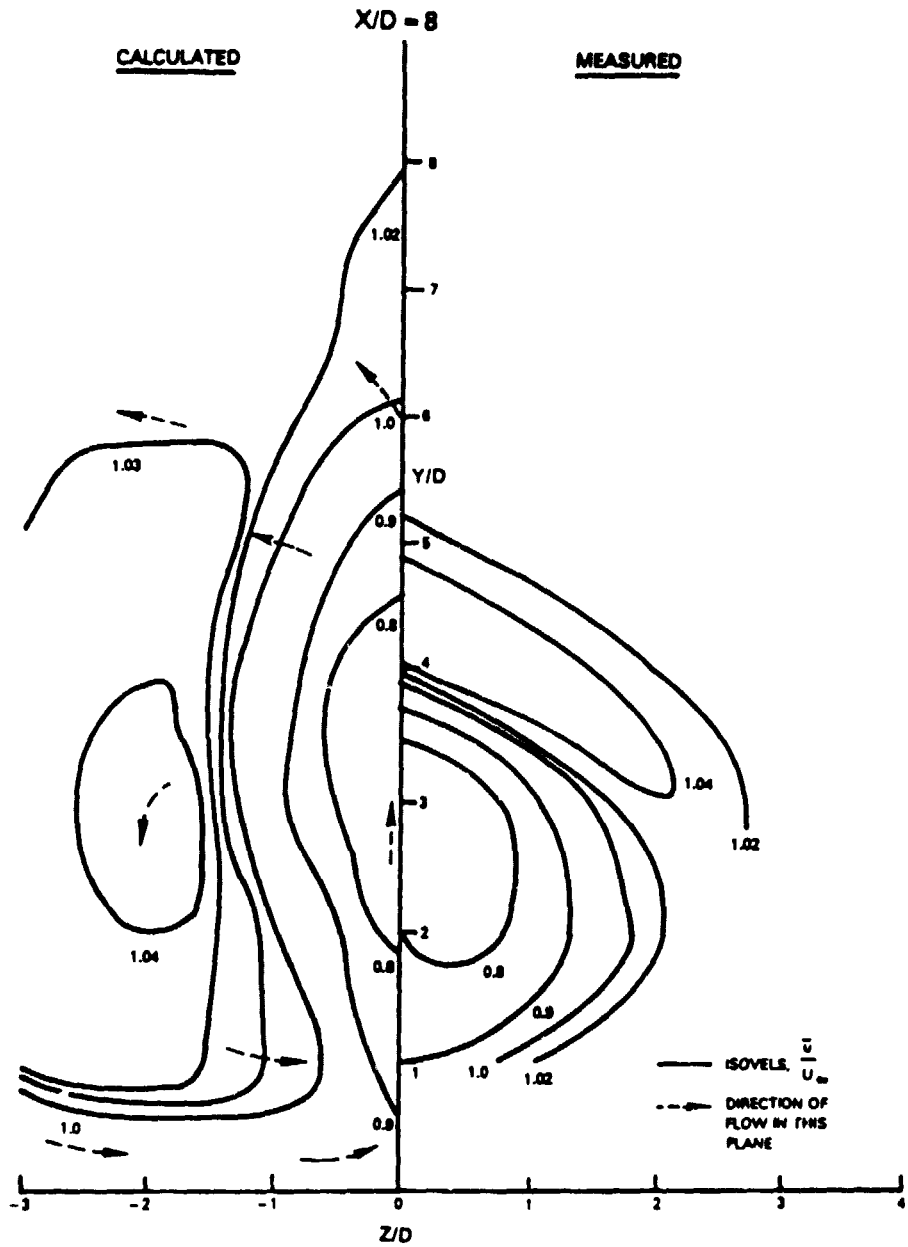

Figure 70 Single Jet in Crossflow - Comparison of Calculated and Measured Isovels of Mean Axial Velocity

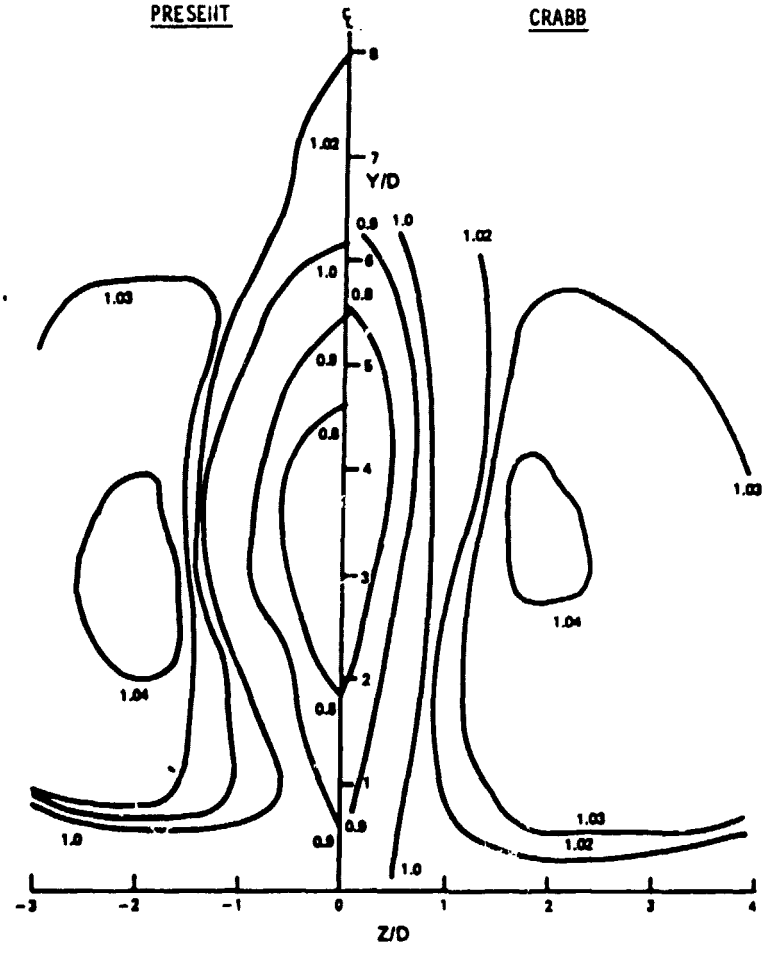

Figure 71 Single Jet in Crossflow - Comparison of Crabb and Present Isovel Calculations of Mean Axial Velocity in Y - Z Plane at x/D of 8

The nature of the present calculations is in close agreement with Crabb's calculations. Crabb used a 22 x 12 x 12 grid with the jet origin represented by 6 x 6 nodes. Consideration of Figure 68 helps in understanding Figure 70; some direction of flow arrows from streaklines have been sketched on Figure 70 from the earlier figure. The calculated vortex pair (symmetrical about the jet centerline) consists of a central region of low axial velocity with a pair of "wings" of high axial velocity wrapped around two-thirds of its circumference.

Figure 70 shows that the calculated jet development is much advanced over the measured development. The central region of low axial velocity is much more diffuse radially and the wrap-around of the high axial velocity "wings" is greater, with the 1.04 $\bar{u}/U_\infty$ isovel divided into two separate islands on either side of the centerline. These results are consistent with the expectations from the present modeling of the jet and the limited calculation grid used. It is most unlikely that a grid independent solution was obtained.

Shown in Figure 72 is a cross-sectional comparison at an x/D equal to 8 of measured and calculated concentration contours of a helium trace gas introduced into the jet. The mass fraction calculations were made with a turbulent Schmidt number of 0.5.

The calculated jet can be seen to be penetrating into the crossflow much more than the measured jet. The vertical spreading of the jet is about the same as measured (despite the increased penetration); the transverse spreading however, is somewhat less than measured, although the calculated 0.2 mass fraction contour has already split into two separate closed lobes. This is consistent with the jet development presented in Figure 70.

The present calculation of concentrations gives results that are comparable to the computations of Claus (Reference 102) using a 20 x 20 x 12 grid. In the plot of Reference 102 the calculated contour for 0.2 mass fraction of helium was a single closed contour, and not the double closed contour seen in Figure 72.

To calculate the row of jets in crossflow extensive use was to be made of the symmetry boundary condition. The symmetry boundary condition can be applied in three basic ways to a row of jets: planes of symmetry placed midway between jets on either side of a jet, planes of symmetry placed through the centers of an adjacent pair of jets, and, one plane of symmetry placed through a jet with another plane placed midway between a pair of jets. For a fixed number of grid nodes the latter configuration permits greatest definition of the flow field.

It was checked that all the symmetry conditions gave the same result. Therefore, the most efficient symmetry arrangement can be used without problems. This permits maximum jet definition to be achieved for a fixed nodal array. Figure 73 shows the symmetry condition used.

X/D = 8

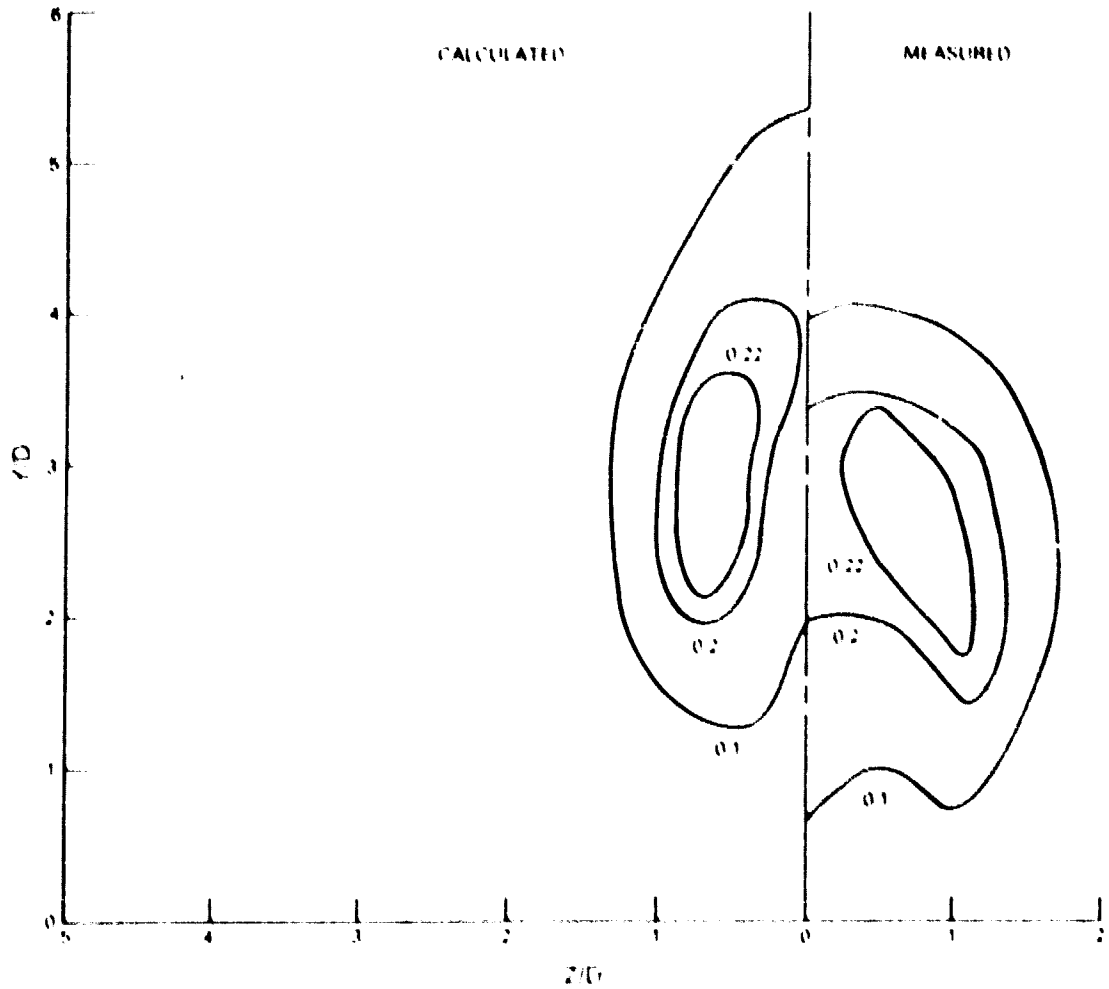

Figure 7. Single Jet in Crossflow - Comparison of Calculated and Measured Concentration Contours

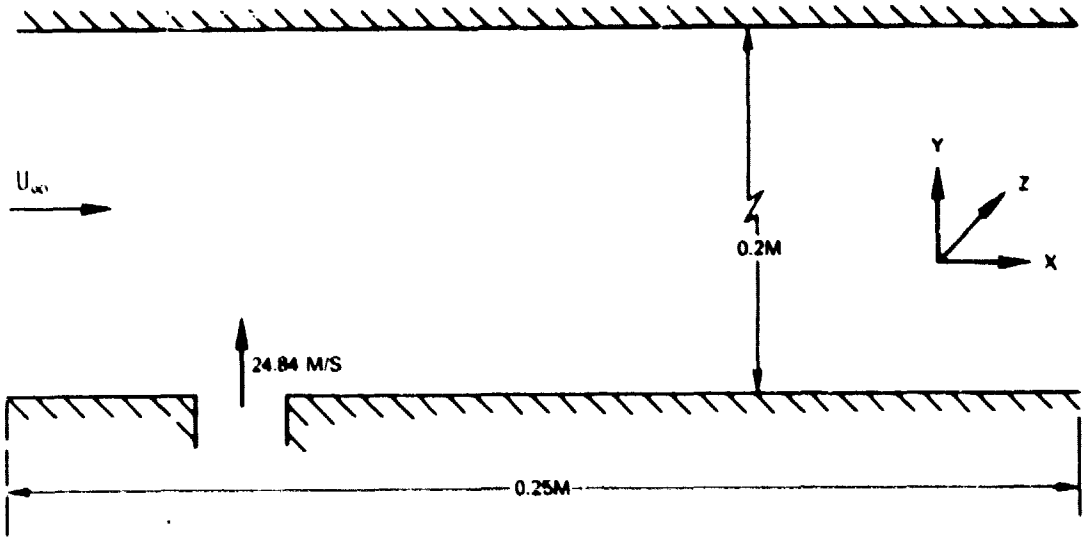

SIDE ELEVATION OF TEST CASE

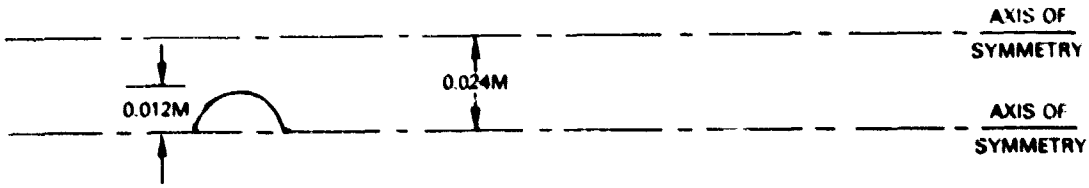

PLAN

Figure 73 Line of Jets in a Crossflow - Planes of Symmetry Used in the Calculation (Test Case 7 - Khan & Whitelaw)

The test case flow field was calculated for jets with a pitch to diameter ratio of 2 and a tunnel height to diameter ratio of 4. The jets had a diameter of 2.54 cm and the tunnel had a width of 30 cm. There were 5 holes distributed uniformly across the tunnel width. The cross-wind velocity was 10.8 m/s. The calculations were made with a 34 x 19 x 11 grid, and were started upstream of the line of jets. The hole was represented by 10 x 5 grid lines as before.

Figure 74 presents normal profiles of dimensionless mean axial velocities at a number of downstream positions both in line with a jet and midway between a pair of jets.

P/D = 2 : H/D = 4

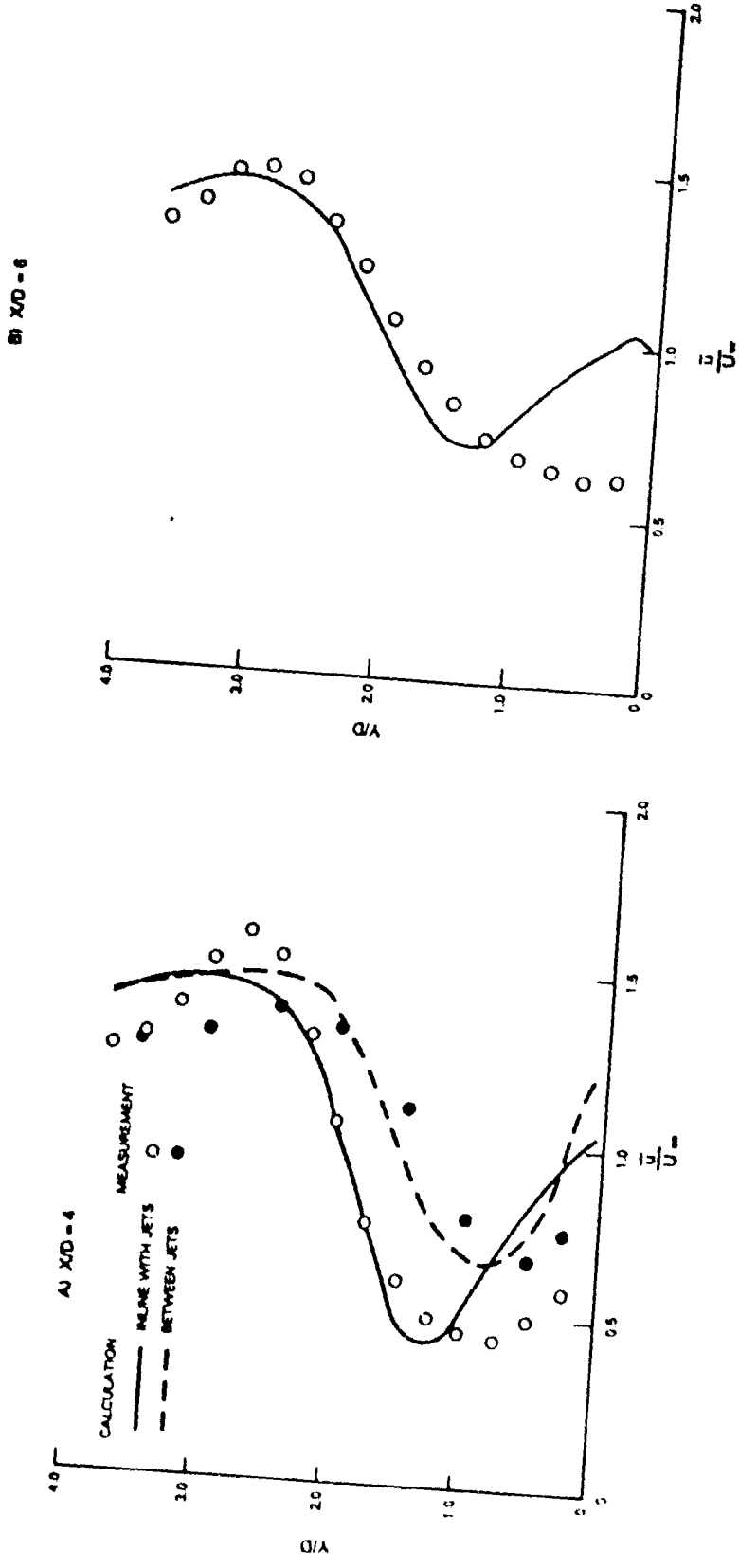

Figure 74 Test Case 7 (Khan & Whitelaw) - Mean Axial Velocities in Line With and Between Jets for Line of Jets in Crossflow

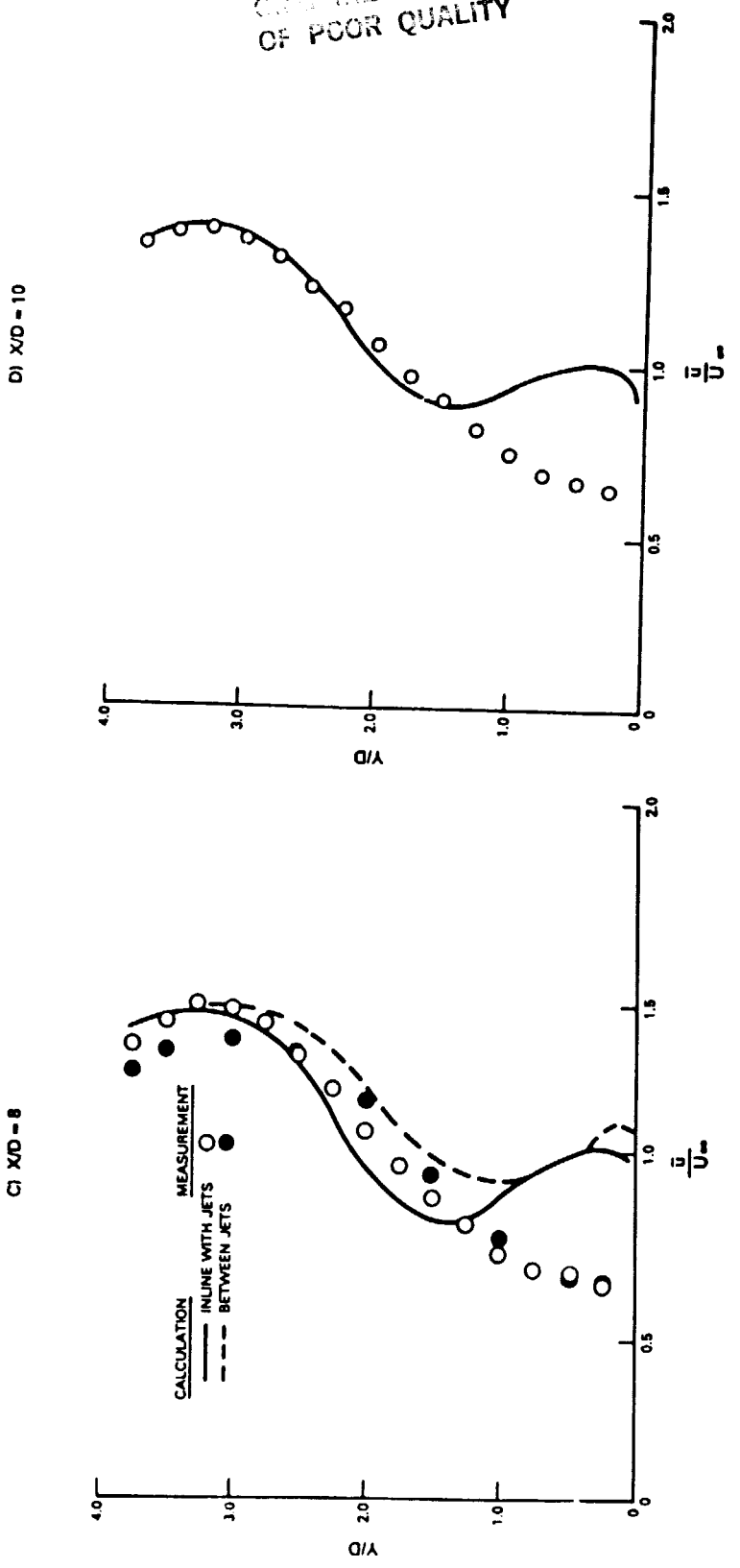

Figure 74 (continued)

The results are simultaneously encouraging and discouraging. They are encouraging because they are better representations of the measured data than the calculations of Khan (Reference 42) and because the profiles for X/D of 4 to 10, both in line and between jets, agree quantitatively well with measurement for Y/D $\geq$ 1.5. They are discouraging because the inner regions of the profile for Y/D $\leq$ 1.5 for X/D > 4 are not qualitatively correct.

Detailed consideration of the profiles reveals that close to the tunnel floor, both in line with and between jets, the calculated flow is accelerated with respect to the cross-wind velocity, and that the flow is not decelerated with increasing downstream distance as fast as in the experiment. Deceleration in this inner region is calculated to take place, but for X/D greater than 10.

The mechanism for acceleration of flow near the tunnel floor appears to be the flow blockage offered to the mainstream by the jet's penetration and lateral spreading which drives the cross-wind toward the wall. This is strongly evident at X/D of 4. This diverted cross-wind flow then expands laterally behind the jets to maintain the axial velocity there, while itself beginning to decelerate, as seen at X/D of 8.

The axial distribution of grid planes was concentrated about the jet entries in order to adequately define the initial events taking place. This results in the pleasing profile comparisons for X/D of 4. Downstream, the axial distribution of grid planes was sparse. It is therefore believed the delayed deceleration of the inner flow arises because of inadequate axial grid planes.

As this calculation required considerable time to reach a converged solution, an economy measure was adopted for subsequent runs. This involved raising the criterion for convergence from the 0.5 percent residual source sum normally used to a value of 5 percent.

A comparison of calculated profiles of mean axial velocity at the two levels of convergence is enough to justify use of the relaxed criterion for subsequent calculations.

Additional calculations were made for jets with the same pitch to diameter ratio of 2, but having a height to diameter ratio of 8. A 34 x 19 x 19 grid was used. Profiles of dimensionless mean axial velocity in the plane of a jet centerline at a number of axial stations are compared in Figure 75.

The comparisons of Figure 75 contrast those of Figure 74 in that for the height to diameter ratio of 8 the profiles close to the floor are reasonably well calculated quantitatively, but the peak of excess velocity is not for X/D greater than 4. In the calculations for the height to diameter ratio of 4 the profiles close to the roof and the excess velocity peak were well represented while those near the tunnel floor were not. The results are similar to those for Crabb's single jet.

P/D = 2 : H/D = 8

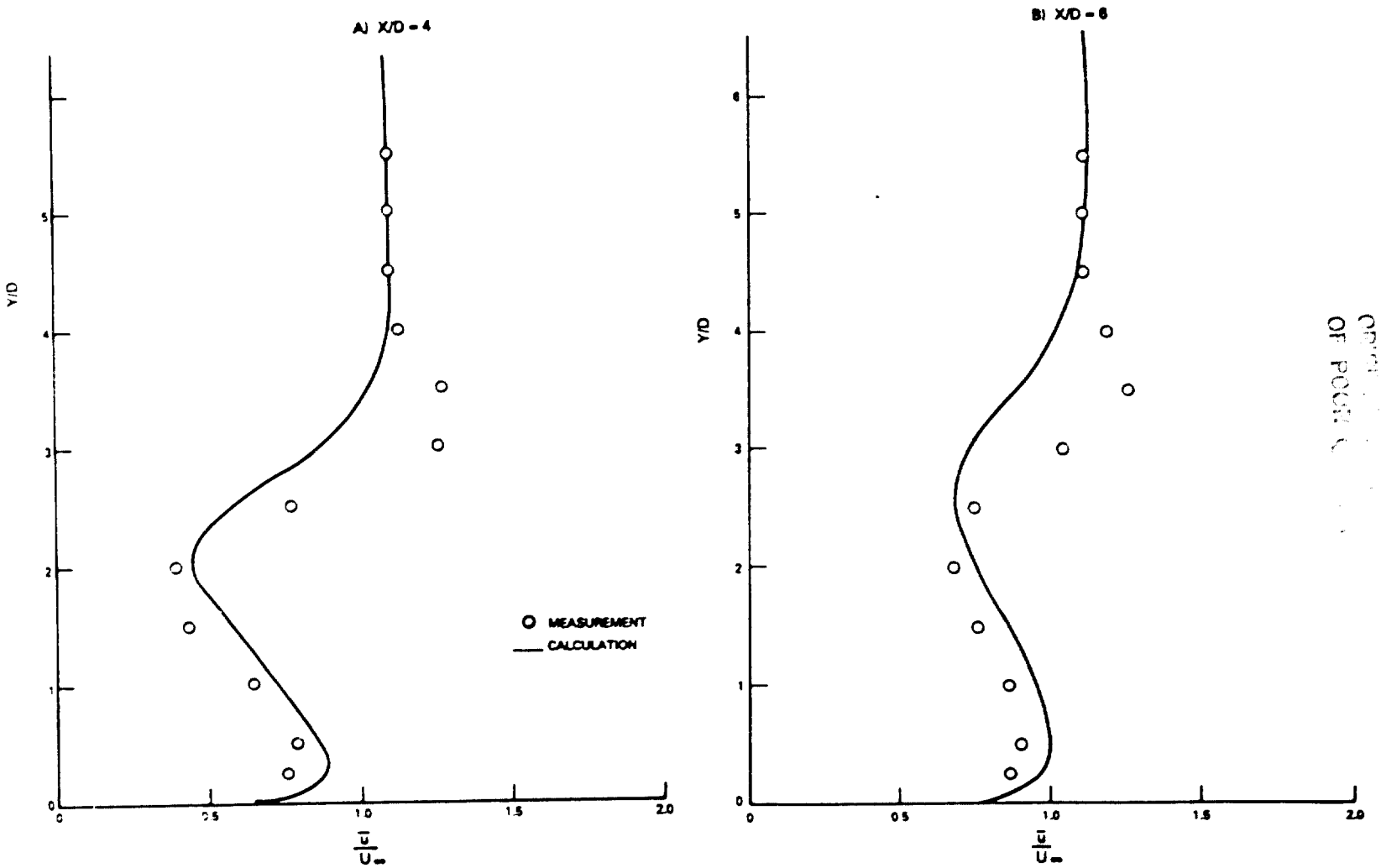

Figure 75 Test Case 7 (Khan & Whitelaw) - Mean Axial Velocities in Line With Jets for Line of Jets in Crossflow

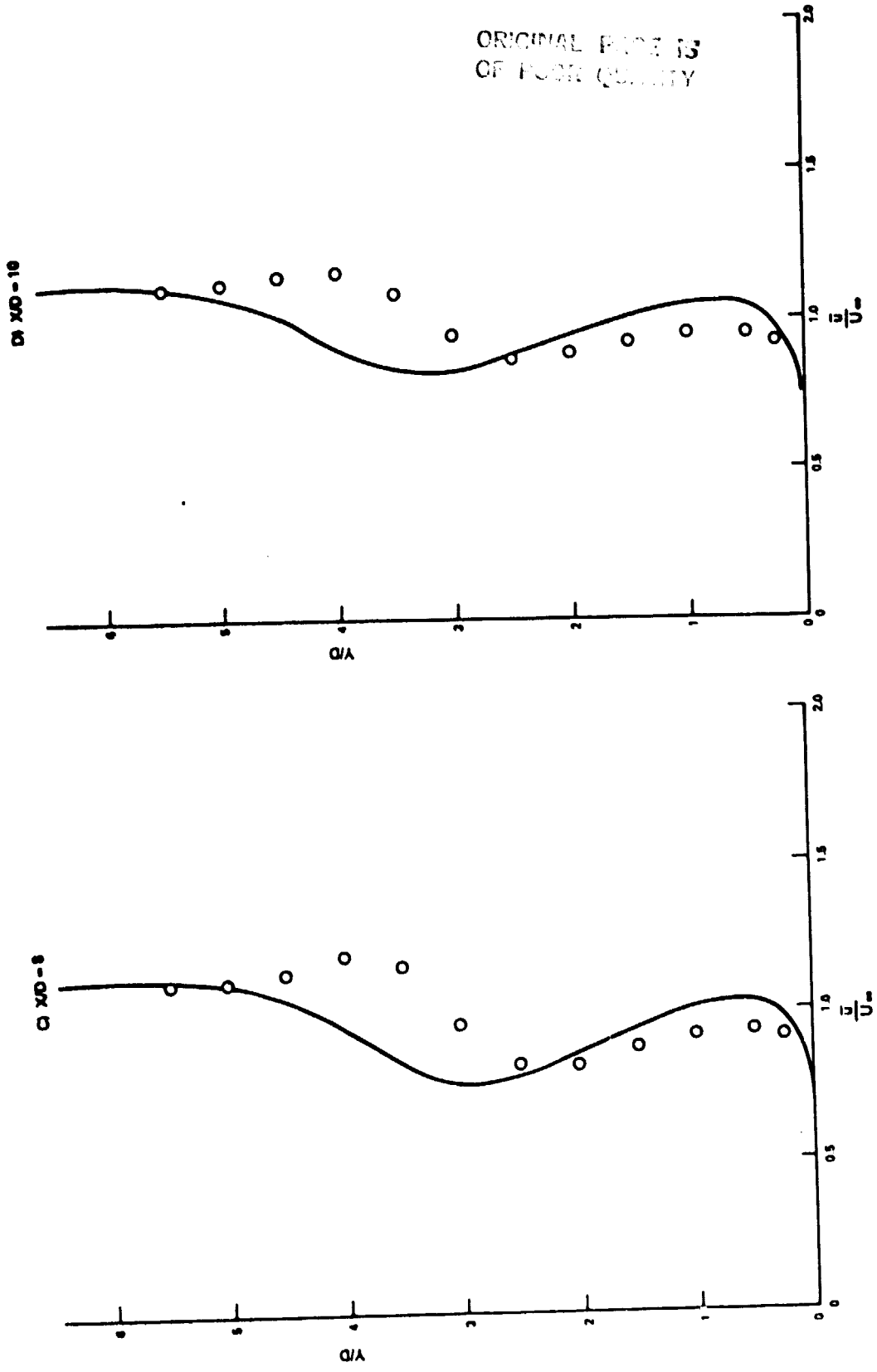

Figure 75 (continued)

Parts of the symmetry boundary condition were checked-out and used in Test Case 7. The remaining symmetry condition (upper and lower) was used to conserve grid nodes for the opposed jets in cross flow test case, Test Case 8. Again, the differences were negligible so the upper and lower symmetry condition was also used.

The case to be considered was for a jet to cross-wind velocity ratio of 2.3 with the opposed lines of jets 4 jet diameters distant from each other and the jets in a line pitched 2 jet diameters apart. Using the symmetry conditions the cross sectional calculation area was 2 jet diameters high with a plane of symmetry, and its width was 1 jet diameter with planes of symmetry on either side. The grid used was 34 x 19 x 11, and the jet origin was represented by 10 x 5 grid lines, as with Crabb's jet.

Figure 76 compares measured and calculated transverse profiles of dimensionless mean axial velocity at three levels from the floor of the wind tunnel, at 6 jet diameters downstream from the hole centerline.

It is immediately apparent from Figure 76 that although the calculation reproduces the shapes of the measured profiles reasonably correctly, there appears to be a mass flow discrepancy between the experiment and the calculations.

The cross-sectional area of the calculation domain, which is for one half jet and uses symmetry planes, is 2D high by D wide, $2D^2$. The cross-wind volumetric flow into this area is $2D^2U_\infty$. For a velocity ratio uj/U_∞ of 2.3 the jet volumetric flow into the calculation domain is one half hole area $\pi D^2/8$, multiplied by $2.3U_\infty$. Hence, the total volumetric flow is the sum of these, or, $2.9032D^2U_\infty$. The mean velocity leaving the section is therefore $1.4516U_\infty$. This simple accounting provides a continuity check on the calculations and measurements. The calculated mean velocities leaving the section satisfy this limit. Consideration of the measured profiles in Figure 76 together with the assumption of a smooth function variation between the Y-planes, indicate that the experiment does not satisfy this continuity check.

If the velocity ratio in the experiment were actually unity instead of 2.3, then continuity would be satisfied. Kahn (Reference 42) did in fact, make some measurements for such a condition, and it is possible some of his figures were mislabelled. In view of this problem the case was not proceeded with.

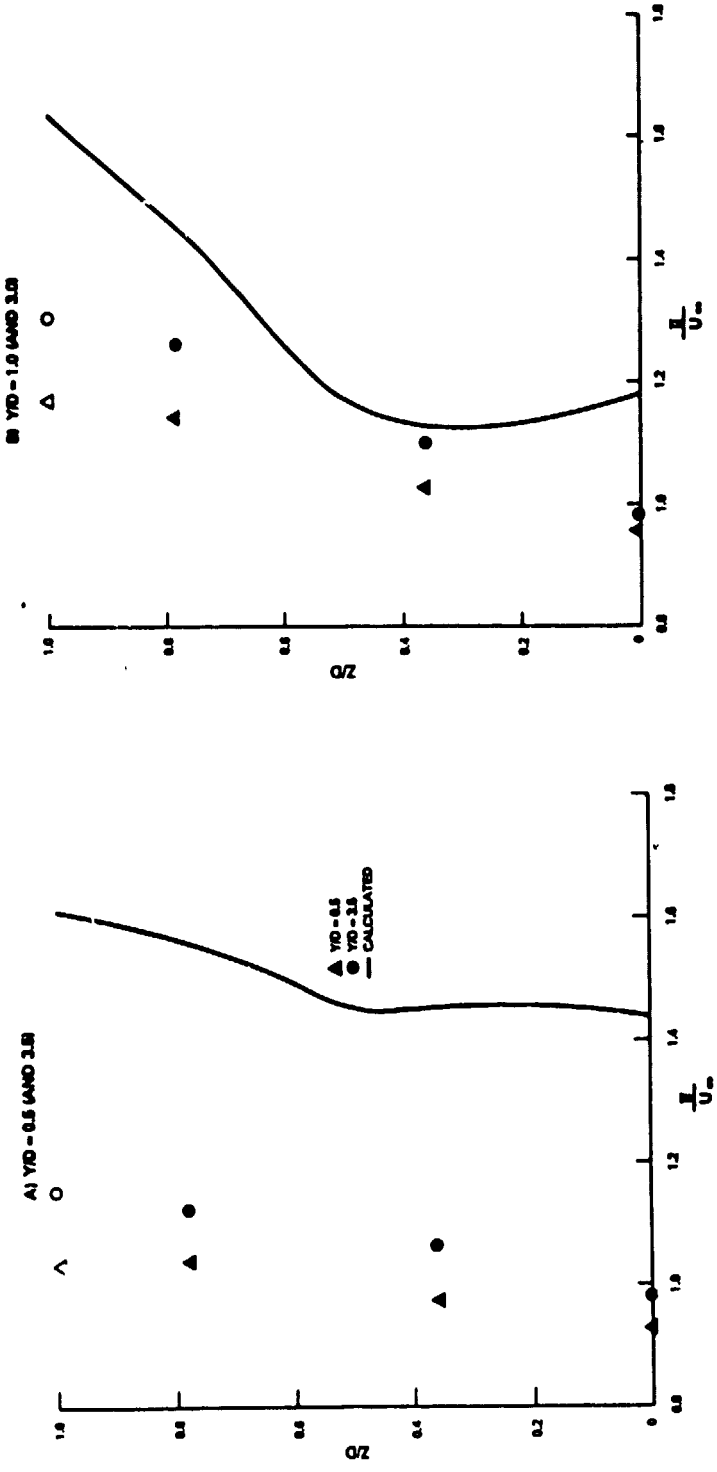

Figure 76 (Test Case 8) Khan's Opposed Rows of Jets in Crosswind - Comparison of Lateral Profiles of Mean Axial Velocity at Several Planes Parallel to Tunnel Floor and at X/D of 6

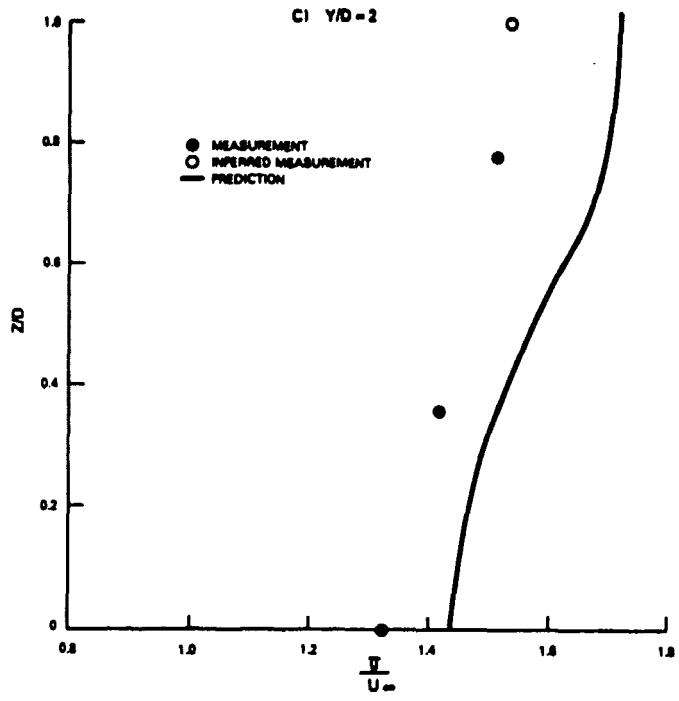

Figure 76 (continued)

8.2.7 Radiation

Test Case 11 was an exact thermal radiation calculation using the spectral method of Semerjian & Segalman. The case used for this study was a reacting flow case from Test Case 9 (Roquemore's experiment). The 2D-TEACH radiation calculation was compared with the more "exact" spectral calculation made using the TIERS code. The radiation fluxes to the wall were compared at two axial locations of 25.3 and 74 cm from the face of the flameholder. The tunnel operating conditions were 2 kg/s airflow and 16 kg/hr propane.

Table 15 summarizes the results of the comparison. Two TIERS calculations were made: one using the full products for combusting propane in air, and one using the "radiation products" assumed in the TEACH radiation calculation, consisting of carbon dioxide and water vapor only.

Table 15

Radiation Comparison

CASE	TEACH	TIERS (CO_2+H_2O)	TIERS (full combustion products)
F L U X 25.3 cm	1.489	0.802	0.367
74 cm	0.090	0.031	0.015

W/cm^2

The comparison shows that the neglect of soot radiation together with the conclusion that radiation heat transfer only affects the flow field to a minor degree for Test Case 9 were justified on a relative basis. However, it does suggest that the single flux method used in TEACH is unacceptably inaccurate.

The conclusion regarding accuracy is somewhat surprising in view of the previous comparisons that Pratt & Whitney Aircraft had made in its own investigations of the radiation model. These comparisons had shown acceptable agreement of the TEACH radiation and gas emissivity models in a flow situation very similar to that of Test Case 9, with a Monte Carlo solution. The maximum wall heat fluxes agreed within 5 percent, and the emmisivities with Pratt & Whitney Aircraft's empirical gaseous emissivity data base. The overall radiation levels in Test Case 9 were very low (less than 1/10th those of the Monte Carlo comparison and less than 1/20th those of gas turbine combustors). It had been observed in the comparison with the Monte Carlo calculations that the single flux model did tend to overestimate at low levels of radiation.

There remain some questions concerning the setup of the TIERS calculation itself, and also how the TEACH radiation model handles intervening gas layers. More investigations are required to resolve these questions.

The TIERS results in themselves indicate that when the overall level of gaseous radiation is low (low operating equivalence ratio), the radiation calculation should include the full range of combustion products, and not just the strong emitters carbon dioxide and water vapor.

Additional comparisons are clearly needed, particularly at more representative radiation levels.

8.3 Assessment of Model Performance

The two equation, K-ε turbulence model performs tolerably well for co-axial jets in confined sudden expansion and for constant density bluff body flows (see References 17, 32 and 80 also). For isothermal variable density systems use of a constant turbulent Schmidt number for turbulent mass transport is inappropriate (see Reference 93 also). Table 16 gives values for turbulent Schmidt numbers that have been found suitable for various flow situations. Using hybrid differencing mean concentration profiles can be calculated reasonably accurately using recommended turbulent Schmidt numbers provided the flow field does not contain a large number of stagnation points. Recirculation zone sizes and strengths and mean velocity profiles can be calculated fairly accurately. Turbulence quantities are calculated with qualitative accuracy.

Table 16

Appropriate Turbulent Schmidt Numbers for Nonreacting Flows and Using Hybrid Differencing and K - ε Turbulence Model

Flow Type	Characteristics	$\bar{\sigma}_t$
Boundary layers	Predominantly unidirectional	0.9
Round free jets	2-D, external entrainment	0.7
Simple recirculation zones	Simple stagnation systems	0.5
Confined round jets	2-D, self-entrainment	0.7
Complex recirculation zones	2 or 3-D, multiple stagnation points, multiple recirculations	0.2

While it is difficult to separate all the effects in the swirling flow cases studied (see Reference 70), it does seem that the K-ε model is inadequate. The critical swirl number range for the existence of an internal recirculation is not calculated correctly. Excessive viscosity (either from the model or false diffusion or both) in the calculation rapidly reduces free vortex swirl to forced vortex swirl, see Figure 77, while flows that are naturally forced vortex in nature are better calculated, Figure 78. The back-pressure effects on the recirculation zone shown in Figure 13 are not calculated at all. Although some swirling flows were calculated tolerably well, the overall model performance has to be considered as poor.

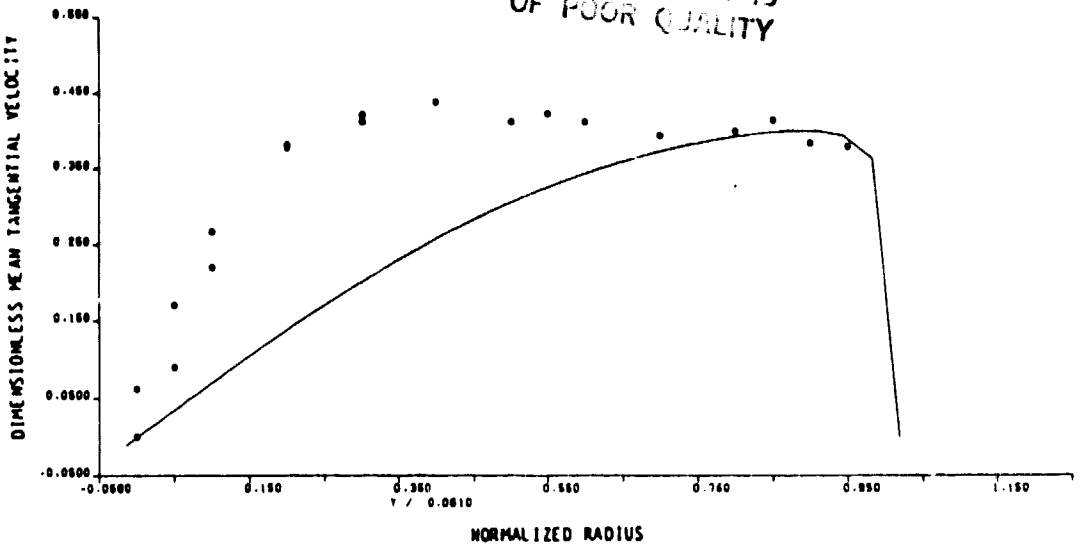

Johnson & Roback's experiment at
30.6 cm from expansion

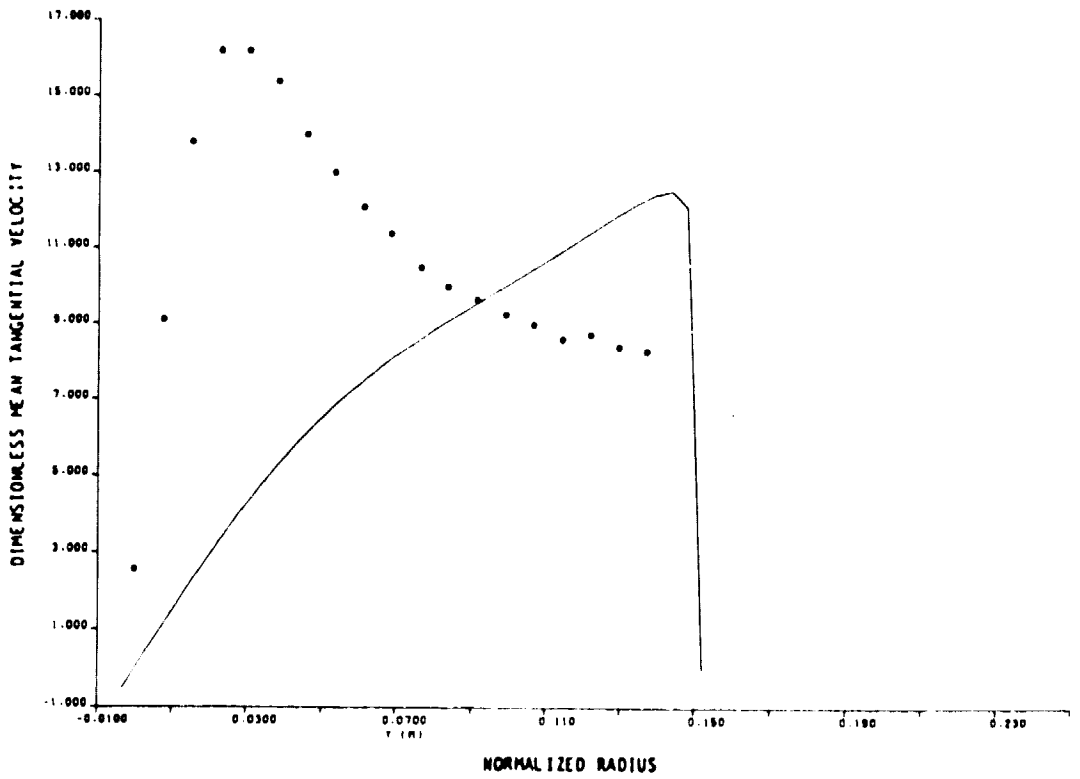

Yoon & Lilley's experiment at
45 cm from expansion

Figure 77 Failure to Calculate Free Vortex/Forced Vortex Core Flows Due to Excessive Viscosity

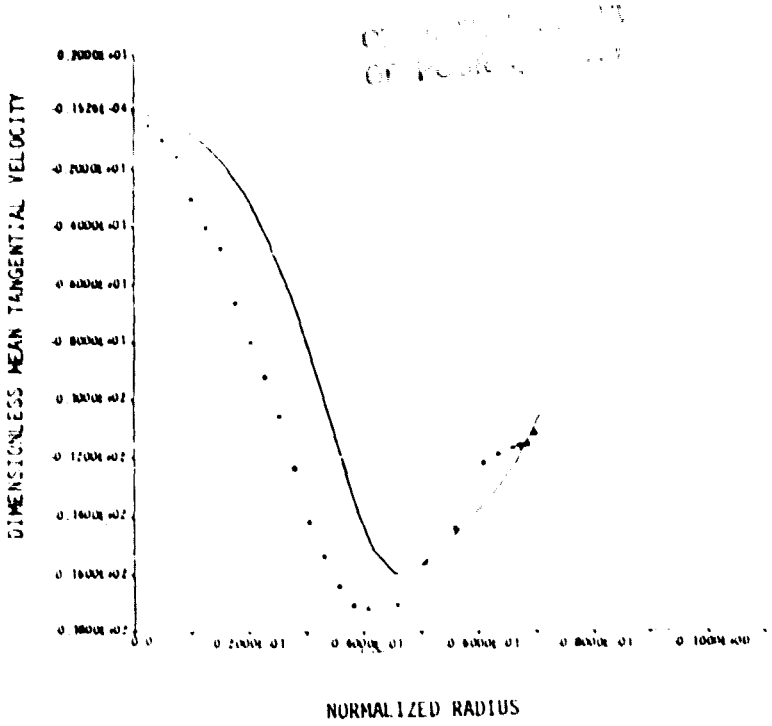

Vu & Gouldin's counterswirl experiment
at 17 cm from confluence

Figure 78 Forced Vortex Flows Are Calculated at Least Qualitatively with K - ε Turbulence Model and Hybrid Differencing

The liquid fuel spray model has performed well so far as it was tested. However, a better statistical approach for the liquid boundary conditions appears desirable.

As anticipated, when compared with a reacting flow of low equivalence ratio at ambient operating conditions, the eddy break-up combustion model showed its lack of "chemical viscosity" due to the infinitely fast reaction rate assumption embodied in it. This is not really so much a fault of the model per se, as it is the result of applying it inappropriately. However, it does show that for calculations at low engine power levels a model with finite-rate chemistry is necessary.

In the jet-in-crossflow studies using 3D-TEACH, the general features of the flows were correct, and some regions of good quantitative agreement were achieved. Unfortunately, the calculations were totally dominated with false diffusion arising from the coarse grids it was necessary to use, so that quantitative accuracy could not really be achieved. However, there was nothing in the calculation at this level to cast doubt on the turbulence model.

The problems of making three-dimensional calculations with the present numerics are highlighted in Table 17. On the basis of this table, the code in its current form can hardly be considered a viable tool for complete, three-dimensional combustion chamber calculations, irrespective of the performance or lack of it in the physical modeling.

Table 17

Comments on Three-Dimensional Calculations Based on Jets-In-Crossflow Experience

General Observations:

- o Difficulties in representing circular jet port with rectilinear grid
- o Convergence rate adversely affected by sudden changes in grid density
- o Inadequate resolution for even single jet (10,000 nodes, 4 MEG machine)
- o Excessive CPU times required even with symmetry boundary condition:

Single jet:	54 mins. (0.5% convergence)
Line of jets:	111 mins. (P2H4 @ 0.5%), 45 mins. (P4H8 @ 5%)
Opposed lines of jets:	305 mins. (5% convergence)

- o Excessive numerical diffusion

Pe > | 2 | everywhere
Pe > 100 over most of field
Pe > 1000 in places

The single-flux radiation model, like the combustion model, was tested using a test-case that was somewhat inappropriate and its suitability at more representative radiation levels remains to be assessed. It is of course, only an interim model.

Further testing of the combustion, spray and radiation models is indicated as necessary. No attempt was made to delineate any effects due to the modeled conservation equations being unweighted. This aspect can only be examined when some of the other, more important first order, effects have been resolved.

It should be noted that the planned step of examining complex flows to determine individual model interactions could not be carried out. This was because of the problems uncovered with the model performances and the lack of suitable experiments. In general, it was not necessary to consider the accuracy of the calculations for turbulence quantities as the mean flows revealed the problems. Detailed analyses of the reasons behind the physical model shortcomings have not been presented.

9.0 CONCLUDING REMARKS

Phase I has proved useful in that it has provided a detailed and systematic examination of the physical modeling used, and it has shown the weaknesses inherent in this modeling. It has also provided substantial insight into the powerful influences exerted on solution accuracy by the inlet boundary conditions, and the numerics used in the computer codes.

The study made it apparent that serious difficulties exist with the present generation of computational fluid dynamics codes for application to the combustor. These difficulties are not perceived as being fatal however. The economic and competitive driving forces in the industry that gave rise to the codes are still real and urgent, and the codes have indeed demonstrated great potential for productivity improvement in addition to great technical capability. Acceptance of computational methods at the working level is continuously growing. Ways to improve the existing methods exist, and others can be devised. There is no reason or need to abandon the effort. Improvement of the codes should be continued.

It was revealed that the two-dimensional code currently is suitable for general engineering use in scale-up, parametric and diagnostic studies. The three-dimensional code is best limited to use in skilled hands as a diagnostic tool for problems of fairly narrow scope. The lack of a viable design tool is a matter of serious concern. Vigorous action is needed to remedy this situation.

10.0 SUMMARY OF RESULTS

A comprehensive study was carried out on the physical modeling embodied in state-of-the-art computational fluid dynamics codes applied to the gas turbine combustor. Although a rather confused and certainly complex picture emerged from this study, a number of clear conclusions were drawn, and a summary of the results is given below:

1. A complete set of good benchmark test cases covering the range of constituent flows describing the gas turbine combustor is not available.

2. A hierarchy of physical modeling exists, and the accuracy achieved with a given model depends as much on preceding models in this hierarchy as on the particular model itself.

3. The turbulence model is deficient in momentum transport for swirling flows, and in mass transport for complicated recirculation zones.

4. The solution accuracy depends to large measure on boundary condition assumptions and to some extent on the calculation grid.

5. Three-dimensional calculations are totally dominated by the TEACH-numerics for practical amounts of computer storage and processing time.

NOMENCLATURE

Commonly Used Symbols in the Text and Figures

Lower Case Symbols

d_f	flameholder diameter
$\bar{f}$	mean mass fraction of species
l_T	length scale of turbulence
$\dot{m}_a$	mass flow rate of air
$\bar{m}_{fu}$	time-mean mass fraction of fuel
$\bar{m}_{ox}$	time-mean mass fraction of oxidant
$\bar{m}_{pr}$	time-mean mass fraction of products of combustion
$\bar{p}$	time-mean static pressure
r	radial axis
t	time
u	axial velocity (along x-axis)
u_j	jet initial velocity
$u_{f,\ell}$	centerline velocity of fuel jet
$\bar{u}_{air}$	mass average velocity of air
v	radial velocity (along r-axis)
w	tangential velocity (along θ-axis)
x	axis in preferred direction of flow

Upper Case Symbols

C_D	droplet drag coefficient
D	jet initial diameter
$\bar{F}$	mean mass fraction of species
H	height of tunnel
H_{fu}	heating value of fuel
K	specific kinetic energy of turbulence
L	latent heat of evaporation for fuel

NOMENCLATURE

Commonly Used Symbols in the Text and Figures (continued)

Upper Case Symbols

M_w	molecular weight
P	pitch of air jets
$\bar{P}_t$	time-mean pressure due to turbulence
R	gas constant
S	source term
SN	swirl number
$\bar{T}$	time-mean temperature
T_g	gas temperature
U_∞	undisturbed mainstream velocity
Y	vertical distance normal to x-axis
Z	transverse distance normal to x-axis

Greek Symbols

Γ	turbulent exchange coefficient
δ_{ij}	Kronecker delta
ε	dissipation rate of K
θ	any scalar quantity
μ_t	turbulent or eddy viscosity
ν	kinematic viscosity
ρ	density
σ_t	turbulent Schmidt number
ϕ	any independent variable
Ω	void fraction

overbar	denotes time-mean, generally
'	denotes a quantity that fluctuates randomly with time

Other symbols are defined in the text.

REFERENCES

1. "Fundamentals of Gas Turbine Combustion," Edit. M. Gerstein, Proc. Workshop at Lewis Research Center, NASA Conference Publication 2087, February 6-7, 1979.

2. Summary Report: DOD Colloquium on Gas Turbine Combustor Modeling, Edit. S.N.B. Murthy, Project SQUID Technical Report PU-R1-79, November 1979.

3. Sturgess, G. J., "Gas Turbine Combustor Design Challenges for 1980's," Paper No. AIAA-80-1285, AIAA/SAE/ASME 16th. Joint Propulsion Conference, Hartford, Connecticut, June 30-July 2, 1980.

4. Odgers, J., "Combustion Modelling Within Gas Turbine Engines, Some Applications and Limitations," AGARD Conference Proceedings No. 275, Proc. Propulsion and Energetics Panel 54th. (B) Specialists' Meeting, DFVLR, Cologne, Germany, 3-5 October, 1979, pp. 25-1 - 25-14.

5. Lilley, D. G., "Flowfield Modeling in Practical Combustors: A Review," J. Energy, Vol. 3, No. 4, July-August 1979, pp. 193-210.

6. Serag-Eldin, M. A. and Spalding, D. B., "Computations of Three-Dimensional Gas Turbine Combustion Chamber Flows," Paper No. 78-GT-142, ASME Gas Turbine Show and Conference, Wembley, England, 1978.

7. Swithenbank, J., Turan, A., Felton, P. G. and Spalding, D. B., "Fundamental Modelling of Mixing, Evaporation and Kinetics in Gas Turbine Combustors," AGARD Conference Proceedings No. 275, Proc. Propulsion and Energetics Panel 54th. (B) Specialists' Meeting, DFVLR, Cologne, Germany, 3-5 October, 1979, pp. 2-1 - 2-21.

8. Abou Ellail, M. M. M., Gosman, A. D., Lockwood, F. C. and Megahed, I. E. A., "Description and Validation of a Three-Dimensional Procedure for Combustion Chamber Flows," Turbulent Combustion, Edit. L. A. Kennedy, Progress in Astronautics and Aeronautics, Vol. 58, AIAA, 1978, pp. 163-190.

9. Khalil, E. E., Spalding, D. B. and Whitelaw, J. H., "The Calculation of Local Flow Properties in Two-Dimensional Furnaces," Int. J. Heat Mass Transfer, Vol. 18, 1975, pp. 775-791.

10. Gosman, A. D. and Ideriah, F. T. K., "TEACH-2E: A General Computer Program for Two-Dimensional, Turbulent, Recirculating Flows," Imperial College, London, England, Mech. Engrg. Report (unnumbered), June 1976.

11. Hinze, J. O., Turbulence, 2nd. Edition, McGraw-Hill, 1975, pp. 20-24.

12. Gosman, A. D., Lockwood, F. C. and Syed, S. A., "Prediction of a Horizontal Free Turbulent Diffusion Flame," 16th. Symposium (International) on Combustion, The Combustion Institute, 1976, pp. 1543-1555, (see discussion).

13. Jones, W. P. and Whitelaw, J. H., "Calculation Methods for Reacting Turbulent Flows: A Review," Combustion and Flame, Vol. 48, 1982, pp. 1-26.

14. Prandtl, L., "Über ein neues Formel System für die Ausgebildete Turbulenz," Nachrichten von der Akad. der Wissenschaft in Göttingen, Math. Phys. Kl., 1945.

15. Kolmogorov, A. N., "Equation of Turbulent Motion of an Incompressible Fluid," Isz. Akd. Nauk. SSR Ser. Phys., Vol. 6, 1942, p. 56.

16. Harlow, F. H. and Nakayama, P. I., "Transport of Turbulence Energy Decay," Los Alamos Scientific Lab. Report LA-3854/UC-34 Physics/TID-4500, 1968.

17. Syed, S. A. and Sturgess, G. J., "Validation Studies of Turbulence and Combustion Models for Aircraft Gas Turbine Combustors," Proc. Symp. Momentum and Heat Transfer Processes in Recirculating Flows, Edit. B. E. Launder and J. A. C. Humphrey, ASME HTD-Vol. 13, ASME Winter Annual Meeting, Chicago, Illinois, November 16-21, 1980, pp. 71-89.

18. Soo, S. L., Fluid Dynamics of Multiphase Systems, Blaisdell Publishing Co., 1967.

19. Williams, A., "Combustion of Droplets of Liquid Fuels: A Review," Combustion and Flame, Vol. 21, 1973, pp. 1-31.

20. Gosman, A. D. and Ioannides, E., "Aspects of Computer Simulation of Liquid-Fuelled Combustors," Paper No. AIAA-81-0323, 19th. Aerospace Sciences Meeting, St. Louis, Missouri, 1981.

21. Lockwood, F. C., Salooja, A. P. and Syed, S. A., "A Prediction Method for Coal-Fired Furnaces," Combustion and Flame, Vol. 38, 1980, p. 38.

22. Magnussen, B. F. and Hjertager, B. H., "On Mathematical Modelling of Turbulent Combustion with Special Emphasis on Soot Formation," Proc. 16th. Symposium (International) on Combustion, The Combustion Institute, 1978, pp. 719-729.

23. Mason, H. B. and Spalding, D. B., "Prediction of Reaction Rates in Turbulent Premixed Boundary Layer Flows," Proc. First Symposium (European) on Combustion, Academic Press, 1973, pp. 601-606.

24. Hottel, H. C. and Sarofim, A. F., Radiation Transfer, McGraw-Hill, New York, 1967, p. 326.

25. Bartelds, H., "Development and Verification of Radiation Models," AGARD Conference Proceedings No. 275, Combustor Modeling, Propulsion and Energetics Panel 54th. (B) Specialists' Meeting, DFVLR, Cologne, Germany, 3-5 October, 1979, pp. 11-1 & 11-20.

26. Spalding, D. B., "A Novel Finite-Difference Formulation for Differential Expressions Involving Both First and Second Derivatives," Intl. J. Numerical Methods in Engineering, Vol. 4, 1972, pp. 551-559.

27. Carretto, L. S., "Two Calculation Procedures for Steady, Three-Dimensional Flows with Recirculation," Proc. Third International Conference on Numerical Methods in Fluid Dynamics, Springer-Verlag, 1972, pp. 60-68.

28. Paceman, D. W. and Rachford Jr., H. H., "The Numerical Solution of Parabolic and Elliptic Differential Equations," J. Soc. Industrial Applied Math., Vol. 3, 1955, pp. 28-41.

29. Roach, P. J., Computational Fluid Dynamics, Aermosa Publishers, New Mexico, 1976.

30. Leonard, B. P., "A Survey of Finite Differences of Opinion on Numerical Muddling of the Incomprehensible Defective Confusion Equation," Applied Mechanics Division, ASME Winter Annual Meeting, New York, December 1979.

31. Boni, A. A., "Comments on the Computational Aspects of Turbulent Combustion," Acta Astronautica, Vol. 6, 1979, pp. 991-995.

32. Sturgess, G. J. and Syed, S. A., "Widely-Spaced Co-Axial Jet, Diffusion-Flame Combustor: Isothermal Flow Calculations Using the Two-Equation Turbulence Model," Paper No. AIAA-82-0113, AIAA 20th. Aerospace Sciences Meeting, Orlando, Florida, January 11-14, 1982.

33. Leonard, B. P., "A Stable and Accurate Convective Modeling Procedure Based on Quadratic Upstream Interpolation," Computer Methods in Applied Mechanics and Engineering, Vol. 19, 1979, pp. 59-98.

34. Raithy, G. D., "Skew Upstream Differencing Schemes for Problems Involving Fluid Flow," Computer Methods in Applied Mechanics, Vol. 9, 1976, pp. 153-164.

35. Johnson, B. V. and Bennett, J. C., "Mass and Momentum Turbulent Transport Experiments with Confined Coaxial Jets," NASA CR-165574, November 1981.

36. Johnson, B. V. and Roback, R., "Mass and Momentum Turbulent Transport Experiments with Confined Coaxial Jets," to be published June 1983.

37. Habib, M. A. and Whitelaw, J. H., "Velocity Characteristics of Confined Jets With and Without Swirl," Paper No. ASME 79-WA/FE-21, ASME Winter Annual Meeting, December 1979.

38. Vu, B. T. and Gouldin, F. C., "Flow Measurements in a Model Swirl Combustor," Paper No. AIAA-80-0076, AIAA 18th. Aerospace Sciences Meeting, January 1980.

39. Yoon, H. K., Five Hole Pitot Probe Time-Mean Velocity Measurements in Confined Swirling Flows, M.S. Thesis, Oklahoma State University, July 1982.

40. Kamatoni, Y. and Greber, I., "Experiments on a Turbulent Jet in a Cross Flow," NASA CR-72893, June 1971.

41. Crabb, D., Jets in Crossflow, Ph.D. Thesis, University of London, England, 1979.

42. Kahn, Z. A., Opposed Jets in Crossflow, Ph.D. Thesis, University of London, England, 1982.

43. Lightman, A. J. and Magill, P. D., "Velocity Measurements in Confined Dual Co-axial Jets Behind an Axisymmetric Bluff Body; Isothermal and Combusting Flows," Air Force Report, AFWAL-TR-81-2018, April 1981.

44. Hutchinson, P., Khalil, E. E., Whitelaw, J. H. and Wigley, G., "The Calculation of Furnace-Flow Properties and Their Experimental Verification," Trans. ASME, J. Heat Transfer, Vol. 98, 1976, pp. 276-283.

45. Mellor, R., Chigier, N. A. and Beer, J. M., "Hollow-Cone Liquid Spray in Uniform Air Stream," Cranfield International Symposium Series, No. 11, Combustion and Heat Transfer in Gas Turbine Systems, Edit. E. R. Norster, Pergamon Press, 1971, pp. 291-305.

46. Holdeman, J. B. and Walker, R. E., "Mixing of a Row of Jets with a Confined Crossflow," AIAA Journal, Vol. 15, 1977, pp. 243-249.

47. Wu, H. L., "Comparison of the Performance of Natural Gas and Oil Flames in a Cylindrical Furnace," J. Inst. Fuel, Vol. 42, No. 343, August 1969, pp. 316-322.

48. Godridge, A. M., Thurlow, G. G. and Wallis, J., "A Method of Studying the Influence of Flame Characteristics on Heat Transfer in Furnaces," J. Inst. Fuel, Vol. 32, No. 214, November 1958, pp. 491-505.

49. Grosshandler, W. L., "Radiation from Nonhomogeneous Fires," Factory Mutual Research Report, RC 79-BT-9, September 1979.

50. Semerjian, H. and Segalman, I., "Turbine Engine Infrared Signature (TEIRS) Program," Pratt & Whitney Aircraft Rept. PWA-5352, June 1976.

51. Ramsey, J. W. and Goldstein, R. J., "Interaction of a Heated Jet with a Deflecting Stream," NASA CR-72613, April 1970.

52. Roquemore, W. M., Bradley, R. P., Stutrud, J. S., Reeves, C. M. and Krishnamurthy, L., "Preliminary Evaluation of a Combustor for Use in Modeling and Diagnostics Development," Paper No. 80-GT-93, ASME Gas Turbine Conference, March 1980.

53. Roquemore, W. M., Britton, R. L. and Sandhu, S. S., "Investigation of the Dynamic Behavior of a Bluff Body Diffusion Flame Using Flame Emission," Paper No. AIAA-82-0178, AIAA 20th. Aerospace Sciences Meeting, Orlando, Florida, January 11-14, 1982.

54. Starner, H. and Bilger, R. W., "LDA Measurements in a Turbulent Diffusion Flame with Axial Pressure Gradients," Combustion Science & Technology, Vol. 21, 1980, pp. 259-276.

55. Kent, J. H. and Bilger, R. W., "Turbulent Diffusion Flames," 14th. Symposium (International) on Combustion, The Combustion Institute, 1973, pp. 616-625.

56. Starner, S. H. and Bilger, R. W., "Measurements of Velocity and Concentration in Turbulent Diffusion Flames with Pressure Gradients," Paper No. AIAA-80-0205, AIAA 18th. Aerospace Sciences Meeting, January 1980.

57. Bilger, R. W. and Beck, R. E., "Further Experiments on Turbulent Jet Diffusion Flames," 15th. Symposium (International) on Combustion, The Combustion Institute, 1975, pp. 541-552.

58. Depsky, J. S., "Laser Velocimetry Measurements in a Methane-Fueled Swirl Combustor," M.S. Thesis, Cornell University, August 1982.

59. Oven, M. J., Gouldin, F. C. and McLean, W. J., "Temperature and Specie Concentration Measurements in a Swirl Stabilized Combustor," 17th. Symposium (International) on Combustion, The Combustion Institute, 1979, pp. 363-374.

60. Baker, R. J., Hutchinson, P., Khalil, E. E. and Whitelaw, J. H., "Measurements of Three Velocity Components in a Model Furnace With and Without Combustion," 15th. Symposium (International) on Combustion, The Combustion Institute, 1975, pp. 553-559.

61. Hutchinson, P., Khalil, E. E. and Whitelaw, J. H., "Measurement and Calculation of Furnace Flow Properties," Journal of Energy, Vol. 1, 1977, pp. 212-219.

62. Founti, M., Whitelaw, J. H. and Hutchinson, P., "Measurements of the Kerosene-Fuelled Flow in a Model Furnace," Journal of Energy, Vol. 4, 1980, pp. 273-278.

63. El Banhawy, Y. and Whitelaw, J. H., "Experimental Study of the Interaction Between a Fuel Spray and Surrounding Combustion Air," Paper No. AIAA-79-7020, 1979.

64. Brum, R. D. and Samuelson, G. S., "Two-Component Laser Anemometry Measurements in a Non-Reacting and Reacting Complex Flow Model Combustor," Combustion Institute Paper WSS/CI 82-53, October 1982.

65. Noyce, J. R., Sheppard, C. G. W. and Yamba, F. D., "Measurements of Mixing and Species Concentration Within a Gas Turbine Type Combustor," Combustion Science and Technology, Vol. 25, 1981, pp. 209-217.

66. Yule, A. J., Sen, A. C., Felton, P. G., Yngut, A. and Chigier, N. A., "A Laser Tomographic Investigation of Liquid Fuel Spray," 18th. Symposium (International) on Combustion, The Combustion Institute, 1981, pp. 1501-1510.

67. Modaress, D., Wuerer, J. W. and Elgobashi, S., "An Experimental Study of a Turbulent Round Two-Phase Jet," Paper No. AIAA-82-0964, AIAA/ASME 3rd. Joint Thermophysics, Fluids, Plasma and Heat Transfer Conference, St. Louis, Missouri, June 7-11, 1982.

68. Soloman, A. S. P., Shuen, J. S., Zhang, Q. F. and Faeth, G. M., "Measurements and Predictions for Non-Evaporating Sprays in a Quiescent Environment," Paper No. AIAA-83-0151, AIAA 21st. Aerospace Sciences Meeting, Reno, Nevada, January 1983.

69. Santoro, R. J., (National Bureau of Standards), Seminar at United Technologies Research Center, 1982.

70. Sturgess, G. J., Syed, S. A. and McManus, K. R., "Importance of Inlet Boundary Conditions for Numerical Simulation of Combustor Flows," Paper No. AIAA-83-1263, to be presented at the AIAA/SAE/ASME 19th. Joint Propulsion Conference, Seattle, Washington, June 27-29, 1983.

71. Rhode, D. L. and Lilley, D. G., "On the Prediction of Swirling Flowfields Found in Axisymmetric Combustor Geometries," Proc. Symp. Fluid Mechanics of Combustion Systems, Edit. T. Morel, R. P. Lohmann and J. M. Rackley, ASME Fluids Engineering Conference, Boulder, Colorado, June 22-23, 1981, pp. 257-266.

72. Rhode, D. L. and Lilley, D. G., "Mean Flowfields in Axisymmetric Combustor Geometries with Swirl," Paper No. AIAA-82-0177, AIAA 20th. Aerospace Sciences Meeting, Orlando, Florida, January 11-14, 1982.

73. Abujelala, M. T. and Lilley, D. G., "Confined Swirling Flow Predictions," Paper No. AIAA-82-0316, AIAA 21st. Aerospace Sciences Meeting, Reno, Nevada, January 10-13, 1983.

74. Yoon, H. K. and Lilley, D. G., "Five-Hole Pilot (sic) Probe Time-Mean Velocity Measurements in Confined Swirling Flows," Paper No. AIAA-83-0315, AIAA 21st. Aerospace Sciences Meeting, Reno, Nevada, January 10-13, 1983.

75. Mathur, M. L. and Maccallum, N. R. L., "Swirling Air Jets Issuing from Vane Swirlers, Part 2: Enclosed Jets," J. Institute of Fuel, May 1967, pp. 238-245.

76. Beyler, C. L. and Gouldin, F. C., "Flame Structure in a Swirl Stabilized Combustor Inferred by Radiant Emission Measurements," Proc. Eighteenth Symposium (International) on Combustion, The Combustion Institute, 1981, pp. 1011-1019.

77. Gouldin, F. C., Depsky, J. S. and Lee, S. L., "Velocity Field Characteristics of a Swirling Flow Combustor," Paper No. AIAA-83-0314, AIAA 21st. Aerospace Sciences Meeting, Reno, Nevada, January 10-13, 1983.

78. Sommer, H. T., "Swirling Flow in a Research Combustor," Paper No. AIAA-83-0313, AIAA 21st. Aerospace Sciences Meeting, Reno, Nevada, January 10-13, 1983.

79. Roquemore, W. M., private communications, 1981, 1982.

80. Syed, S. A. and Sturgess, G. J., "Velocity and Concentration Characteristics and Their Cross-Correlation for Co-Axial Jets in a Confined Sudden Expansion, Part II: Predictions," Proc. Symp. Fluid Mechanics of Combustion Systems, Edit. T. Morel, R. P. Lohmann and J. M. Rackley, ASME Fluids Engineering Conference, Boulder, Colorado, June 22-23, 1981, pp. 150-167.

81. Schlichting, H., Boundary Layer Theory, 4th. Edit., McGraw-Hill, 1960, pp. 466-467.

82. Barber, T. J. and Anderson, O. L., "Evaluation of an Analysis for Axisymmetric Internal Flows in Turbomachinery Ducts," Proc. Symp. Flow in Primary, Non-Rotating Passages in Turbo-Machines, Edit. H. J. Herring, A. Soler and W. G. Steltz, ASME Winter Annual Meeting, New York, December 2-7, 1979, pp. 107-114.

83. Habib, M. A., private communication, July 2, 1980.

84. Gouldin, F. C., private communication, March 3, 1982.

85. Srinivasan, R. and Mongia, H. C., "Numerical Computations of Swirling Recirculating Flow - Final Report," NASA CR-165196, September 1980.

86. Rhode, D. L., "Predictions and Measurements of Isothermal Flow-Fields in Axisymmetric Combustor Geometries," Ph.D. Thesis, Oklahoma State University, Stillwater, Oklahoma, December 1981.

87. Bruce, T. W., Mongia, H. C. and Reynolds, R. S., "Combustor Design Criteria Validation Volume I - Element Tests and Model Validation," AVRADCOM Report USARTL-TR-78-55A, March 1979.

88. Mongia, H. C. and Reynolds, R. S., "Combustor Design Criteria Validation Volume III - User's Manual," AVRADCOM Report USARTL-TR-78-55C, February 1979.

89. Lilley, D. G. and Rhode, D. L, "A Computer Code for Swirling Turbulent Axisymmetric Recirculating Flows in Practical Isothermal Combustor Geometries," NASA Contractor Report 3442, February 1982.

90. Beer, J. M. and Chigier, N. A., Combustion Aerodynamics, John Wiley & Sons, Inc., 1972.

91. Roberts, L. W., "The Prediction of Turbulent Swirling Pipe Flow," Report EF/TN/A/37, Imperial College, London, England, April 1971.

92. Lilley, D. G., private communication, March 1983.

93. Sturgess, G. J. and Syed, S. A., "Multi-Specie Isothermal Flow Calculations of Widely-Spaced Co-Axial Jets in a Confined Sudden Expansion, with the Central Jet Dominant," Paper No. AIAA-82-1156, AIAA/SAE/ASME 18th. Joint Propulsion Conference, Cleveland, Ohio, June 21-23, 1982.

94. Yuen, M. C. and Chen, L. W., "On Drag of Evaporating Liquid Droplets," Combustion Science & Technology, Vol. 14, 1976, pp. 147-154.

95. Roquemore, W. M., et al, "Influence of the Vortex Shedding Process on a Bluff-Body Diffusion Flame," Paper No. AIAA-83-0335, AIAA 21st. Aerospace Sciences Meeting, Reno, Nevada, January 10-13, 1983.

96. Sturgess, G. J. and Syed, S. A., "Dynamic Behavior of Turbulent Flow in a Widely-Spaced Co-Axial Jet Diffusion Flame Combustor," Paper No. AIAA-83-0575, AIAA 21st. Aerospace Sciences Meeting, Reno, Nevada, January 10-13, 1983.

97. Stockman, J. and Betz, H., "Study of Visible Exhaust Smoke from Aircraft Jet Engines," Department of Transportation Report No. FAA-RD-71-22, June, 1971.

98. Whelan, P. F., "The Mechanism of Carbon Formation in Combustion," Paper presented to Inst. Mech. Engrg., London, March 1961.

99. Proc. Course "Prediction of the Performance of Combustion Chambers and Furnaces," The Pennsylvania State University, State College, Pennsylvania, April 19-21, 1978.

100. Magill, P. D., Lightman, A. J., Orr, C. E., Bradley, R. P. and Roquemore, W. M., "Simultaneous Velocity and Emission Measurements in a Bluff-Body Combustor," Paper No. AIAA-82-0883, AIAA/ASME 3rd. Joint Thermophysics, Fluids Plasma, and Heat Transfer Conference, St. Louis, Missouri, June 7-11, 1982.

101. Roquemore, W. M., telephone conversation, March, 1983.

102. Claus, R. W., "Analytical Calculation of a Single Jet in Cross-Flow and Comparison with Experiment," Paper No. AIAA-83-0238, AIAA 21st. Aerospace Sciences Meeting, Reno, Nevada, January 10-13, 1983.

APPENDIX A1

EXAMPLE OF RETRIEVAL SYSTEM FOR DATA BASE

Figure A-1 shows the flow diagram of a retrieval system. The following comments regarding the classification and contents of the elements comprising the data base management retrieval system may be interpreted as applying to the description of the files within a virtual machine environment.

All large computer systems have available powerful data management systems. However, these systems often require that the data base be written in a manner that is peculiar to a particular machine. The format used for the input control and data source elements described below was chosen so as to make the data base (viz-a-viz, the computer program to manipulate the base) readily usable on other computers. Also, because this retrieval system has been designed primarily to be illustrative, little attention has been paid to making this version fail-safe, and methods of producing output that can be used directly by another computer program have not been included.

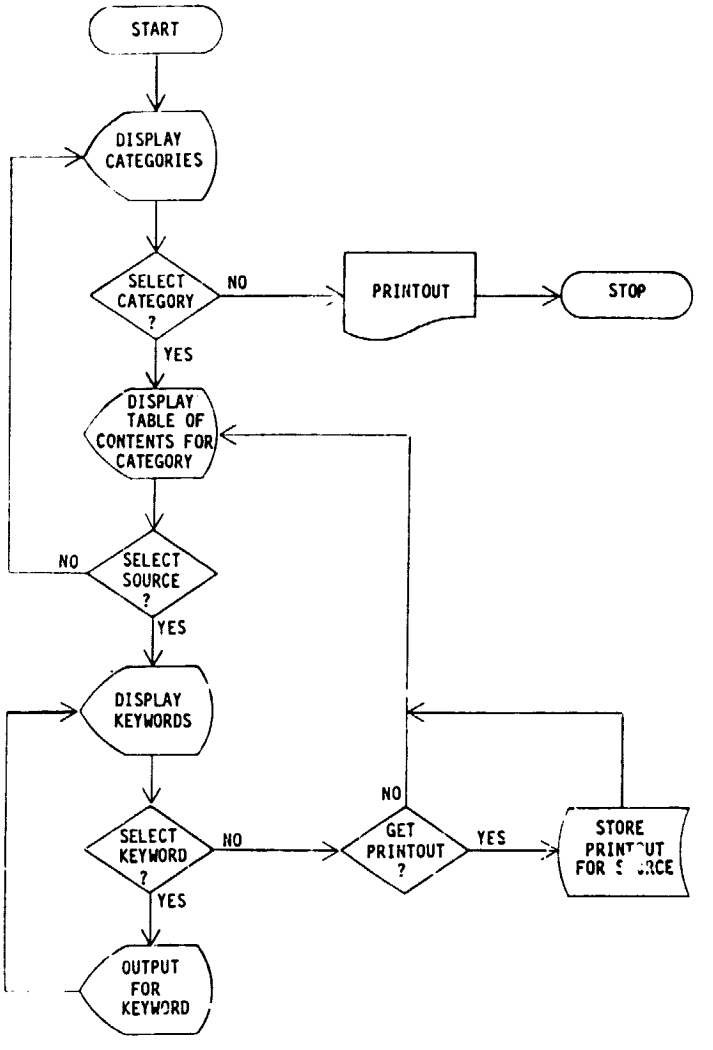

Figure A-1 Flowchart Showing Operation of Data Base Management Computer System

Input Control Elements

There are two types of input control elements in the file. The first of these element types contains the names of the categories of data contained in the data base. The categories currently available are shown in Table A-1. The prefix TOC (for Table of Contents) has been appended to each category. Each full name (prefix + category) appearing in columns 1 through 12 of the card images listed in Table A-1 refers to the name of an element (the second type of input control element) to which the program can refer to determine the sources of data available in the data base. The retrieval program displays for the user the descriptive information contained in columns 21 through 72 during the category selection process. An example of the second type of input control element is shown in Table A-2. Each entry in this table consists of three card images. The first card image contains the name of an element containing all of the information for one source of benchmark quality data. The next two card images contain abbreviated bibliographical information in columns 7 through 72 to aid the user in selecting the appropriate source. The computer program displays these latter cards during the selection process.

Table A-1

Categories Contained in the Data Base

TOCISOTHRM	FLUID MECHANICS - ISOTHERMAL FLOW
TOCEXOTHRM	FLUID MECHANICS - EXOTHERMIC FLOW
TOCSPRAYS	SPRAYS, TWO-PHASE FLOWS
TOCKINETICS	COMBUSTION KINETICS
TOCTURBULNT	TURBULENT COMBUSTION
TOCSOOT	SOOT FORMATION AND DESTRUCTION
TOCRADIATION	RADIATION - ANALYTICAL AND EXPERIMENTAL

Table A-2

Example of Table of Contents Element - TOCRADIATION

```
RADGODRIDGE
      GODRIDGE,THURLOW,WALLIS - METHODS FOR STUDYING FLAME CHARACT. ON
      HEAT TRANSFER IN FURNACES, J.INST.FUEL, 1958 (EXPERIMENTAL)BMARK=3
RADGROSSHDLR
      GROSSHANDER - RADIATION FROM NONHOMOG. FIRES, FACTORY MUTUAL
      REPT., 1979 (ANALYTICAL),BMARK=8
RADOSUWAN
      OSUWAN - RADIATIVE HEAT TRANSFER IN CYLINDRICAL TEST FURNACE,
      PHD DISSERTATION, 1971 (EXPERIMENTAL AND ANALYTICAL), BMARK=4
RADSEMERJ
      SEMERJIAN AND SEGALMAN-TURBINE ENGINE INFRARED SIGNATURE (TEIRS)
      PROGRAM, PRATT AND WHITNEY,1976, (ANALYTICAL),BMARK=9
RADWU
      WU-COMP. OF PERFORMANCE OF GAS + OIL FLAMES IN CYLINDRICAL FURNACE,
      J.INST.FUEL,1969 (EXPERIMENTAL),BMARK=3
```

If a new source is added to the data base for a particular category, then a data source element (described below) is created for the source and added to the file and the Table of Contents element for its category is amended. If a new category is created, then the element shown in Table A-1 is amended, the data source elements for the new sources are added to the file, and a Table of Contents element is created. This simple procedure permits modifications to be made to the data without the necessity of altering the computer program. Furthermore, portability of the data base is enhanced.

Data Source Elements

Each data source element contains the information from a single reference. The element consists of card images containing bibliographical and descriptive information, commentary and data. Portability of the data source elements is assured since card images from one computer system can be readily converted for use on another system.

Each element consists of two major sections. Each card image for the first section consists of a 6-character keyword followed by up to 66 characters of alphanumeric data. The keywords are listed in Table A-3. Columns 73 through 80 of the standard 80-column card image are not used by the retrieval program described below. Keywords less than 6 characters in length are left-justified and filled with blanks. Card images containing the same keyword are grouped in consecutive order. The keywords can be used to control the flow of the data base retrieval program.

Table A-3

Keywords Used in the Data Base

Keyword	Full-Name
CATEGO	CATEGORY
SUBCAT	SUBCATEGORY
SOURCE	SOURCE
EXPERI	EXPERIMENT DESCRIPTORS
BENCHM	BENCHMARK EXPERIMENT RATING
COMMEN	COMMENTARY
MEASUR	MEASURED PARAMETERS
VARIED	VARIED PARAMETERS
INITIA	INITIAL CONDITIONS MEASURED
INSTRU	INSTRUMENTATION
GEOMET	GEOMETRY
TOC	TABLE OF CONTENTS
ENDKEY	END KEYWORDS

The computer program assumes that the keywords will be encountered in the order shown in Table A-3. This restriction is not inherent in the data base. Except as noted, there is no restriction concerning the number of card images having the same keyword except that these card images must be grouped together as noted earlier. Obviously, it is logical to expect that only one card image will be encountered for some keywords. A brief description of each of the keywords in Table A-3 as interpreted by the computer program will now be given.

Keywords CATEGO and SUBCAT

The keyword CATEGO refers to the category, or class, for which the data in the source are relevant. For completeness, the data may be further classified by subcategory (SUBCAT). The categories shown in Table A-1 in practice refer to the subcategories. Only one entry for each of these keywords is expected.

Keyword SOURCE

Entries under SOURCE refer to the bibliographical information such as authors, source title, archival reference, date of publication, authors' organization, etc.

Keyword EXPERI

Five entries are made under this keyword. The first entry is interpreted as the type of data (experimental, analytical, or both) contained in the citation. The second entry refers to the dimensionality of the experiment (or analysis). The third entry describes the medium (e.g., air) while the fourth card image refers to the injectant (e.g., droplets of JP-4). The fifth entry consists of a one-line description of the experiment or analysis.

Keyword BENCHM

The single card image using this keyword gives the benchmark rating, 0 through 10, where 10 represents the highest rating.

Keyword COMMEN

This keyword contains commentary that may aid in the interpretation of the data or in qualifying the benchmark rating.

Keywords MEASUR, VARIED, INITIA and INSTRU

These keywords are used to describe the parameters measured and varied, the initial conditions measured, and the types of instrumentation used.

Keyword GEOMET

The geometry used in the experiment or analysis is described in this section. In some cases, reference is made to tabular information describing the geometry presented under the keyword TOC.

Keyword TOC

This keyword refers to the Table of Contents for the source which lists the tables and figures available in the data source. The format of each of these card images is as follows:

Cols. 1-6	TOC (left-justified)
Cols. 7-12	TABLE or FIGURE (left-justified)
Cols. 13-20	Table or Figure number (integer, right-justified)
Cols. 21-72	Description (alphanumeric data)

In the present context, a TABLE consists of one or more lines of alphanumeric information (e.g., a table of fuel properties); a FIGURE consists of numeric data that can be manipulated or plotted. TABLE entries precede FIGURE entries. Up to 999 tables and 999 figures may be included in the data source element.

Keyword ENDKEY

This keyword is used to terminate the keyword section.

The second section of the data source element is the data section. The information for each table and figure is entered in the same order as the tables and figures are listed in the Table of Contents.

The first line for each TABLE consists of a 72-character alphanumeric title, left-justified. The second line contains an integer, M, right-justified to the tenth column, that indicates how many lines of information follow for this table. The next M card images each contain up to 72 characters of alphanumeric data, left-justified.

The first line for each FIGURE consists of a 72-character alphanumeric title, left-justified. The second card image contains the integers, M and N, right-justified to columns 10 and 20, respectively. The integer M refers to the number of card images that follow the column labels (e.g., the number of entries for the independent variable); the integer N refers to the number of dependent variables ($N \leq 5$).

The next three card images contain alphanumeric information that may be used to label the data columns. Each card image contains N+1 fields of alphanumeric data, 10 characters per field. The computer program inserts blanks between the fields when printing the data as an aid to readability. Each of the following M lines contains a value for the independent variable and the corresponding values for the N dependent variables. The format is (6E10.5).

An example of a data source element is presented in Table A-4.

Table A-4

Example of Data Source Element

```
CATEGO  RADIATION
SUBCAT
SOURCE  GODRIDGE,A.M.,G.G.THURLOW,AND J. WALLIS:
SOURCE  A METHOD OF STUDYING THE INFLUENCE OF FLAME CHARACTERISTICS
SOURCE  ON HEAT TRANSFER IN FURNACES, J.INST.FUEL,
SOURCE  VOL.31, NO.214, NOVEMBER 1958, PP.491-505,
SOURCE  (BRISTISH COAL UTILIZATION RESEARCH ASSOCIATION)
EXPERI  EXPERIMENTAL
EXPERI  AXISYMMETRIC
EXPERI  AIR
EXPERI  TOWN GAS OR METHANE
EXPERI  RADIATION IN CYLINDRICAL FURNACE WITH CONCENTRIC FUEL/AIR JETS
BENCHM  3
COMMEN       THE 3-IN.SQ. ANNULAR AIR PASSAGE DUMPS INTO THE 5-IN.DIA.
COMMEN  FURNACE. THE GAS JET DIAMETERS ARE 3/8 AND 3/16 IN.
COMMEN  NEGLECTING THE THICKNESS OF THE GAS INJECTION TUBE,
COMMEN  WHICH PROTRUDES SLIGHTLY INTO THE FURNACE, ONE CAN
COMMEN  ESTIMATE THE O.D. OF THE AIR PASSAGE.
COMMEN       RESULTS ARE ALSO REPORTED FOR PARTIALLY-PREMIXED MIXTURES
COMMEN  OF FUEL AND AIR. THESE RESULTS ARE NOT INCLUDED IN THE DATA BASE.
COMMEN  A FEW TEST RESULTS WERE OBTAINED COMPARING THE HEAT ABSORBED
COMMEN  PER UNIT WALL AREA FOR TOWN GAS AND METHANE AT NEARLY THE SAME
COMMEN  HEAT INPUT RATE. THE DIFFERENCES DO NOT APPEAR TO BE SIGNIFICANT.
COMMEN       THE WALL HEAT FLUXES ARE DETERMINED FROM THE TEMPERATURE
COMMEN  DROP ACROSS AN ACCURATELY MACHINED SOLID REFRACTORY ROD INSERTED
COMMEN  INTO THE WALL. THE EMISSIVITY OF THIS MATERIAL AND THE ROD
COMMEN  SURFACE TEMPERATURE (I.,E.,THE SURFACE □SEEN□ BY THE COMBUSTION
COMMEN  GASES) ARE NOT REPORTED. THE USEFULNESS OF EITHER THE FLAME
COMMEN  RADIATION DATA OR THE WALL HEAT FLUX DATA IN ASSESSING THE
COMMEN  ACCURACY OF A RADIATION MODEL IS SOMEWHAT LIMITED BY THE LACK
COMMEN  OF INFORMATION ON THE SURFACE TEMPERATURE.
COMMEN       THE AUTHORS ESTIMATE SOOT CONCENTRATION--NOT MEASURED--
COMMEN  FROM THE EMISSIVITY DATA. THEY CONCLUDE THAT THE VALUES OBTAINED
COMMEN  ARE CONSISTENT WITH REPORTED VALUES FOR LOW C/H RATIO FUEL
COMMEN  OILS AND STATE:□THIS AGREEMENT HELPS JUSTIFY THE RADIATION
COMMEN  MEASUREMENTS IN THIS TRIAL.□ FLAME LUMINOSITY IS NEGLECTED
COMMEN  IN ASSESSING THE AXIAL RADIANT HEAT TRANSFER VARIATION.
COMMEN       THE BENCHMARK RATING IS BASED ON (1)THE LACK OF WALL
COMMEN  TEMPERATURE INFORMATION, (2) THE LACK OF INFORMATION
COMMEN  INDICATING WHETHER RADIATION FROM LUMINOUS FLAMES WAS
COMMEN  IMPORTANT, AND (3)THE FACT--COMMON TO MANY EXPERIMENTS--
COMMEN  THAT LOCAL RESULTS MAY BE INFLUENCED BY THE DEGREE OF
COMMEN  MIXEDNESS.
MEASUR  WALL HEAT FLUX
MEASUR  CO2 DISTRIBUTION
MEASUR  AXIAL VARIATION OF COMBUSTION TEMPERATURE
MEASUR  PROPERTIES OF INJECTANT-TOWN GAS (TABLE 1)
VARIED  AIR-FUEL RATIO
VARIED  GAS INJECTOR TUBE DIAMETER
INITIA  FUEL FLOW RATES
INITIA  AIR-FUEL RATIO
INSTRU  THERMOCOUPLES--2 PER HEAT FLUX BLOCK
INSTRU  WATER-COOLED HEAT EXCHANGER FOR CALORIMETRY
INSTRU  □MONO□ RECORDER AND □FYRITE□ APPARATUS FOR CO2
INSTRU  SUCTION PYROMETER WITH PT-PT-13%RH THERMOCOUPLE
INSTRU  RADIATION PYROMETERS
GEOMET  CYLINDRICAL FURNACE,LENGTH=40 IN., I.D.=5 IN.
GEOMET  CENTRAL FUEL INJECTOR TUBE,3/8-IN. AND 3/16-IN. DIA.
GEOMET  CONCENTRIC AIR INJECTOR - 3 SQ.IN. (APPROX.) -- SEE COMMENTARY
TOC   TABLE      1  PROPERTIES OF TOWN GAS
TOC   TABLE      2  OTHER DATA AVAILABLE IN REPORT
TOC   FIGURE     1  EMISSIVITY VS AXIAL DISTANCE
TOC   FIGURE     2  WALL HEAT FLUX VS AXIAL DISTANCE
TOC   FIGURE     3  FLAME RADIATION FLUX VS AXIAL DISTANCE
ENDKEY
```

Table A-4 (continued)

Example of Data Source Element

TABLE 1 PROPERTIES OF TOWN GAS
7
NET CALORIFIC VALUE (BTU/CU.FT.) DETERMINED FROM CALIBRATION RUNS
RUN 1 Q=469
RUN 2 Q=465
RUN 3 Q=457
RUN 4 Q=462
RUN 5 Q=452
NO OTHER PROPERTY DATA REPORTED
TABLE 2 OTHER DATA AVAILABLE IN REPORT
11
C
AXIAL DISTRIBUTIONS REPORTED FOR THE FOLLOWING:
EMISSIVITY--LAMINAR FLOW
AVERAGE GAS TEMPERATURE--LAMINAR AND TURBULENT FLOW
RADIATION FROM FLAME--LAMINAR FLOW
CO2 CONCENTRATION--LAMINAR AND TURBULENT FLOW
WALL HEAT FLUX--LAMINAR FLOW
C
SELECTED INTEGRATED VALUES
PREMIXED FUEL-AIR RESULTS FOR LAMINAR AND TURBULENT FLOW
COMPARISONS OF WALL HEAT FLUXES USING TOWN GAS AND METHANE
FIGURE 1 EMISSIVITY (EPS) VS AXIAL DISTANCE(X)

4	4			
A/F	=5	=6.5	=5	=6.5
INJ.DIAM.	=3/16	=3/16	=3/8	=3/8
X-INCHES	EPS	EPS	EPS	EPS
8.0	0.0	0.31	0.0	0.0
13.0	0.37	0.33	0.31	0.03
20.5	0.22	0.13	0.44	0.38
29.0	0.44	0.21	0.42	0.30

FIGURE 2 WALL HEAT FLUX (QWALL,BTU/HR-FT**2)) VS AXIAL DISTANCE(X)

8	4			
A/F	=5	=6.5	=5	=6.5
INJ.DIAM.	=3/16	=3/16	=3/8	=3/8
X-INCH	QWALL	QWALL	QWALL	QWALL
0.0	900.0	825.0	500.0	300.0
5.0	1350.0	1175.0	950.0	675.0
10.0	2550.0	2075.0	1800.0	1350.0
12.5	3100.0	2500.0	2250.0	1725.0
15.0	3350.0	2650.0	2575.0	2100.0
20.0	3400.0	3050.0	2450.0	2600.0
25.0	3275.0	3275.0	2300.0	2675.0
30.0	3000.0	3000.0	2100.0	2575.0

FIGURE 3 FLAME RADIATION FLUX (QRAD,ERG/SEC-CM**2)) VS AXIAL DISTANCE(X)

8	4			
A/F	=5	=6.5	=5	=6.5
INJ.DIAM.	=3/16	=3/16	=3/8	=3/8
X-INCHES	QRAD10**-7	QRAD10**-7	QRAD10**-7	QRAD10**-7
5.0	1.05	1.35	0.95	0.70
10.0	2.85	3.40	1.80	1.60
12.5	3.95	3.50	2.30	2.30
15.0	4.15	3.15	2.95	2.85
18.5	4.10	2.25	3.60	3.20
20.0	4.00	2.05	3.80	3.15
22.5	3.85	1.95	3.90	2.95
30.0	2.95	1.85	3.30	2.20

Program Operation

The computer program, control elements, and data source elements are contained in a named file. A flowchart summarizing the essential operations of the computer program used to retrieve and display the data is shown in Figure A-1. The computer program is executed as follows:

```
@ASG,A FILE NAME
@USE FILE,FILE NAME
@ADD FILE.START
```

The element START allocates storage for the logical units (Table A-5) used by the program. These logical units include the print file (PRINT) which is assigned to logical unit 20; logical units 8 through 14 are scratch (temporary) units. The computer program is then started. The element describing the categories of data contained in the data base (see Table A-1) is then read and stored.

Table A-5

Logical Units Used by the Program

Logical Unit Number	Purpose
5	Input unit - terminal
6	Output unit - terminal used for input
8	Data source element contents except keywords TOC, COMMEN and ENDKEY and data
9	Data source element - COMMEN
10	Data source element - Table of Contents
11	Data source element - TABLE data
12	Data source element - FIGURE data
13	CATEGORIES element (Table A-1)
14	TOC category element (e.g., Table A-2)
20	Print file

The categories are displayed and the user selects the category that is to be examined. The table of contents element for this category is read and stored. Then, the program retrieves the information contained in the data base for each source listed in the Table of Contents. The first subsection consists of the information for the keywords CATEGO, SUBCAT, SOURCE, EXPERI and BENCHM. The second subsection lists the entries for the keyword COMMEN. The next subsections display the data for keywords MEASUR, VARIED, INITIA, INSTRU and GEOMET, respectively. Finally, the Table of Contents (for TABLE and FIGURE data) is displayed. The user then selects the TABLE or FIGURE to be viewed.

After displaying each subsection, TABLE or FIGURE, the program pauses so that (1) the user may clear the screen if a video terminal without a scrolling provision is being used and (2) the user may elect to continue with the current source or proceed to the next source. If the user elects to proceed to the next source, the program will ask the user if a printed copy of the current source is desired.

After each source is examined, the categories will again be displayed and the above sequence may be repeated. When the user terminates the session, the program will display the command(s) necessary to obtain a printout and it will insert the necessary information into the runstream to detach all logical units (except 5 and 6) shown in Table A-5. After program termination, the user then logs-off the computer.